PROBABILISTIC RELATIONS BETWEEN THERMO-MECHANICAL RESPONSE AND MICROSTRUCTURE OF HETEROGENEOUS ENERGETIC MATERIALS FOR SHOCK/NONSHOCK LOADING

A Dissertation

Presented to

The Academic Faculty

by

Seokpum Kim

In Partial Fulfillment

of the Requirements for the Degree

Doctor of Philosophy in the

School of Mechanical Engineering

Georgia Institute of Technology

December, 2016

PROBABILISTIC RELATIONS BETWEEN THERMO-MECHANICAL RESPONSE AND MICROSTRUCTURE OF HETEROGENEOUS ENERGETIC MATERIALS FOR SHOCK/NONSHOCK LOADING

Approved by:

Dr. Min Zhou, Advisor
School of Mechanical Engineering
Georgia Institute of Technology

Dr. Suhithi Peiris
AFRL, Munitions Directorate
Eglin Air Force Base, FL

Dr. Shuman Xia
School of Mechanical Engineering
Georgia Institute of Technology

Dr. H. Jerry Qi
School of Mechanical Engineering
Georgia Institute of Technology

Dr. Julian Rimoli
School of Aerospace Engineering
Georgia Institute of Technology

Dr. Woo Il Lee
Mechanical and Aerospace Engineering
Seoul National University, Korea

Date Approved: August, 2016

To my parents and sister

ACKNOWLEDGEMENTS

I would like to thank all the people who have helped me during my Ph.D. study. First of all, I want to thank my parents and my sister for their huge support and encouragement. I must thank all of my advisors. To Dr. Min Zhou, thank you so much for your guidance. You have always helped me overcome academic challenges. With your guidance, I was able to perform profound and interesting research and proceed to the next stage of my life. I also thank my committee members, Dr. Suhithi Peiris, Dr. Shuman Xia, Dr. Jerry Qi, Dr. Julian Rimoli, and Prof. Woo Il Lee. Thanks are also due to my previous advisors, Prof. Kangyul Huh at POSTECH and Prof. Woo Il Lee at SNU for research and career advice. I am grateful to Dr. Yasuyuki Horie who has not only provided research directions and valuable insights but also shown himself as a great role model of researcher. I also sincerely acknowledge the close collaboration with Dr. Welle and Dr. Molek at the Air Force Research Lab.

I also want to thank those who have provided me consultations and help for my future career. Special thanks to Dr. Sam Ryu, Dr. Aly Megahed. I also thank Dr. Lindsay, Dr. Yoo, Dr. Pemberton and Dr. Hardin in AFRL. I have special friends to thank. I have made so many good memories at Georgia Tech with my friends. Thanks to MJ, GTKSA-ME friends, GTKSA officers, KSEA-YGPF friends, friends at St Andrew Kim Korean Catholic Church and GT Catholic Center. I am also grateful to my lab members, Ananda, Siddharth, Barrett, Yan, Yifan, Chris Lammi, Chris Miller, Junghwan, Seongseop, Kwangsub, Jongboo, Ushasi, Amir, Yaochi, Dr. Qu, and Dr. Yang. To Sister Philippa (必立), thank you for your prayers.

Finally, I gratefully acknowledge support of my research and education from the US Defense Threat Reduction Agency (DTRA), the Air Force Office of Scientific Research (AFOSR), the Air Force Research Lab (AFRL), and the Kwangjeong Lee Chonghwan Educational Foundation (KEF).

TABLE OF CONTENTS

Page

LIST OF TABLES

LIST OF FIGURES

LIST OF SYMBOLS

Finite Element Discretization	B_{Ij}^0	nodal gradient $\left(B_{Ij}^0 = \partial N_I / \partial X_j\right)$
	δ_{ij}	Kronecker delta
	$\bar{\boldsymbol{t}}^0$	traction vector
	f_{iI}^{ext}, f_{iI}^{int}	external and internal nodal force
	f_{iI}^{kin}	Kinetic nodal force
	$\boldsymbol{F}$	deformation gradient tensor
	$\boldsymbol{P}$	1st Piola-Kirchhoff stress tensor
	$\boldsymbol{S}$	2nd Piola-Kirchhoff stress tensor
	u_i	components of the displacement vector
	δu_{iI}	virtual nodal displacement
	x_i	components of the position vector in the deformed configuration
	N_I	shape function (= interpolation function)
	δW^{ext}	virtual external work
	δW^{int}	virtual internal work
	δW^{kin}	virtual kinetic work
Cohesive Element Model	δ_{nc} , δ_{tc}	critical separations in normal direction and in tangential direction
	η_0	initial elastic limit of the cohesive separation
	Φ	cohesive energy
	λ	cohesive separation
	λ_u	maximum value of λ
	$\overline{T}$	cohesive traction
	T_{max}	maximum traction strength

Parameters in Constitutive Relations

a_T	WLF shift factor which is multiplied to frequency ω
$\beta,\ \kappa$	thermal softening parameters
c_p	specific heat
C_1 , C_2	WLF parameters that adjust the modulus curves at various temperatures to the master curve
$\mathbf{D}'$	deviatoric part of the rate of deformation tensor
$\overline{\varepsilon}$	equivalent plastic strain, $\overline{\varepsilon} = \int_0^t \dot{\overline{\varepsilon}}\, dt$
$\dot{\overline{\varepsilon}}_0$, $\dot{\overline{\varepsilon}}_m$	reference strain rates
ε_0	reference strain
G	shear modulus
G_e	long term modulus when the binder is fully relaxed
G_i	modulus of i-th mode
$\tilde{\mathbf{I}}$	fourth order identity tensor
k	thermal conductivity
$\mathbf{L}$	tensor of elastic moduli
λ, μ	Lamé's first and second constants
m, a	rate sensitivity parameters for a low strain rate and a high strain rate
N	strain hardening exponent
$\vec{q}$	heat flux vector
ρ	density
$\bar{\sigma}$	Misses equivalent stress
σ_0	quasi-static yield stress
T_0	reference temperature

Parameters in Constitutive Relations	∇T	temperature gradient
	τ_h	hydrostatic part of the Kirchoff stress, $\tau_h = \tau_{11} + \tau_{22} + \tau_{33}$
	$\boldsymbol{\tau}'$	deviatoric part of the Kirchoff stress
	$\hat{\boldsymbol{\tau}}'$	deviatoric part of the Jaumann rate of the Kirchhoff stress
	τ^r	relaxation time of a viscoelastic material
	ω	wave frequency of a given mode for a viscoelastic material
	$\dot{W}^p$, $\dot{W}^{fric}$	the rate of plastic work and the rate of frictional dissipation
Parameters for Hotspot and Ignition Analysis	d	diameter of the dominant hotspot
	d_c	minimal diameter of a hotspot required for thermal runaway at temperature T
	E_c , Σ_c , Π_c	cutoff input energy, velocity, and power flux in James relation
	η	grain volume fraction
	m	shape parameter of the Weibull probability distribution
	$P(t)$	cumulative probability of ignition
	S_v , ΔS_v	specific surface area and its variations
	σ	standard deviation of the normal distribution
	t_0	cutoff time below which the probability of ignition is zero
	t_{50}	time at which the probability of ignition is 50%
	$t_{bound,i}$	upper and lower limits of the time to ignition for the i-th sample
	U_S , U_P	shock velocity and particle velocity
	v_c	critical impact velocity below which no ignition is observed

SUMMARY

An approach is developed to predict the ignition sensitivity of heterogeneous energetic materials under shock and nonshock loading as a function of microstructure. The underlying issue of impact-induced initiation of chemical reactions is driven by the deposition of mechanical work into energetic materials in the form of localized heating or the development of hotspots. These hotspots govern the ignition of energetic materials. The aim of this study is to understand the mechanisms of hotspot evolution, computationally predict the ignition sensitivity, and analyze the effects of loading and microstructural attributes on hotspot development and material ignition sensitivity. A computational framework based on a Lagrangian cohesive finite element method (CFEM) is developed. This framework is used to statistically analyze the material sensitivity, accounting for microstructural attributes in terms of morphology, constituent properties, inclusions, and defects. Multiple samples with statistically similar microstructural attributes are generated in a controlled manner and used to obtain a quantitative measure for the statistical variation in ignition behavior due to material heterogeneity.

To relate loading and microstructure to the onset of chemical reaction, a hotspot-based criticality criterion is established. The analysis involves the quantification of hotspots via the CFEM simulations. The approach yields criticality conditions in terms of the critical impact velocity, critical time required for ignition, and total energy required for ignition under a given loading rate. The stochasticity of the material behavior is analyzed using a probability distribution as a function of microstructural attributes including grain volume fraction, grain size, amount of metallic inclusions, and specific binder-grain interface area. A probability superposition model is proposed to delineate the effects of different sources of stochasticity.

The ignition threshold for granular explosives (GXs) and polymer-bonded explosives (PBXs) under shock and nonshock loading are predicted. The particular thresholds predicted are the James-type ignition threshold and the Walker-Wasley ignition threshold. The dependence of the ignition probability on material and microstructure is analyzed for a wide range of loading conditions. The microstructure – ignition threshold relations with the probability envelopes developed in this study provide a guide for the design of new energetic materials.

CHAPTER 1: INTRODUCTION

1.1 Background

Safety in the handling of explosives and the vulnerability to accidental stimuli relate to the sensitivity of the materials [1]. Therefore, researchers have shown increased interest in the sensitivity, but the mechanisms of solid high explosives' reactivity are intricate and still not well understood [2], particularly in the case of shock and non-shock ignition by impact loading. The initiation of heterogeneous energetic composites driven by a projectile has been studied over several decades [3-5]. It has been well established (1) that the initiation starts from an ignition event through subsequent growth to detonation, and (2) that for heterogeneous explosives such as plastic bonded explosives, the local ignition events are induced by the formation of critical hot spots that result in self-sustained reactions [6, 7]. However, events from ignition to growth and finally to steady detonation are a complicated process. Therefore, macroscale reactive burn calculations typically dismiss the initial ignition event parametrically but rather focus on the growth to detonation [8-10]. With such an approach, the consideration of microstructure effects is intricate, and therefore often ignored or simplified to a few parameters.

This research recognizes the limitations of previous approaches and rather focuses on the modeling and simulation that capture underlying physics of initial ignition event at the mesoscale level. The approach of this research accounts for microstructural heterogeneities such as individual constituents, microstructure morphologies, and bonding at the interfaces. The damage accumulations and subsequent hotspot generations are explicitly modelled in this study to evaluate the ignition sensitivity of heterogeneous explosives. The goal of this research is to establish the relationship between microstructural aspects and the performance of explosives in terms of ignition sensitivity.

1.2 Hotspot Theory of Initiation

Ignition and subsequent detonation are caused by exothermic chemical reaction at hotspots of energetic solids. It is well known that bulk temperature rise due to overall compression under impact loading is too low to activate the chemical reaction, and therefore, the bulk temperature rise does not explain the mechanism of the actual explosion of energetic materials. The material heterogeneity of PBX is an important factor that induces localized energy dissipations. Unlike homogeneous explosives such as liquids [11], PBX is a composite material that is inherently heterogeneous [12]. The mechanical energy imparted from an impactor on a heterogeneous material is converted into heating in localized regions, known as hotspots.

Pores exist in energetic materials with various sizes. Mang et al. [13] measured mean size and size distribution of pores in PBX 9501 with the size scale of 0.1 – 20 μm using ultra-small-angle neutron scattering. They reported that the mean pore diameter does not change appreciably with increasing pressure from 70 to 200 MPa, but volume fraction of pores decreases with increasing pressure. Pore collapse has been studied as one of the main hotspot formation mechanism under shock loading. Bourne and Milne [14] studied possible ignition mechanism during pore collapsing for a shocked material. The focus of their research, however, is not on the stress concentration at the pore but on the temperature rise of the gas encapsulated in the pore. Bourne and Field [15] found that the hydrodynamic pressures generated by high-speed jet during cavity collapse cause the ignition. Austin et al. [16, 17] recently used ALE3D coupled with a reactive model, and quantified the effect of stress concentration at a pore under shock loading on hotspot evolution, accounting for shear banding on crystallographic planes.

Frictional dissipation is one of the main initiation mechanisms. Chidester et al. [18] calculated frictional energy dissipation of LX-10 subject to a low-pressure impact and obtained the threshold velocity for reaction. Chaudhri [19] observed the reaction front in β-lead azide using a high-speed camera, and found that reaction-generated stress wave induces new reaction sites ahead of an existing reaction front, and the new reaction is caused by frictional dissipation. Browning and Scammon [20] established an ignition model based on inter-granular frictional dissipation, chemical kinetics, and heat transfer, and obtained the time to ignition and velocities required for reaction. Gruau et al. [21] performed computational analyses of impact tests on PBX. In their numerical model, frictional heating is assumed to depend on the macroscopic pressure and plastic shear strain rate. Their study showed that frictional dissipation leads to ignition. Curtis et al. [22] used similar test configuration to Gruau et al. [21] (Steven Test) for their numerical study, and found that a frictional coefficient substantially affects the ignition behavior.

Another type of material heterogeneity that induces hotspot formation comes from a microstructure morphology such as grain sizes, shapes, and grain-binder interactions. Czerski and Proud [23] studied the effect of grain shapes and size on material sensitivity. They performed a Gap test on RDX granules and failed to observe any clear difference in sensitivity between the sizes of 10-30 μm and 100-300 μm. However, they found that grain shape influences on the sensitivity. Grains that have greater surface roughness with many dimple-like features showed more sensitive results. Bardenhagen et al. [24] analyzed microstructure morphology of a mock PBX (sucrose/HTPB) in 3D using X-ray microtomography and obtained the bimodal grain size distribution. Skidmore et al. [25] compared the grain size distribution of HMX before and after manufacturing PBX 9501 and found that the peak volume fraction of large particles among bimodal size particles

shifted toward smaller diameter, indicating the press processing breaks the large particles. Swallowe and Field [26] carried out drop-weight sensitivity tests on PBXs with different types of binder and concluded that the mechanical interactions between a binder and energetic crystals influence on the material sensitivity. Welle et al. [27] studied the microstructural effect on ignition of pressed HMX. The authors measured specific surface area and void distance distribution for different types of HMX microstructure and plotted the ignition criteria on James space (Power flux – energy flux). The authors found that energy threshold is influenced by the microstructure.

Once the temperature at the hotspot increases high enough to overcome the activation energy of the exothermic chemical reaction, then the hotspot location becomes the initiation site. However, it is also possible that a hotspot may not lead to ignition depending on its characteristics. Field et al. [28] used the concept of "critical hotspot" which indicates the hotspots that cause ignition, and provided the variables that determine the characteristics of critical hotspots – hotspot size, temperature, and duration. Although a hotspot may reach to high temperature and generate heat through reaction, the rate of heat deprived by the surrounding of the hotspot through conduction can be more significant than the rate of heat accumulated from the exothermic reaction process, resulting in quenching of the hotspot. Bowden and Yoffe [6, 7] showed that the hotspot needs to have the size of 0.1-10 μm, the duration of 10^{-5} - 10^{-3} s, and the temperature higher than 700K.

The concept of "criticality threshold" has been further developed by several researchers, mainly focusing on the hotspot size-temperature threshold for thermal runaway. Semenoff [29] obtained a solution of the heat diffusion equation with heat generation due to reaction. Frank Kamenetskii [30] solved the heat conduction equation

but with varying temperature distribution. Based on the works from Semenoff [29] and Frank Kamenetskii [30], Thomas [31] studied the effect of surface cooling. The author used one-step zero-order Arrhenius reaction equation together with heat diffusion equation, assuming steady state. Boddington et al. [32] considered the amount of reactant consumption when using chemical reaction, and obtained the critical threshold. Tarver et al. [33] developed 3-step chemical kinetics models for HMX and TATB decomposition and obtained the critical size-temperature relations. Later, Tarver et al. [34] further developed the model and proposed 4-step chemical kinetics model for thermal decomposition of HMX. Henson et al. [35] compiled experimental data of temperature-ignition time and obtained a linear relationship on log time-inverse temperature scale over a wide range of time (from nanoseconds to a day). A chemical decomposition model is proposed, and parameters are calibrated based on the relationship obtained. Walker and Wasley [36] took a different approach to obtain the criticality. Instead of determining critical hotspot threshold, they focused on the critical energy flux input on the material and obtained the empirical threshold criteria known as $P^2\tau$ = constant. James [37] further developed this empirical threshold by including energy cutoff.

1.3 Computational Modeling of Energetic Materials

1.3.1 Numerical Methods Using Eulerian and Lagrangian Approaches

Shock and non-shock responses of energetic materials at the mesoscale level are often analyzed using a hydrocode including finite discretization approaches such as finite element method (FEM), finite difference method (FDM), and finite volume method (FVM). A hydrocode can directly model the microstructure of the energetic solids in which heterogeneities are of vital importance for hotspot formation mechanisms, and

solve large deformation, transient and dynamic response of material. Benson [38] summarized governing equations, time integration schemes, mesh and element definitions, and other schemes commonly used in hydrocodes including Lagrangian, Eulerian, and Arbitrary Lagrangian-Eulerian (ALE) approaches.

The Eulerian approach in continuum level simulation can handle high-intensity shock response, whereas Lagrangian approach often faces numerical challenges due to severe material deformation and mesh distortion. Benson and Conley [39] performed Eulerian FEM calculations on HMX powder with an imposed velocity of U_p = 1 km/s, and studied the effect of viscosity. They observed that the shock front spreads out and the jetting is suppressed due to the viscosity. Baer [40] performed Eulerian CTH calculations with and without reactive model and studied the behavior of shocked HMX crystals with a velocity of U_p = 1 km/s. They observed highly fluctuating overall stress and energy localization due to crystal interactions. Menikoff [41] conducted Eulerian FEM calculation on HMX powder and obtained the effect of load intensity – a low intensity loading (U_p = 200 m/s) results in dispersed wave and partly compacted grains behind the shock due to the average stress lower than the yield strength, a moderate load intensity (U_p = 500 m/s) results in sufficient distortion of grains for fully compacted HMX without porosity, a high intensity loading (U_p = 1000 m/s) results in sharp wave front similar to shock wave. Recently, there have been several attempts to combine a thermo-mechanical approach using Eulerian FEM and reaction burn models. Zhang et al. [42] investigated shock to detonation transition of HMX pack and PBX using an Eulerian approach with a reaction model. To handle diffusion at the grain boundaries, their strategy is to smooth out the discontinuity over a few mesh points. They, however, prescribed the hotspot locations in a random fashion after the shock passage in the simulation, and obtained the relationship between hotspot spacing and the detonation. Rai and Udaykumar [43]

performed Eulerian FEM calculations coupled with a chemical kinetics model on pressed HMX subject to a shock pulse loading. The hotspots are generated and evolved via void collapse, plastic energy dissipation, chemical reaction, and thermal diffusion. They found that the angle of a narrow void with respect to the stress wave direction affects the criticality of initiation.

The Lagrangian approach can explicitly track grain boundaries and interfaces of crack surfaces, therefore, has great advantages over Eulerian approach for analyses of fracture, contact, and friction on heterogeneous energetic materials. Wu and Huang [44] performed static tensile tests on PBX 9501 using Lagrangian FEM framework. The authors studied the grain-binder interfacial fracture using cohesive elements, and analyzed stress and strain for different binder types. Gruau et al. [21, 45] considered the friction induced ignition of PBX during dynamic impact test. However, the friction is considered only at the PBX boundary between the PBX sample and the impactor. Panchadhara et al. [46] studied impact responses of granular HMX pack using Lagrangian discrete finite element method, and analyzed the effect of frictional dissipation and plastic heating on hotspots over the loading range of v = 50 – 500 m/s. Having the same computational technique, Gilbert et al. [47] characterized the distribution of hotspots and analyzed the effect of packing density of HMX grains and the loading intensity. Although the Lagrangian approach has great strength on explicit capture of many damage mechanisms, its applications have been limited to low and moderate load intensity regime, because high intensity loading (v > 500 m/s) often induces challenges in handling cracks and contact detection and ensuring accurate interactions between fractured interfaces.

Arbitrary Lagrangian Eulerian (ALE) method incorporates the benefits from both Lagrangian approach and Eulerian approach. ALE method is introduced by Hirt et al. [48]

and further developed for practical application as explained in Ref. [49]. The simulation proceeds with the Lagrangian approach, and then remapping is performed so that the variables in Lagrangian mesh are interpolated onto the Eulerian grid. Since the ALE method involves frequent remapping between Lagrangian and Eulerian approaches, challenges are on ensuring conservation and consistency of mass and momentum [50].

1.3.2 Other Numerical Methods

Molecular dynamics (MD) framework can analyze the atomistic behavior of the material at pico- and nanosecond scale. This framework allows us to analyze the fundamental reaction mechanisms in energetic materials. For example, Zhu et al. [51] showed how different temperatures change the energy release process of Al-metal oxide by analyzing chemical bonding during the reaction. Eason and Sewell [52] performed an MD simulation on RDX having a nano-scale pore subject to a shock loading with various intensities and observed fluid jetting by pore collapse under a high-intensity shock. Lee et al. [53] performed a Reactive MD (RMD) simulation as well as a continuum-level simulation on RDX. The RMD calculation they performed provided chemical changes and the thermodynamic properties, and the mirrored continuum simulation showed rapid changes in thermo-mechanical response in the reactive flow. The limitation of the MD framework is on the small time scale (ps – ns) and the length scale (nm – μm) that the analysis can handle.

While a finite discretization approaches such as FEM, FDM, and FVM are frequently used at the continuum scale for heterogeneous solids, there are several studies on energetic composite using other numerical schemes. For example, a discrete element method (DEM) is known as an effective approach for severe deformation and

discontinuity at the continuum level. Kline et al. [54] performed one-dimensional DEM calculations on PBX 9501 subject to a shock pulse loading. Their approach focused on mechanical shock wave propagation without chemical reaction, and the results were compared to experimentally obtained velocity profiles. Jun-Ling et al. [55] performed a Brazilian test on a 2-D PBX microstructure, similar to Wu and Huang [44] but using a DEM approach instead, and found that the sample with interfacial cracks can hold the load until the transgranular fracture occurs. The shortcomings of the DEM approach are explained in Ref. [56]. Another example is a Free-Lagrange method in which the connectivity of grid connectivity is allowed to change [57]. Ball et al. [58] studied the response of air cavity subject to underwater shock using the Free-Lagrangian framework, and showed the collapsing of a pore as experimentally observed by Borune and Field [59].

1.3.3 Modeling of Shock Response

A shock response of the material shows interesting characteristics which cannot be observed under low-intensity loading. One example of shock characteristics is a sharp rise of stress wave front. Even if a gradually increasing impact wave is imposed on the surface, the stress wave front becomes stiffer as it propagates [60], because the wave speed of highly compressed part is faster than that of less compressed part of the material. Ideally, the stiffening of the wave front becomes infinitely thin, which causes numerical instability from the perspective of modeling. The concept of adding “artificial viscosity” is proposed by von Neumann and Richtmyer [61], to assign a finite width at the shock front.

Modeling of material behavior under high pressure requires an accurate equation of state (EOS) which provides a relation between state variables of the material such as

pressure, specific volume, or temperature. Some of the widely used EOS models in modeling shocked material are Mie-Grüneisen EOS [62] and Birch–Murnaghan EOS [63]. Measurement of pressure-volume relation provides useful information for parameter fittings of other EOS models. The relation between pressure and volume (*P*-*V*) is also a simple type of EOS. As described in Ref. [64], this *P*-*V* relation can be transformed to other types of relations with different combinations of variables such as particle speed or shock speed using the jump conditions. The relations that are commonly used for shock response are *P*-*V* (pressure-volume), *P*-U_p (pressure-particle speed), and U_s-U_p (shock speed-particle speed) relation.

Shock impact of explosive involves violent reaction that leads to detonation. Analysis on detonation process utilizes Hugoniot relations from both unreacted material and reacted material. Using Chapman-Jouguet (CJ) theory, we can determine the condition of discontinuity at steady 1-D detonation front, assuming the detonation reaction zone is infinitesimally thin. The CJ point lies on the intersection of Hugoniot P-V curve (Rankine-Hugoniot relation) of reacted material and Rayleigh line. A theory of Zel'dovich-von Neumann-Doring (ZND) condition is an extension of CJ theory with a consideration of finite reaction zone at the detonation front [65].

1.3.4 Reactive Burn Model

Researchers have developed reactive burn models to analyze the propagation of reaction throughout the material. A few examples of commonly used models are Forest Fire [8], Ignition and Growth (I&G) [9], and JTF model [10]. Menikoff and Shaw provided detailed reviews on the Forest Fire model [66] and the I&G model [67]. These models do not account for microstructure morphology and do not specify the locations of

hotspot formation in the material. Instead, the models assume that small portion of the material near the shock front reacts based on empirical observations. The reaction rate is determined by one or a few of such factors as pressure, temperature, and entropy. The constitutive relations, mainly equation of state (EOS), of unreacted material and reacted material are used to predict the detonation wave. Mixture model based on the volume fractions and the properties of individual constituents have been adopted for the prediction of effective shock EOS of explosive composites. Prediction of EOS of reacted material based on individual chemical products is very complicated, since the minute change in chemical reaction path leads to a significantly different response. Therefore, most EOS models of reacted material used in detonation calculations are designed for either gas phase using averaged properties of all gaseous products or mixture of product gas and solid in which all gaseous products are treated as one type of material. In either case, the EOS models of reacted material have parameters that are obtained empirically.

Since the reactive models do not explicitly capture hotspot formation mechanisms which greatly affect the initiation process, there have been many attempts to incorporate hotspot formation. One of the notable efforts is done by Horie et al. [68] who proposed a physical-based reactive burn model and tried to link the statistically aggregated hotspot distributions and hydrodynamic formulations. The distribution of hotspots in this model is not from direct simulation, but it is estimated based on energy deposition parameters and the number and size of potential hotspot sites. The potential hotspot quantities are approximated using the number of particle-particle contact sites.

1.4 Statistical Approach

The hotspot generation mechanisms are heavily influenced by such factors as material heterogeneity, constituent properties, and defects. The nature of these influences causes the ignition process to be fundamentally stochastic. Recognizing this reality, researchers have carried out numerous studies on this topic. For example, Dienes et al. [69-71] conducted pioneering studies on impact ignition through the statistical modeling of microcracking and frictional heating. Nichols and Tarver [72] used statistical hotspot models and investigated the effects of pressure, hotspot size, and hotspot number density. Hamate et al. [73, 74] developed a mechanical reactive burn model using a statistical approach of hotspot evolution. These studies provide an understanding of effects of cracks or hotspot characteristics on initiation using analytical models of crack growth or hotspot aggregation. However, the effects of randomly distributed inhomogeneities and corresponding initiation probability of explosives remain to be quantified.

Probabilistic approaches have long been used to study the mechanical behavior of materials with randomly distributed defects. For example, Hassold et al. [75] used the Weibull distribution and the Gumbel distribution (a double exponential form of the Weibull distribution) to analyze the effects of defect density, domain size, and spring modulus on the probability of failure. The idealized structures consist of springs with random defects. Using the Weibull and modified Gumbel distributions, Duxbury et al. [76] analyzed the failure probability of idealized structures comprised of fiber bundles with random defects. Andersons et al. [77] performed tension tests on fibers with random defects and obtained the distribution of strengths. Concerning the effect of random material properties, Silberschmidt et al. [78] studied stochastic crack propagations in brittle materials with spatially random variations of stiffness. These studies show that

random defects and the fluctuations of material properties are primary sources for stochasticity in material response.

In composite materials, interactions between two different phases cause the following issues that single-phase materials do not have. One key factor that dominates the fracture in composites is the interfacial strength between constituents. Several studies [44, 79-81] have highlighted the effects of debonding of particle/matrix interfaces in composites. Yanase et al. [82] developed a constitutive model that relates the discontinuity of displacements to traction for the quasi-static deformation of composites, accounting for the effect of imperfect particle binder interfaces. Another key factor in the composite material is its inherent random morphology of different phases. Ostoja-Starzewski [83] used randomly distributed and periodically distributed fibers in composites, and performed a numerical analysis to determine how the effective elastic moduli, the effective constitutive response, and the geometric patterns of damage change. Vel and Goupee [84, 85] analyzed the effects of the random microstructural morphology of two-phase composites on material properties such as Young's modulus, the thermal expansion coefficient, and principal stresses at failure in tension and compression. In most cases, however, as Freudenthal describes [86], "inhomogeneity expressed in the form of the statistical scatter of observed characteristics is the result of both the submicroscopic defects and the macroscopic random inhomogeneities in the material." Obviously, the uncertainty in material behavior is not caused by individual sources of inhomogeneities alone, but rather by the combined effect of multiple factors. More discussions on the effect of multiple sources of heterogeneity are given in Chapter 4.

1.5 Objectives of This Study and Thesis Outline

The aim of this study is to understand the mechanisms of hotspot evolution, develop a numerical framework for a dynamic response of solid explosives subject to a wide range of impact intensity, and computationally predict the initiation sensitivity accounting for microstructural heterogeneities. The final goal is to establish microstructure-loading-sensitivity relationships for designing explosives with tailored attributes and safety envelopes. Specifically, microstructural attributes considered for establishing the relationships include grain volume fraction, grain size distribution, random morphology, the bonding strength between grains and a binder, and the inclusions of metallic particles. The loading intensity considered varies from a non-shock regime (U_p = 50 m/s) to a shock regime (up to U_p = 1200 m/s). To achieve the objectives, this study focuses on the following subjects.

- *Developing a computational framework.*

  A numerical framework is developed for mesoscale simulation subject to a shock and non-shock loading. The framework is based on Lagrangian cohesive finite element method (CFEM) which accounts for large deformation, microcracking, frictional heating, and thermal conduction. The computationally generated samples used for the CFEM calculations have similar features as in experimental samples such as grain morphologies, average grain size, and volume fraction. Hotspots are generated by various energy dissipation mechanisms including visco-elastic deformation, plastic deformation, frictional heating at the grain boundaries and at the transgranular fracture surfaces. Chapter 2 discusses the method of microstructure generation and the CFEM framework.

- *Establishing hotspot criticality and probabilistic initiation sensitivity.*

  Hotspots are generated by various dissipation mechanisms driven by mechanical loading, then react exothermally. However, hotspots may quench depending on their characteristics. A critical hotspot whose temperature is high enough to overcome the heat loss due to diffusion will lead to ignition. The stability of an explosive material is determined by hotspot criticality. Chapter 3 discusses the thermal criticality threshold of a hotspot and shows the evaluation of ignition sensitivity in terms of loading intensity and microstructural attributes. Because the ignition sensitivity is highly stochastic due to material heterogeneities, a probabilistic approach is introduced to analyze the variations in ignition sensitivity arising from random variations in microstructure morphology.

- *Combined probability accounting for multiple sources of heterogeneity*

  The randomness of hotspot generation is caused by a combined effect of various stochastic sources in the sample. Chapter 4 discusses the development of an approach that computationally predicts the probability of ignition of polymer-bonded explosives (PBXs) accounting for the combined effect of two sources of stochasticity in microstructural attributes – random morphologies of constituent phases and the bonding strength of the grain-binder interfaces. The probability of ignition arising from one source of stochastic variation is quantified and analyzed separately from another source. The two probability functions are then combined using relations between the time to criticality and microstructure attributes. Although only two sources of stochasticity are considered for the combined probability, the approach developed in this

chapter can be applied to an analysis on the effect of three or more sources of stochasticity combined.

- *Effect of metallic inclusions on the initiation sensitivity*

  The inclusions in PBXs affect the ignition sensitivity. Some modern high explosive mixtures contain aluminum (Al) particles for enhanced performance, and the addition of Al particles desensitizes the explosives. However, there has been little basic scientific research on the influence of aluminum addition on explosive ignition and ignition sensitivity, be it in the context of accidental insults or design loads. Chapter 5 discusses the ignition desensitization of PBX via aluminization. Specifically, it analyzes the effect of Al addition on crack densities, hotspot fractions, and ignition probability.

- *Predictions on shock initiation threshold of pressed HMX*

  The ignition sensitivity test subject to a shock loading utilizes a very thin flyer with the thickness in the micrometer scale. With this approach, a sensitivity threshold is analyzed in terms of shock intensity and the thickness of the flyer represented as pulse duration. Chapter 6 discusses the prediction on ignition threshold of energetic materials with different grain sizes. The probability of ignition is analyzed for various loading conditions.

- *Probabilistic relations between the sensitivity of PBXs and microstructural attributes under shock/nonshock loading*

  The analysis of shock initiation threshold is expanded to PBXs with different types of binder and initial defects for a wide range of load intensity including shock and nonshock regime (U_p = 200 – 1200 m/s). Chapter 7 discusses the

initiation thresholds of PBX 9404 and PBX 9501 and how the sensitivity changes as the initial debonding level increases. The stochastic nature of initiation behavior is analyzed and represented in terms of probability distribution functions, and the material-dependent ignition probability map is obtained.

Finally, Chapter 8 discusses a summary and recommendations for future work.

CHAPTER 2: MESOSCALE MODELING FRAMEWORK

2.1 Introduction

This chapter presents the numerical modeling framework used in this study for the analysis on dynamic response of heterogeneous explosives subject to shock and non-shock loading. The framework is based on 2-D Lagrangian cohesive finite element (CFEM) accounting for large deformation, energy dissipations due to plastic and viscoelastic deformation, transgranular crack propagation in arbitrary directions, debonding at the interfaces, frictional heating. The framework is initially developed by Barua [87], and further improved for this study by adding the capability of handling initial voids and initial defects in the microstructure and shock response under extreme pressure with numerical stability and reliability. The framework is designed to model fully coupled thermo-mechanical behaviors of explosive composites and predict the ignition sensitivity. However, chemical reaction and subsequent flame propagation are not directly captured. Instead, the calculation focuses on various hotspot generation mechanisms at the grain scale due to mechanical loading, and the algorithm for determination of hotspot criticality is borrowed from the existing Frank-Kamenetskii [88] type thermal explosion model. The details of the hotspot criticality conditions are given in Chapter 3. In this Chapter 2, the numerical scheme for modeling thermo-mechanical behavior is delineated. Chapter 2.2 discusses the method of microstructure generation for polymer bonded explosives (PBXs) and granular beds with voids. Chapters 2.3-2.6 discuss the finite discretization, constitutive relations, a cohesive element method, and a contact/penalty algorithm. The major challenges of developing the framework are on attaining a numerical stability during the contact-repulsion process and the sliding friction under severe pressure in a multi-body system. The reliability test is performed and presented in Chapter 2.6. The parameters used in the constitutive relations are provided with the corresponding

references in this Chapter 2. After this chapter, Chapters 3-6 provide detailed explanations of the analysis on the sensitivity and the comparison with experiments, which serves as the validation of the framework.

2.2 Microstructure Generation

PBX consists of energetic particles and a polymer binder. The energetic particles comprise most of PBX microstructure (volume fraction up to 92%) to maximize the energy output of PBX. Although energetic materials are often used as a form of PBX composite in practice, many researchers have studied the dynamic behavior of the energetic particles without a binder experimentally [89, 90] as well as numerically [47, 91]. This section explains the computational methods for two types of microstructure generation: a granular bed with voids and a two- or three-phase PBX.

Granular bed with voids

In this study, energetic crystals are represented as circular grains for simplicity, whose shape is commonly used for computational modeling as in Ref. [47, 91]. Two types of granular bed microstructure are generated – one with monomodal grain size and the other with bimodal grain size. For microstructures with a monomodal grain size, a volume fraction up to $\eta \sim 50\%$ is easily attainable by randomly distributing the circles in a fixed domain. A higher volume fraction is obtained via the following process. The first step is to arrange the particles in an orderly manner, leaving out a certain number of particles to match the desirable volume fraction ($\eta = 70\%$). The second step is a shuffling step in which random movements are assigned to the particles so that the arrangement of the particles becomes disordered. The microstructure is then converted to a mesh by assigning

a mesh grid to all particles. The space between particles remains as a void which does not have mesh. This process is shown in Figure 1(a).

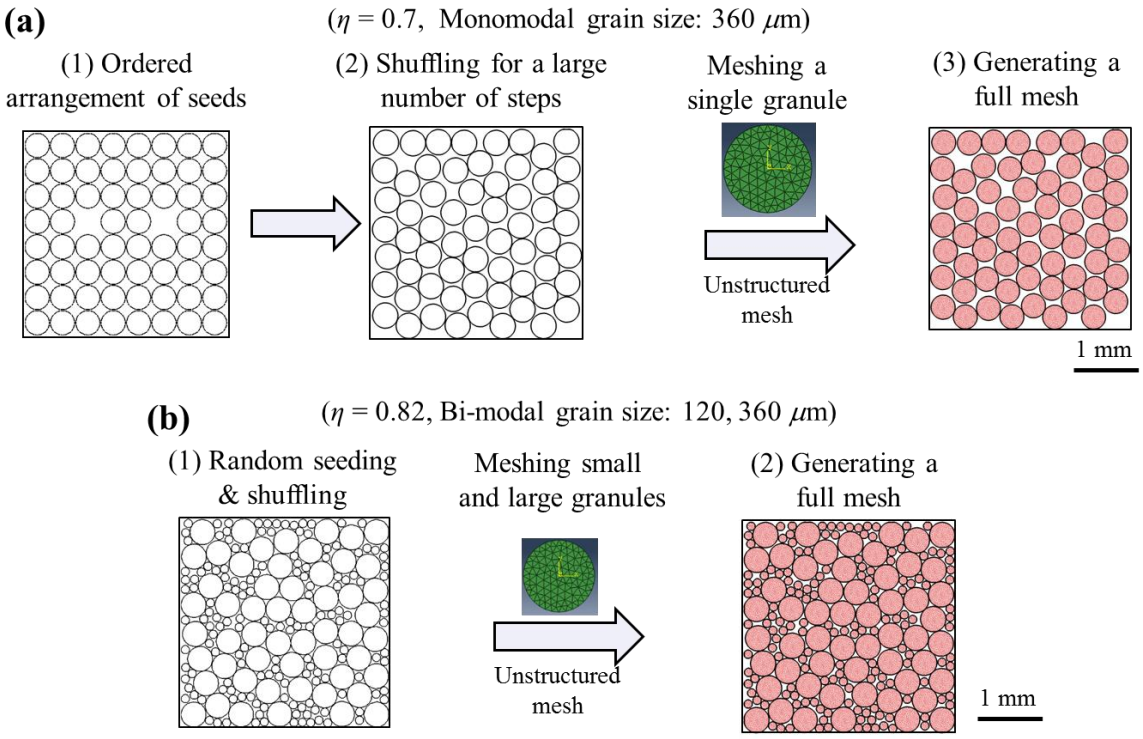

Figure 1. Methods of microstructure generation for (a) monomodal grain size and (b) bimodal grain size

A higher volume fraction of grains can be obtained in a microstructure with bimodal grain sizes. As more the disparity of the sizes between big and small grains there is in the microstructure, the higher maximum volume fraction we can obtain. In this study, the volume fraction of η = 82% is obtained from the microstructure with the large grain size of 360 μm and the small grain size of 120 μm. The large grains are randomly distributed to an empty domain first, and then small grains fill the gaps. A random shuffling, as explained in the previous paragraph, is applied when many trials for the small

grain insertion fail. Once the microstructure has the target volume fraction, a mesh grid is assigned to the grains. This process is shown in Figure 1(b).

PBX microstructure

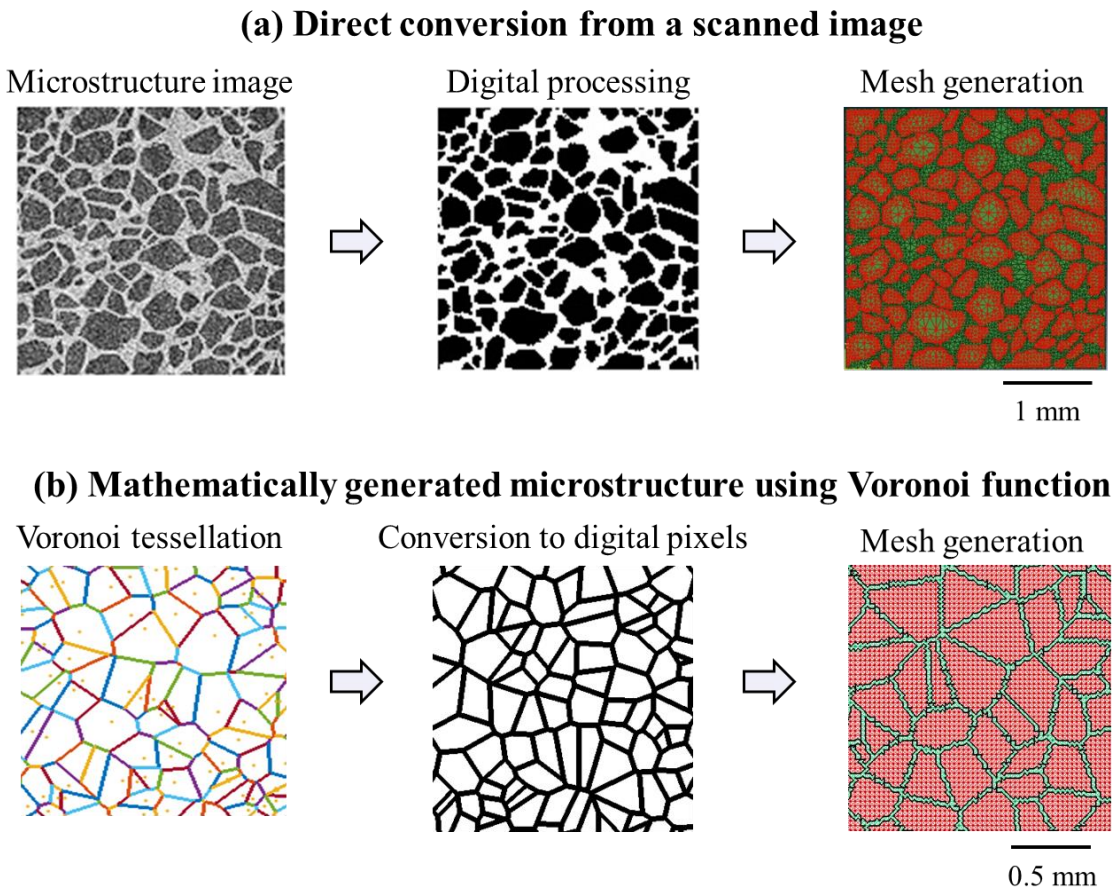

Figure 2. Methods for PBX microstructure generation with (a) a direct conversion from a scanned image and (b) Voronoi tessellation function

The PBX microstructure generated here has the total solid volume fraction of η = 100% consisting of grains and a binder without voids. For an accurate modeling of grain-binder geometry, a direct conversion from a scanned image is considered as shown in Figure 2(a). Although this method provides an accurate microstructure geometry, it does

not allow us to generate multiple samples with random morphology but similar attributes, which is an important requirement for statistical analysis. In addition, such attributes such as volume fraction, average grain size, and grain size distribution should be precisely controlled by a user. To satisfy these requirements, a mathematical formulation using the Voronoi tessellation function is adopted. This function provides a random polygonal shape of grains, and the microstructure attributes can be controlled by the distribution of seeds and the thickness of the boundary lines. Figure 2(b) shows the process of microstructure generation using the Voronoi tessellation function.

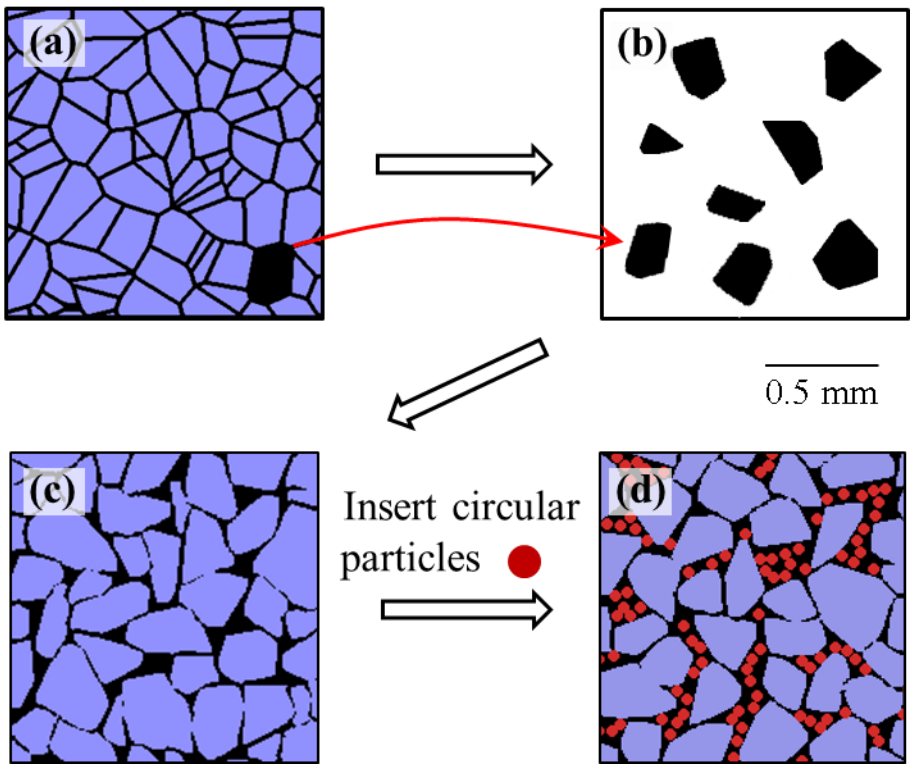

Figure 3. Method of microstructure generation using a Voronoi tessellation function and a grain library

The microstructure generated using the Voronoi function has a binder with uniform thickness, although, in real PBX microstructure, the binder has a random

thickness. Therefore, a new method is developed to generate more realistic microstructure. Figure 3 shows the process of the new microstructure generation method. This new method utilizes the Voronoi tessellation function as a basis (Figure 3(a)). The grains in the microstructure generated by a Voronoi are detected and separately stored in a grain library (Figure 3(b)). Then, the grains are randomly distributed in a fixed domain (Figure 3(c)). To make the grains more rounded, each grain is expanded slightly. PBX microstructure shown in Figure 3(c) can be used for PBX calculations. Chapter 4 delineates this microstructure generation method using the Voronoi tessellation function with two scales of grain sizes. Also, the attributes of the computationally generated microstructures are quantified and compared to the scanned image of PBX in Chapter 4. This method can be further extended for aluminized PBX by adding circular particles in the microstructure as shown in Figure 3(d). The shape of aluminum particles is chosen to be circular based on the powder shape reported in Ref. [92]. Here in this chapter, only the computational method of microstructure generation is presented. Since the analysis in each chapter requires different types of microstructure, the microstructural details such as grain size distribution and average grain size are presented in every chapter.

2.3 Finite Element Discretization

This section describes the finite element equations used in this study. A detailed derivation of the finite element method is provided in Ref. [93]. The framework in this study is based on a two-dimensional constant strain triangular element with an explicit time integration scheme. The motion is approximated as

$$x_i(\boldsymbol{X}, t) = x_{iI}(t) N_I(\boldsymbol{X}), \tag{2-1}$$

where $\boldsymbol{X}$ is the position vector in the initial configuration, x_i is the components of the position vector in the deformed configuration, and N_I is the shape function or interpolation function. Similarly, the displacement, $\boldsymbol{u} = \boldsymbol{x} - \boldsymbol{X}$, is discretized as

$$u_i(\boldsymbol{X}, t) = u_{iI}(t) N_I(\boldsymbol{X}). \tag{2-2}$$

The velocity and acceleration are the material time derivative of the displacement and the velocity, respectively, with the form of

$$\begin{aligned} \dot{u}_i(\boldsymbol{X}, t) &= \dot{u}_{iI}(t) N_I(\boldsymbol{X}) \text{ and} \\ \ddot{u}_i(\boldsymbol{X}, t) &= \ddot{u}_{iI}(t) N_I(\boldsymbol{X}). \end{aligned} \tag{2-3}$$

The deformation gradient $\boldsymbol{F}$ is written as

$$F_{ij} = \frac{\partial x_i}{\partial X_j} = \frac{\partial N_I}{\partial X_j} x_{iI} \ . \tag{2-4}$$

So far, kinematic variables are discretized using the nodal shape function. The principle of virtual work gives the internal, external and inertial forces with the discretized nodal components. The principle of virtual work is

$$\delta W^{int} + \delta W^{kin} = \delta W^{ext}, \tag{2-5}$$

where δW^{ext} is the virtual external work, δW^{int} is the virtual internal work, and δW^{kin} is the virtual inertial work or virtual kinetic work. The virtual work can be discretized into the virtual displacement and the nodal force. The virtual internal work is

$$\delta W^{int} = \delta u_{iI} f_{iI}^{int} = \int_{\Omega_0} \delta F_{ij} P_{ji} \, d\Omega_0 = \delta u_{iI} \int_{\Omega_0} \frac{\partial N_I}{\partial X_j} P_{ji} \, d\Omega_0 \ , \tag{2-6}$$

where δu_{iI} is the virtual nodal displacement, f_{iI}^{int} is the internal nodal force, $\boldsymbol{P}$ is the nominal stress or the 1st Piola-Kirchhoff stress. Similar to Eq. (2-6), the virtual external work is

$$\delta W^{ext} = \delta u_{iI} f_{iI}^{ext} = \int_{\Omega_0} \delta u_i \rho_0 b_i \, d\Omega_0 + \int_{\Gamma_0} \delta u_i \bar{t}_i^{\,0} \, d\Gamma_0 \,, \tag{2-7}$$

where f_{iI}^{ext} is the external nodal force, $\boldsymbol{b}$ is the body force, ρ_0 is the initial density, and $\bar{\boldsymbol{t}}^0$ is the traction vector. The virtual kinetic work is

$$\begin{aligned} \delta W^{kin} = \delta u_{iI} f_{iI}^{kin} = \int_{\Omega_0} \delta u_i \rho_0 \ddot{u}_i \, d\Omega_0 = \\ = \delta u_{iI} \int_{\Omega_0} \rho_0 N_I N_J \, d\Omega_0 \, \ddot{u}_{jJ} = \delta u_{iI} M_{ijIJ} \ddot{u}_{jJ} \,, \end{aligned} \tag{2-8}$$

where f_{iI}^{kin} is the kinetic nodal force and M_{ijIJ} is the mass matrix given by

$$M_{ijIJ} = \delta_{ij} \int_{\Omega_0} \rho_0 N_I N_J \, d\Omega_0 \,, \tag{2-9}$$

where δ_{ij} is Kronecker delta. By combining Eqs. (2-6), (2-7), and (2-8), the principle of virtual work gives

$$\delta u_{iI} \left(M_{ijIJ} \ddot{u}_{jJ} + f_{iI}^{int} - f_{iI}^{ext} \right) = 0 \,, \tag{2-10}$$

which, therefore, leads to

$$M_{ijIJ} \ddot{u}_{jJ} + f_{iI}^{int} = f_{iI}^{ext} \,. \tag{2-11}$$

In Eq. (2-11), the subscript $i = j$ because of the Kronecker delta, the mass matrix in Eq. (2-9) can be rewritten as

$$M_{IJ} = \int_{\Omega_0} \rho_0 N_I N_J \, d\Omega_0 \,. \tag{2-12}$$

which simplifies Eq. (2-11) to the following form.

$$M_{IJ}\ddot{u}_{iJ} + f_{iI}^{int} = f_{iI}^{ext} \tag{2-13}$$

Here, the external nodal force is written as

$$f_{iI}^{ext} = \int_{\Omega_0} N_I \rho_0 b_i \, d\Omega_0 + \int_{\Gamma_0} N_I \bar{t}_i^0 \, d\Gamma_0 \,, \tag{2-14}$$

and the internal nodal force is written as

$$f_{iI}^{int} = \int_{\Omega_0} \left(B_{Ij}^0\right)^T P_{ji} \, d\Omega_0 = \int_{\Omega_0} \frac{\partial N_I}{\partial X_j} P_{ji} \, d\Omega_0 \,, \tag{2-15}$$

where B_{Ij}^0 is the nodal gradient $\left(B_{Ij}^0 = \partial N_I / \partial X_j\right)$. For two-dimensional constant strain triangular (CST) element, the nodal gradient can be re-written using the Voigt notation as

$$B_{Ij}^0 = \frac{\partial N_I}{\partial X_j} = \boldsymbol{B}^0 = [\boldsymbol{B}_1^0 \quad \boldsymbol{B}_2^0 \quad \boldsymbol{B}_3^0] = \frac{1}{2A_0}\begin{bmatrix} Y_{23} & Y_{31} & Y_{12} \\ X_{32} & X_{13} & X_{21} \end{bmatrix}, \tag{2-16}$$

where A_0 is the area of the undeformed element, $Y_{IJ} = Y_I - Y_J$ and $X_{IJ} = X_I - X_J$. In Eq. (2-15), the nominal stress (or 1st PK stress) $\boldsymbol{P}$ is not symmetric. To simplify the equation using the Voigt notation, the symmetric form of the stress which is the 2nd PK stress $\boldsymbol{S}$, is used with the relationship of $\boldsymbol{P} = \boldsymbol{S} \cdot \boldsymbol{F}^{\boldsymbol{T}}$. The internal nodal force in Eq. (2-15) is converted to the form of

$$f_{iI}^{int} = \int_{\Omega_0} \frac{\partial N_I}{\partial X_j} F_{jk} S_{ik} \, d\Omega_0 \,. \tag{2-17}$$

The nodal gradient in Eq. (2-17) is re-defined including the deformation gradient $\boldsymbol{F}$ as

$$B_{ikjI}^{0\prime} = \underset{(i,k)}{\text{sym}}\left(\frac{\partial N_I}{\partial X_i} F_{jk}\right). \tag{2-18}$$

Using Eq. (2-18), Eq. (2-17) can be simplified to

$$\boldsymbol{f}_I^{int} = \int_{\Omega_0} (\boldsymbol{B}_I^{0\prime})^T \{\boldsymbol{S}\}\, d\Omega_0 \,. \tag{2-19}$$

For two-dimensional constant strain triangular (CST) element, the nodal gradient is simplified to

$$\boldsymbol{B}^{0\prime} = \begin{bmatrix} Y_{23}x_{,X} & Y_{23}y_{,X} & Y_{31}x_{,X} \\ X_{32}x_{,Y} & X_{32}y_{,Y} & X_{13}x_{,Y} \\ Y_{23}x_{,Y} + X_{32}x_{,X} & Y_{23}y_{,Y} + X_{32}y_{,X} & Y_{31}x_{,Y} + X_{13}x_{,X} \end{bmatrix} \\ \begin{bmatrix} Y_{31}y_{,X} & Y_{12}x_{,X} & Y_{12}y_{,X} \\ X_{13}y_{,Y} & X_{21}x_{,Y} & X_{12}y_{,Y} \\ Y_{31}y_{,Y} + X_{13}y_{,X} & Y_{12}x_{,Y} + X_{21}x_{,X} & Y_{12}y_{,Y} + X_{21}y_{,X} \end{bmatrix}, \tag{2-20}$$

where $x_{,X}$, $x_{,Y}$, $y_{,X}$, $y_{,Y}$ are

$$\begin{aligned} x_{,X} &= N_{I,X}x_I = \frac{1}{2A_0}(Y_{23}x_1 + Y_{31}x_2 + Y_{12}x_3)\,, \\ x_{,Y} &= N_{I,Y}x_I = \frac{1}{2A_0}(X_{32}x_1 + X_{13}x_2 + X_{21}x_3)\,, \\ y_{,X} &= N_{I,X}y_I = \frac{1}{2A_0}(Y_{23}y_1 + Y_{31}y_2 + Y_{12}y_3)\,, \\ y_{,Y} &= N_{I,Y}y_I = \frac{1}{2A_0}(X_{32}y_1 + X_{13}y_2 + X_{21}y_3)\,. \end{aligned} \tag{2-21}$$

Therefore, the internal nodal force in CST element is represented as

$$\boldsymbol{f}^{int} = \{f_{x1}\ f_{x2}\ f_{x3}\ f_{y1}\ f_{y1}\ f_{y1}\}^T = \int_{\Omega_0} (\boldsymbol{B}^{0\prime})^T \begin{Bmatrix} S_{11} \\ S_{22} \\ S_{12} \end{Bmatrix} d\Omega_0 \,. \tag{2-22}$$

The external nodal forces include cohesive force and contact force both of which are applied to the node of the element. The body forces such as gravity or electromagnetic forces are not considered in this study.

The explicit time integration scheme in this study utilizes the Newmark β-method [94] with $\beta = 0$. The specific forms of the nodal acceleration, velocity, and displacement are

$$\begin{aligned} \{\ddot{\boldsymbol{u}}\}_n &= [\boldsymbol{M}]_n^{-1} \cdot \left(\{\boldsymbol{f}^{ext}\}_n - \{\boldsymbol{f}^{int}\}_n\right), \\ \{\dot{\boldsymbol{u}}\}_n &= \{\dot{\boldsymbol{u}}\}_{n-1} + \frac{1}{2}\Delta t(\{\ddot{\boldsymbol{u}}\}_{n-1} + \{\ddot{\boldsymbol{u}}\}_n), \\ \{\boldsymbol{u}\}_n &= \{\boldsymbol{u}\}_{n-1} + \Delta t\{\dot{\boldsymbol{u}}\}_{n-1} + \frac{1}{2}\Delta t^2\{\ddot{\boldsymbol{u}}\}_{n-1}, \end{aligned} \tag{2-23}$$

where subscript n is the current time step, $n-1$ is the previous time step, Δt is the time increment between the current time step and the previous time step, $\{\boldsymbol{u}\}$ is the nodal displacement vector, $\{\dot{\boldsymbol{u}}\}$ is the nodal velocity vector, and $\{\ddot{\boldsymbol{u}}\}$ is the nodal acceleration vector.

2.4 Cohesive Element in CFEM Framework

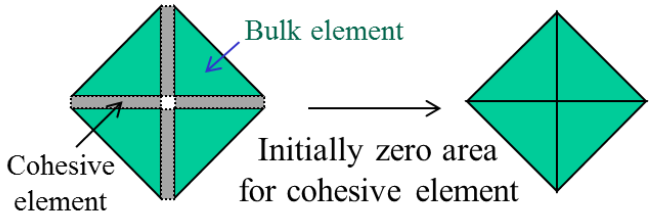

Figure 4. Cohesive elements embedded in between bulk elements

The cohesive finite element method (CFEM) provides an accurate modeling scheme for various failure processes, and therefore, is suitable for analyzing damage evolution during the dynamic response of heterogeneous energetic composites. As an application of CFEM framework, Xu and Needleman studied the dynamic crack growth in a brittle material [95] and at the interface of a PMMA/Al bi-material assuming both materials are elastic [96]. Camacho and Ortiz [97] investigated arbitrary crack propagations from the contact surface of an elastoplastic material. As an application to polymers, Rahul-Kumar et al. [98] investigated the interfacial fracture of polymers during t-peel test and compressive shear test. Zhai et al. [99] modeled the crack propagations in the heterogeneous microstructure of an alloy and studied the effect of morphology. The cohesive finite element method in this study is used to analyze the impact response of energetic composites and to model the arbitrary crack nucleation and propagation in heterogeneous microstructures.

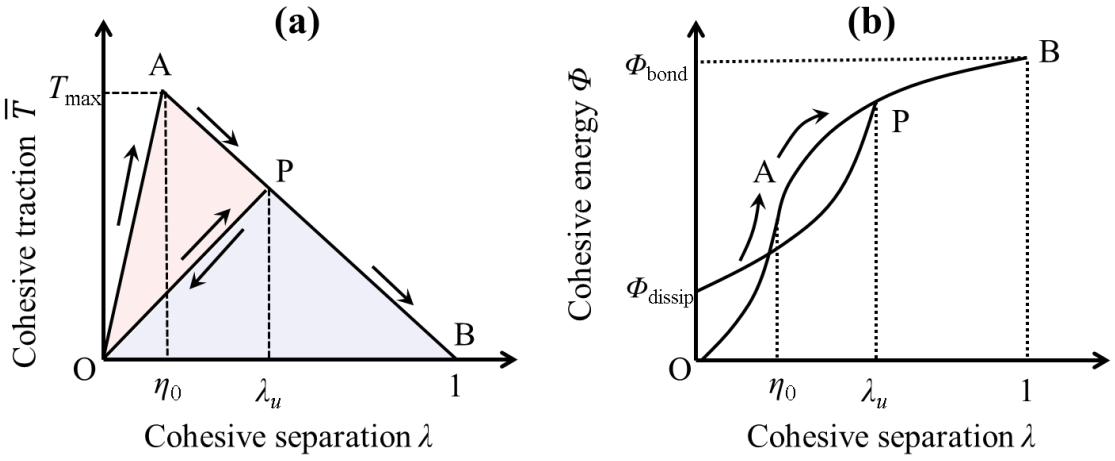

Figure 5. Constitutive relations of cohesive element (a) between separation λ and traction $\overline{T}$ and (b) between separation λ and cohesive energy Φ

The cohesive element is embedded along the boundaries of every bulk element throughout the entire domain. The initial area of the cohesive element is zero, as shown in Figure 4. The cohesive element follows a bi-linear traction-separation cohesive relation. Figure 5(a) shows the constitutive relation of the cohesive element between separation λ and traction $\overline{T}$ and Figure 5(b) shows the cohesive energy Φ in terms of cohesive separation λ.

The specific form of the constitutive relation between the cohesive separation λ and the traction $\overline{T}$ is

$$\overline{T} = \begin{cases} \left(T_{max}\frac{1-\eta}{1-\eta_0}\right)\frac{\lambda}{\eta}, & \text{for } 0 \le \lambda \le \eta \\ \left(T_{max}\frac{1-\eta}{1-\eta_0}\right)\frac{1-\lambda}{1-\eta}, & \text{for } \eta < \lambda \le \eta \end{cases} \tag{2-24}$$

where T_{max} is the maximum traction strength, η_0 is the initial elastic limit of the cohesive separation. The cohesive separation λ is the ratio between the maximum allowed separation and the current separation of the cohesive element, which varies between 0 and 1. The line $\overline{OA}$ in Figure 5(a) indicates the initial elastic range of cohesive separation, where the separation is reversible. The parameter λ_u is used to record the maximum value of λ that the cohesive element has ever reached during the simulation. If λ_u becomes bigger than the initial elastic limit η_0 ($\eta_0 < \lambda_u < 1$), then the traction $\overline{T}$ is reduced, and the irreversible damage is accumulated in the cohesive element. The parameter η is defined as $\eta = \max(\eta_0, \lambda_u)$ to account for the irreversible separation.

The cohesive separation λ is composed of normal separation δ_n and tangential separation δ_t as

$$\lambda = \begin{cases} \sqrt{\left(\frac{\delta_n}{\delta_{nc}}\right)^2 + \left(\frac{\delta_t}{\delta_{tc}}\right)^2}, & \text{for } \delta_n \geq 0 \\ \left|\frac{\delta_t}{\delta_{tc}}\right|, & \text{for } \delta_n < 0 \end{cases} \tag{2-25}$$

where δ_{nc} and δ_{tc} are the critical separations in normal direction and in tangential direction, respectively. The cohesive traction can be decomposed into the normal traction T_n and the tangential traction T_t as

$$\begin{aligned} T_n &= \overline{T}(\lambda,\eta)\frac{\delta_n}{\lambda\delta_{nc}} \quad \text{and} \\ T_t &= \overline{T}(\lambda,\eta)\frac{\alpha\delta_t}{\lambda\delta_{tc}} \end{aligned} \tag{2-26}$$

where α is defined as $\alpha = \delta_{nc}/\delta_{tc}$. The cohesive energy Φ has the form of

$$\Phi(\lambda,\eta) = \begin{cases} \Phi_{bond}\left(\frac{1-\eta}{1-\eta_0}\right)\left(\frac{\lambda^2}{\eta}\right), & \text{for } 0 \leq \lambda \leq \eta \\ \Phi_{bond}\left(\frac{1-\eta}{1-\eta_0}\right)\left(1-\frac{(1-\lambda)^2}{1-\eta}\right), & \text{for } \eta < \lambda \leq 1 \end{cases} \tag{2-27}$$

where Φ_{bond} is the bonding energy of the material. The energy dissipated from a cohesive element Φ_{dissip} can be calculated from the following form of equation.

$$\Phi_{dissip} = \begin{cases} 0, & \text{for } \lambda \leq \eta_0 \\ \Phi(\eta,\eta_0) - \Phi(\eta,\eta) = \frac{\eta-\eta_0}{1-\eta_0}\Phi_{bond}, & \text{for } \eta_0 \leq \lambda \leq \eta \\ \Phi(\lambda,\eta_0) - \Phi(\lambda,\eta) = \frac{\lambda-\eta_0}{1-\eta_0}\Phi_{bond}, & \text{for } \lambda \leq \lambda \leq 1 \\ \Phi_{bond}, & \text{for } \lambda > 1 \end{cases} \tag{2-28}$$

The cohesive element is considered as failed if the cohesive separation λ reaches the limit (λ = 1), and the bonding energy is Φ_{bond} assumed to be converted to the surface energy.

The cohesive parameters of PBX 9501 are experimentally studied by Tan et al. [81]. The cohesive parameters used for the HMX grains, the Estane binder, and the interface between HMX and the binder are listed in Table 1.

Table 1. Cohesive parameters for HMX and Estane

Material Property	HMX-HMX	Estane-Estane	HMX-Estane
Critical separations δ_{nc}, δ_{tc} (μm)	5.0	10.0	4.62
Maximum traction (MPa)	100	38.4	35.0

The experimentally measured stress-strain response involving the fracture of PBX 9501 is compared to the calculation with the cohesive parameters chosen as in Table 1. The comparison as provided in Figure 10 of Ref. [87] shows a good agreement between the experiments and the calculations.

2.5 Constitutive Relations of the Material

The hydrostatic part of the stress tensor carried by the material follows the Birch-Murnaghan equation of state (B-M EOS) with the form of

$$\tau_h = \frac{3}{2} K_0 \left(\frac{dV}{dV_0} \right) \left\{ \left(\frac{dV}{dV_0} \right)^{-\frac{7}{3}} - \left(\frac{dV}{dV_0} \right)^{-\frac{5}{3}} \right\} \left[1 + \frac{3}{4} \left(K_0' - 4 \right) \left\{ \left(\frac{dV}{dV_0} \right)^{-\frac{2}{3}} - 1 \right\} \right], \qquad (2\text{-}29)$$

where $\tau_h = \tau_{ii} = \tau_{11} + \tau_{22} + \tau_{33}$ is the hydrostatic part of the Kirchoff stress which is the product of the Jacobian and the negative of the hydrostatic pressure. K_0 is the bulk

modulus, and $K_0' = (\partial K_0/\partial P)_{P=0}$. dV/dV_0 is the derivative of the volume with respect to the initial volume, which is equal to the Jacobian (J = det($\boldsymbol{F}$)) with $\boldsymbol{F}$ being the deformation gradient. For the implementation of the B-M EOS, a time incremental form is used. The time rate of change of the Jacobian is

$$\frac{\partial}{\partial t}\left(\frac{dV}{dV_0}\right) = \left(\frac{dV}{dV_0}\right)\mathrm{tr}(\boldsymbol{D}) \tag{2-30}$$

and the rate of change of the hydrostatic Kirchhoff stress is a function of the Jacobian and rate of deformation, i.e.,

$$\frac{\partial \tau_h}{\partial t} = f\left(\frac{dV}{dV_0}, \mathrm{tr}(\boldsymbol{D})\right). \tag{2-31}$$

The B-M EOS parameters of HMX are $K_0 = 16.71\ GPa$ and $K_0' = 7.79$ as in Ref. [100]. The initial bulk modulus K_0 of the Estane binder decreases as the temperature increases as shown in Ref. [101]. The set of initial bulk moduli K_0 in Ref. [101] and K_0' = 12.95 are used for the Estane binder.

The deviatoric part of the constitutive behavior of the HMX grains is described by an elasto-viscoplastic model. The specific form of the constitutive relation used is

$$\hat{\boldsymbol{\tau}}' = \mathbf{L} : \left(\mathbf{D}' - \mathbf{D}_{\mathrm{p}}'\right), \tag{2-32}$$

where $\mathbf{L}$ is the tensor of elastic moduli and $\hat{\boldsymbol{\tau}}'$ is the deviatoric part of the Jaumann rate of the Kirchhoff stress. For isotropic elastic response,

$$\mathbf{L} = 2\mu\tilde{\mathbf{I}} + \lambda\mathbf{I}\otimes\mathbf{I}. \tag{2-33}$$

Here, $\tilde{\mathbf{I}}$ is the fourth order identity tensor, λ and μ are Lamé's first and second constants. $\mathbf{D}'$ in Eq. (2-32) is the deviatoric part of the rate of deformation, which can be decomposed into an elastic part and a viscoplastic part as

$$\mathbf{D}' = \mathbf{D}'_e + \mathbf{D}'_p, \tag{2-34}$$

where $\mathbf{D}'_p$ is the viscoplastic part of $\mathbf{D}'$ in the form of

$$\mathbf{D}'_{\mathrm{p}} = \frac{3\dot{\bar{\varepsilon}}}{2\bar{\sigma}}\boldsymbol{\tau}', \ \text{with} \ \bar{\sigma}^2 = \frac{3}{2}\boldsymbol{\tau}' : \boldsymbol{\tau}'. \tag{2-35}$$

Here, $\bar{\sigma}$ is the Misses equivalent stress, $\boldsymbol{\tau}'$ is the deviatoric part of the Kirchoff stress, and $\dot{\bar{\varepsilon}}$ is the equivalent plastic strain rate which has the form of

$$\left.\begin{aligned} \dot{\bar{\varepsilon}} &= \frac{\dot{\bar{\varepsilon}}_1 \dot{\bar{\varepsilon}}_2}{\dot{\bar{\varepsilon}}_1 + \dot{\bar{\varepsilon}}_2}, \\ \dot{\bar{\varepsilon}}_1 &= \dot{\bar{\varepsilon}}_0 \left[\frac{\bar{\sigma}}{\mathrm{g}(\bar{\varepsilon}, T)}\right]^m, \\ \dot{\bar{\varepsilon}}_2 &= \dot{\bar{\varepsilon}}_{\mathrm{m}} \exp\left[-a\,\mathrm{g}(\bar{\varepsilon}, T)\right], \\ \mathrm{g}(\bar{\varepsilon}, T) &= \sigma_0 \left(1 + \frac{\bar{\varepsilon}}{\varepsilon_0}\right)^N \left\{1 - \beta\left[\left(\frac{T}{T_0}\right)^\kappa - 1\right]\right\}, \end{aligned}\right\} \tag{2-36}$$

where $\bar{\varepsilon} = \int_0^t \dot{\bar{\varepsilon}}\, dt$ is the equivalent plastic strain, $\dot{\bar{\varepsilon}}_0$ and $\dot{\bar{\varepsilon}}_m$ are reference strain rates, m and a are rate sensitivity parameters for a low strain rate and a high strain rate, respectively, σ_0 is the quasi-static yield stress, ε_0 is a reference strain, N is the strain hardening exponent, T_0 is a reference temperature, and β and κ are thermal softening parameters. The function $\mathrm{g}(\bar{\varepsilon}, T)$ represents the quasi-static stress-strain response at ambient temperature. The above relations consider strain hardening and strain-rate dependence of plasticity. The details of the above constitutive relations and descriptions

of the parameters can be found in Ref. [102]. The parameters of the plasticity model for HMX used in this study are listed in Table 2. The parameters are calibrated to match the experimental wave profile obtained by Dick et al.[103].

Table 2. Parameters in viscoplastic constitutive model of HMX

σ_0 (MPa)	ε_0	N	T_0 (K)	β
260	5.88×10^{-4}	0.0	293	0.0
$\dot{\bar{\varepsilon}}_0$ (s^{-1})	m	$\dot{\bar{\varepsilon}}_m$ (s^{-1})	a (MPa^{-1})	κ
1×10^{-4}	100.0	8.0×10^{12}	22.5	0.0

The deviatoric part of the constitutive behavior of the polymer binders is described by a Prony series. The shear modulus G is assumed to vary with the relaxation time τ^r as in the form of

$$G(t) = G_e + \sum_{i=1}^{n} G_i \exp\left(-\frac{t}{\tau_i^r}\right) \tag{2-37}$$

where G_e is the long term modulus when the binder is fully relaxed, and τ_i^r and G_i are the relaxation time and the modulus of i-th mode, respectively. The modulus as a function of the relaxation time can be obtained from the modulus measured with a range of loading frequency. The modulus of the binder is highly dependent on the temperature. Therefore, the modulus curve over a range of stress wave frequency varies as the temperature changes. The Williams–Landell–Ferry (WLF) factor is an empirical form that shifts the modulus curves at various temperatures and superimposes the curves at a reference temperature to establish a master modulus curve. The specific form is

$$\mathrm{Log}(a_T) = -\frac{C_1(T-T_{ref})}{C_2+(T-T_{ref})}, \tag{2-38}$$

where C_1 and C_2 are WLF parameters that adjust the modulus curves at various temperatures to the master curve, and a_T is the shift factor which is multiplied to the frequency. As shown in Mas et al. [104], the storage modulus $G'(\omega)$ can be represented in terms of the Prony series parameters by using the equation of

$$G'(\omega) = G_e + \sum_{i=1}^{n} G_i \frac{\omega^2 \left(\tau_i^r\right)^2}{1+\omega^2 \left(\tau_i^r\right)^2} , \quad (2\text{-}39)$$

where ω is the wave frequency of a given mode. The Prony series parameters of Estane binder used in this study are shown in Ref. [104].

The thermal conduction is calculated through the Fourier's law with the form of

$$\vec{q} = -k\nabla T , \quad (2\text{-}40)$$

where $\vec{q}$ is the heat flux density, k is conductivity, and ∇T is the temperature gradient. Table 3 shows the parameters of density (ρ), specific heat (c_p), and thermal conductivity (k) for HMX and the Estane binder.

Table 3. Material properties of HMX and the Estane binder

Properties	HMX	Estane
Density ρ (kg·m^{-3})	1910	1190
Specific Heat c_p (kJ·kg^{-1}·K^{-1})	1.254	1.500
Thermal conductivity k (W·m^{-1}·K^{-1})	0.52	0.2

2.6 Contact Algorithm

Once the cohesive element fails and the fracture occurs, the newly generated free surfaces may penetrate each other. Therefore, a constraint should be applied to the element boundaries to restrain the overlap between the elements with the free surfaces. The CFEM framework developed in this study detects the overlap and utilizes a penalty function to strongly repel the penetrated surfaces. This section consists of two parts – contact detection algorithm and penalty algorithm.

Contact detection algorithm

During the simulation, all element overlaps should be accurately detected, which is not a trivial process if multiple fractured elements interact together. The contact detection model in this CFEM framework utilizes a surface-based method. The basic idea of the contact detection model is to check whether a free surface of an element crosses over the boundaries of another element having a free surface. Figure 6 shows the two possible scenarios of overlapping elements. Considering two elements (Ele 1 and Ele 2) having a free surface for each element, the free surface of Ele2 may intersect the free surface of Ele1 (Scenario 1) as shown in Figure 6(a), or the free surface of Ele2 may intersect one of the boundaries of Ele1 (Scenario 2) as shown in Figure 6(b). Once a cohesive element fails, the element numbers of the two adjoining bulk elements are included in the potential contact list. Then, the contact detection model scans all elements in the list and checks the penetration for all possible pairs.

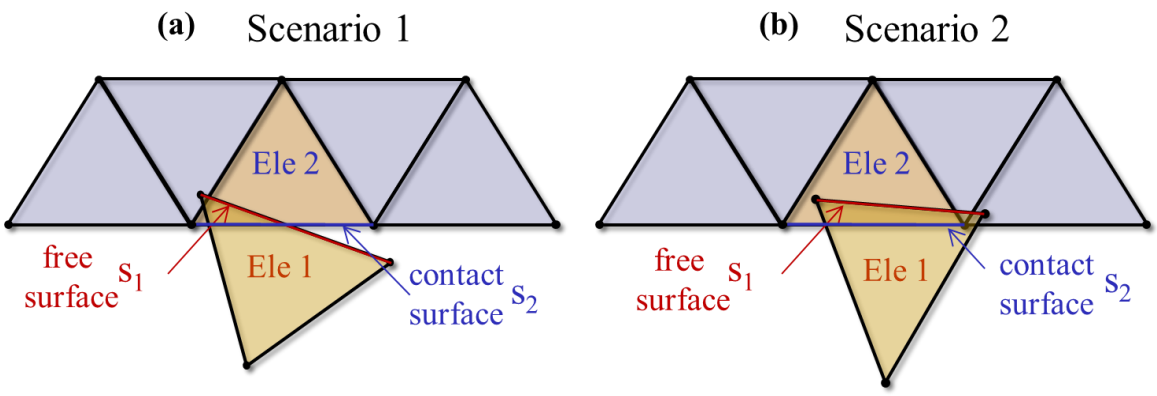

Figure 6. Overlap scenarios between two free surfaces S_1 and S_2; (a) Scenario 1: a free surface crosses over another free surface and (b) Scenario 2: the free surface S_2 crosses over a boundary of an element which possesses the other free surface S_1

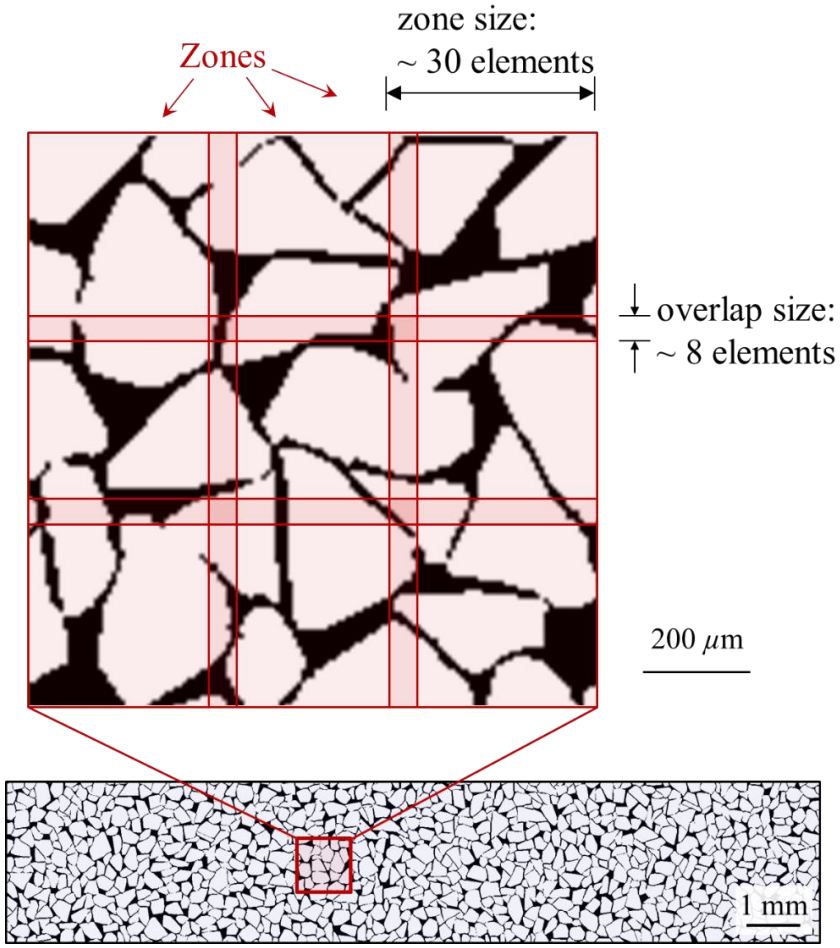

Figure 7. A domain consisting of multiple zones for element contact detection

The contact detection for all potential elements requires a significant amount of computational cost, since the number of investigation increases by the square of the number of the elements (# of checks = $0.5n(n-1)$). Therefore, several optimization schemes are included in the calculation. The first scheme involves dividing the domain into several zones as shown in Figure 7. If a cohesive element fails, the two adjoining bulk elements are assigned to the potential contact list of the zone to which the bulk elements belong. The contact detection calculation is performed based on the potential contact list of each zone separately. To account for the element contact at the zone boundary and ensure all potential contact cases, the zones are arranged to have narrow overlap areas. Although the performance chart is not presented here, the efficiency reaches its maximum if each zone includes roughly 1000 bulk elements. A smaller zone size requires too many zones to cover the domain, and a bigger zone size results in too many elements in each zone.

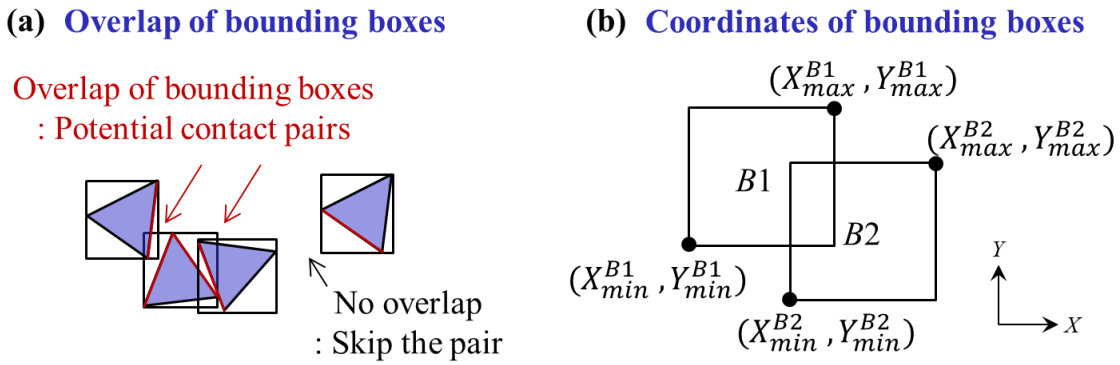

Figure 8. Bounding box scheme for contact detection

The second optimization scheme involves a bounding box of an element. The bounding box is a minimum rectangular box embracing the element. The contact detection calculation involving the free surfaces is preceded by the confirmation of the overlap of

the corresponding bounding boxes. For the elements whose bounding boxes do not overlap are not considered as the potential contact pairs as shown in Figure 8(a). The confirmation of the overlap between two bounding boxes requires much less computational costs than the contact detection of two elements with free surfaces. The specific form of the condition for the overlap of two bounding boxes is

$$\begin{aligned} &X_{max}^{B1} > X_{min}^{B2} \text{ and} \\ &X_{min}^{B1} < X_{max}^{B2} \text{ and} \\ &Y_{max}^{B1} > Y_{min}^{B2} \text{ and} \\ &Y_{min}^{B1} < Y_{max}^{B2} \end{aligned} \tag{2-41}$$

where the superscripts $B1$ and $B2$ represent the two bounding boxes, X_{max} and Y_{max} are the maximum X and Y coordinate values, respectively, and X_{min} and Y_{min} are the minimum X and Y coordinate values, respectively. Figure 8(b) shows the notations of the coordinate used in Eq. (2-41). The condition in Eq. (2-41) holds true irrespective of the relative location of the bounding boxes. The bounding box $B1$ is located at the upper left of the bounding box $B2$ in Figure 8(b). The same condition in Eq. (2-41) can be applied even if the notations of the boxes are switched ($B1$ at lower right and $B2$ at upper left).

Penalty/Friction algorithm

The penalty method inhibits the overlap of two elements by applying a penalty force to the penetrated surface. The magnitude of the normal penalty force is proportional to the penetration depth, and the magnitude of the tangential penalty force is determined by friction. The tangential penalty force is set to zero if the friction is negligible. The penalty algorithm in this study uses a master/slave pairing method, and the direction of the

penalty force and the penetration depth are determined with respect to the master element as shown in Figure 9.

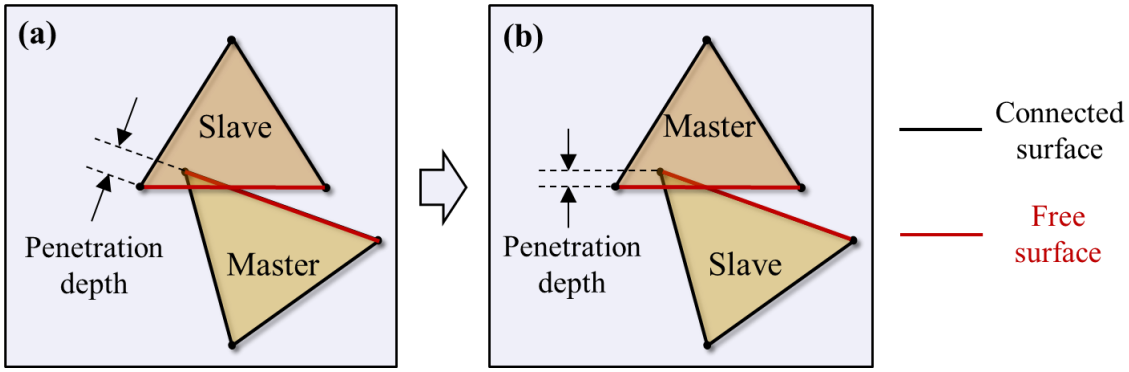

Figure 9. Master/slave combination and the corresponding penetration depth

A penetration depth is obtained for a random assignment of master/slave for a contact element pair as shown in Figure 9(a). Then, the master/slave assignment is switched for the same element pair, and the penetration depth is obtained as shown in Figure 9(b). After comparison of the two penetration depths, the combination having a smaller penetration depth is chosen for the master/slave pair.

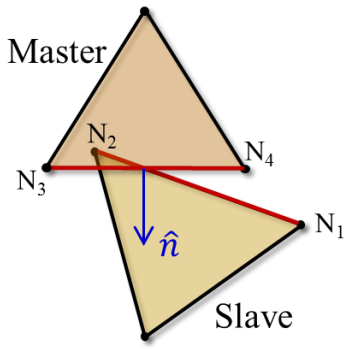

Figure 10. Node numbering scheme and normal direction of master free surface

The direction of the penalty force, $\hat{n}$, is normal to the free surface of the master element as shown in Figure 10. Specifically, the penalty force acting on the free surface of the master element is in the direction of $-\hat{n}$, and the opposite direction for the slave element. The magnitude of the penalty force is a function of penetration depth, velocity, and acceleration of the nodes N_1, N_2, N_3, and N_4 in Figure 10. The penalty force is represented as

$$f_p = f\left(a_p, v_p, \alpha d_p\right), \tag{2-42}$$

where f_p is the magnitude of the penalty force, a_p is the penalty acceleration, v_p is the penalty velocity, d_p is the penetration depth, α is a factor that controls the effect of penetration depth. The value of α is chosen to be small (< 0.01) to achieve numerical stability under high pressure. Even with such a small value of α, the penetrated elements become detached in a few time steps, because the penalty force is accumulated at every time step, and the other terms (penalty acceleration and velocity) add the separation force to the final penalty force.

The magnitude of penalty acceleration a_p is either the same as the relative acceleration if the two elements are accelerating toward each other, or zero if the two elements are accelerating away from each other. The specific form of the equation is

$$a_p = \begin{cases} H(a_{rel}^n) \cdot a_{rel}^n, & \text{for } N_1 \text{ and } N_2 \\ H(-a_{rel}^n) \cdot a_{rel}^n, & \text{for } N_3 \text{ and } N_4 \end{cases} \tag{2-43}$$

where $H(\cdot)$ is Heaviside step function and a_{rel}^n is the relative acceleration with the form of

$$a_{rel}^n = a_{avg}^n - a_i^n \ , \tag{2-44}$$

where a_i^n is the current acceleration of the i-th node (i = 1,2,3,4) in the normal direction $\hat{n}$ and a_{avg}^n is the weighted average of the accelerations at the nodes N_1, N_2, N_3, and N_4 in Figure 10. The specific form of the weighted average a_{avg}^n is

$$a_{avg}^n = \begin{cases} \dfrac{a_1^n + w_1 a_3^n + (1-w_1)a_4^n}{2}, & \text{for } N_1 \\ \dfrac{a_2^n + w_2 a_4^n + (1-w_2)a_3^n}{2}, & \text{for } N_2 \\ \dfrac{a_3^n + w_3 a_1^n + (1-w_3)a_2^n}{2}, & \text{for } N_3 \\ \dfrac{a_4^n + w_4 a_2^n + (1-w_4)a_1^n}{2}, & \text{for } N_4 \end{cases} \tag{2-45}$$

where w_i (i = 1,2,3,4) is the weight for each node with the form of

$$\begin{aligned} w_1 &= \overline{N_1N_4}/(\overline{N_1N_3} + \overline{N_1N_4}) \\ w_2 &= \overline{N_2N_3}/(\overline{N_2N_3} + \overline{N_2N_4}) \\ w_3 &= \overline{N_2N_3}/(\overline{N_1N_3} + \overline{N_2N_3}) \\ w_4 &= \overline{N_1N_4}/(\overline{N_1N_4} + \overline{N_2N_4}) \end{aligned} \tag{2-46}$$

where $\overline{N_iN_j}$ (i,j = 1,2,3,4) is the distance from N_i to N_j . The equations for the penalty velocity v_p are the same as Eqs. (2-43), (2-44), (2-45), and (2-46) with the replacement of 'a' by 'v' in the equations.

The force on the i-th node of the free surface is

$$f_i = m_i(a_{p,i} + \frac{v_{p,i}}{dt} + \alpha \frac{d_p}{dt^2}) \tag{2-47}$$

where $a_{p,i}$ and $v_{p,i}$ are $a_p$and v_p of i-th node, respectively, and m_i is nodal mass, dt is the computational time increment. The penalty force f_p should satisfy the action-reaction force

law. Specifically, the sum of the penalty forces at nodes N_1 and N_2 should have the equal magnitude to the sum of the penalty forces at nodes N_3 and N_4. The penalty force is obtained from the following force-balance constraint.

$$\begin{aligned} f_{p,1} &= \frac{f_1 - (f_3 + f_4)/2}{2} \\ f_{p,2} &= \frac{f_2 - (f_3 + f_4)/2}{2} \\ f_{p,3} &= \frac{f_3 - (f_1 + f_2)/2}{2} \\ f_{p,4} &= \frac{f_4 - (f_1 + f_2)/2}{2} \end{aligned} \tag{2-48}$$

where $f_{p,i}$ (i = 1,2,3,4) is the penalty force applied to the i-th node.

The friction algorithm is based on the Coulomb friction model. For a tangential motion occurring on a contact surface, the magnitude of a frictional force is estimated to stop the motion. The specific form is

$$f_e^t = m \cdot (a_{rel}^t + \frac{v_{rel}^t}{dt}) \tag{2-49}$$

where f_e^t is the estimated frictional force, m is nodal mass, a_{rel}^t and v_{rel}^t are relative acceleration and relative velocity in tangential direction, respectively. The value of a_{rel}^t is obtained from Eqns. (2-44), (2-45), and (2-46) with the replacement of 'n' by 't' (i.e., normal direction by tangential direction), and the value of v_{rel}^t is obtained similarly with the replacement of 'a' by 'v'.

The magnitude of a frictional force is limited by normal force multiplied by a frictional coefficient μ as shown in the following constraint.

$$f_{fric} \leq \mu \cdot f^n \tag{2-50}$$

where f^n is the normal force on the free surface and f_{fric} is the frictional force. Therefore, the specific form of the frictional force f_{fric} is

$$f_{fric} = \min(\mu \cdot f^n, f_e^t). \tag{2-51}$$

Green et al. [105] obtained the frictional coefficient of approximately 0.3 – 0.7 for PBX9404, and Chidester et al. [18] used the coefficient of 0.5 as the average value of Green et al [105]. Dickson et al. [106] reported that the frictional coefficient for PBX 9501 is between 0.4 and 0.5. The frictional coefficient of 0.5 is chosen for this study.

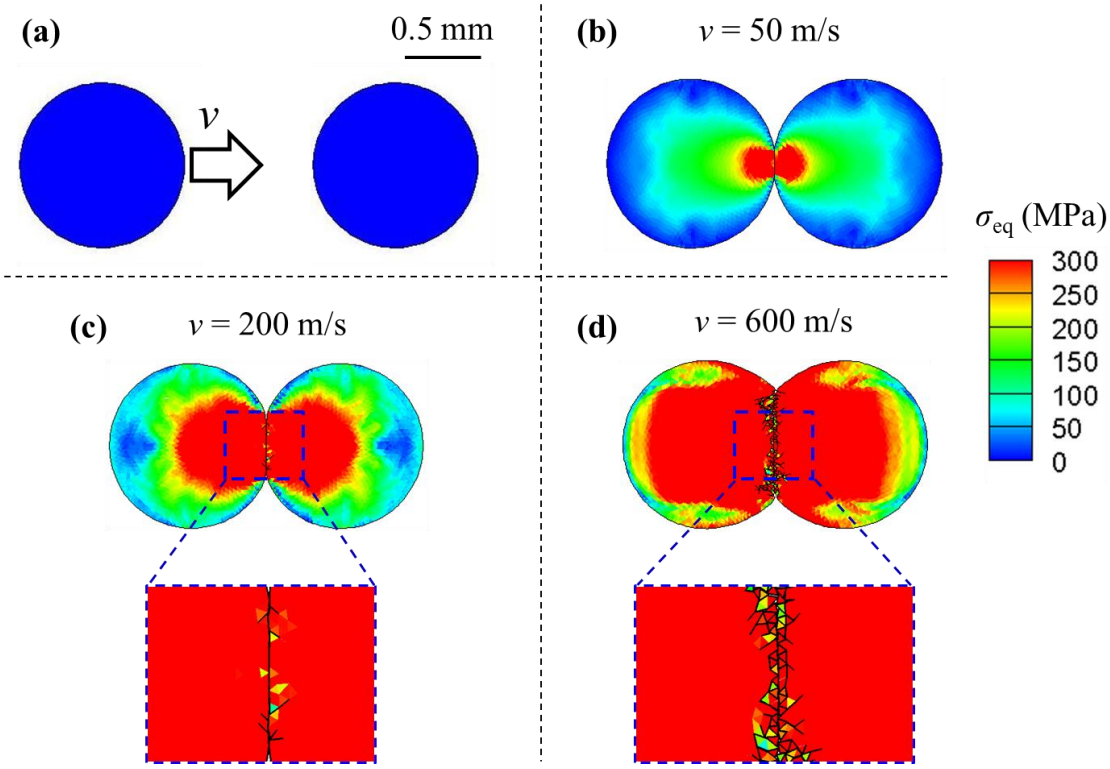

Figure 11. Particle-particle collision test to verify the contact algorithm

To verify the implementation of the penalty and friction algorithm, particle-particle collision tests are performed with low (v = 50 m/s), high (v = 200 m/s), and very high (v = 600 m/s) initial velocities. In Figure 11(a), the initial velocity is imposed on the left particle toward the particle on the right. The two particles have an equal size and equal HMX material properties. Figures 11 (b),(c), and (d) show the contact moment when the deformation is the most severe. For all velocities tested, the contact algorithm implemented provides reliable responses at the initial particles surfaces and the fractured surfaces as shown in the close-up views in Figure 11 (c-d).

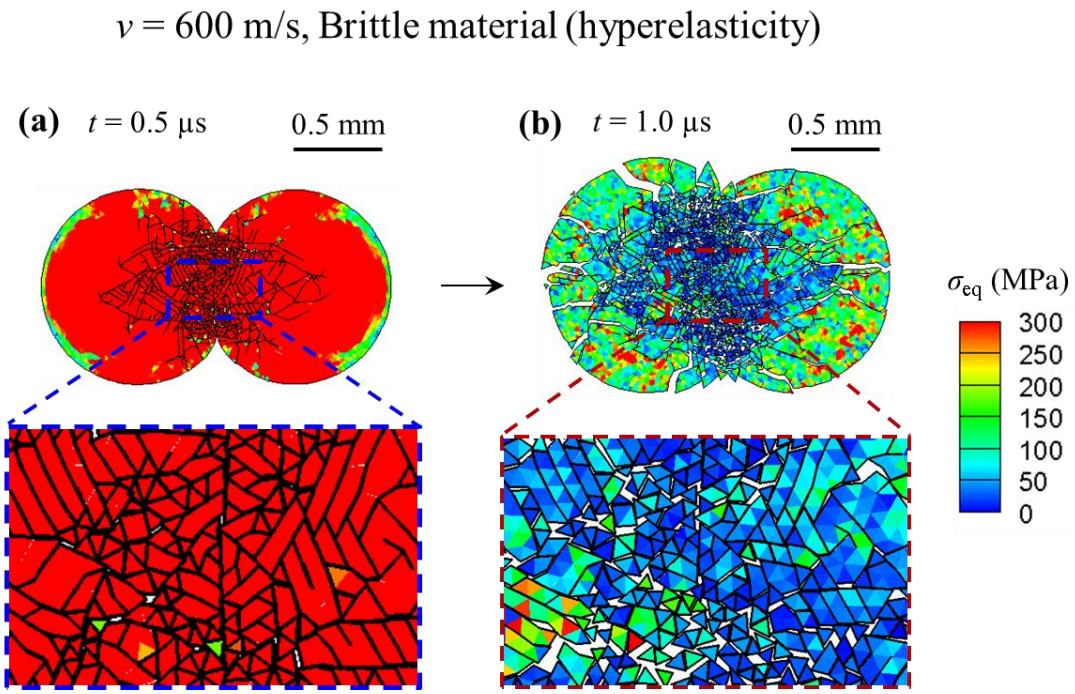

Figure 12. Particle-particle collision involving significant amount of fractures

Multi-body contact involving high pressure and large deformation is computationally a challenging problem. To ensure the performance and the reliability of the implemented algorithm under such conditions, a particle collision test with a significant amount of fracture is performed. The plasticity constitutive relation of HMX

is replaced by a hyper-elasticity constitutive relation to make the material brittle and create more fractures. The specific hyper-elasticity model used for this reliability test is the Saint Venant-Kirchhoff model which is an extension of the linear elastic law involving the rate relation, $\dot{\mathbf{S}} = \mathbf{C}:\dot{\mathbf{E}}$, where $\mathbf{C}$ is the 4th order tangent modulus tensor, $\dot{\mathbf{S}}$ is the rate of PK2 stress, $\dot{\mathbf{E}}$ is the rate of Green strain. Figure 12(a) shows the contact moment when the deformation is at the most severe stage. The close-up view shows numerous cracks and the contact between the cracks. After the impact, the particles break into pieces. Although HMX would deform plastically under such a severe impact condition, this impact test without the plasticity model provides numerically challenging fracture environment for the contact algorithm. A reliable response is observed under multi-body contact situations with the contact algorithm implemented.

CHAPTER 3: IGNITION PROBABILITY BASED ON HOTSPOT CRITICALITY

This chapter is based on the work published in Ref. [107] and Ref. [108] in collaboration with Ananda Barua.

3.1 Introduction

The goal in this chapter is to develop a framework for computationally predicting and quantifying the stochasticity of the ignition process in PBXs under impact loading. The focus is on the influence of microstructure geometry on the critical time to ignition and the critical impact velocity below which no ignition occurs. This is accomplished by accounting for three key issues. The first issue involves the analysis of thermal and mechanical responses of heterogeneous energetic materials at the micro-level. This analysis uses a recently developed capability based on the cohesive finite element method (CFEM) [87, 109-111]. The second concerns hotspot generation and an ignition criterion for the thermal runaway of critical hotspots. The criterion of hotspot criticality is determined by connecting locally heated high temperature spots due to thermos-mechanical processes to the ignition process defined as the thermal run-away phenomenon in the localized high temperature regions. The third issue is the effect of random fluctuations in the microstructure geometry on the ignition response of PBX. This issue is handled by subjecting sets of statistically similar microstructure samples to identical overall loading and characterizing the statistical distribution of the ignition responses of the samples. The quantification of this distribution as a function of microstructural attributes including grain volume fraction, grain size, specific grain-binder interface area, and the stochastic variations of these attributes is used to identify the microstructural attributes which play dominant roles in determining the ignition behavior of these materials.

In experiments, there is a degree of stochasticity associated with the thermal runaway of hotspots in that quantities such as load intensity required to cause ignition, time to ignition from onset of loading, and total energy input at ignition may vary from sample to sample. One source of the stochasticity is variations in material microstructure and loading conditions. The issue of impact-induced ignition needs to be approached from a probabilistic viewpoint (see, e.g., Ref. [112]). Such studies may involve a statistical study using various levels of critical hotspot density and correlation of the results with experimental data. We focus on the stochasticity arising out of variations in microstructure geometry. Our approach to assess the sensitivity of explosives combines the deterministic analysis using our micromechanical cohesive finite element method (CFEM) and a stochastic treatment of the numerical results from a large number of microstructure instantiations. This is essentially the computational equivalent of carrying out a large number of experiments under the same conditions. This analysis will help establish microstructure-performance maps for developing PBXs with tailored attributes.

3.2 Thermal Criticality Threshold

Mathematically, the criterion at the junction of the first (thermal-mechanical) phenomenon which provides hotspots and the second (thermal-chemical) phenomenon which leads to thermal runaway can be stated as

$$d(T) \geq d_c\,(T) \tag{3-1}$$

where, d is the diameter of the dominant hotspot resulting from a loading event whose interior temperatures are at or above temperature T and d_c is the minimal diameter of a hotspot required for thermal runaway at temperature T. Note that the right-hand side of

Eq. (3-1) represents the boundary between "ignition" and "non-ignition" in the d - T space and reflects material attributes. Information about this material properties part of the criterion has to be obtained independently, from experiments or thermal-chemical calculations. In the current paper, this information comes from hotspot size-temperature threshold relations for solid explosives derived from thermal-chemical reaction calculations. The rest of this paper focuses on the two sides of the criterion in Eq. (3-1) first the right-hand side, then the left-hand-side. It is important to point out at the outset that because the hotspot state represented on the left hand side of Eq. (3-1) can be the result of either shock or non-shock loading and the thermal-chemical threshold condition embodied on the right hand side of Eq. (3-1) is independent of loading, the criterion proposed here should in general apply to both non-shock and shock loading.

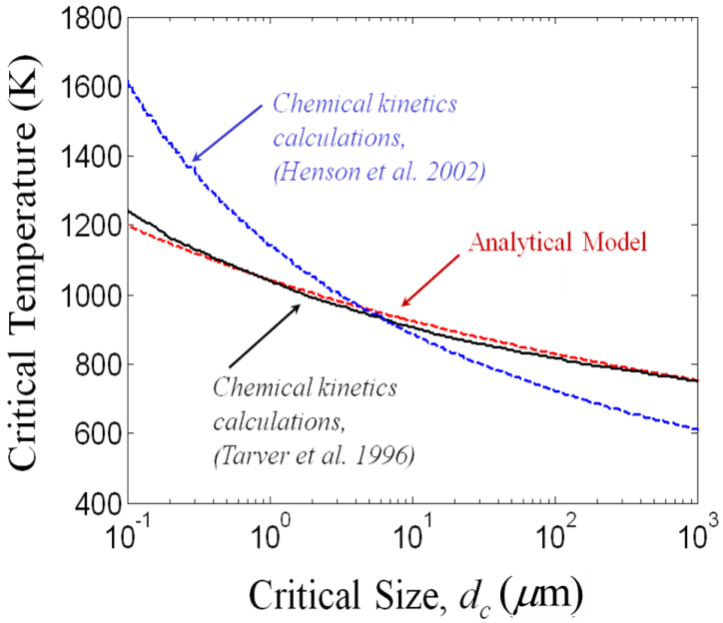

Figure 13: Temperature-hotspot size threshold curves for ignition or thermal runaway of HMX, data from chemical kinetics calculations performed by Tarver et al. [33] is shown, along with the analytical relation in Eq. (3-2), which is fitted to Tarver et al.'s data. For comparison, Henson's data [35] are also shown, but not used in the material specific analyses of this study.

At present, hotspot sizes and temperatures cannot be measured experimentally. Hence, we need to rely on theoretical estimates to predict thermal criticality of hotspots. Criticality occurs when the temperature in a hotspot of a given size and shape is high enough so that the rate of temperature increase due to chemical reaction is higher than the rate of temperature decrease due to heat loss through conduction (and other dissipative processes if any) across the surface of the hotspot. The thermal criticality threshold is used to relate the size and temperature of hotspots at the critical condition in Eq. (3-1). Solutions of the heat diffusion equation with heat generation due to reaction have been used to predict the temperature rise in hotspots for a range of canonical shapes (spherical, planar circular, elliptical, etc.). The analytical formulation can be expressed as [2]

$$d_c = f(T_s, \text{material properties, shape}), \tag{3-2}$$

where T_s is the temperature at the surface of the hotspot. The specific form of Eq. (3-2) obtained from the solution of the heat diffusion equation is presented on page 202 in Ref. [2]. The relation considers pure explosive materials following single-step Arrhenius reaction kinetics and is independent of the loading conditions (shock or nonshock). In summary, the analytical formulation can be used to estimate the critical size of a hotspot with a specific shape, at a given surface temperature.

Tarver et al. [33] performed chemical kinetics calculations to analyze the criticality issue for HMX and 2,4,6-triamino-1,3,5- trinitrobenzene explosives. The calculations consider multistep reaction mechanisms and the pressure and temperature dependence of reactants and products. The black line in Figure 13 shows the calculated critical temperature as a function of size for spherical hotspots in HMX [33]. For comparison, the analytical formulation as fitted to Tarver et al.'s data [Eq. (3-2)] from Ref. [2] for a

spherical hotspot is also plotted in Figure 13 (red line). The fit provides a good description of Tarver et al.'s data [33]. This is of interest since Tarver et al. [33] considered a three-step reaction pathway for the decomposition of HMX. The close agreement with the analytical response suggests that over this range of ignition times, there could be a single rate-limiting step in the ignition mechanism.

It must be noted that Henson [35] suggested a similar possibility since the data for ignition time as a function of temperature appears to be close to linear on the log-log scale. Specifically, he also performed chemical kinetics calculations and came up with a critical size vs. temperature relationship for hotspots in HMX, which is shown in Figure 13 in blue. The disparity between the results from Tarver et al. [33] and Henson [35] may stem from the way in which the hotspot temperatures are calculated. In this paper, the relation provided by Tarver et al. [33] is used to identify critical hotspots. It is noted that, although there is a numerical difference in the relations provided in Refs. [33] and [35], the qualitative nature and the trend of the response are be similar regardless of which set of data is used.

Critical hotspots are identified using the threshold condition in Eq. (3-1). The right-hand side of the equation uses Tarver et al. [33]'s numerical data (shown in Figure 13). The left-hand side of Eq. (3-1) is obtained by analyzing the hotspot distributions from the CFEM calculations. To account for the variation of temperature within a hotspot (note that temperatures at different spatial locations within a hotspot are different and ΔT_{thres} is the lowest temperature at the periphery), Tarver et al.'s criterion is stated as a band of $\pm$10% about the mean value. Any hotspot is considered to be critical when it crosses the lower threshold limit (90% of the average threshold). Taking into consideration the stochastic nature of arbitrary microstructures, we employ an approach

to identify the time to criticality t_c measured from the onset of dynamic loading. Specifically, instead of one single hotspot, criticality is regarded as being reached if the critical hotspot density in a specimen reaches a level equal to or greater than 0.22 mm^{-2}. This level corresponds to 2 critical hotspots in a 3mm square domain. It is important to point out that variations in the choice of this parameter do not significantly change the results. Specifically, for a change of critical hotspot density from 0.11 to 0.44 mm^{-2}, the maximum variation in tc is within 6% for a PBX microstructure having a packing density of 0.82 in several calculations with impact velocities between v = 50 and 250 m/s. This shows that the value of the critical hotspot density chosen is quite reasonable and does not cause large changes in results. Although this treatment contains a degree of arbitrariness, it allows relative comparisons to be made when used consistently for difference cases. It should be pointed out that calculations are carried out using mesh sizes from 10 – 20 μm. The results converge as the mesh size is decreased beyond 15 μm. Specifically, the variation of hotspot size leads to a variation of time to criticality t_c of less than 5% for a 33% reduction in the mesh size from 15 to 10 μm, suggesting that the mesh resolution chosen (15 μm) is adequate for the purpose of the current study.

The time since the onset of dynamic loading at which criticality is reached is taken as the critical time (t_c) and the energy imparted to the specimen per unit load contact area up to this time is taken as the critical input energy density (E).

3.3 Materials

3.3.1 Materials Considered

For the analysis of hotspot criticality, both granular HMX (GXs) and HMX/Estane PBXs are used. The actual microstructure is obtained from Ref. [113] and has a grain

volume fraction of 0.82. This microstructure is used to model the PBX, as shown in Figure 14(a). Additionally, a set of five idealized microstructures are used to model granular HMX. These samples are generated using monomodal and bimodal size distributions of circular grains [representative micrographs are shown in Figure 14(b) – Figure 14(f)]. For this set of five microstructures, two grain sizes are used, with the smaller being 120 μm and the larger being 360 μm. The microstructures analyzed, along with their attributes are listed in Table 4.

For the analysis of ignition probability, we focus on the stochasticity arising out of variations in microstructure geometry. Our approach to assess the sensitivity of explosives combines the deterministic analysis using our micromechanical cohesive finite element method (CFEM) and a stochastic treatment of the numerical results from a large number of microstructure instantiations. This is essentially the computational equivalent of carrying out a large number of experiments under the same conditions.

In the following analyses each sample represents a single microstructure instantiation. A 'statistically similar set' consists of a number of microstructures having the same overall packing density η, average grain size d and grain size distribution. In addition to these attributes, the analysis also considers sets of microstructures having specified variations in the specific surface area of the grains (ΔS_v) and the grain size distribution. Specifically, the sensitivity of a particular PBX composition is evaluated by performing numerical 'experiments' on multiple instantiations of statistically similar microstructures. The goal of this approach is to ascertain the dominant trends which relate microstructure to ignition sensitivity. Specifically, the variations at the microstructure level are related to the variations in the probability of ignition.

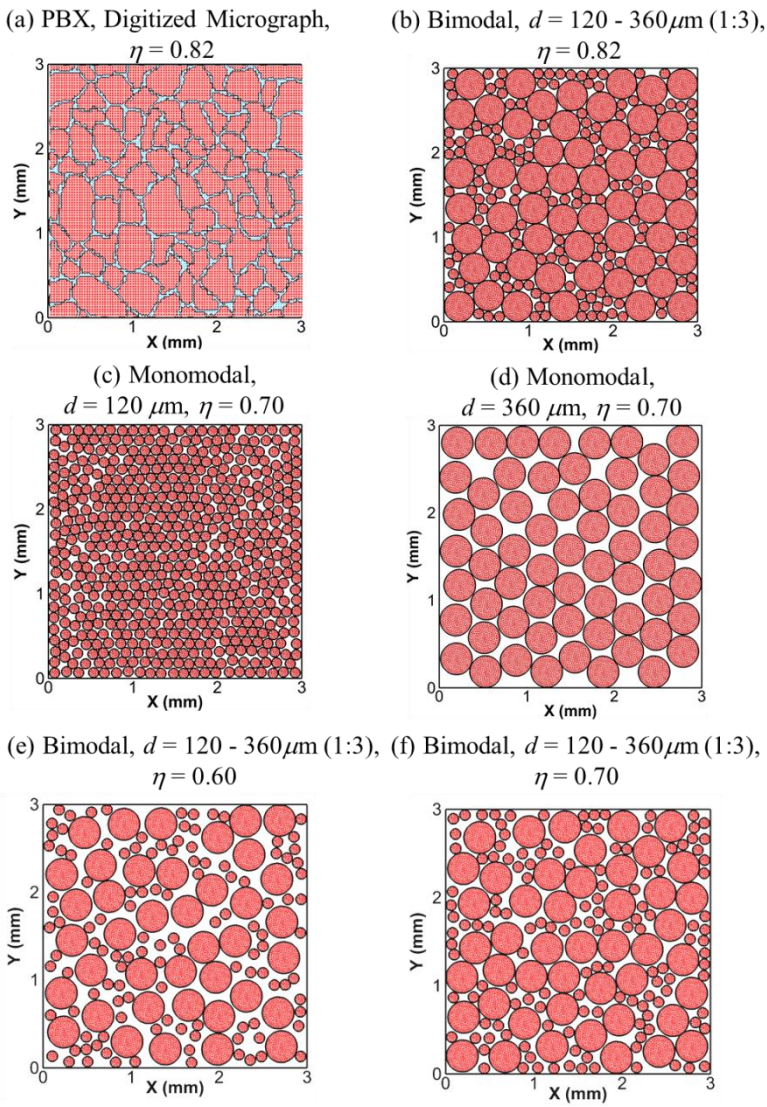

Figure 14: Microstructures used for hotspot criticality analysis—digitized image of a PBX and idealized microstructures for granular HMX with different grain size distributions, (a) digitized image of a PBX, (b) bimodal GX, d = 120–360 μm and η = 0.82, (c) monomodal GX, d = 120 μm and η = 0.70, (d) monomodal GX, d = 360 μm, η = 0.70 (e) bimodal GX, d = 120–360 μm and η = 0.60, and (f) bimodal GX, d = 120–360 μm and η = 0.70.

Table 4: Microstructure used for hotspot criticality analysis

Microstructure	Grain volume fraction (η)	Average grain Size (μm)	Attributes
GX (15 instantiations)	0.60	120 – 360 (1:3)	Bimodal
	0.70	120 – 360 (1:3)	Bimodal, Mono-modal
	0.82	120 – 360 (1:3)	Bimodal
PBX (Digitized)	0.82	287.4	Real

To analyze the stochasticity of ignition behavior, a large number of microstructure are generated. The benefits of using computationally-generated microstructures here are (1) large (>1,000) numbers of sample instantiations can be obtained and (2) sets of samples with attributes that conform to prescribed statistical distribution functions, averages and random fluctuations can be obtained in a controlled manner. These considerations are especially important for the current analyses, as will become clearer later.

The microstructures generated have multifaceted grains with monomodal and bimodal distributions of sizes. The microstructures having monomodal size distributions are generated using the Voronoi tessellation function. This is a geometric method that allows us to define a statistical sample space in a relatively straightforward way. The packing density is varied by properly altering the average thickness of the binder phase between neighboring grains. The mean grain size is 250 μm, with a standard deviation of 90 μm. Note that in the generation of microstructures using Voronoi tessellation, the energetic granules are effectively 'grown' in place, subject to spatial constraint, whereas in actual PBXs, the grains are grown in solution and pressed or cast to the desired density and composition. In Ref. [87], a limited study was carried out on the shape and size of

granules generated using Voronoi tessellation. It is found that the effect of the method on shape is on the same order as that on grain size distribution.

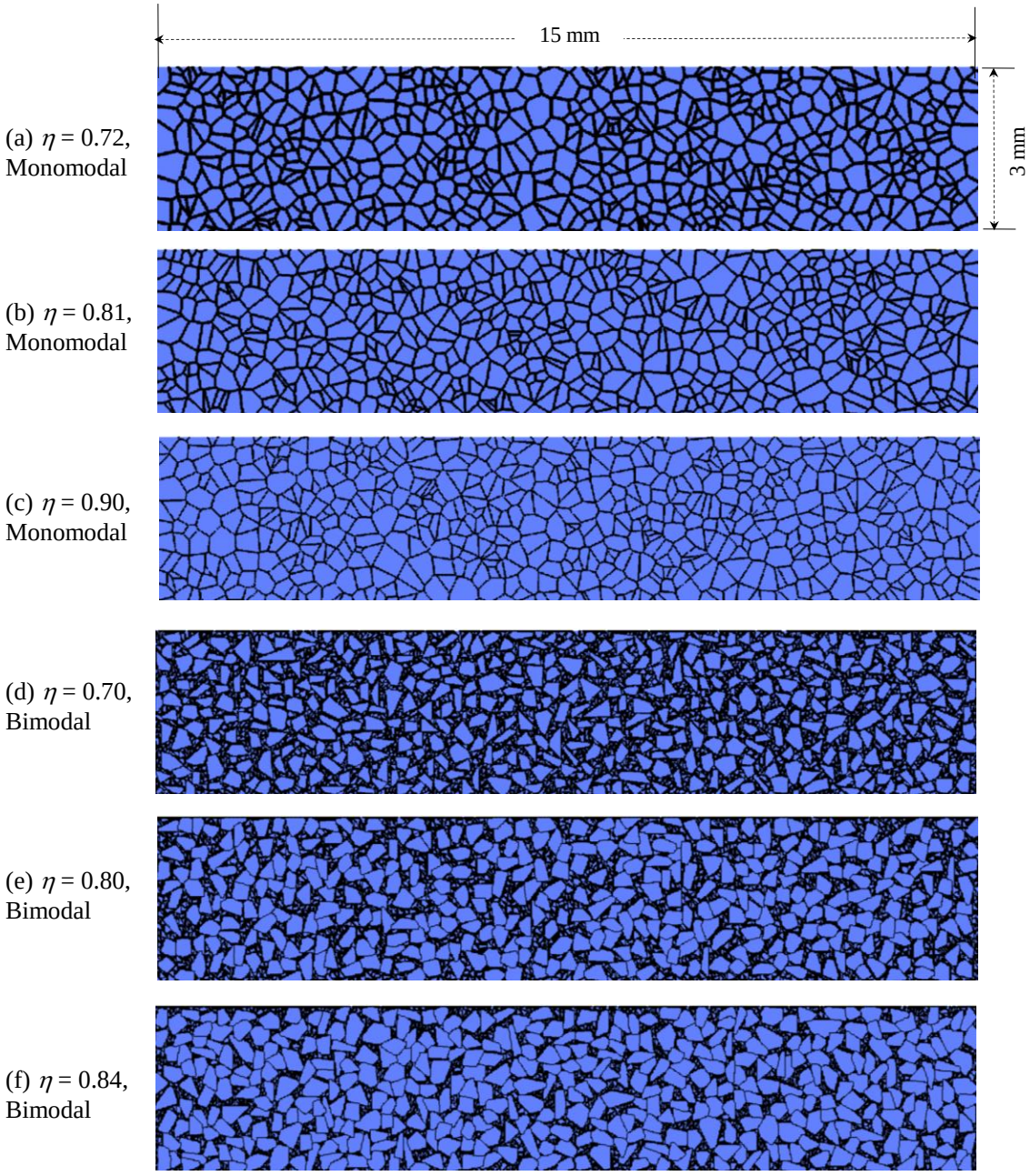

Figure 15: Microstructures with different grain volume fractions (η = 0.70 - 0.90) and grain size distributions (monomodal, bimodal).

To generate microstructures with bimodal size distributions, a grain library is used. This library consists of grains extracted from monomodal microstructures which are generated using the Voronoi tessellation method. To achieve higher packing densities, the larger grains ($d > 250$ μm) are initially placed at random locations up to a specified volume fraction (e.g., $\eta = 0.40$). Subsequently, smaller grains ($d < 100$ μm) are placed between the larger grains, until the desired volume fraction ($\eta = 0.70 – 0.84$) is reached. The time required to generate a micrograph increases with the desired packing density. To reduce the time required in generating micrographs with high packing densities ($\eta > 0.80$), a random shuffling algorithm is employed. Specifically, if a grain cannot be placed in the domain, the locations of the existing grains are randomly altered until an empty region can be found for that particular grain. Naturally, such a method cannot be used indefinitely, since beyond a certain packing density, grains of a particular size can no longer be accommodated. This method allows relatively high packing densities (up to 0.84) to be achieved. For the bimodal distributions, the two mean grain sizes are ~61 μm and ~287 μm. The average standard deviations for the smaller and larger sizes are 20.53 μm and 40.6 μm, respectively.

A total of six different microstructural configurations are considered. The volume fraction is in the range of $\eta = 0.70 – 0.90$, involving both the monomodal and bimodal grain size distributions. One representative micrograph is shown for each of the six configurations in Figure 15(a-f). The microstructures analyzed, along with their attributes, are listed in Table 5. The grain size distributions for the microstructures in Figure 15 are shown in Figure 16. For each microstructural setting listed in Table 5, up to thirty statistically identical samples (random instantiations) are generated. To illustrate the random variations in microstructure geometry within one particular set, Figure 17 shows

10 microstructures having the same packing density of η = 0.81 and monomodal grain size distribution.

Table 5: Microstructures used for the analysis on ignition probability

Microstructure	Grain volume fraction (η)	Average grain Size (μm)	Standard deviation (μm)	Average specific surface area, S_v (mm^{-1})
PBX – Monomodal	0.72	235.1	87.4	15.65
	0.81	250.1	90.0	16.38
	0.90	264.3	92.1	17.37
PBX – Bimodal	0.70	64.3 – 251.2	19.7 – 45.3	25.26
	0.80	61.0 – 301.7	21.4 – 31.6	21.06
	0.84	59.6 – 307.5	20.5 – 44.9	18.00

The variations of grain size distribution within a particular set of microstructures with otherwise similar attributes (volume fraction, average grain size) can also affect the variability in the ignition response. For this purpose, two additional sets of microstructures are generated with large and small variations in grain size distribution. Figure 34(a-d) quantifies the distributions of mean grain size and the distributions of the variations in the grain size relative to the mean grain sizes for these two sets of microstructures. The volume fraction of the grains is η = 0.81 and the size distribution is monomodal.

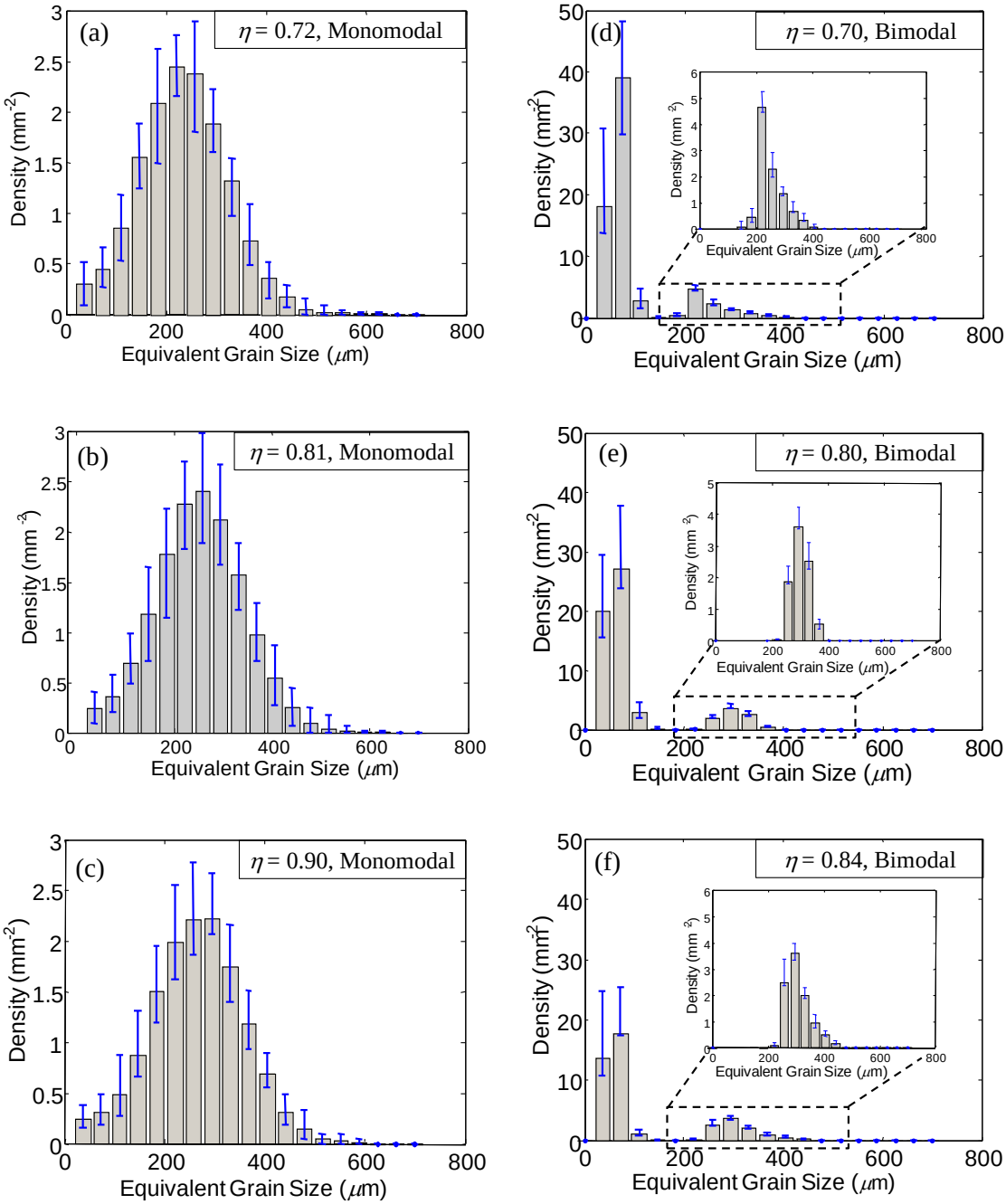

Figure 16: Grain size distributions for the microstructures shown in Figure 15

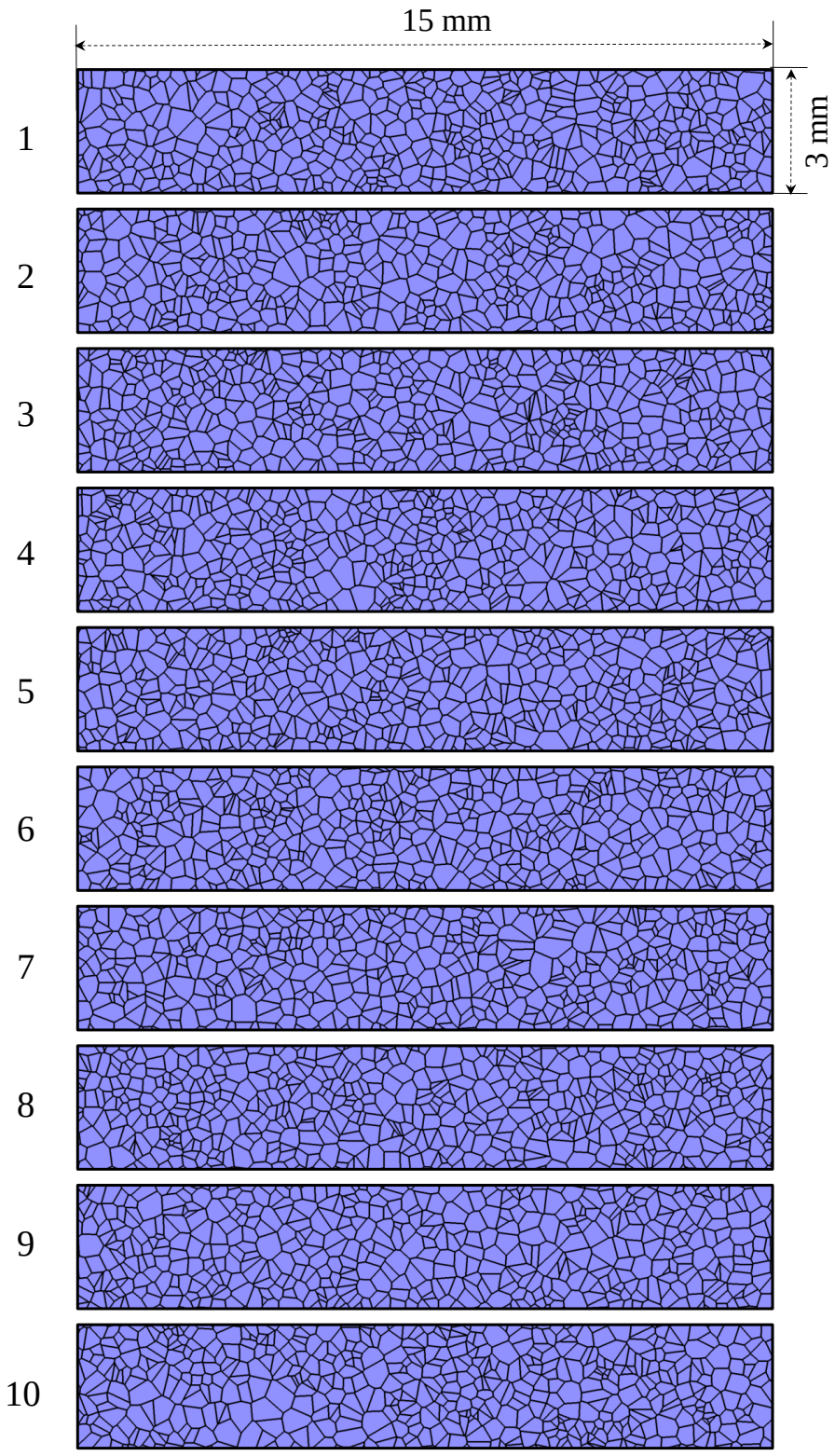

Figure 17: Multiple instantiations of microstructures having a grain volume fraction of η = 0.81 and the monomodal size distribution.

3.3.2 Quantification of Stochasticity

The stochastic nature of microstructural heterogeneities such as varying grain size and random constituent morphologies necessitates a statistical approach in the quantification of hotspot formation. This in turn requires an account of stochasticity in the application of the ignition criterion and hotspot threshold method. The analysis of hotspot criticality reflects such a probabilistic viewpoint.

To account for the stochastic variations in microstructures, sets of 10-50 microstructures with statistically similar attributes are constructed and used. The stochasticity analysis begins with running a fully dynamic thermomechanical impact response simulation and measuring the time to criticality for each sample in the microstructure sets. The different times to criticality in each set are taken together to quantify the stochastic variation in the behavior of the material with a particular attribute combination. The microstructural attributes considered are HMX volume fraction (η) which is often referred to as the packing density, grain size distribution (mean grain size δ and standard deviation σ), area of the interface between the HMX phase and the polymer binder per unit volume (S_v, often referred to as the specific interface area), and the statistical variations of these quantities among samples in each microstructure set. These quantities measure the stochastic variations in the microstructures and, along with the load intensity represented by the impact velocity (v), constitute the input to our statistical model. On the other hand, the times to criticality measure the stochastic variations in material behavior and represent the output in our statistical model. The output also includes the threshold impact velocity below which no ignition is observed (v_c) for a particular statistical microstructure configuration (Figure 15).

Once an ensemble (or a set of microstructures) is defined, the distribution of the time to criticality can be uniquely determined for any given load intensity. For each set of microstructures having a given combination of statistically similar attributes, the time to criticality (t_c) is evaluated as a cumulative probability distribution. Naturally, the time to criticality is different for different instantiations of microstructure. The times to criticality (t_c) obtained from all calculations in a set are

$$\boldsymbol{t_c} = \left(t_{c,1},...,t_{c,\xi}\right), \quad \xi = \text{number of instantiations.} \tag{3-3}$$

The data in Eq. (3-3) allows the cumulative probability distribution of t_c to be computed. The results are fitted to the Weibull distribution function [114]. By relating the variation of this distribution to the microstructural attributes (input parameters), we can identify relationships between the ignition sensitivity and microstructure conditions of PBXs. The distribution function can also be used to determine other statistical measures of ignition response, such as the expected mean time to criticality t_{exp}, median time to criticality t_{50} and the critical impact velocity below which no ignition occurs (v_c). These measures can be related to empirical ignition thresholds for explosives, in the form of the Walker-Wasley relation [36] and the modified Hugh James relation discussed in Ref [107].

3.3.3 Loading Configurations

Calculations are performed using three different loading configurations. The first is a 3-mm square microstructural region shown in Figure 18(a). The size of the sample is chosen to

(1) obtain a sufficiently large representative sample of the microstructures—note that this sample size is at least one order of magnitude larger than the length scale of the mean grain size for this type of PBX, giving reasonable representation of the microstructures; and

(2) allow nominally homogeneous states of stress to be reached through stress wave reverberation over the duration of the calculations. This configuration simulates the conditions of split Hopkinson pressure bar experiments.

The specimen is initially stress-free and at rest. The loading configuration is designed to simulate the conditions of nominally uniaxial strain, therefore, the lateral (left and right) boundaries are fixed. The velocity boundary condition at the top surface and the fixed displacement boundary condition at the bottom surface allow prescribed overall deformation rates to be imposed. Loading is effected by applying a constant normal velocity on the top of the sample. The strain-rate $\dot{\varepsilon}$ is calculated by dividing the velocity of the top surface v by the initial height of the specimen. This is a 2D model and the conditions of plane-strain prevail. Since the bottom surface is fixed, this configuration considers the effect of stress wave reflection. For a typical calculation for the PBX, the wave reaches the bottom surface at ~ 1.15 μs. This can be considered as a delay time before the stress distribution becomes nominally uniform in the sample.

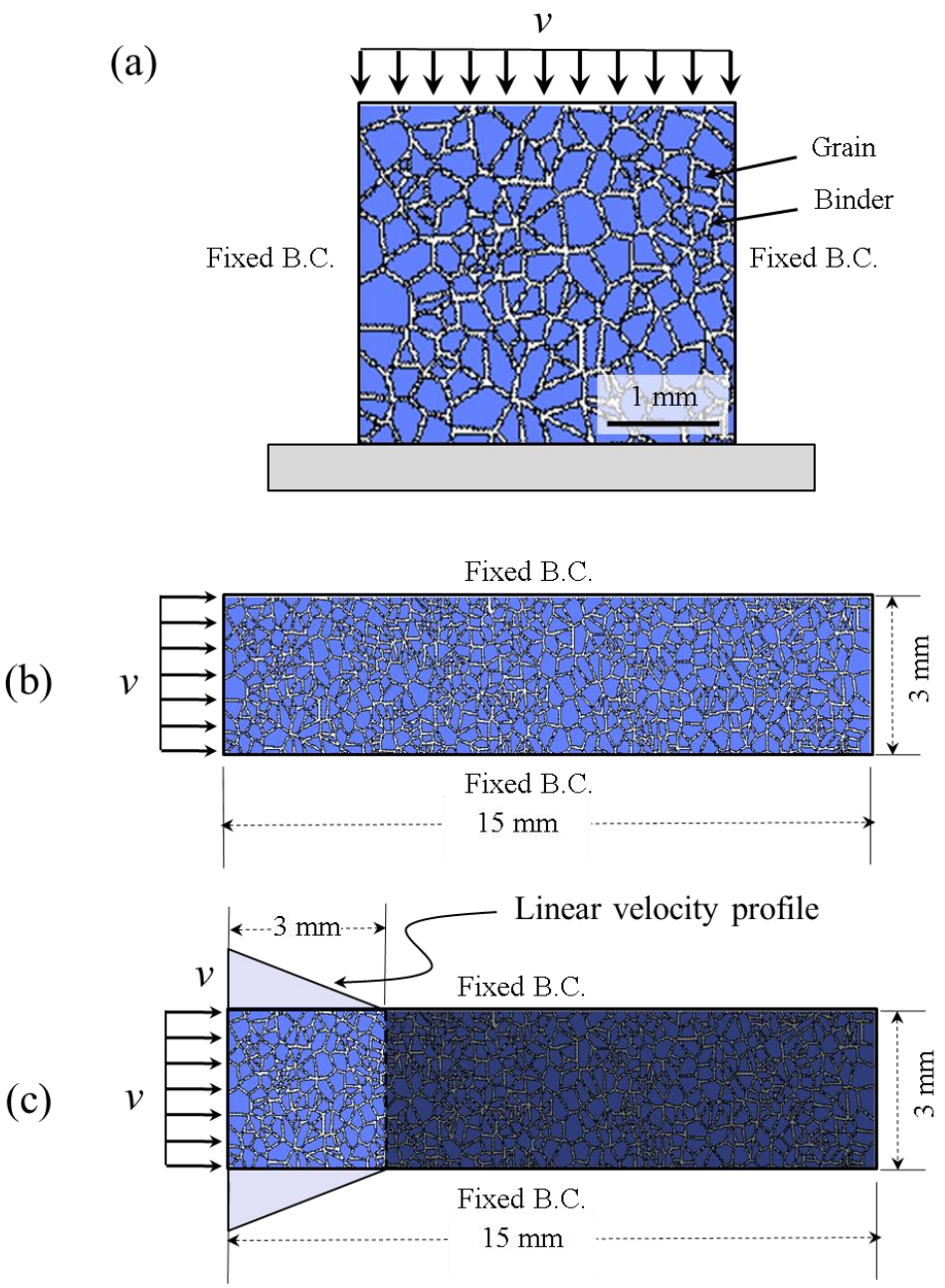

Figure 18: Loading configurations analyzed, (a) smaller (3mm3 mm) specimen and (b) long specimen with aspect ratio of 5:1 (15mm3 mm) (c) macroscopically uniform loading without stress wave propagation.

The second loading configuration involves a 15mm × 3mm rectangular microstructural region. This configuration is shown in Figure 18(b). The upper and lower boundaries are constrained such that lateral expansion (up for the upper edge and down for the lower edge) does not occur. This configuration approximates the normal impact loading of an infinitely wide material block under conditions of macroscopic uniaxial strain. The imposed constant boundary/piston velocity approximately simulates loading under a constant input stress level. The specimen length is chosen to allow approximately the first 5.5-8.5 μs of the propagation of the stress wave from the left surface toward the right to be analyzed, before the wave arrives at the right end. The imposed boundary velocity v is varied between 50 and 350 m/s, yielding overall strain rates of $\dot{\varepsilon} = (16.7 - 116.7) \times 10^3/\mathrm{s}$ [for the loading configuration in Figure 18(a)]. Since the configuration in Figure 18(b) focuses on the transient response of microstructures, the relevant discussions are limited to times before the stress wave reaches the boundary on the right [Figure 18(b)].

An important quantity for analyzing the effect of specimen length is the ratio between the domain size in the loading direction and the effective thickness of the steady stress wave. For very small specimens (the ratio being less than unity), the loading configuration allows the effects of high strain rates and full stress wave reflection being analyzed. The loading configuration in Figure 18(a) is designed with this type of conditions in mind. On the other hand, for the second loading configuration [Figure 18(b)], the ratio is much larger than unity. That configuration allows the response under conditions of transient stress waves to be analyzed. Naturally, this effect is also dependent on the speed of sound through the specimen and the boundary velocity.

The third loading configuration is shown in Figure 18(c). This configuration is similar to the configuration in Figure 18(b). Used to simulate loading under a uniform state of stress without the effects of stress wave propagation, this configuration involves a linear initial particle velocity distribution over the 3 mm × 3 mm region on the left. Other aspects of this configuration are the same as those for the loading configuration in in Figure 18(b). The prescribed initial particle velocity decreases linearly from the imposed boundary velocity v to 0 over the 3 mm length of the region. This treatment generates a macroscopically "uniform" deformation state in an average sense in the 3 mm × 3 mm region. This configuration allows the ignition behavior to be studied for conditions of macroscopically uniform deformations, without the effects of transient stress wave propagation.

3.4 Results and Discussions

3.4.1 Hotspot Fields

Dissipation associated with mechanisms operative at the grain-level causes localization of thermal energy or the formation of hotspots [109]. The evolution of the size, shape and distribution of hotspots vary significantly with the microstructure and loading. Significant variations in boundary conditions and sample configurations can be encountered during loading. In this section, we discuss a set of calculations on the PBX and GX to quantify the effects on hotspot fields of binder and stress wave reflection.

Small samples with wave reflections

Figure 19 and Figure 20 show, respectively, the evolution of hotspots in the grains and binder for a PBX with η = 0.82 at $t = 1 - 4\ \mu s$. The impact velocity is v = 100 m/s. The calculation is performed using loading configuration 1. Initially at $t = 1 - 2\ \mu s$, hotspots are few and form in locations of stress concentration due to grain-grain interactions. At higher levels of overall deformation [Figure 19(c)], high temperatures occur at locations of grain-grain interaction and along cracks within the grains, with the latter being a more significant heating mechanism. At $t = 4\ \mu s$, transgranular fracture of grains result in high temperature rises on the order of 200 – 300 K in the grains [see Figure 19(d)]. Although there is frictional dissipation due to sliding at grain/binder interfaces, the temperature rises in the binder is consistently lower than that in the grains [see Figure 20(c-d)].

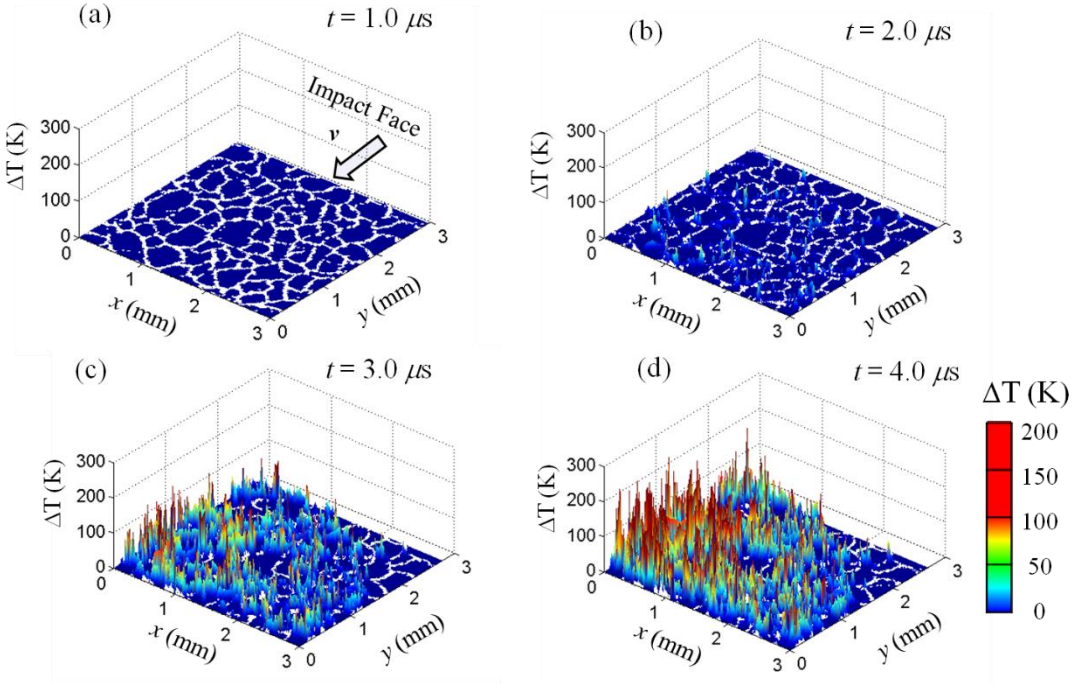

Figure 19: Evolution of temperature field in the HMX granules of the PBX (η = 0.82, v = 100 m/s, $\dot{\varepsilon} = 33.3\times10^3\ s^{-1}$).

The temperature rise in the GX having $\eta = 0.82$ at $t = 1 - 4\ \mu s$ is shown in Figure 21. The impact velocity is again v = 100 m/s. Compared with that in the PBX, the temperature rise during the first 1-2 μs is lower in the GX, since most of the deformation is accommodated by the rearrangement of the grains and elastic intergranular interactions. However, at higher levels of overall deformation ($t = 3 - 4\ \mu s$), fracture of grains and frictional dissipation lead to significantly higher temperature increases throughout the microstructure. The temperature rises are approximately homogeneous in the domain, since the stress wave equilibrates over time (due to multiple reflections from the top and bottom boundaries).

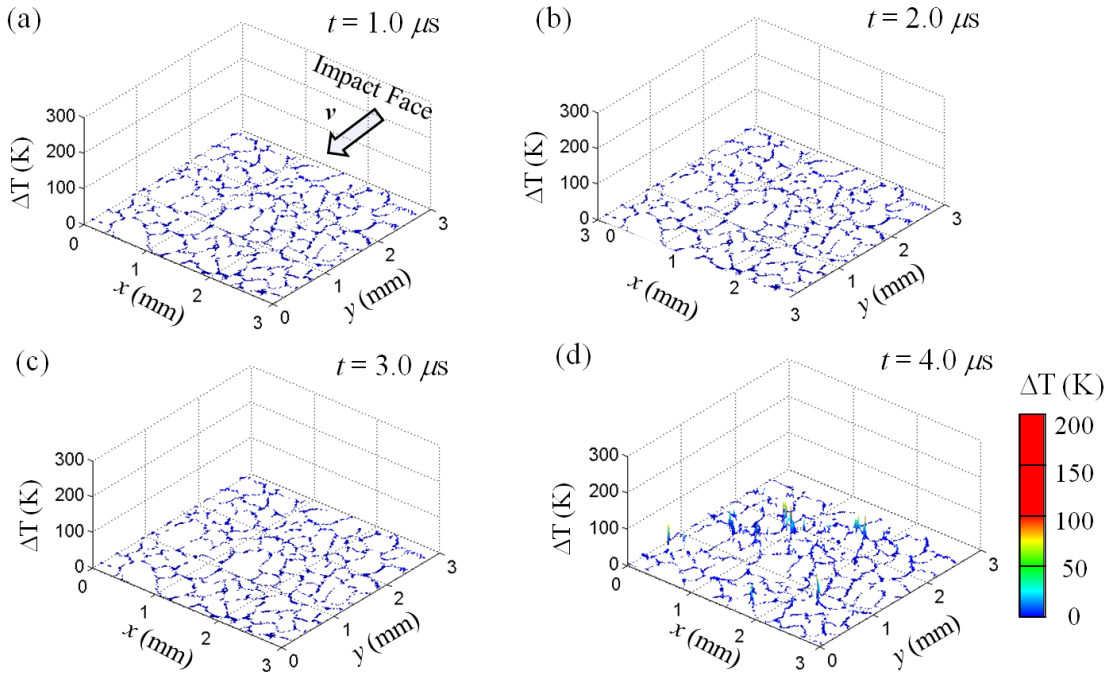

Figure 20: Evolution of the temperature field in the binder of the PBX, (η = 0.82, v = 100 m/s, $\dot{\varepsilon} = 33.3\times10^3$ /s).

Crushing of the smaller grains typically result in multiple fragments, increasing the surface area available for frictional dissipation. Thus, higher temperature rises are

primarily seen at locations where smaller grains are fragmented. Whereas, the fracture of larger grains generally results in fewer fragments. Consequently, the locations of the higher temperature increases are interspaced by the larger grains [Figure 21(d)]. At higher levels of overall deformation, transgranular fracture occurs in both smaller and larger grains.

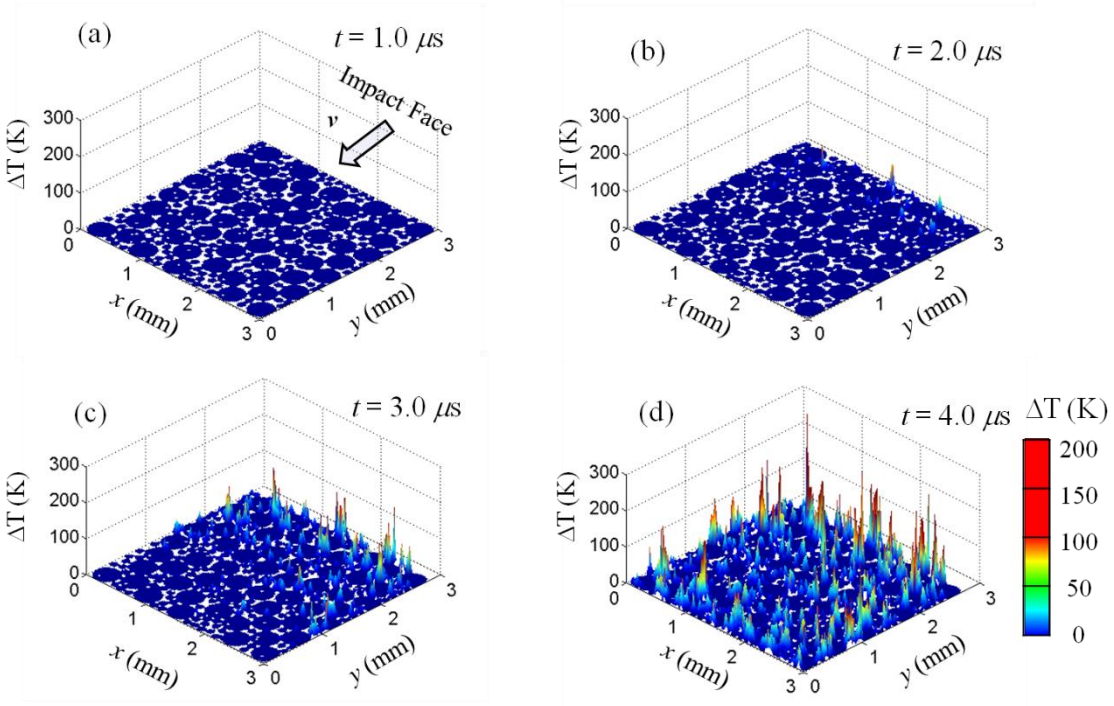

Figure 21: Distribution of Evolution of the temperature field in the GX, (η = 0.82, v = 100 m/s, $\dot{\varepsilon} = 33.3\times10^3$ s^{-1}).

Large samples without wave reflections

The next set of calculations illustrates the effect of stress wave propagation in long microstructures [loading configuration 2, Figure 18(b)]. Figure 22 shows the distributions of temperature in a PBX microstructure with a packing density of η = 0.82 at $t = 6.0 - 7.6\ \mu s$. The impact velocity is v = 100 m/s. Note that the sample is long so wave reflection

does not occur for the duration analyzed. The times shown here are later than those in the previous figures for the small samples for which wave reflection occurs. The temperature increases are highest near the impact surface and gradually decrease away from it. This is a consequence of the stress wave continuing to propagate towards the unstressed material. For this impact velocity, the failure mechanisms (transgranular fracture and sliding frictional heating along crack faces, intergranular interaction and heating due to binder deformation and crack face friction) occur much behind the initial stress wave front. This results in severe temperature rises of the order of 300 – 400 K in the grains. High temperature rises also occur in the binder phase, but are lower than those in the grains.

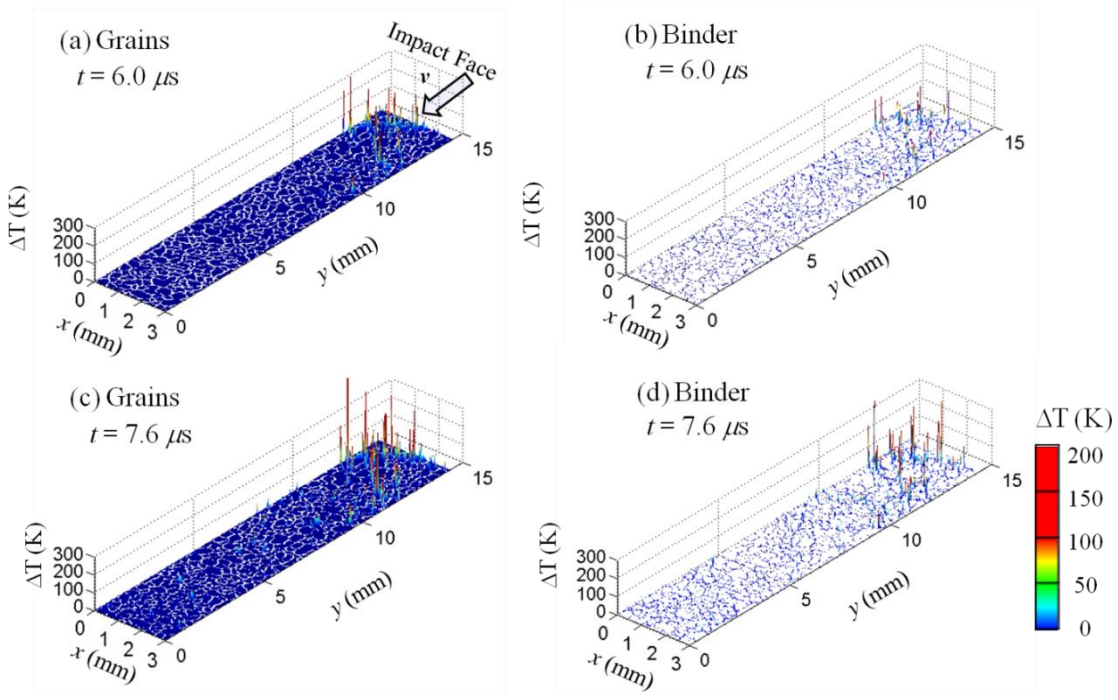

Figure 22: Evolution of the temperature field in the grains and binder for loading configuration 2 (PBX, η = 0.82, v = 100 m/s).

Figure 23(a-b) shows the distribution of temperature in a long GX sample with a packing density of η = 0.82 at $t = 4.0 - 6.0\ \mu s$. The impact velocity is v = 100 m/s.

Similar to those in the PBX, the temperature rises are highest near the impact surface. However, due to the absence of any binder, more intergranular interactions occur, resulting in significantly higher hotspot density (number of hotspots per unit area).

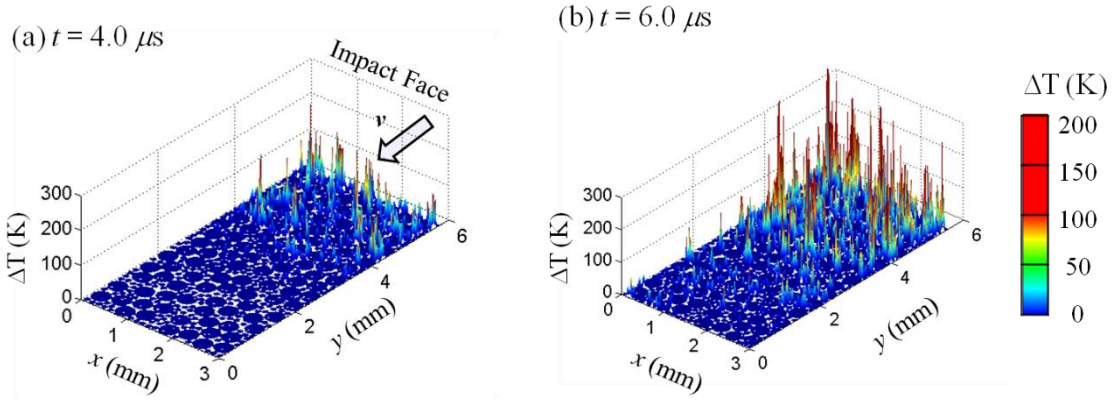

Figure 23: Evolution of the temperature field in HMX for loading configuration 2 (GX, η = 0.82, v = 100 m/s).

The responses of the short [loading configuration 1, Figure 18(a)] and long samples [loading configuration 2, Figure 18(b)] are significantly different. For both GX and PBX, the shorter samples experience more uniform temperature rises as a result of multiple stress wave reflections. On the other hand, in the longer samples the temperature decreases with distance from the loading surface. The overall more uniform hotspot distributions in the smaller samples can be more directly correlated to the initial microstructure and loading conditions. In subsequent discussions on characterizations of the temperature fields and size distributions of the hotspots, the focus is primarily on calculations using loading configuration 1.

3.4.2 Effect of Initial Porosity

Porosity is present in all GXs and has a significant influence on their impact sensitivities. In applications, it is desirable to have lower porosity for higher energy output. The effect of porosity is analyzed by deforming three GX microstructures having initial volume fractions of η = 0.60, 0.70 and 0.82 [Figure 14(b, e-f)], respectively. Figure 24 (a-c) show the distribution of temperature at t = 5.4 μs. The impact velocity is v = 100 m/s. The calculations are performed using loading configuration 1 [Figure 18(a)]. Clearly, the temperature increases with η for the same value of overall strain. For η = 0.60, the temperature increases are low and only occurs at locations of grain-grain interactions. Higher volume fractions decrease the initial porosity, thereby enhancing grains-grain interactions and transgranular fracture. The overall effective wave speed also increases with the volume fraction. Consequently, under the same impact velocity microstructures having higher grain volume fractions experience high temperature increases over a larger domain.

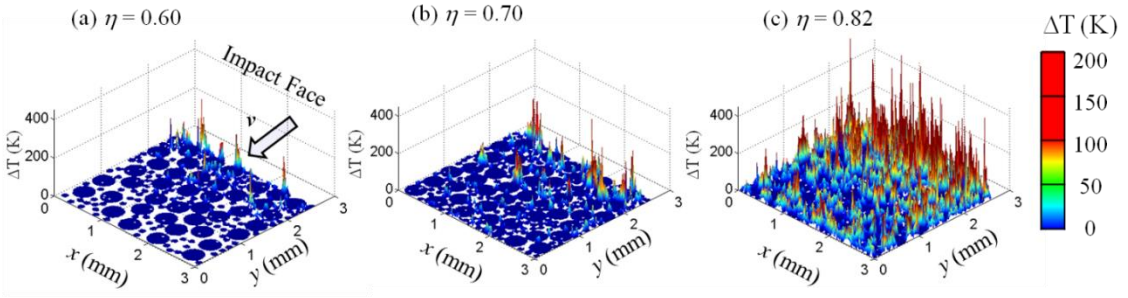

Figure 24: Distribution of hotspots in GX with different initial volume fractions: (a) η = 0.60, (b) η = 0.70, and (c) η = 0.82, (Bimodal GX, d = 120 – 360 μm, v = 100 m/s, $\dot{\varepsilon} = 33.3 \times 10^3$ s^{-1}, t = 5.4 μs).

3.4.3 Effect of Impact Velocity

The effect of loading rate is analyzed by deforming the PBX microstructure in Figure 14(a) and the GX microstructure in Figure 14(b) at the two impact velocities of v = 50 and 250 m/s. The corresponding strain rates are the range of $\dot{\varepsilon} = (16.7 - 116.7) \times 10^3$/s. The calculations are performed on the PBX and GX microstructures using loading configuration 1 [Figure 18(a)]. Figure 25 shows the distributions of temperature at a nominal strain of 10.0%.

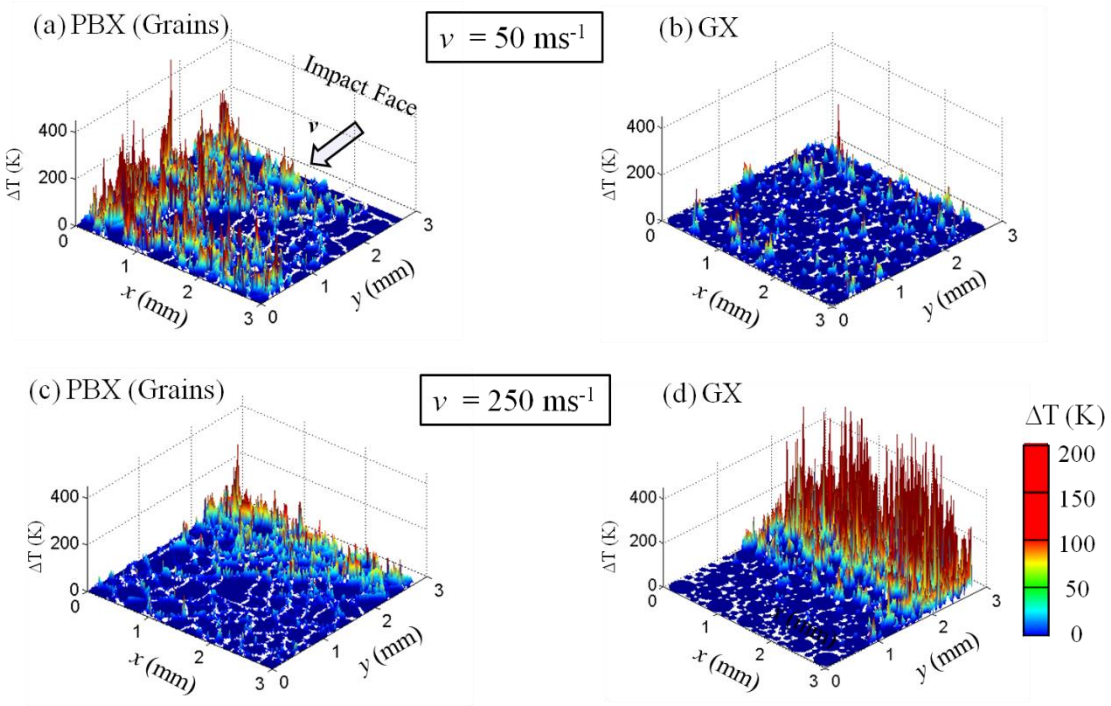

Figure 25: Distribution of hotspots in HMX at the same nominal strain of ε = 10.0 %, (a) PBX , v = 50 m/s, (b) GX, v = 50 m/s, c) PBX, v = 250 m/s, and (d) GX, v = 250 m/s, [η = 0.82, $\dot{\varepsilon}$ = (16.7 – 83.3)× 10^3 s^{-1}]

At a low impact velocity of 50 m/s, the temperature increase in the PBX is higher than that in the GX. In the PBX, the binder is softer, allowing the temperature rise to be spread out over the entire microstructure. Additionally, the absence of any porosity in the

PBX leads to higher stresses, subsequent fracture and frictional dissipation. In contrast, in the GX, rearrangement of the grains reduces the stress in the early part of loading. At later stages of loading, fragments generated from grain fracture occupy the vacant areas (pores), resulting in lower overall stresses compared to the PBX. This leads to a lower temperature increase for the GX.

However, at higher impact velocities (v = 250 m/s), grain-grain interaction and transgranular fracture become the primary dissipation mechanisms even at early stages of loading. For both PBX and GX [Figure 25(c-d)], the distribution of hotspots is concentrated near the impact face where the most severe temperature increases occur. The temperature increase in the GX is higher than that in the PBX (in contrast to the behavior seen at the lower impact velocity). For the PBX, deformation of the binder reduces the stress level and prevents grain-grain interactions in the early part of loading. On the other hand, the GX experiences grain-grain interactions and transgranular fracture immediately upon impact, which results in high temperature increases. Thus, for the conditions analyzed, the GX appears to be less sensitive at low impact velocities whereas the PBX is less sensitive at higher impact velocities.

3.4.4 Effect of Grain Size Distribution

Several studies have tried to correlate the size [115], morphology [23] and surface area [116] of crystalline granules with impact sensitivity. Czerski [23] reported that there was no clear correlation between size and the sensitivities of small (~10 μm) and medium (~100 μm) sized RDX particles. Lecume [117] suggested that the surface roughness may affect shock sensitivity. The sensitivity of GX is also dependent on the strength of shock loading. Chakravarty et al. [118] found that at low pressure and long duration shock waves, larger grain sizes correspond to higher impact sensitivity.

To illustrate the effect of grain size on hotspot field, three different GX microstructures having the same volume fraction ($\eta = 0.70$) are analyzed: (A) monomodal, d = 120 μm, (B) monomodal, d = 360 μm, and (C) bimodal, d = 120-360 μm (henceforth referred to as microstructure A, B and C, respectively). Figure 26(a-c) shows the distributions of temperature in the 3 mm square specimens, at t = 8.0 μs for an impact velocity of v = 100 m/s. The temperature increases at the same amount of nominal strain are quantitatively similar for all cases, indicating that grain size may not have a significant influence on impact sensitivity.

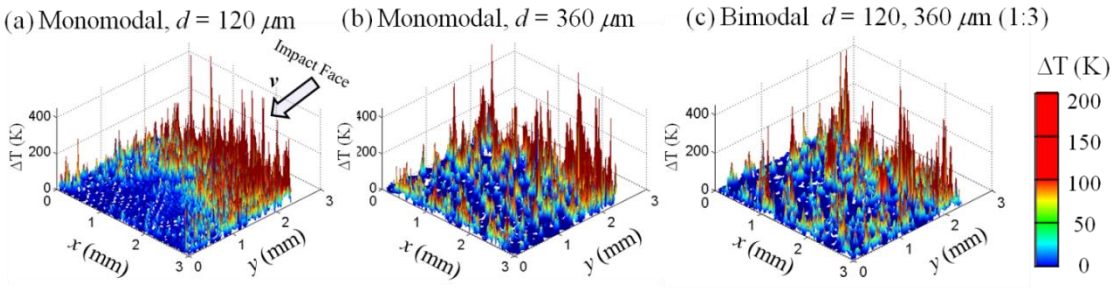

Figure 26: Distribution of hotspots in GX with different grain size distributions: (a) monomodal, d = 120 μm, (b) monomodal, d = 360 μm, and (c) bimodal, d = 120 – 360 μm (η = 0.70, v = 100 m/s, $\dot{\varepsilon} = 33.3 \times 10^3$ s^{-1}, t = 8.0 μs)

3.4.5 Connecting Hotspot Statistics to Thermal Criticality Data

Hotspot distributions are analyzed using Eq. (3-1) to identify critical hotspots. To illustrate the process of how critical hotspots are identified, Figure 27(a-d) shows the hotspots detected in the grains for a calculation on a PBX specimen with a HMX volume fraction of η = 0.82. The imposed boundary velocity is 100 m/s. In general, the sizes and temperatures of hotspots increase with time, as shown by the group of hotspots which

move towards the threshold region for time between t = 5.2 – 7.2 μs. The three curves denote Tarver's criticality data stated as a band of $\pm$ 10% about the mean value, as previously discussed. A hotspot is considered to be critical when it crosses the lower threshold limit (90% of the average threshold). The figure shows that the hotspots, up to a time of t = 6.8 μs, are below the threshold and not considered critical. At t = 7.2 μs, the hotspots having the highest temperatures cross the lower threshold. Once the criterion is satisfied, the material is assumed to have reached the critical state for thermal runaway. The time (measured from the beginning of loading) at which this is taken as the time to criticality (t_c) and is obtained for different cases of impact velocity, grain volume fraction and size distribution.

Figure 28(a) shows the variation of critical time, t_c with boundary velocity, v for PBX and GX microstructures having an initial volume fraction of η = 0.82 [Figure 14(a-b)]. The calculations are performed for a range of impact velocities between v = 50 and 250 m/s, using loading configuration 1 [Figure 18 (a)]. The results are fitted to a curve of the form vt^n = constant to illustrate the overall trends. In general, for both PBX and GX, as the boundary velocity increases, the time to criticality decreases. This is similar to the shock response of explosives [37, 119, 120].

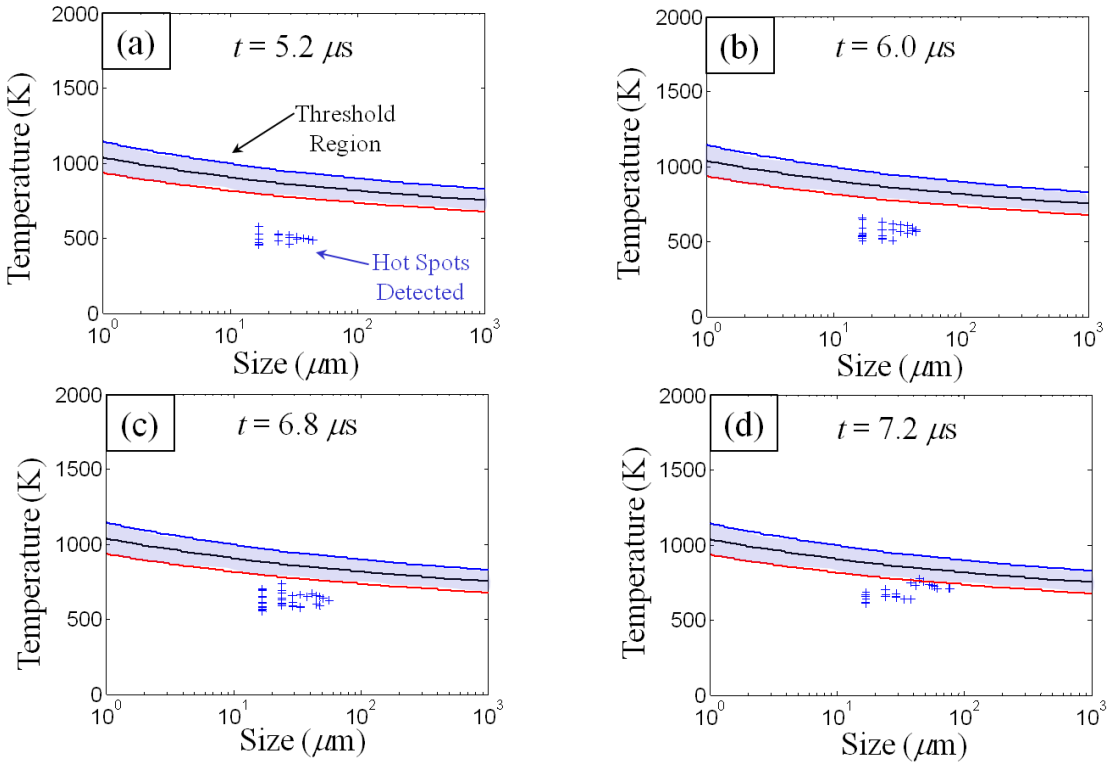

Figure 27: Size and temperature of hotspots relative to Tarver's ignition threshold at different times between t = 5.2 – 7.2 μs [PBX], η = 0.82, v = 100 m/s)

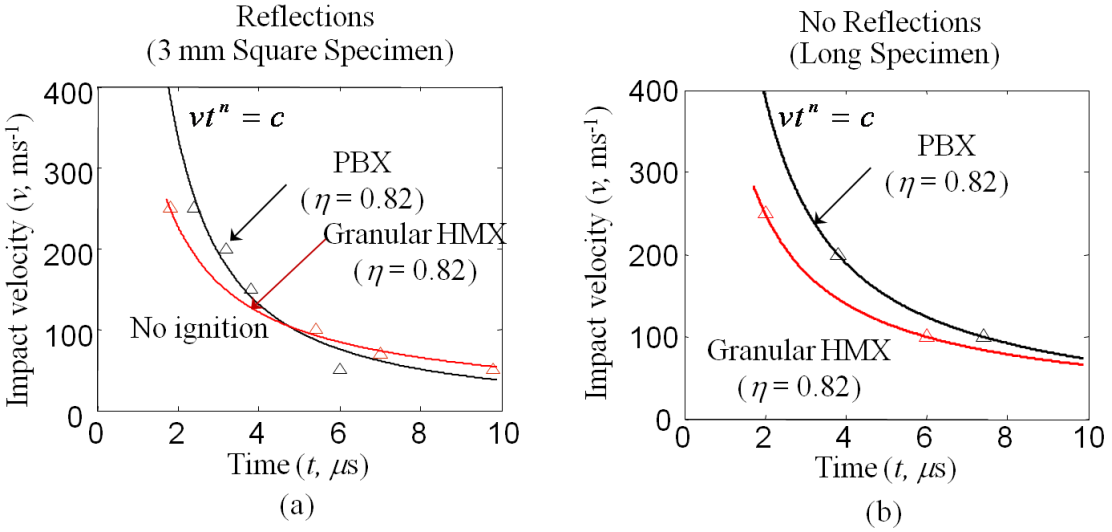

Figure 28: Time to criticality for PBX and GX using (a) 3 mm square specimen and (b) long specimen (η = 0.82, v = 50 - 250 m/s)

At high impact velocities (v > 100 m/s), the time to criticality for the PBX is 2 – 4 times that for the GX. In case of the PBX, the binder deforms to absorb the loading due to the impact, thereby preventing direct grain-grain interactions and minimize fracture during the initial stages of loading. On the other hand, at lower impact velocities (v < 100 m/s), the PBX is more sensitive than the GX and has a lower time to criticality. This is due to the higher confinement stresses which arise from the lack of room for compaction, leading to greater fracture and higher temperature rises in the grains. For the loading configuration used and over the range of conditions analyzed, t_c continues to decrease as v increases [Figure 28(a)] and there does not appear to be a minimum time required for ignition regardless of impact velocity. On the other hand, the range of data does not appear to suggest the existence of a low velocity cutoff below which no ignition occurs. One possible explanation is that the successive wave reflections from the top and bottom surfaces [Figure 18(a)], leads to continuing accumulation of elastic strain energy in the specimen. This accumulation can lead to sudden fracture and frictional dissipation with sustained loading, causing high temperature rises even at low impact velocities.

Figure 28(b) shows the results of calculations having the same initial conditions as those in Figure 28(a), but for loading configuration 2 [Figure 18(b)]. Two important differences are clear in the responses of the short and long samples. First, in the calculations using the long specimen show [Figure 18(b)] the PBX is always less sensitive than the GX. However, the difference in sensitivities of the PBX and GX increases with the impact velocity, suggesting that the protective effect of the binder in the PBX is more pronounced under severe loading. Second, for a long specimen no critical hotspots are obtained at impact velocities lower than 100 m/s. This indicates the existence of a minimum velocity below which no critical hotspots (and ignition) occur. The existence of

the lower velocity threshold can be explained on the basis of the constant strength of the stress wave behind the initial wave front. Hence no significant temperature increase occurs in the grains once the stress wave has passed.

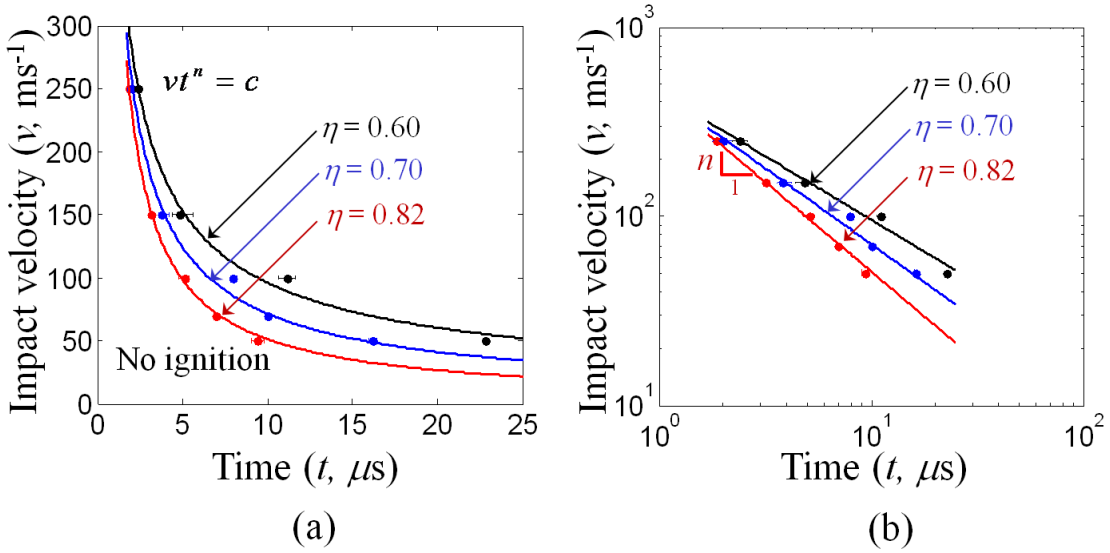

Figure 29: Time to criticality for GX having a range of initial grain volume fractions η = 0.60 – 0.82, plotted using (a) linear scale (b) log-log scale (η = 0.70 – 0.82, v = 50 - 250 m/s)

The effect of porosity is analyzed by comparing the criticality response of three GX microstructures having initial volume fractions of η = 0.60, 0.70 and 0.82 [Figure 14(b, e-f)]. Figure 29(a-b) shows the variation of the critical time, t_c as a function of the boundary velocity, which is varied between v = 50 and 250 m/s. The calculations are performed using loading configuration 1 [Figure 18(a)]. Overall, the higher the initial volume fraction η, the more sensitive is the GX. The variation in response with η is small at high impact velocities, with a delay time of $t_c \sim 4$ μs for all values of η considered. The similarity in response is due to the fact that at high impact velocities, grain fracture (and fragmentation) occurs almost immediately upon impact, leading to high temperature increases in the grains near the impact surface. However, the sensitivity is significantly

different at low impact velocities, with a critical time of t_c = 9.0 and 23.0 μs, for η = 0.60 and 0.82, respectively, for impact velocity v = 50 m/s.

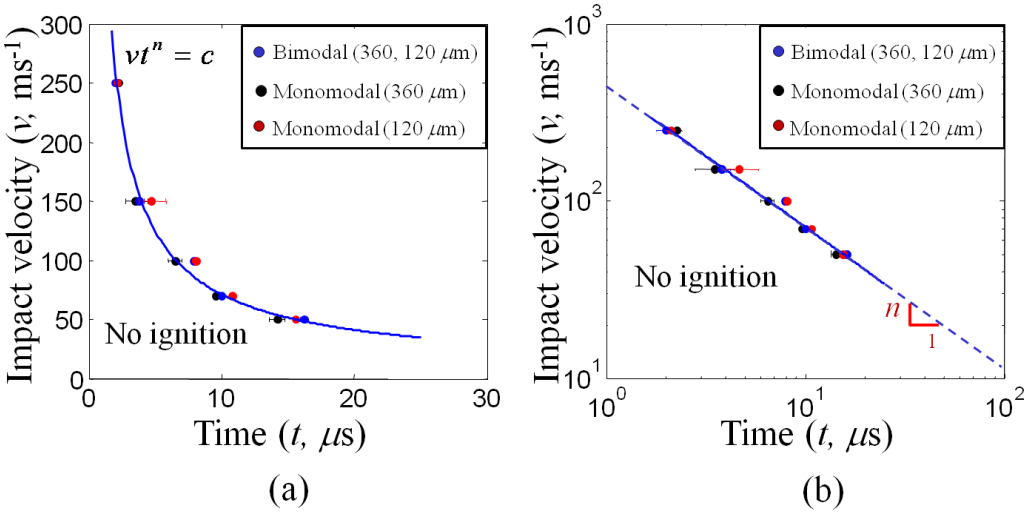

Figure 30: Time to criticality for GX having different grain size distributions: monomodal, d = 120 μm, d = 360 μm, and bimodal, d = 120 – 360 μm, plotted using (a) linear scale (b) log-log scale (η = 0.70, v = 50 - 250 m/s).

The effect of grain size on criticality is investigated using microstructures A, B and C as in Figure 26. Figure 30(a-b) shows the variation of the critical time, t_c as a function of the boundary velocity, which is varied between v = 50 and 250 m/s. The calculations are performed using loading configuration 1 [Figure 18(a)]. The time to criticality for all three microstructures A, B and C overlap each other, indicating that the grain size distribution (monomodal, bimodal) does affect the ignition sensitivity. This is also indicated by the hotspot distribution in the microstructures [see Figure 26(a-c)] which shows similar temperature increases for all cases. In all cases, the dominant heating mechanism is sliding friction at grain boundaries and at surfaces generated by grain fracture. It is noted that at higher load intensities including shock loading, there may be additional mechanisms (such as dislocations, phase transformation, and collapse of voids

or defects) which may cause the response to be more sensitive to grain size or grain size distribution. Such factors are not considered here.

3.4.6 Probabilistic Approach using Statistically Similar Samples

The variations in the time to criticality t_c among different samples subject to the same loading result from the variations in microstructure geometry. It is possible to generate ensembles with desired numbers of samples that share certain microstructural attributes that are similar to prescribed levels of accuracy. The microstructure attributes of initial interest in this regard are grain volume fraction and grain size distribution. The number of microstructure instantiations or the 'sample set size' required for a particular analysis is limited by the computational time, since the CFEM calculations are computationally heavy. For example, the simulation of the impact response of one of the samples in this chapter takes a wall clock time of approximately one week while running on 24 computing cores on a parallel computer cluster. The microstructure space analyzed here covers volume fractions in the range of η = 0.70 – 0.90, with both monomodal and bimodal grain size distributions for each volume fraction level. Specifically, six microstructural settings [three volume fraction levels (0.72, 0.81 and 0.90) for monomodal grains and three volume fraction levels (0.70, 0.80 and 0.84) for bimodal grains] are considered, as shown in Figure 16. The range of impact velocity of interest is v = 100 – 250 m/s and up to four different impact velocity levels (100, 150, 200, and 250) are considered for each microstructure set. The number of microstructure set and impact velocity combinations studied is 6 × 4 = 24.

Each of the six sets of microstructures must include multiple samples. Clearly, a higher number of instantiations in each set leads to a more accurate quantification of the

probability distribution function of the ignition behavior. Wild and von Collani [121] used a sample size of 50 for their analysis of explosive sensitivity. To illustrate the effect of the sample set size on the results, an analysis is conducted with sample sets that include 10, 20 and 30 instantiations. The calculations are performed using microstructures with a packing density of η = 0.81 having a monomodal grain size distribution [representative microstructure shown in Figure 15(b)]. The impact velocity is v = 100 m/s. Figure 31(a) shows the probability distributions of the time to criticality for sample sizes of 10, 20 and 30. Clearly, the overall trend and the functional relation are captured well by all three sample sizes. Based on this result, the number of instantiations for each microstructural set is chosen to be 20 from here on. The resulting total number of calculations is approximately 500.

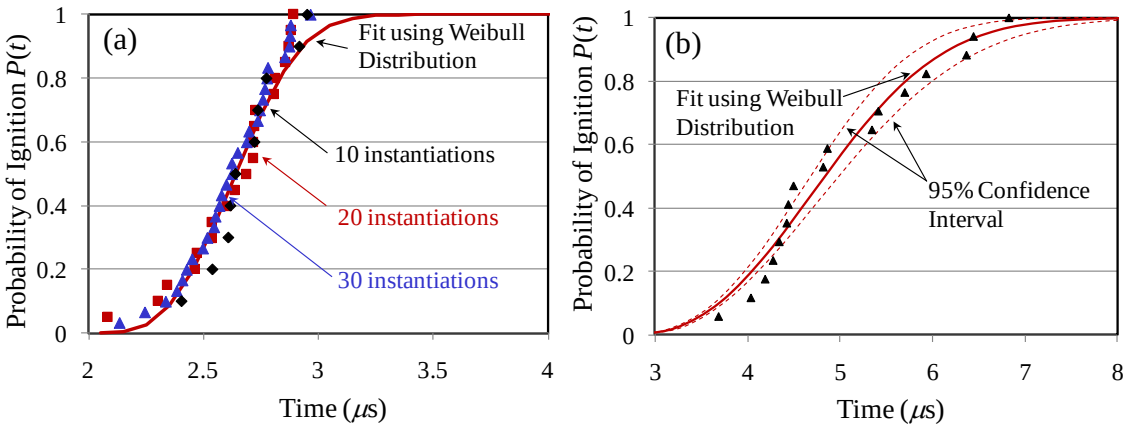

Figure 31: (a) Probability distributions of times to criticality obtained from calculations using 10, 20 and 30 different microstructure instantiations like that in Figure 17 with statistically similar microstructural attributes (η = 0.81, monomodal, S_v = 16 mm^{-1}). The impact velocity is v = 200 m/s. (b) Illustration of the Weibull distribution (red solid line) with the data points from calculations (black triangles). The 95% confidence interval bounds are shown using red dotted lines (η = 0.70, bimodal, v =100 m/s).

3.4.7 Confidence Level and Confidence Interval

In quantifying the safety of explosives, it is particularly important to establish confidence levels and confidence intervals for data reported. In the case of combustion in gases due to spark ignition, the 95% or 90% confidence interval is widely used in the presentation of probability estimates based on limited number of samples. For instance, Eckhoff et al. [122] represented the probability of ignition as a function of input energy and calculated the upper and lower limits of the probability distribution with a confidence level of 95%.

For the calculations presented in this paper, it is assumed that the distribution of the values occurs on either side of the Weibull distribution of t_c in an unbiased manner. For such a situation, the confidence interval can be computed assuming the variation to be normally distributed around the Weibull distribution. Specifically, the confidence interval for a 95% confidence level is [123]

$$t_{bound,i} = t_{c,i}\left(\eta, v\right) \pm 1.96 \frac{\sigma}{\sqrt{\xi}}, \tag{3-4}$$

where $t_{bound,i}$ represents the upper and lower limits of the time to ignition for the i-th sample, σ is the standard deviation of the normal distribution of the variation, and ξ is the number of samples. To provide a quantitative perspective for this relation, Figure 31(b) shows the ignition times of a set of PBX microstructures with a packing density of η = 0.81 and a monomodal size distribution of grains. The impact velocity is 200 m/s. The probability distribution of t_c is fitted to a Weibull distribution as shown by the solid line in Figure 31(a). The confidence envelopes [shown in dotted lines in Figure 31(a)] represent the probabilistic bounds within which 95% of the results are expected to lie.

3.4.8 Probability Distribution of Time to Criticality

Figure 32(a-f) shows the probability distributions of the time to criticality t_c for microstructures with different volume fractions (η = 0.72 – 0.90) and grain size distributions (monomodal, bimodal). The impact velocity is in the range of v = 100 – 250 m/s. For each case, no critical hotspots are formed before a minimum cutoff time t_0. Both the minimum value and the overall distribution of the ignition time depend on microstructural attributes and loading condition.

The distribution of t_c is affected by impact velocity. In general, the time to criticality values span over a range, with lower impact velocities giving rise to wider ranges. This means that the distribution of time to criticality is more spread out at lower impact velocities. In other words, different samples show larger difference in behavior at lower impact velocities. This observation reflects the fact that at lower impact velocities (e.g., $v \leq 100$ m/s), the stresses and rates of deformation are lower, which leads to longer times for failure to occur and hotspots to evolve; as a result, hotspots are more spatially spread out and more significantly influenced by random material heterogeneities. At high impact velocities (e.g., $v > 100$ m/s), on the other hand, severe deformation and grain failure occur near the impact surface early in the loading process. Therefore, dissipation and heating are the most intense near the impact face and gradually decrease toward the front of the propagating stress wave. Consequently, dominant hotspots are more concentrated near the impact surface, resulting in shorter times to criticality for hotspots and less variations among different samples in term of t_c.

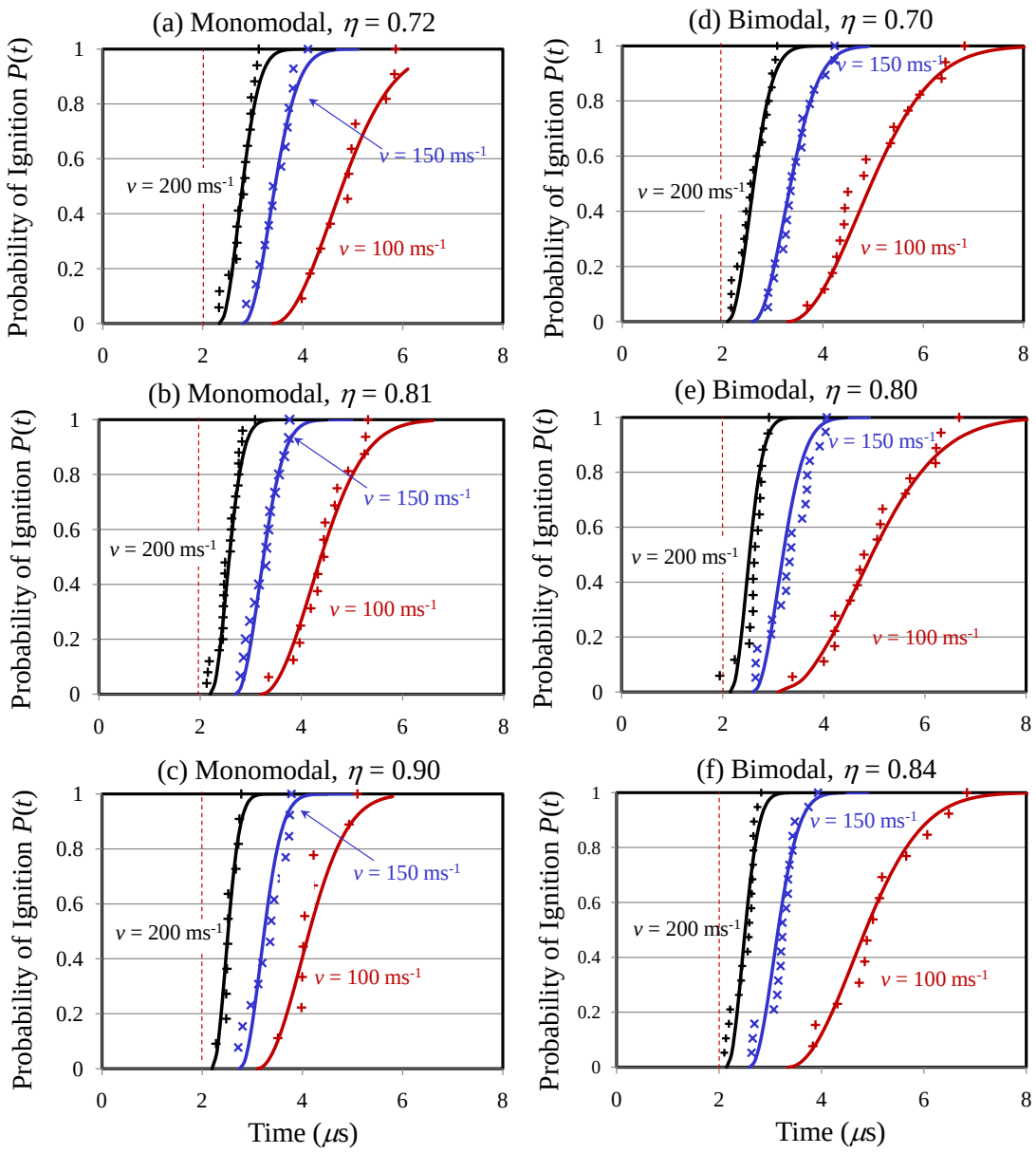

Figure 32: Cumulative probability distributions of the time to criticality for microstructures with different grain volume fractions (η = 0.72 - 0.90) and grain size distributions (monomodal, bimodal) for impact velocity v = 100 – 200 m/s

Figure 32(a-c) shows the distributions of the time to criticality for microstructures with monomodal grain size distributions. The packing density η is 0.72, 0.81 and 0.90, respectively. The corresponding results for microstructures with bimodal grain size

distributions at η = 0.70, 0.80 and 0.84 are shown in Figure 32(d-f), respectively. As the packing density increases, the material becomes stiffer and generates higher levels of overall stress at the same impact velocity. Higher stresses lead to higher rates of dissipation and higher temperature increases. Consequently, the time to criticality is in general shorter at higher grain volume fractions. The distributions of t_c for the lower packing densities of η = 0.72 [Figure 32(a)] and η = 0.70 [Figure 32(d)] are over wider ranges compared with the distributions for the corresponding higher packing densities in Figure 32(b-c) and Figure 32(e-f).

Variations in the distribution of grain size also affect the sensitivity of PBX. In general, the time to criticality is more spread out for bimodal microstructures than for monomodal microstructures at the same packing density and the same load intensity [see, e.g., Figure 32(a-c) and Figure 32(d-f)]. The level of difference between the two types of microstructures depends on load intensity. At impact velocities above 150 m/s, the difference is small and the responses for both monomodal and bimodal distributions are similar. However, at lower impact velocities ($v \leq$ 100 m/s), the distributions of t_c for bimodal microstructures are spread out over much wider ranges of time than the distributions for monomodal microstructures. The average particle sizes in monomodal distributions are larger than the average particle sizes in bimodal distributions, giving rise to higher levels of heterogeneity and more significant differences in behavior among different samples in the same set. In contrast, the smaller grains in microstructures with bimodal grain size distributions can rearrange and more effectively absorb the loading to keep stresses and temperature rises lower, leading to longer times to criticality and larger variations among samples in each set. To simply put, bimodal grain distributions lead to less sensitive PBXs under otherwise identical conditions.

3.4.9 Quantification and Effects of Variations of Microstructural Attributes

Some microstructure attributes can be more easily and precisely controlled in materials design and synthesis. The overall packing density η and the average grain size are two such attributes. Other attributes are more difficult to control accurately, and the distribution of grain size is one. The distributions of grain size of samples within a set of statistically similar microstructures which have, for example, the same packing density η and the same average grain size δ, may be quite different. As it turns out, the differences in grain size distribution among samples have a significant impact on the stochastic behavior of PBXs, as we will show below. For this reason, it is necessary to define a parameter (or parameters) which can be used to quantify the variations among microstructures which are statistically "similar" according to some commonly used measures (such as packing density and average grain size) but may be different in ways that can make their behaviors vary significantly from each other.

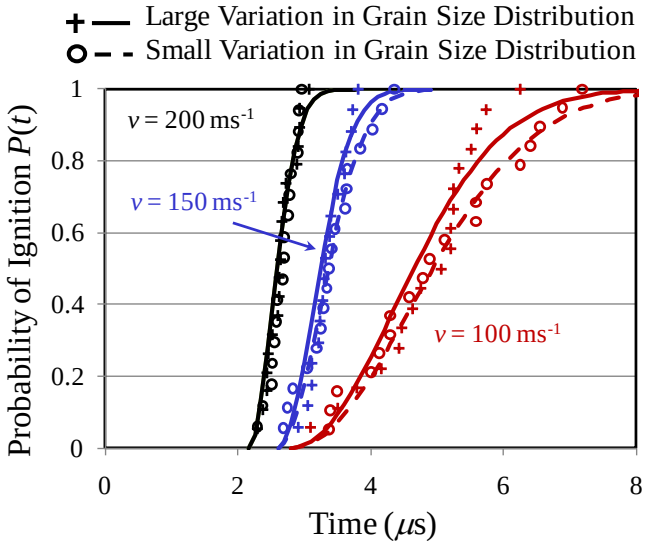

Figure 33: Cumulative probability distributions of the time to criticality for microstructures with different levels of variations in grain size distributions for v = 100 – 200 m/s (η = 0.81).

To illustrate this point, we consider the effect of the variations of grain size distribution among samples in a given microstructure set on the time to criticality. Figure 33 shows the distributions of the time to criticality for two sets of microstructures. One set has large (*L*) and the other has small (*S*) variations among the grain size distributions, as shown in Figure 34(a-b). Specifically, the two sets of microstructures have the same grain volume fraction of $\eta = 0.81$ and the same overall average size density histograms as represented by the grey columns. The variations of grain size distribution here referred the error bars in the histograms. These error bars show the range of the grain size density among the samples in a microstructure sample set. To understand the charts, note that each of the 20 microstructure samples (or instantiations) in a set has a histogram quantifying its grain size distribution. The heights of the grey columns represent the averages of the 20 histograms and the error bars denote the maximum and minimum densities among the 20 histograms. Figure 33 shows the results for three impact velocities between 100 – 200 m/s. At high impact velocities, the variations in the time to criticality are similar for both sets. However, at a lower velocity of $v = 100$ m/s, the two sets show similar behavior at the low end of the curves (time to criticality up to $t \sim 5$ μs) but diverge at the high end ($t > 5$ μs) of the curves. Specifically, the set with large variations in grain size distributions (set *L*) has a steeper profile and less variation in response than the set with smaller variations in grain size distributions (set *S*). The outcome that set *L* has larger variations among the samples but shows smaller variations in response is inconsistent with the logically expected trend. *The result suggests that the samples in the two sets of microstructures are not sufficiently similar in a statistical sense. In other words, simply having the same packing density, average grain size and average grain size distribution is not sufficient to guarantee statistical similitude of microstructures when it comes to impact-induced ignition of PBXs.*

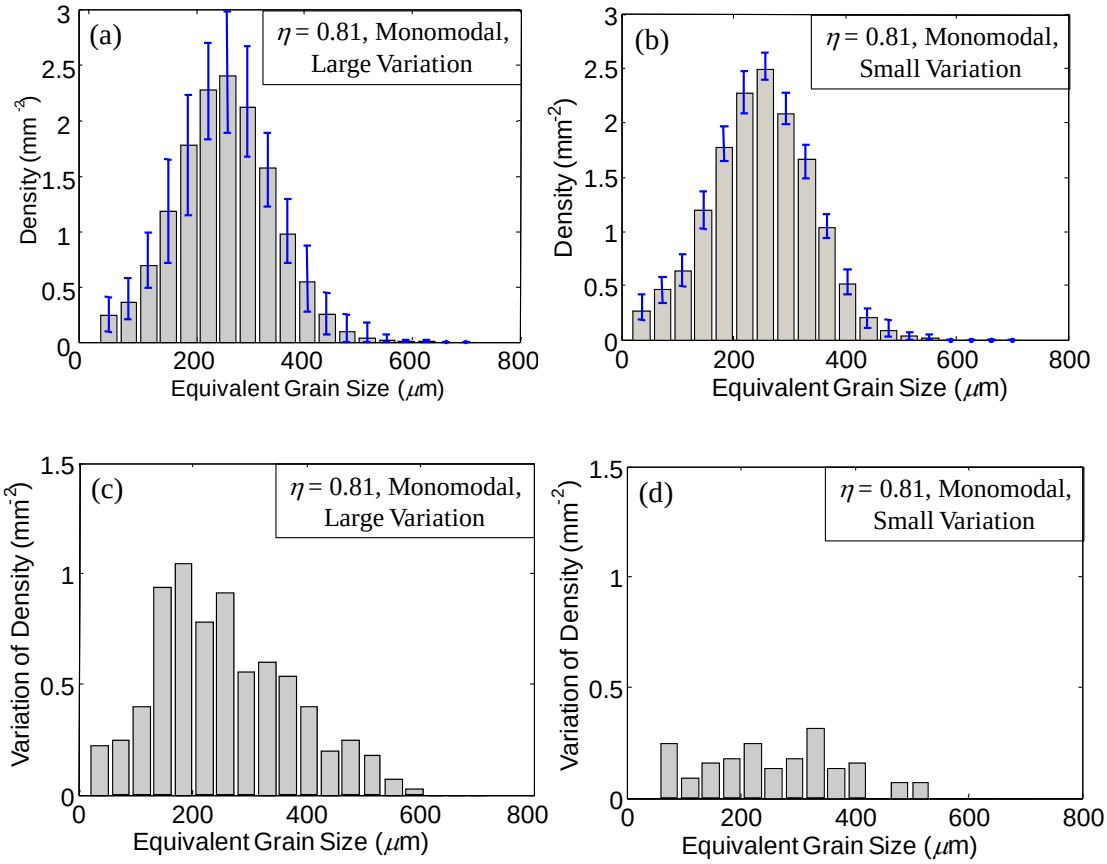

Figure 34: Grain size distributions for microstructures having the same grain volume fraction of η = 0.81 with (a) large grain size distribution variations and (b) small grain size distribution variations about the mean grain size distribution. Quantification of the variations are in (c) and (d), respectively.

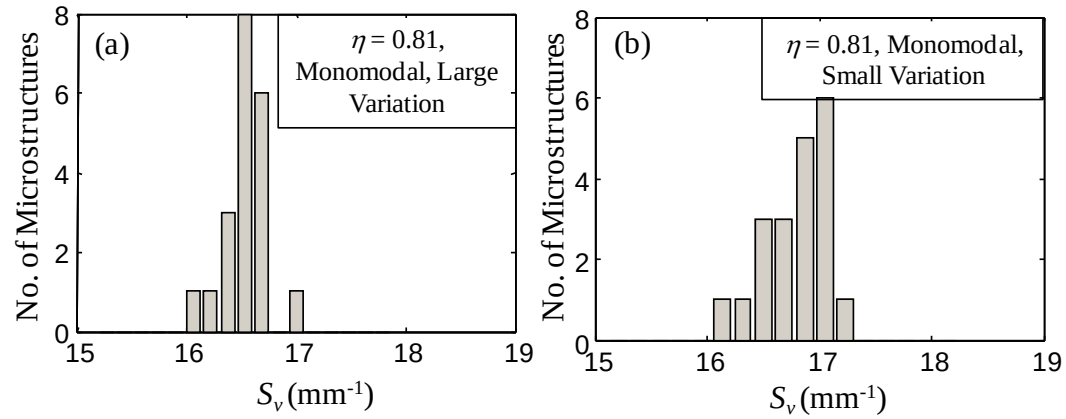

Figure 35: Interface area per unit volume (specific interface area) for microstructures with large and small variations in grain size distributions (η = 0.81, monomodal).

To understand the reason, we consider the correlation between the variations in grain size distributions (shape of the histogram profiles) and the specific interfacial area (S_v) between the HMX grains and the polymer binder in the composite. Figure 35(a-b) shows the distributions of S_v for the 20 samples in each of the two sets of microstructures in Figure 34(a-d). Significant differences are seen between the two histograms, i.e., there is no common trend in the profiles of S_v. It is well known that the specific interfacial area is an important parameter determining the ignition behavior of PBXs [124, 125]. To properly delineate the statistical trends in behavior, more systematically constructed microstructure sample sets must be developed.

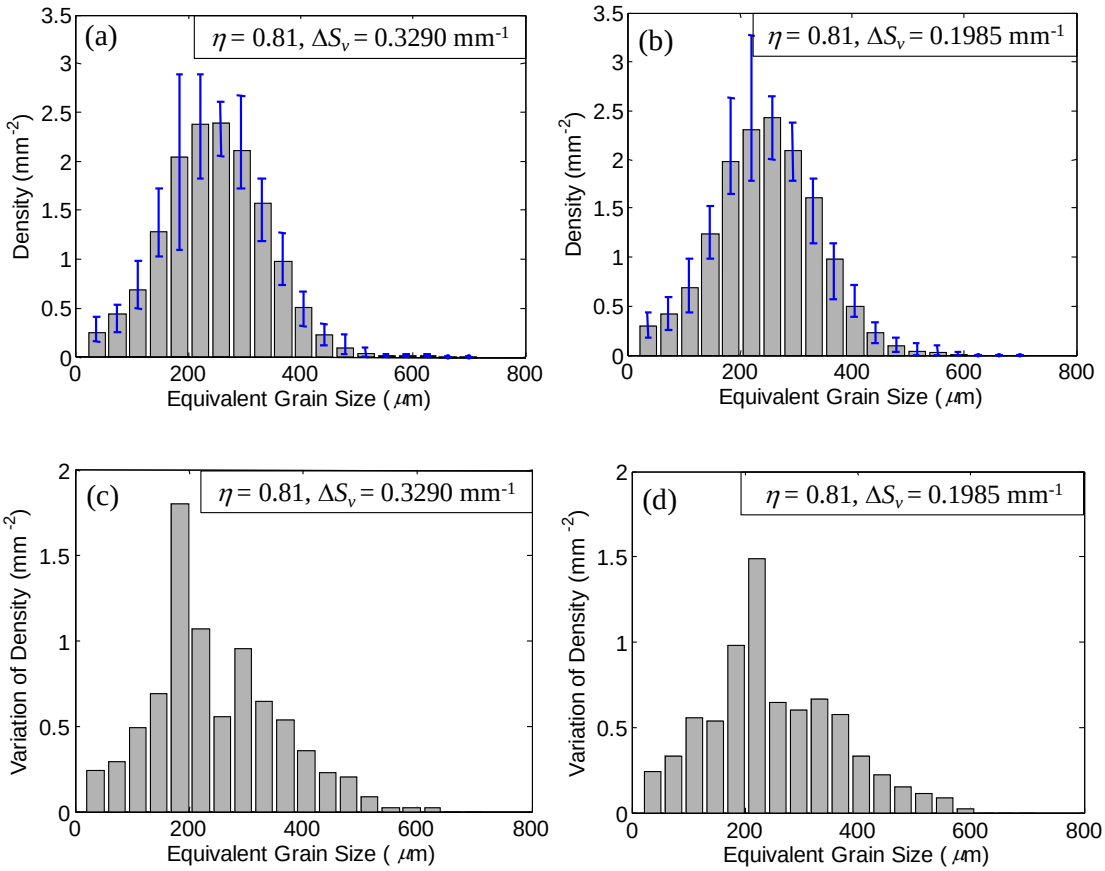

Figure 36: Grain size distributions for microstructures having the same grain volume fraction of η = 0.81 with different variation of the specific surface area of (a) ΔS_v = 0.3290 mm^{-1} and (b) ΔS_v = 0.1985 mm^{-1} about the mean S_v = 16 mm^{-1}. Quantification of the variations are in (c) and (d), respectively.

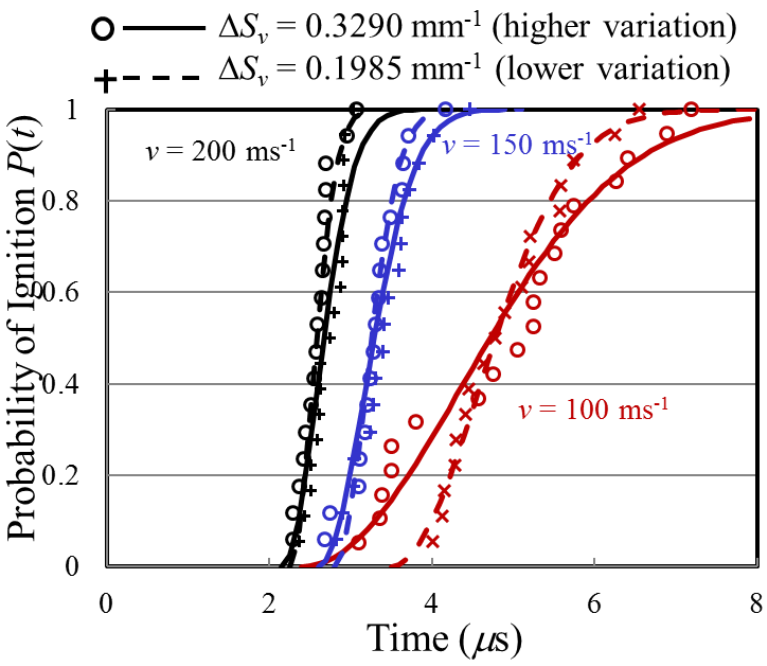

Figure 37: Cumulative probability distributions of the time to criticality for microstructures with different variations in interface area per unit volume (ΔS_v = 0.1985 – 0.3290 mm^{-1}) for v = 100 – 200 m/s.

To this end, we consider the effects of both the specific surface area S_v and its statistical variation ΔS_v on the ignition response. Two sets of microstructures are presented in Figure 36, one with a large ΔS_v of 0.3290 mm^{-1} and the other with a small ΔS_v of 0.1985 mm^{-1}. For both sets of calculations, the microstructures have monomodal size distributions with the same packing density of η = 0.81 and the same average specific surface area, S_v of 16 mm^{-1}. The distributions of the time to criticality for microstructures presented in Figure 36 are shown in Figure 37. The impact velocity is varied between 100 – 250 m/s. The results in Figure 37 show that higher values of ΔS_v correspond to higher spreads in the time to criticality. The difference in the spread of data increases as the impact velocity decreases. Specifically, at v = 100 m/s, for a ΔS_v of 0.3290 mm^{-1}, t_c lies between 3.0 – 7. 0 μs, whereas for a ΔS_v of 0.1985 mm^{-1}, t_c lies between 4 – 6.5 μs. This shows that the

variations in microstructures can be reasonably well quantified by ΔS_v in the context of impact-induced ignition of PBXs. In the following sections, ΔS_v is used to develop microstructure-performance scaling relationships.

3.4.10 Weibull Distribution Model for Ignition Sensitivity

Historically, the Weibull distribution [114] has been widely used in failure analysis and reliability prediction. The effect of the intensity of loading on the time to criticality can be compared to the effect of stress on the life of a mechanical component [121]. Thus, the Weibull distribution lends itself to be an excellent choice for modeling the sensitivity of explosives to impact loading. For instance, in Ref. [126] the Weibull model was applied to compare the sensitivities of RDX, HMX, PETN and other popular explosives with varying grain size distributions.

Physically, critical hotspots develop only after some time has elapsed from the onset of loading. To account for this effect, a modified form of the Weibull distribution function with a lower threshold time is used. The specific form [127] used here is

$$P(t) = 1 - e^{-\Phi(t)}, \quad \Phi(t) = \begin{cases} 0, & t < t_0; \\ \left(\dfrac{t - t_0}{\tau} \right)^m, & t \geq t_0. \end{cases} \tag{3-5}$$

In the above expressions, $P(t)$ is the cumulative probability, t is the time to criticality, t_0 is the cutoff or threshold time below which the probability of ignition is zero, τ is a scale parameter which affects the slope of the distribution curve and m is a shape parameter. The parameters m, τ and t_0 together determine the Weibull distribution function [Eq. (3-5)] for different material and load combinations. These parameters can be related

to the microstructure (packing density, grain size, grain size distribution, interfacial area per unit volume and the statistical variations of these parameters) and impact velocity v. They can also be used to determine the threshold impact velocity v_c below which no sample in a given material set reaches thermal criticality for ignition, as we will show later. In particular, the objective is to establish explicit functional forms for the relations.

3.4.11 Physical Basis for Weibull Distribution Model

The Weibull probability distribution function is a mathematical model independent of physical processes. The ignition of explosives is a physical process involving localized mechanical heating that is heavily affected by microstructural heterogeneity and the kinetics of chemical reactions. It is desirable to link physical mechanisms and associated variables affecting the ignition process to the model quantifying the probabilistic initiation behavior. Care needs to be taken so as to not oversimplify the problem.

To address this issue, Terao [128] and later Gilbert and Gonthier [129] used a probabilistic model to account for the stochasticity of ignition phenomena. In Terao's model, the stochasticity is accounted for by a function $\mu(t)$ which represents the probability of ignition per unit mass per unit time for a fixed amount of gas. Fundamentally for gases, μ is related to the probability of collision and subsequent reaction between molecules in a system. This probability depends on temperature T of the gas system. Terao's approach to modeling ignition in gases lends itself to the modeling of impact-induced ignition in solid high explosives. This is accomplished by accounting for the wave propagation process and temperature rise as functions of time and spatial distance from the impact surface.

Specifically for a loading event, the cumulative probability of ignition at time *t* is taken as $P(t)$. The inverse probability $[1 - P(t)]$ is the probability of survival or the fraction of samples not having ignited at time *t*. Note that $P(0) = 0$ and $P(\infty) = 1$. Now, it can be shown that the ignition probability per unit volume per unit time is [128],

$$\mu(t) = -\frac{1}{V}\frac{d\left[\ln(1-P)\right]}{dt}, \tag{3-6}$$

where *V* is the volume of the specimen involved. For an impact-induced loading event in solid high explosive in one spatial dimension (plane loading waves), the volume of the specimen under stress increases linearly with time, that is, $V = A_c ct$, where A_c is the cross sectional area of the specimen and $c(\eta)$ is the effective wave velocity through the composite which depends on packing density η.

If a functional form of $\mu(t)V(t)$ can be determined, the explicit form of the probability distribution $P(t)$ can be obtained from via the integration of Eq. (3-6). To identify the form of $\mu(t)V(t)$, another set of calculations is performed under conditions of uniform loading without stress wave propagation. Although for dynamic loading, it is hard not to generate stress waves in experiments, computationally a loading configuration can be devised to create the right conditions such that no stress wave front sweeps through the material. Such a configuration uses a linearly distributed initial velocity field with *v*, the imposed boundary velocity at $x = 0$ and $v = 0$ at $x = 3$ mm, as in loading configuration 3 in Figure 18(c). This initial condition creates a state of nominally homogeneous uniaxial strain state over the 3 mm length of the specimen involving the initial velocity distribution. Throughout the calculation, the boundary velocity imposed at $x = 0$ is $v = 200$ m/s. The hotspot analysis focuses only on the 3 mm region, since only this region experiences the

macroscopically homogenous state of stress without the influence of a propagating stress wave front. Under this condition, the volume V in Eq. (3-6) is the volume of the 3 mm region and is a constant which does not change with time.

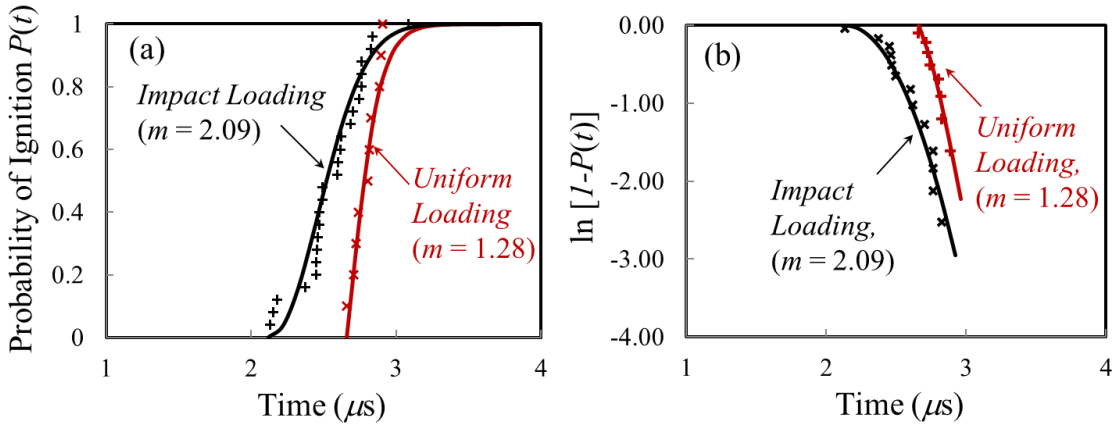

Figure 38: Comparison of the effects of uniform and transient impact loading on the shape parameter m; (a) in *P-t* space and (b) in *Q-t* space (monomodal, η = 0.81, v = 200 m/s).

Figure 38(a) shows a comparison of the probability distributions of t_c for two calculations, one uses loading configuration 2 [Figure 18(b)] and the other uses loading configuration 3 [Figure 18(c)]. Both cases involve an imposed boundary velocity of v = 200 m/s on monomodal microstructures having a volume fraction of η = 0.81. Figure 38(b) shows the variation of ln[1-P(t)] with the time to criticality t_c. The results are fitted to a power-law function of the form,

$$\int_0^t \mu(t)V(t)dt = \ln\left[1-P(t)\right] = -\left(\frac{t-t_0}{\tau}\right)^m . \qquad (3\text{-}7)$$

The fit for ln[1-P(t)] as a function of t can be used to determine the value of m [refer to Eq. (3-7)]. Using Eq. (3-7), one can determine the probability of ignition per unit time for volume V as

$$\mu(t)V(t) = \frac{m}{\tau^m} t^{m-1}. \tag{3-8}$$

Integrating Eq. (3-6) along with Eqs. (3-7) and (3-8), we get

$$\int_0^P d\left[\ln(1-P)\right] = -\frac{m}{\tau^m}\int_{t_0}^{t} t^{m-1} dt. \tag{3-9}$$

This yields the probability P as a function of t as

$$\ln(1-P) = -\left(\frac{t - t_0}{\tau}\right)^m. \tag{3-10}$$

Equation (3-10) can be recast into the modified Weibull distribution in Eq. (3-5). This derivation shows that the Weibull distribution as a quantification for the probability of ignition is not just a numerical fit, but rather a consequence of the physics of the ignition processes whose overall probability of ignition per unit time can be described by Eq. (3-8).

The parameter m determines the shape of the Weibull distribution curve and hence is often referred to as the shape parameter. Tsue et al. [130] analyzed the ignition time in the droplet experiment using the Weibull distribution and categorized the curves into three types which correspond to $m > 1$, $m < 1$, and $m = 1$, respectively, for droplets having a constant volume. The analysis revealed that $m > 1$ is caused by driving forces for ignition that intensify with time. If $m = 1$, the onset rate of ignition is independent of time. From the fitting in Figure 38(b), it can be seen that for the uniformly loaded case, $m = 1.28 > 1$, reflecting that fact that the temperature and therefore the probability for ignition increases as the loading event progresses. For the case with wave propagation, $m = 2.09$, signifying a higher rate of increase of the probability for ignition resulting from the combined effects

of increasing temperature (the increases of the peak and average temperatures behind the propagating wave front under non-shock loading was analyzed by Barua et al. [110]) and increasing volume of material involved. This value is close to the theoretical value of m = 2 for the special case with μ (and the overall average temperature) being constant behind the propagating wave front typically encountered during shock loading. Note that, however, for wave propagation considered here (non-shock loading), the spatial distribution of temperature is non-uniform behind the stress wave front, i.e., temperature increases are highest near the loading surface at the left end [see Figure 18(b)] and lowest near the stress wave front (toward the right). This non-uniformity of temperature causes the density of probability of ignition to be spatially non-uniform. Consequently, $\mu(t)$ must be interpreted as the average probability of ignition per unit time per unit volume for materials behind the current stress wave front.

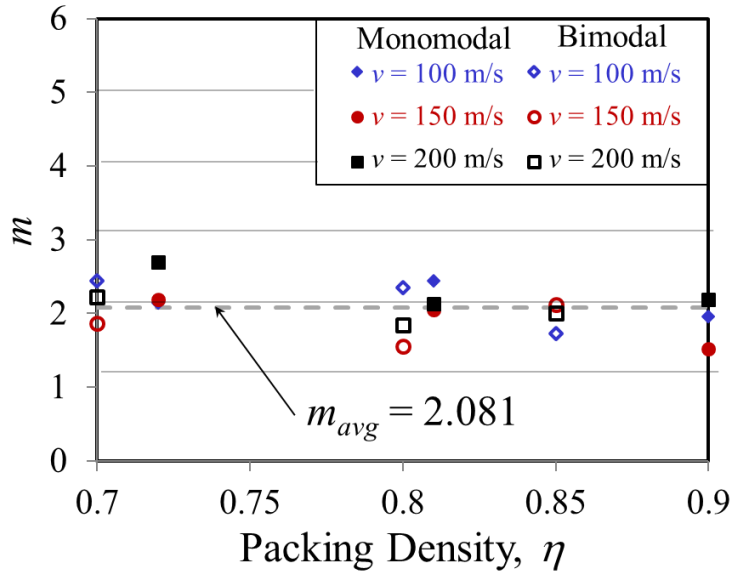

Figure 39: Weibull parameter m as a function of grain volume fraction over a range of impact velocity (v = 100 – 200 m/s)

Figure 39 shows the values of m obtained by fitting Eq. (3-5) to the computationally predicted ignition times for all combinations of microstructure (monomodal and bimodal, η = 0.70 – 0.90) and impact velocities (v = 100 – 250 m/s) considered. The values do not change significantly with microstructural attributes or impact velocity. The average value for all calculations is 2.081. This shows that under the conditions analyzed, m is primarily dependent on the loading configuration and is not significantly influenced by microstructure or loading intensity.

3.4.12 Effect of Microstructure and Impact velocity on Threshold Time t_0

The parameter t_0 quantifies the threshold time before which no ignition is observed. Figure 40(a-b) show the values of t_0 obtained from the Weibull analysis for all cases of microstructure (monomodal and bimodal; η = 0.70 – 0.90) and impact velocities (v = 100 – 250 m/s) considered. For both monomodal and bimodal microstructures, as the boundary velocity increases, the threshold time t_0 decreases. This is expected since an increase in impact velocity leads to earlier fracture and frictional dissipation in the grains. This in turn, results in earlier formation of critical hotspots. The relationship between the threshold time and impact velocity can be quantified as

$$v^{n'} t_0 = C'(\eta), \tag{3-11}$$

where n' and C' are functions of packing density η and are not sensitive to the monomodal or bimodal nature of the grain size distribution. At low impact velocities, the threshold time is lower for lower packing densities. Specifically, the threshold time decreases by ~16% as the packing density increases from 0.72 to 0.90. However, at higher impact velocities, this decrease is smaller. At 200 m/s, no significant effect of packing density on

the threshold time is seen. Under the conditions analyzed, the grain size distribution does not significantly affect t_0. The values of n' and C' for the different microstructures analyzed are listed in Table 6.

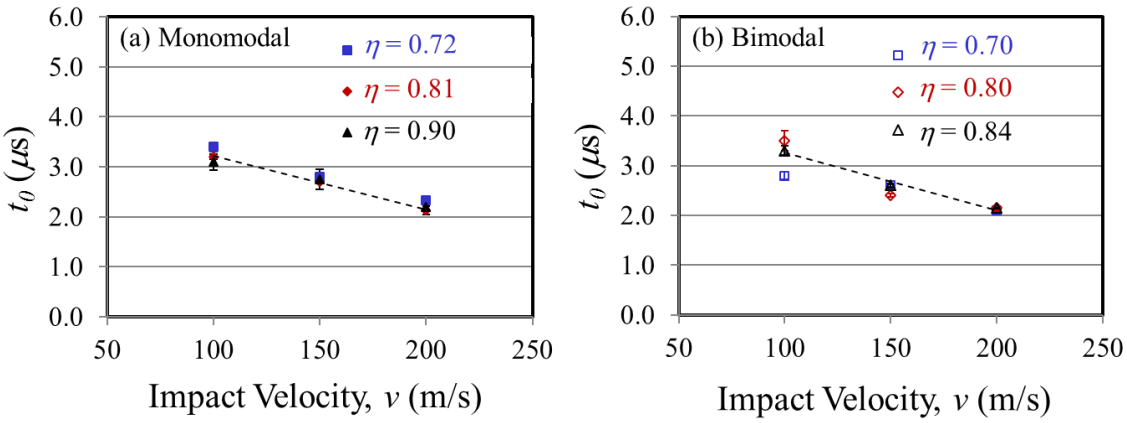

Figure 40: Threshold ignition time t0 as a function of grain volume fraction over a range of impact velocity (v = 100 – 200 m/s) for microstructures with (a) monomodal and (b) bimodal grain size distribution (the bounds show the 95% confidence intervals).

Table 6. Parameters used in Eqs. (3-9), (3-14), and (3-15)

Microstructure	Grain volume fraction (η)	n	n'	C	C'	k	$\rho_0 c_0$ (kg m^{-2}s^{-1})
PBX – Monomodal	0.72	0.42	0.23	21.20	7.34	17.0	3.29
	0.81	0.41	0.28	19.18	8.93	15.2	3.74
	0.90	0.40	0.26	17.87	8.36	12.5	4.73
PBX – Bimodal	0.70	0.37	0.22	15.03	5.99	10.0	3.36
	0.80	0.53	0.15	31.20	4.67	18.0	3.88
	0.84	0.46	0.31	23.96	9.83	9.5	4.44

3.4.13 Effect of Microstructure and Impact velocity on Scaling Parameter τ

The scaling parameter τ influences the overall slope (and spread) of the probability distribution of the time to criticality t_c. Figure 41(a-b) quantify the variation of τ as a function of impact velocity in the range of v = 100 to 200 m/s. The microstructures have grain volume fractions between η = 0.72 and 0.90 and different (monomodal and bimodal) size distributions. In general, τ varies with both microstructure and load intensity. For all microstructures, τ decreases (and $1/\tau$ increases) as the impact velocity increases. A higher τ corresponds to a wider range of distribution of t_c. At the same impact velocity, τ decreases as the grain volume fraction increases, indicating that the probability distribution of t_c narrows to a shorter time range. This is expected since higher grain volume fractions lead to higher stresses and earlier ignition, resulting in lower spreads in the probability distribution.

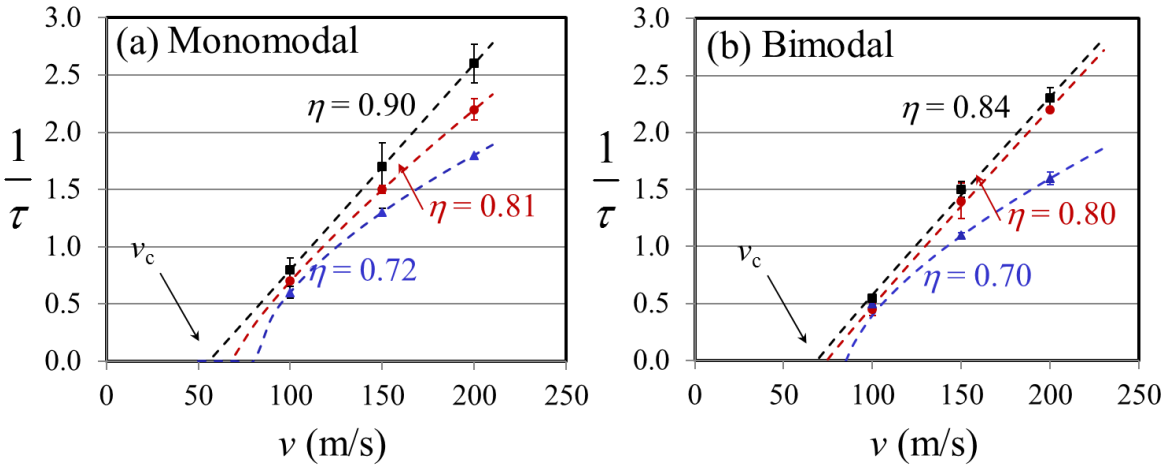

Figure 41: Scaling parameter τ as a function of impact velocity for microstructures with a range of grain volume fractions (η = 0.72 – 0.90), (a) monomodal and (b) bimodal grain size distributions. The bounds show 95% confidence intervals.

Grain size distribution also affects the variation of τ with v. For a particular impact velocity, τ is lower for monomodal distributions and higher for bimodal distributions. This difference is related to the fact that the range of time to ignition is higher for bimodal microstructures.

A value of $\tau = \infty$ $(1/\tau = 0)$ indicates that the probability of ignition is zero. The velocity at which this occurs (v_c) can be determined by extrapolating the curves in Figure 41(a-b) to the horizontal axis. To obtain this critical velocity v_c, an exponential relation between τ and v is used to fit the results. This relation is of the form

$$\frac{1}{\tau} = \frac{1}{\tau_{\text{ref}}}\left(\frac{v - v_c}{v_{\text{ref}}}\right)^{\alpha}, \tag{3-12}$$

where τ_{ref} and v_{ref} are constants, v_c is the critical impact velocity below which no ignition is observed, and α is a fitting parameter that is a function of microstructure. The values of the constants τ_{ref} and v_{ref} are listed in Table 7.

Table 7. Parameters used in Eqs. (3-10), (3-11), and (3-12)

Parameter	Units	Value
τ_{ref}	μs	1.0
v_{ref}	m/s	55.0
α_0	-	1.35
S_0	mm^{-1}	1.0
ΔS_0	mm^{-1}	20.0
v_0	m/s	21.5

Parameter α controls the variation of $1/\tau$ with impact velocity. $1/\tau$ decreases with α when the packing density and impact velocity are fixed. A scaling law is developed to quantify α as a function of the grain volume fraction η and the variation of the specific interface area ΔS_v. The resulting relation is

$$\alpha(\eta, \Delta S_v) = \alpha_0 \eta^{2.0} \left(1 + \frac{\Delta S_v}{\Delta S_0}\right)^{-3.6}, \tag{3-13}$$

where α_0 and ΔS_0 are constants, as listed in Table 7. This relation consists of a dimensionless term obtained by normalizing ΔS_v by reference value ΔS_0. Over the range of conditions analyzed, the specific surface area S_v does not affect α; therefore, it does not appear in Eq. (3-13). Overall, α increases with packing density η. It is particularly sensitive to the packing density, as indicated by the exponent of 2.0 above. This high sensitivity can be attributed to the high stresses carried by PBXs at higher packing densities.

On the other hand, α decreases as the variation of specific surface area ΔS_v increases. This decrease can be explained by the physical effect of ΔS_v. As ΔS_v increases, the probability distribution of t_c becomes more spread out, which results in lower values of $1/\tau$. This, in turn, results in lower values of α.

3.4.14 Effect of Microstructure on Threshold Velocity v_c

The threshold velocity v_c is the impact velocity below which no ignition is observed. The existence of a threshold velocity was proposed by James [37, 119] based on the asymptotic nature of experimental data. The determination of v_c is important in

design, manufacturing and transport of explosives as it relates to the safe handling limit. There have been numerous studies on low velocity impact testing of explosives [21, 131]. Most of the studies on explosive survivability focus on a limited number of "go" and "no-go" experiments performed on different batches of samples. For obvious reasons, such experiments are not amenable to studying the effects of microstructure or property variation on the stochastic response of energetic composites.

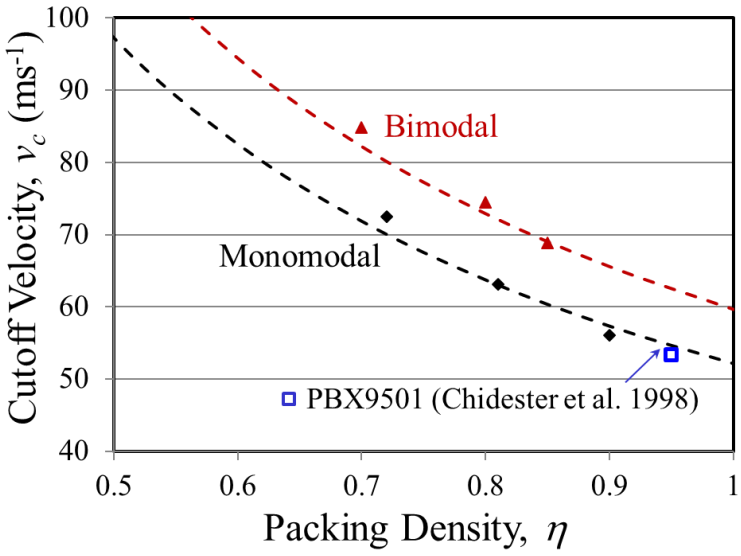

Figure 42: Comparison of experimental threshold velocity v_c for PBX9501 and numerically predicted values as a function of grain volume fraction (η = 0.70 - 0.90) and grain size distributions (monomodal, bimodal).

The Weibull model, on the other hand, can help establish a relationship between the threshold velocity and microstructure attributes. Analyzing the variation of $1/\tau$ with v makes it possible to obtain the threshold impact velocity as the impact velocity at which $1/\tau$ goes to 0. This is done by fitting Eq. (3-12) to the results of calculations, yielding v_c as a function of microstructure.

Figure 42 shows the threshold velocity v_c as a function of the grain volume fraction for microstructures with both monomodal and bimodal grain size distributions. Clearly, the threshold velocity decreases as the grain volume fraction increases. This is expected since the same impact velocity induces higher overall stresses in microstructures with higher grain volume fractions. To better illustrate the trends, v_c can be expressed as a function of the grain volume fraction and the specific interface area in the form of

$$v_c\left(\eta, S_v\right) = v_0 \eta^{-1.2}\left(1+\frac{S_v}{S_0}\right)^{0.3}, \tag{3-14}$$

where v_0 and S_0 are constants. Here, a dimensionless term is obtained by normalizing S_v using a reference value S_0. The values of the constants in Eq. (3-14) are listed in Table 7. Note that the variation in specific interface area (ΔS_v) does not affect the threshold impact velocity.

Equation (3-14) shows that a microstructure having a higher packing density is more prone to ignition and growth of reaction, provided that the specific interface area S_v is kept constant. If the two curves in Figure 42 for monomodal and bimodal microstructures are extended to a volume fraction of 1.0, the threshold velocities for η = 1.0 can be obtained. Note that, here, the η = 1.0 case is not a single crystal, but rather a polycrystalline aggregate of HMX grains. It is well known that a single crystal of HMX is hard to ignite [132]. However, a polycrystalline solid with weak grain boundaries can fracture along grain boundaries as well as in the interior of grains, leading to extensive local frictional dissipation. Hence, a polycrystalline HMX aggregate can be highly susceptible to impact-induced ignition.

The threshold velocities for the microstructures with the bimodal grain size distributions are higher than the corresponding values for microstructures with the monomodal distribution having the same overall grain volume fraction (see Figure 42). This reflects the fact that the specific interface area for the bimodal microstructures ($S_v \approx 25$ mm^{-1}) is significantly higher than that for the monomodal microstructures ($S_v \approx 16$ mm^{-1}). Equation (3-14) indicates that microstructures with smaller grain sizes are less susceptible to impact-induced ignition. However, a distribution with smaller grain sizes may affect other material attributes (such as strength and integrity) in different ways. Also, fine grains may give rise to smaller distances between hotspots, making detonation more homogeneous and influencing the propagation of the detonation wave. This issue is related more to the chemistry of the ignition process than to the thermo-mechanical response which is the focus of discussions here.

One way to validate the results from mesoscale calculations is to compare the predicted threshold velocity v_c with available experimental data. Using Eq. (3-14), we determined that the threshold velocity for a PBX with 95% HMX is between 54 and 63 m/s, depending on the grain size distribution. Chidester and coworkers [131] measured the threshold impact velocities for a variety of high explosives. Specifically, the threshold velocity for PBX9501 with a density of 1.843 g/cm^3 was found to be approximately 53.04 m/s. Gruau et al. [21] reported that the minimum projectile velocity required for the ignition of PBX samples were 60-84 m/s in experiments. The range of threshold velocities obtained from our calculations correlates well with the available experimental data.

The approach outlined above for determining the threshold impact velocity is an approximation. The reason is that the threshold impact velocity obtained here is based on extrapolation of the data for higher impact velocities. A more accurate method for

evaluating v_c is to run a series of calculations with successively lower impact velocities. This approach is similar to the Bruceton method [126]. However, there are two issues with this approach. The first is that it involves a large number of calculations since multiple cases need to be considered at velocities in the neighborhood of the threshold velocity. Secondly, a more serious issue encountered while using this approach is that at velocities near the threshold, enough time needs to be allowed for the material behind the stress wave to equilibrate. This necessitates a very large domain size and excessively long run times for the finite element calculations, even on parallel supercomputers.

3.4.15 Median Time to Criticality t_{50}

It is of interest to obtain some measure of the average or expected time to criticality as a function of microstructure and loading conditions. This type information is useful for comparing different types of explosives. It can also be used to validate the statistical model against well-established relations from experiments for the ignition of explosives, such as the Walker-Wasley relation [36] or the threshold relation proposed by James [37].

Two measures of average can be estimated from the Weibull distribution. The first is the expected time to criticality t_{exp}. This measure represents the weighted mean of the time to criticality $t_{exp} = t_0 + \tau \cdot \Gamma(1 + 1/m)$, where $\Gamma(\cdot)$ is the gamma function. An alternative measure is the time at which 50% of the samples have developed critical hotspots or the time at which the probability of ignition is $P(t_{50}) = 0.5$. This time is denoted as t_{50} and it represents the median value of the Weibull distribution. The t_{50} is a commonly used measure for quantifying the sensitivity of explosives. It is analogous to h_{50} used in drop-weight testing, which is the drop height resulting in a probability of ignition of 0.5 [133]. In experiments dealing with spark ignition of gases, the criterion for defining the

minimum ignition energy (MIE) is the spark energy level with a 50% probability of ignition [134]. In subsequent analyses, t_{50} is used as a measure of explosive sensitivity or susceptibility to ignition.

The Weibull distribution allows the probability distribution of the time to criticality t_c to be quantified as functions of microstructure and loading conditions. From the Weibull distribution, the median time to criticality t_{50} can be calculated as [135]

$$t_{50} = t_0 + \tau\left[\ln(2)\right]^{1/m}. \tag{3-15}$$

The variation of t_{50} as a function of critical impact velocity and microstructure parameters can be used to identify trends which determine ignition sensitivity in PBXs. Equation (3-15) allows the Weibull form to be reduced to an ignition threshold relation similar to the James relation [37] in the v-t_{50} space (see Appendix in Ref. [108]).

3.4.16 Impact Velocity and Median Time to Criticality t_{50}

The effect of grain volume fraction on the median time to criticality t_{50} is investigated using monomodal microstructures. Figure 43(a-b) show the variation of t_{50} as a function of impact velocity in the range of v = 100 and 250 m/s. The calculations are performed using loading configuration 2 [Figure 18(b)]. The curves are fitted to the functional form

$$\left(v - v_c\right)^n t_{50} = C\left(\eta\right) \tag{3-16}$$

to illustrate the overall trends, similar to what is done in Barua et. al. [107]. The values of n and C for the different microstructures analyzed are listed in Table 6. The calculation of

t_{50} uses a set of 20 microstructure samples for each combination of packing density and loading condition. In general, as the impact velocity increases the time to criticality decreases. Higher grain volume fractions lead to more sensitive PBX. The variation in response with η is small at higher impact velocities and large at lower impact velocities. The diminishing effects of microstructure on response at high impact velocities reflects the fact that grain fracture occurs almost immediately upon onset of loading at high impact velocities, leading to high temperature increases in grains near the impact surface. The difference in t_{50} between the microstructures shown in Figure 43(a) at a high impact velocity of 200 m/s is 0.4 μs and 1.0 μs at 100 m/s.

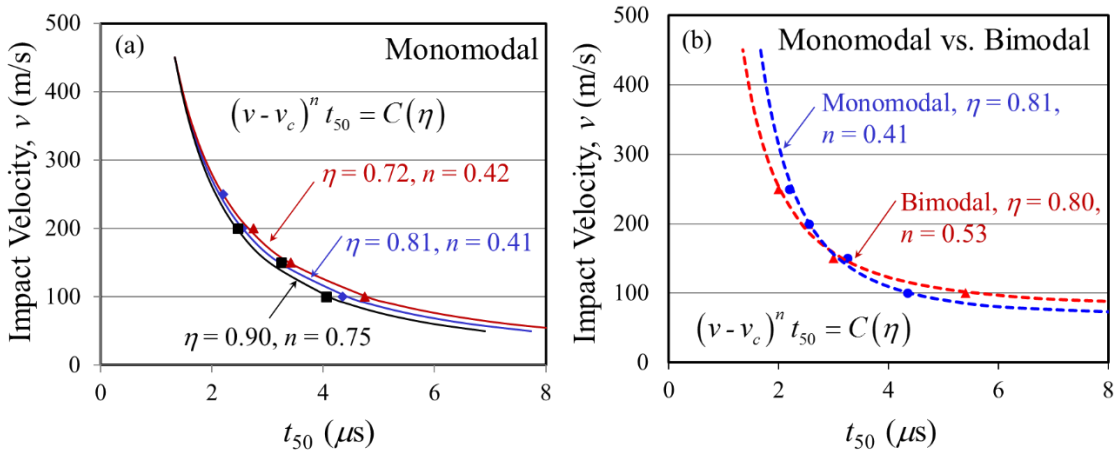

Figure 43: Relation between impact velocity and median time to criticality for (a) microstructures with a range of initial grain volume fractions having monomodal grain size distribution, (η = 0.72 – 0.90, v = 100 - 200 m/s); and (b) microstructures with monomodal and bimodal grain size distributions (η ~ 0.80, v = 100 - 200 m/s).

Figure 43(b) compares the variations of t_{50} with impact velocity for monomodal and bimodal microstructures having the same grain volume fraction of $\eta \approx 0.80$. The calculations are performed for impact velocities between v = 100 and 250 m/s. At high impact velocities (v > 200 m/s), t_{50} for both size distributions are similar with the

monomodal distribution showing slightly higher t_{50} than the bimodal distribution. On the other hand, at lower impact velocities (v < 200 m/s), the monomodal microstructures have lower time to criticality and are, therefore, more susceptible to ignition than the bimodal microstructures. Specifically, at v = 100 m/s, the bimodal microstructures are ~20% safer than the monomodal microstructures.

3.4.17 Axial Stress and Median Time to Criticality t_{50}

The relation between axial stress (sometimes referred to as pressure, especially for shock loading) and time to criticality can provide important information regarding the key mechanisms governing ignition sensitivity. Several researchers have focused on the shock initiation threshold of PBX and GX [37, 136-138]. For example, Hayes [136] explored the shock sensitivity of porous HMX and found that coarse materials are more sensitive in the low-shock pressure regime (pressure < ~5 GPa) and less sensitive in the high pressure regime. A similar effect was also observed in pressed RDX by Spear and Nanut [125]. Khasainov et al. [124] suggested that this shock sensitivity reversal in PBXs is due to a change in critical hotspot size resulting from differences in the specific interface area of the granules. The dependence of ignition sensitivity on input stress is a complex issue which involves two aspects: (1) the formation of critical hotspots and (2) the propagation of reaction in hotspots and associated thermal runaway. By analyzing the stress vs. time to criticality relationship from a statistical perspective using mesoscale calculations, we can address the first issue in some detail.

The distribution of stress varies significantly with time and distance from the impact face [110]. One way to characterize stress is to analyze the average stress in the loading direction across the width of the specimen. To determine the relationship between

the axial stress and the median time to criticality (σ_x–t_{50} relation), the average axial stress behind the propagating wave front is used.

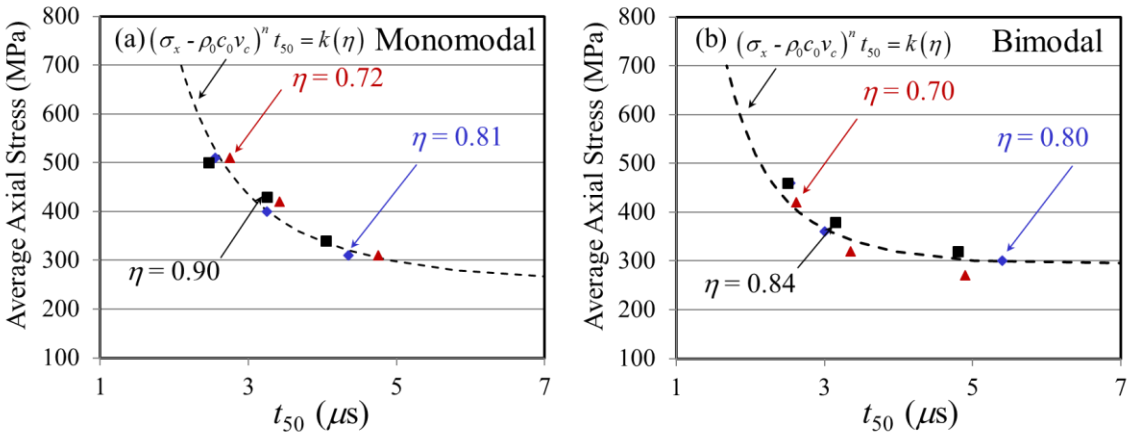

Figure 44: Relation between average axial stress and median time to criticality for (a) microstructures with a range of initial grain volume fractions having monomodal grain size distribution, (η = 0.72 – 0.90, v = 100 - 200 m/s); and (b) microstructures with a range of initial grain volume fractions having bimodal grain size distribution, (η = 0.70 – 0.84, v = 100 - 200 m/s);

The effect of grain volume fraction on the relationship between σ_x and t_{50} is first investigated using monomodal microstructures having grain volume fractions between η = 0.70 and 0.90. Figure 44(a-b) show the variation of t_{50} with σ_x for microstructures having monomodal and bimodal grain size distributions for impact velocities between v = 100 and 200 m/s. The calculations are performed using loading configuration 2 [Figure 18(b)]. The curves are fitted to a functional form which can be derived from Eq. (3-16) as

$$\left(\sigma_x - \rho_0 c_0 v_c\right)^n t_{50} = k\left(\eta\right), \tag{3-17}$$

where ρ_0 is the effective density and c_0 is the effective initial longitudinal stress wave speed through the material. The values of ρ_0 and c_0 are provided in Table 6. Equation (3-17) is similar to the relation proposed by Walker and Wasley [36]. In general, Eq. (3-17) provides a good fit to the results from calculations. The relation between σ_x and t_{50} collapses to a single curve for all the monomodal and bimodal microstructures analyzed, suggesting that this relation is not sensitive to the microstructural mechanisms underlying the responses of PBXs under the conditions studied. Indeed, the primary heating mechanism is fracture and friction which is heavily influenced by shear stresses as well as hydrostatic pressure. To distinguish the differences in responses, it is important to consider the deviatoric part of the stress tensor. Indeed, recent results (not shown here) suggest that the equivalent stress can be used as a measure to evaluate the effect of microstructure on the time to criticality. Specifically, high input shear stresses (equivalent stress > ~0.5 GPa) almost invariably lead to the formation of critical hotspots irrespective of the packing density. On the other hand, at lower levels of the equivalent stress, microstructures having higher packing densities have a lower time to criticality and are, therefore, more susceptible to ignition. This issue shall be the subject of a future publication.

3.5 Conclusion

This study in this section has focused on three new developments. The first is a systematic method for the characterization of hotspot fields resulting from non-shock impact loading of granular explosives (GXs) and polymer-bonded explosives (PBXs). This new method uses the radial distribution function (RDF) and yields quantifications of the size distribution, shape and distances of hotspot fields as function of microstructures and loading.

The second development is a new criterion for establishing the ignition conditions of heterogeneous energetic materials in general conditions. This criterion, similar to a "yield" or failure criterion in mechanics of materials, links the hotspot size-temperature states in a loading event to the threshold size-temperature conditions of hotspots which are regarded as materials properties. Since hotspot quantification can be explicitly obtained through simulations (CFEM in the case of this paper) or experiments regardless of loading and because threshold hotspot size-temperature pairs are material attributes, this criterion applies to both shock and non-shock conditions.

The third development is an approach for computationally predicting and quantifying the stochasticity of the ignition process in polymer-bonded explosives. The method involves subjecting sets of statistically similar microstructure samples to identical overall loading and characterizing the statistical distribution of the ignition response of the samples. The analyses have focused on the influence of random microstructure geometry variations on the critical time to ignition and the critical impact velocity below which no ignition occurs.

Both the hotspot quantification method and the new ignition criterion have been used to analyze the behavior of granular HMX and polymer-bonded HMX with different microstructures. For different loading configurations and materials, the study has yielded the critical impact velocity for ignition and critical time required for ignition as a function of material and impact velocity. The microstructural samples are from both real materials and systematic computations. The analysis also concerns different loading conditions (rates, wave reflections). Results show that fracture of energetic grains and subsequent friction along crack faces constitutes the most important heating mechanism in general.

For the PBXs at moderate and high impact velocities, grain fracture and friction are primarily responsible for heating. For the GXs, initial porosity plays the most important role in heating in terms of heating rate but not hot-spot size and spacing. In contrast, grain size of GX appears to have negligible influence on ignition. The effect of porosity is most pronounced at low impact velocities and negligible at high impact velocities when localized fracture and friction near impact face dominate.

Wave reflections from confined boundaries (associated with small samples, larger impactor) multiply stress and temperature increases, making even low velocity impact dangerous if loading is maintained over sufficiently long durations. While for large samples (no wave reflections), GX is more susceptible to ignition at all impact velocities. For small, confined samples, GX is more susceptible at high impact velocities, while PBX is more susceptible at low impact velocities, when deformed to the same level of total strain. For the range of impact velocities considered, PBX is 2-4 times safer (in terms of critical impact velocity) than HMX at high impact velocities. On the other hand, PBX is similar to or worse off than granular HMX at low impact velocities (if total deformation is the same).

The probability distribution of the time to criticality (t_c) largely follows the Weibull distribution. This probability distribution is quantified as a function of microstructural attributes including grain volume fraction, grain size and specific binder-grain interface area along with the stochastic variations of these attributes. The relations reveal that the specific binder-grain interface area and its stochastic variation have the most influence on the critical time to ignition and the critical impact velocity below which no ignition is observed. The predicted threshold velocity v_c for ignition is consistent with

available experimental data for a PBX with 95% HMX content. The v_c for a bimodal distribution of grain sizes is lower compared with that for a monomodal distribution having the same overall packing density.

Lower grain volume fractions lead to wider spreads in the distribution of the time to criticality. Microstructures having bimodal grain size distributions exhibits lower ignition sensitivity than microstructures having monomodal grain size distributions under the conditions analyzed. Finally, it is shown that the probability distribution in the Weibull form can be reduced to an ignition threshold relation similar to the James relation in the *v*-*t* space.

The study has focused exclusively on the influence of microstructure geometry variations on the critical time to ignition at given load intensity and the critical impact velocity below which no ignition occurs. It must be pointed out that the ignition response is also affected by the stochasticity in constituent properties at the microstructure level and load conditions. Those effects are the subject of the next section. Quantification of those effects is necessary for a complete picture of the stochastic nature of ignition sensitivity of solid high explosives to emerge.

CHAPTER 4: PROBABILISTIC IGNITION BEHAVIOR FROM MULTIPLE SOURCES OF STOCHASTICITY

This chapter is based on the work published in Ref. [139].

4.1 Introduction

This study focuses on the effects of two sources of stochastic variations at the microstructural level on hotspot development in a PBX. The random variations considered are associated with the morphologies of constituent phases and the bonding strength of the grain-binder interfaces. Microstructures with statistically similar properties are generated with variations in the morphologies of the grains and binder and in the interfacial bonding strength between the grains and the binder. The probability of ignition arising from one source of stochastic variation is quantified and analyzed separately from another source. The two probability functions are then combined using relations between the time to criticality and microstructure attributes. The specific mathematical form used is the three-parameter Weibull distribution function.

4.2 Framework of Analysis

4.2.1 Microstructure

The microstructures that this paper analyzes simulate PBX consisting of HMX grains and an Estane binder. Typical shape of energetic grains in the computationally generated microstructure used for the mesoscale simulation are either circular [91, 140] or polygonal generated by the Voronoi tessellation method. Simulations of the Brazilian compression test using PBX microstructures generated by the Voronoi tessellation method yield results that match the results of experiments reasonably well [44]. Although the microstructures generated by the Voronoi method have more realistic shapes of grains,

they have monomodal size distribution, whereas HMX crystals in PBX9501 have bimodal size distributions [81].

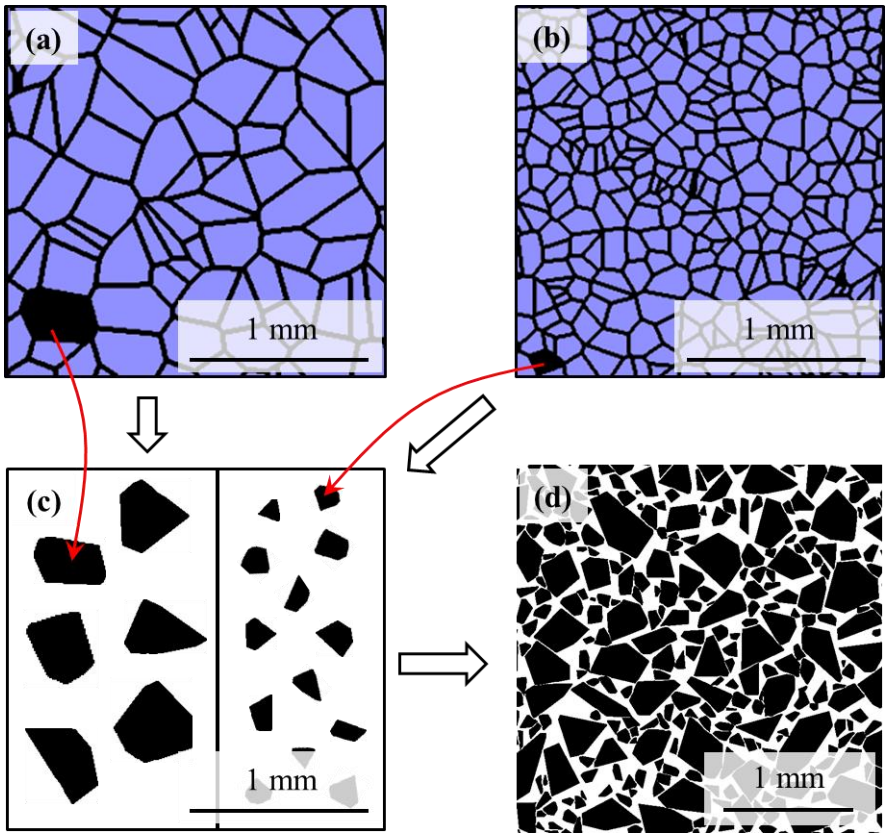

Figure 45: Generation of microstructures with bimodal size distributions; (a-b) Microstructures generated by Voronoi tessellation: (a) with coarse grains and (b) with fine grains; (c) Grain library with coarse and fine grains extracted from the microstructures of Voronoi tessellation; (d) Microstructure with bimodal size grains that are randomly placed.

To obtain microstructures that are similar to PBX9501, we use a grain library with a bimodal grain size distribution. This library consists of grains extracted from microstructures generated by the Voronoi tessellation method. Two microstructures, one with large grains (see Figure 45(a)) and the other with small grains (see Figure 45(b)), are generated. The grains in each microstructure are detected and stored separately in the grain

library as shown in Figure 45(c). Finally, grains in the library are randomly distributed on the microstructure domain as seen in Figure 45(d). To achieve a high packing density, the larger grains (d > 200 μm) are initially placed at random locations up to a specified volume fraction (e.g., η = 0.55–0.60). Subsequently, smaller grains (d < 200 μm) are placed between the larger grains, until the desired volume fraction (η = 0.81) is reached. The time required for generating a micrograph increases with the desired packing density. To reduce the time required in generating micrographs with a high packing density (η > 0.70), a random shuffling algorithm is employed. Specifically, if a grain cannot be placed in the domain, the locations of the existing grains are randomly altered until an empty region can be found for that particular grain. Naturally, such a method cannot be used indefinitely. There is a packing density beyond which grains can no longer be accommodated. This method is capable of achieving a relatively high packing density of η ~ 0.81. For the bimodal distributions, the two mean grain sizes are ~123 μm and ~289 μm. The average standard deviation for the smaller size is 37.2 μm and the large size is 49.9 μm.

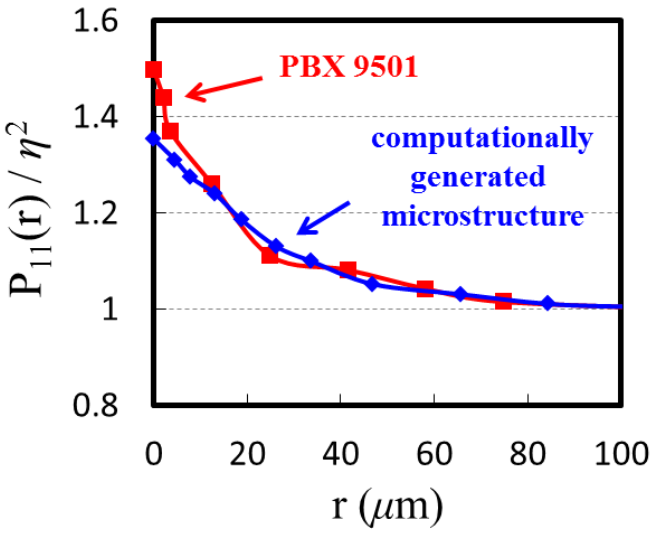

Figure 46: Comparison of the two-point correlation functions of the microstructure of PBX 9501 [141] and computationally generated microstructure.

The evaluation of the computationally generated microstructure is performed by comparing the two-point correlation function of PBX 9501 microstructure and that of computationally generated microstructure. The gray-scale image of the PBX 9501 microstructure (η = 0.70) was obtained by Liu [141]. The microstructure of PBX 9501 typically includes HMX grains close to 95% by mass fraction (92% by volume fraction). However, as Mas et al. [142] observed, some particles are too small to be resolved by micrographs, resulting in less volume fraction than actual PBX9501 is composed of. Figure 46 shows that the two-point correlation function of PBX 9501 microstructure strongly matches that of the computationally generated microstructure (η = 0.74) from the grain library approach. Multiple microstructures with the same attributes are generated based on the approach described previously. To illustrate the random variations in microstructure morphology, Figure 47 shows five samples with the same packing density of η = 0.81.

In addition to having variations in constituent morphologies, the microstructures have statistical variations in the bonding strength between the binder and the grains. In modeling, these variations manifest in the maximum traction (S_{max}) of the cohesive relation that determines the strengths of the interfaces in the normal and shear directions. Details of the framework used are given in Barua et al. [87].

The effect of interfacial bonding strength is analyzed using two microstructure groups. The first group has spatially uniform bonding strengths between the phases but randomly varying phase morphologies. Sample sets in this group have one of six levels of the maximum traction ($S_{\max}$ = 0.1, 17.5, 35, 70, 100, and 1000 MPa) and each set consists of twenty microstructure samples. This group has a total of $20 \times 6 = 120$

samples. The critical displacement is 4.62 μm for all of the six sets which represent different levels of fracture energy (γ_c) in the range of $0.231 - 2310\, J/\mathrm{m}^2$. The maximum traction of 35 MPa corresponds to a fracture energy of $\gamma_c = 81\ \mathrm{J/m^2}$ which matches the experimental data in Ref. [81]. The traction of $S_{max} = 0.1\ MPa$ implies essentially very weak bonding strength at the interfaces in the microstructures. The strength level of $S_{max} = 1000\ MPa$, which is much higher than the intergranular bonding strength between HMX crystals ($S_{max}^{HMX} = 100$ MPa as in Ref. [87]), is a hypothetical value used to explore trend in the ignition probability of microstructures with a very high interfacial strength level.

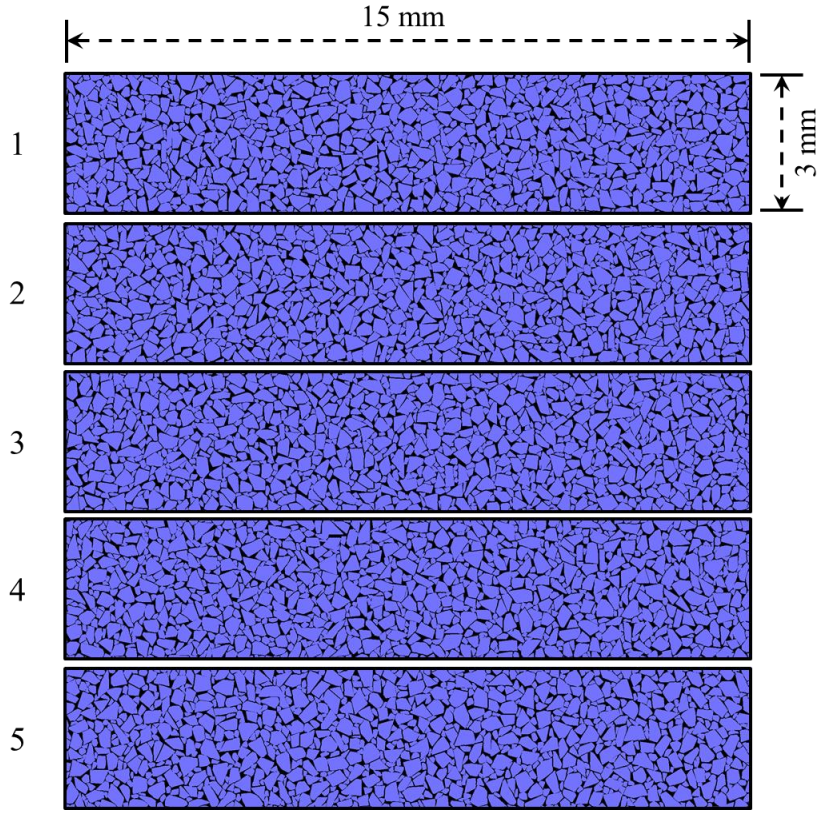

Figure 47: Multiple samples of computationally generated microstructures with a bimodal grain size distribution and a grain volume fraction of η = 0.81.

Table 8. Cohesive parameters at grain-binder interface

Types of bonding strength	Maximum traction S_{max} (MPa)
Random variation in strengths (Gaussian Distribution)	μ : 35 S_{max} : 7
Uniform strength	0.1
	17.5
	35
	70
	175

The second microstructure group has samples with interfacial bonding strengths that vary spatially. The stochastic variations of the maximum traction occur at the grain-binder interfaces, not inside the grains or the binder. The bonding strength is assumed to follow the Gaussian distribution with an average of 35 MPa, which is one of the six uniform values in the first group. The standard deviation of the bonding strength is 7 MPa, which is 20% of the average value, as shown in Figure 48(a). The selection of the standard deviation follows the experimental results in Ref. [81], which show a scatter of 10-20% around a linear fit of data near the maximum cohesive stress. As an example of the spatially varying interfacial strength, Figure 48(b-c) shows a close up view of HMX grain boundaries, with the color coding of the strength levels given in Figure 48(a). The constitutive relation of cohesive bonding is described in Ref. [99], and the values of the

cohesive parameters for the first and second microstructure groups are listed in Table 8. The material property parameters (i.e., elastic moduli and density) are listed in Table 9.

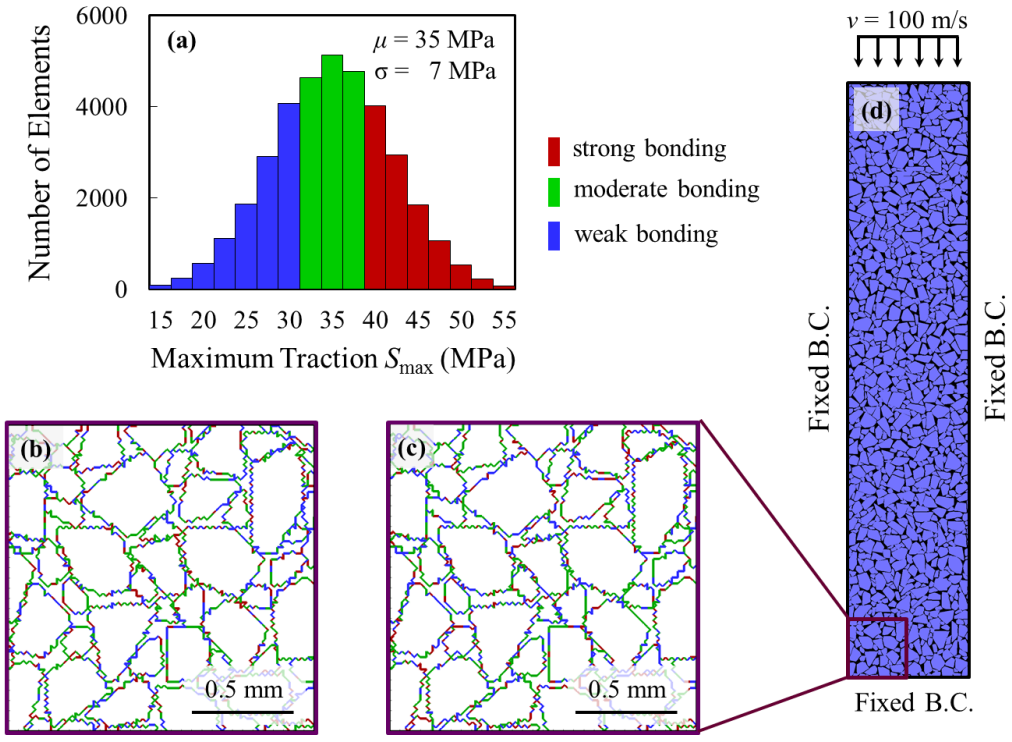

Figure 48: Illustration of microstructures with spatially varying bonding strength between the HMX grains and Estane binder; (a) Gaussian distribution of the interfacial strength (mean (μ) = 35 MPa, standard deviation (σ) = 7 MPa); (b-c) Spatially varying interfacial bonding along boundaries between HMX grains and Estane binder, the red, green, and blue colors represent strong, moderate, and weak bonding strength levels, respectively; and (d) Configuration of the loading and boundary conditions used in the analysis.

In the following discussion, "M_U" refers to the microstructure with uniform interfacial bonding strength, and "M_V" refers to the microstructure with stochastic variations in interfacial bonding strength.

Table 9. Material parameters for HMX and Estane

Material Property	HMX	Estane
Bulk modulus *K* [MPa]	15700	3650
Shear modulus *G* [MPa]	8300	Prony series [104]
Density ρ [g/cm^3]	1.90	1.19

4.2.2 Loading Configuration

Figure 48(d) shows the loading configuration used. The sample size is $15\ mm \times 3\ mm$. A low impact velocity yields a distribution of ignition probability that is wider than a high impact velocity does for a statistically similar microstructure set, as reported in Ref. [108], accentuating the effect of the random morphological variations in the materials' microstructures. However, a low impact velocity lengthens the time to criticality, necessitating a larger microstructure for the simulation in order to avoid stress wave reflection from the opposite fixed end of the sample. At an impact velocity of v = 100 m/s, approximately ~ 9.5 μs of loading and response without stress wave reflection can be analyzed.

The microstructure is initially stress-free and at rest. Once loading begins, the impact velocity is imposed at the top end of the sample shown in Figure 48(d). Over the initial period of time ($0 \leq t < 0.5\ \mu s$), the boundary velocity is linearly ramped from zero to the maximum of v = 100 m/s The left and right side boundaries are constrained such

that lateral motions do not occur. This configuration approximates the normal impact loading of an infinitely wide material block under the conditions of macroscopically uniaxial strain. For all calculations presented, initial temperature is T = 300 K.

4.2.3 Issues Analyzed

The analysis is performed in the following steps. First, calculations are carried out using multiple sets of instantiations with the loading condition shown in Figure 48(d). Following the calculations, the ignition criterion [107] is used to scan the microstructure for hotspots and detect critical hotspots that have reached the size-temperature threshold. With this approach, once an ensemble (or a set of microstructure instantiations) is defined, the distribution of the time to criticality can be uniquely determined for the microstructure set. For each set with a given combination of statistically similar attributes, the time to criticality (t_c) is evaluated as a cumulative probability distribution. The distribution of the time to criticality obtained from each set is fitted to the Weibull distribution with three parameters [127] in the form of

$$P(t) = 1 - \mathrm{e}^{-\Phi(t)}, \quad \Phi(t) = \begin{cases} 0, & t \le t_0 \\ \left(\dfrac{t - t_0}{\tau} \right)^m, & t \ge t_0 ; \end{cases} \tag{4-1}$$

where t is the time to criticality, t_0 is the minimum time to criticality, or the cutoff time to criticality below which the probability of ignition is zero, τ is a time-scaling parameter that affects the slope of the distribution curve, and m is a shape parameter. From the Weibull equation, the median time to criticality (t_{50}) can be obtained by

$$t_{50} = t_0 + \tau\left[\ln(2)\right]^{1/m} . \quad (4\text{-}2)$$

Barua et al. [108] provided a physical basis for the Weibull distribution fit to the probability of time to criticality using Terao's model [128]. They showed that m = 2 for loading conditions involving a propagating stress wave front, which is the case for the configuration in Figure 48(d) and throughout this section. Under the condition that the shape parameter (m) has a constant value of 2, the Weibull distribution in Eq. (4-1) is determined by two parameters, one is the median time to criticality (t_{50}) and the other is the time-scaling parameter (τ). The relationship between parameters in Eq. (4-1) is given by Eq. (4-2).

The microstructure and CFEM model we utilize in this paper are two-dimensional, with conditions of plane strain. It is worth noting that the cutoff impact velocity obtained using this framework is in good agreement with the threshold velocity for ignition measured from experiments [108]. Although desirable, a three-dimensional framework would be much more computationally intensive and numerically challenging. Such a framework which needs to account for all the physical processes considered by the 2D framework here, including distributed fracture, internal friction, and frictional heating, is not currently available.

4.3 Results and Discussions

A systematic quantification of the probabilistic distributions of time to criticality is carried out, focusing on (i) the effect of different levels of uniform interfacial strength (S_{max} = 0.1 - 1000 MPa), (ii) the effect of random variations in the interfacial strength about the mean value, (iii) the effect of random phase morphology variations, and (iv) the

combined effect of random interfacial bonding and microstructure morphological variations.

4.3.1 Probability of Ignition with Uniform Interface Strength

To provide a basis for systematic comparison, the probability of ignition for microstructures with spatially uniform interfacial bonding strength is analyzed. The analysis involves a microstructure group consisting of six sets of instantiations. Each set of instantiations has one of six uniform interfacial strength levels (S_{max} = 0.1, 17.5, 35, 70, 100, and 1000 MPa). In the following discussion, "Distribution-U" refers to the ignition probability distribution that results from random variations of phase morphology among statistically similar (see Ref. [108] for the definition and quantification) microstructures with uniform interfacial bonding strength (M_U). The Distribution-U's from the six sets of instantiations are shown in Figure 49(a). The median time to criticality increases as the interfacial bonding strength increases (see Figure 49(b)). The microstructures with very high interfacial strength (e.g., S_{max} = 1000 MPa) in general require longer times to reach criticality, such that many of them do not reach critical within the time window of loading without reflection from the bottom boundary (up to ~ 9.5 μs).

The data are fitted to the Weibull distribution (Eq. (4-1)) for five of the six levels of uniform interface strength (S_{max} = 0.1, 17.5, 35, 70, and 100 MPa). The median times to criticality ($t_{50,U}$) calculated using (4-2) are a function of the interfacial strength (S_{max}). The median time increases as the interfacial strength increases. The trend can be well described by a linear relation as in Figure 49(b).

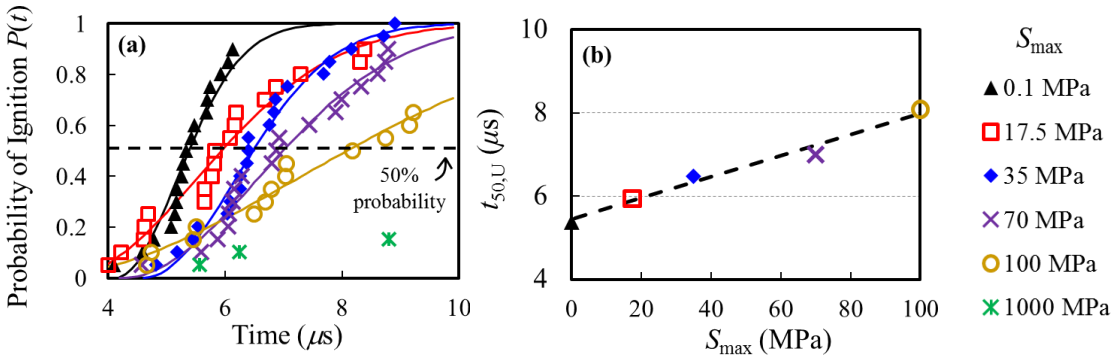

Figure 49: Effect of the level of uniform interfacial strength on the time to criticality; (a) Distributions of ignition probability for statistically similar microstructures with six levels of uniform interfacial strengths (S_{max} = 0.1, 17.5, 35, 70, 100, and 1000 MPa); (b) Median time to criticality (t_{50}) as a function of uniform interfacial strength.

Since the time to criticality is determined by localized heating in the sample, a correlation exists between the hotspot development and time to criticality $t_{C,U}$. Two parameters, hotspot number density (number of hotspots per unit volume of material, N_U) and hotspot area fraction (A_U), are quantified from the twenty samples with uniform interfacial strength (M_U) of S_{max} = 35 MPa, and are related to the ignition time of corresponding microstructure. The threshold of T = 400 K is used to cut off the temperature field and detect hotspots at t = 6 μs after impact. The top 3 × 3 mm^2 portion of the domain is analyzed. Figure 50(a) shows that microstructures with a higher number density of hotspots require less time to criticality, and Figure 50(b) shows the same trend for the total area fraction of hotspots. Overall, more hotspot quantities (i.e., area fraction and number density of hotspots) are observed from microstructures that ignite earlier time than from those that ignite later time, indicating that the development of hotspots is one factor that determines the ignition sensitivity of the microstructure.

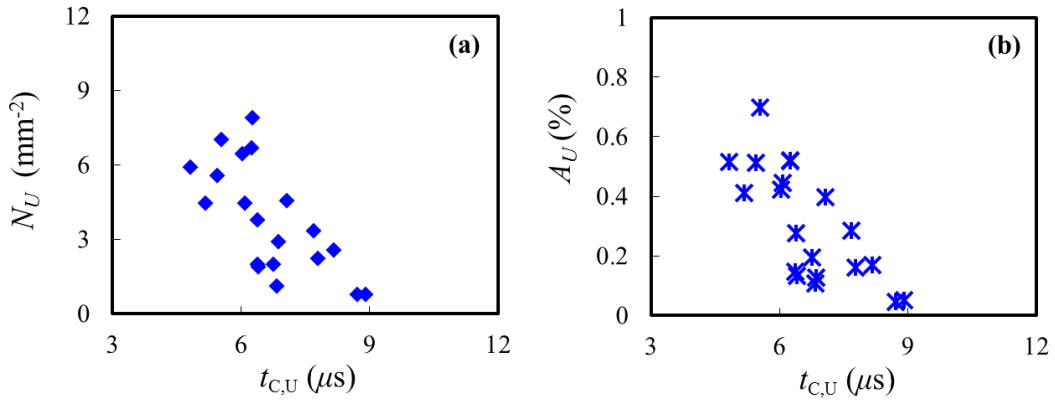

Figure 50: Effect of hotspot field on the ignition time ($t_{C,U}$) of M_U; (a) Relation between the number density of hotspots (N_U) and $t_{C,U}$; (b) Relation between the total area fraction A_U of hotspots and $t_{C,U}$.

4.3.2 Effects of Fluctuations in Interface Strength

The effect of spatial variations of the interface strength is analyzed using three microstructure samples. The first sample (M_U), which serves as a base line case for comparison, has uniform interface strength of S_{max} = 35 MPa. The other two samples (M_V) have the same microstructure morphology that the first sample has, but involve stochastically varying interfacial strengths as described in Sec 2.1. Since the variations in interfacial strength are randomly distributed, the grain-binder configuration denoted by strength color of one microstructure among the two samples differs from that of the other microstructure as shown in Figure 48(c-d). Figure 51(a-c) show the temperature distributions for the three cases at 6 μs after impact. The overall appearances of the hotspot fields for the three bear resemblance. However, both locations and peak temperatures of the critical hotspots are different. The variations in interfacial bonding strength provide a perturbation to the thermomechanical processes in the materials, causing the temperature distributions to be different. For a microstructure set with the same phase morphology

having random variations in interfacial strength, the stochastic growth of hotspot leads to the ignition time to be different from sample to sample, giving rise to the probability distribution of time to criticality.

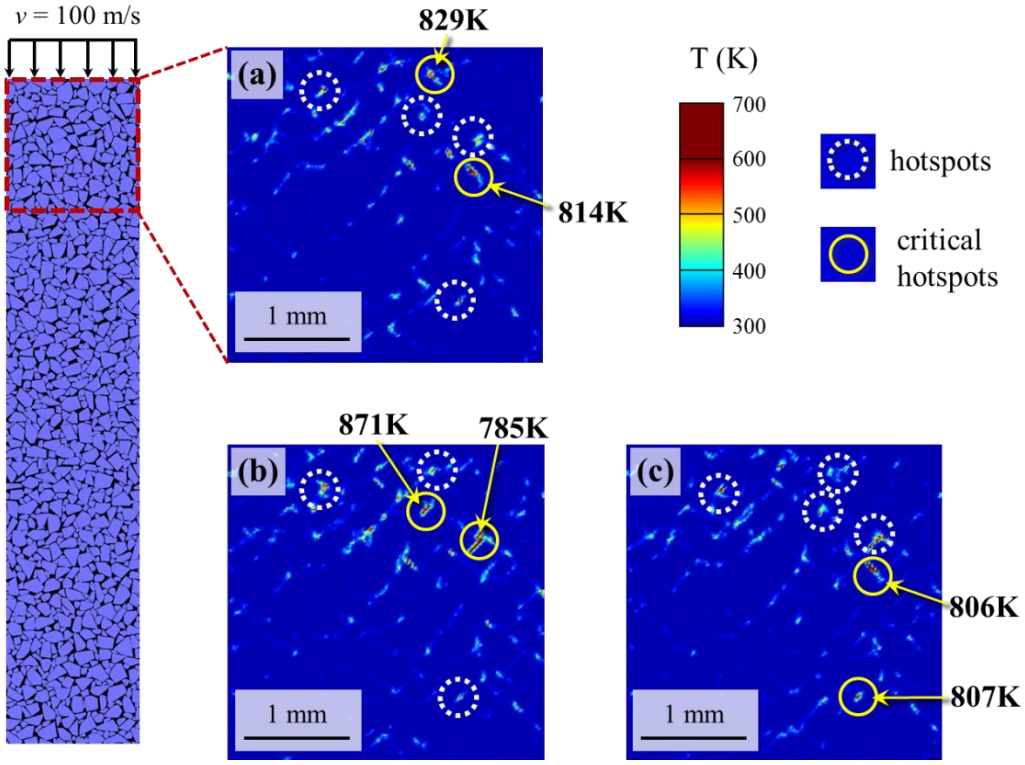

Figure 51: Temperature field and hotspot locations at t = 6 μs (a) from a microstructure with uniform interfacial strength and (b-c) from the same microstructure with varying interfacial strength. Circles indicate the hotspots (in white dotted line) and the critical hotspots (in yellow solid line).

The resemblance of hotspot field between M_U and M_V is quantified for all twenty microstructure morphologies. Specifically, twenty sets of new samples are generated, with each set based on a baseline microstructure morphology from one of the twenty microstructures of M_U, providing a total of $20 \times 20 = 400$ samples. All four hundred samples have randomly varying binder-grain bonding strengths. The number density and

the total area of hotpots are obtained from each sample set of M_V. The average values of hotspot number density (N_V) and hotspot area fraction (A_V) from each sample set of M_V are related to the hotspot number density (N_U) and hotspot area fraction (A_V) from the baseline sample in M_U as shown in Figure 52(a-b). The results show that the data points follow $N_V = N_U$ and $A_V = A_U$ closely, with a slight bias toward the side of the case with both sources of stochasticity, suggesting that the hotspot field is primarily determined by its microstructure morphology, and the variations in interfacial bonding strength makes perturbation on hotspot evolution.

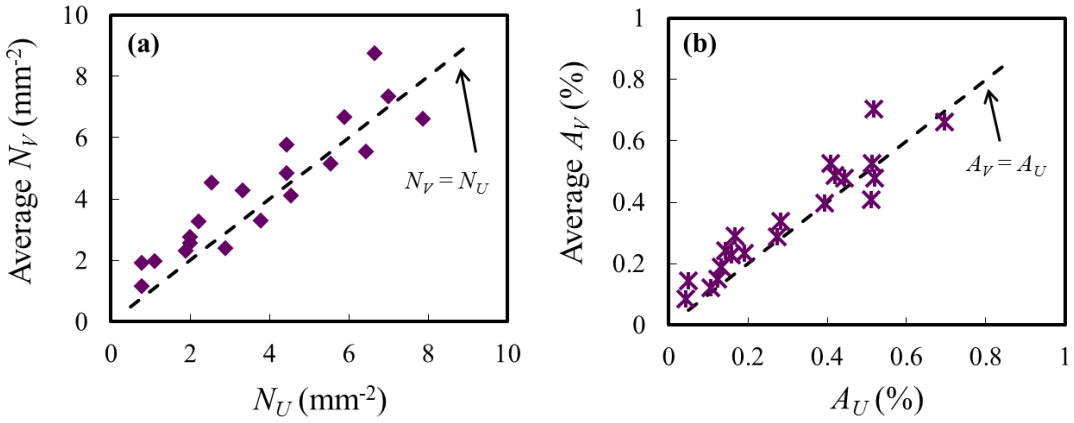

Figure 52: Correlation between the hotspot field of M_U and the average quantity of hotspot field of M_V; (a) Relation between the average number density of hotspots (N_V) from M_V and the number density of hotspots (N_U) from M_U; (b) Relation between the average area fraction of hotspots (A_V) from M_V and the area fraction of hotspots (A_U) from M_U.

4.3.3 Combined Effects of Variations in Microstructural Morphology and Interface Strength

The combined effect of two sources of stochasticity –phase morphology changes and variations in interfacial strength are analyzed. Among the twenty microstructures with

the uniform interfacial strength of 35 MPa, three microstructures are chosen as examples for this analysis. When they are assigned uniform interfacial strength, their ranking order of ignition times is as follows. The first microstructure, referred to as $\{A\}$, yields the earliest time to criticality ($t_{C,U}\{A\} = 4.82\ \mu s$); the second microstructure, referred to as $\{B\}$, yields the median time to criticality ($t_{C,U}\{B\} = 6.41\ \mu s$) among the twenty samples in the set; and the third microstructure chosen, referred to as $\{C\}$, yields the longest time to criticality ($t_{C,U}\{C\} = 8.92\ \mu s$) among the twenty samples as shown in Figure 53(a). Now, these three samples are used to generate three new sets of samples, each based on one of the three original samples. These three new sets, each consisting of twenty samples, constitute a total of 60 samples. The samples in each set have the same microstructure morphology as the corresponding one among the three representative microstructures chosen (A, B, or C), but have binder-grain bonding strengths that vary randomly from location to location around the original uniform strength of 35 MPa (see Figure 48(b-c)).

Figure 53(b) shows the probability of ignition as a function of time for the three new sets of microstructures. The term "Distribution-V" refers to the probability distribution of the time to criticality arising from the random fluctuations in interfacial strength only. In other words, each of the three new sets of samples yields one "Distribution-V". The results show that the Distribution-V's from the first microstructure (i.e., A), the second microstructure (i.e., B), and the third microstructure (i.e., C) lie between $4.42 - 6.23\ \mu s$, $5.19 - 8.41\ \mu s$, and $5.52 - 9.29\ \mu s$, respectively.

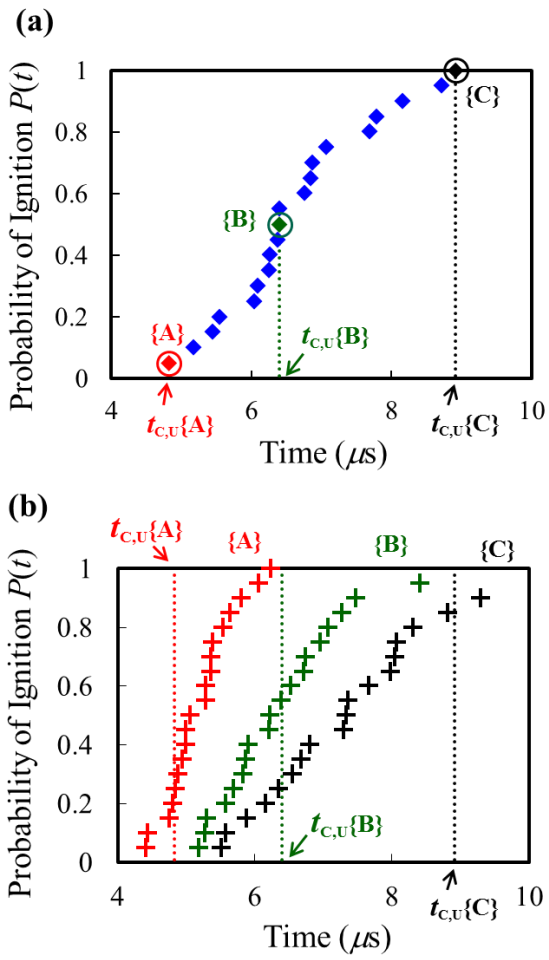

Figure 53: Relation between Distribution-V and the ignition time of the corresponding M_U; (a) Distribution-U. The names {A}, {B}, and {C} represent the microstructure morphologies that generate the earliest ($t_{C,U}${A}), median ($t_{C,U}${B}), and latest ($t_{C,U}${C}) time to criticality, respectively; (b) Distribution-V's from the selected microstructure morphologies, {A}, {B}, and {C}. The dotted vertical lines represent the ignition times of corresponding M_U.

Two interesting features are observed when the Distribution-V's are compared with their baseline ignition times ($t_{C,U}${A}, $t_{C,U}${B}, and $t_{C,U}${C}) in Distribution-U. The first feature is that the baseline ignition time ($t_{C,U}${A}, $t_{C,U}${B}, and $t_{C,U}${C}) in Distribution-U (Figure 53(a)) is not the mean ignition time for the corresponding sample sets giving rise

to Distribution-V. Specifically, for microstructure morphology $\{A\}$ which has the shortest ignition time $t_{C,U}\{A\}$, the corresponding ignition times in Distribution-V are mostly later than $t_{C,U}\{A\}$ [note the dotted vertical line in Figure 53(b)]. On the other hand, the opposite is observed for microstructure morphology $\{C\}$ which has the longest ignition time $t_{C,U}\{C\}$ – the corresponding ignition times in Distribution-V are mostly earlier. For microstructure morphology $\{B\}$, the corresponding ignition times in Distribution-V straddle both sides of $t_{C,U}\{B\}$.

The second feature is that the ranking order of mean ignition time of Distribution-V's for the three new sample sets follow the same order of the ignition time for the three baseline microstructures in Distribution-U, i.e., $t_{C,U}\{A\}$, $t_{C,U}\{B\}$, and $t_{C,U}\{C\}$. As discussed in Sec. 3.2, the hotspot locations in the microstructures with uniform interfacial strength are similar to the hotspot locations in the corresponding microstructures with random fluctuations in interfacial strength around the uniform strength value, as seen in Figure 51(a-c). The similarity in hotspot locations shows that sites for the occurrence of dominant hotspots are primarily determined by microstructure morphology and material heterogeneity. In contrast, fluctuations in interfacial strength cause stochastic field (e.g., temperature) perturbations that "modulate" the degree of localization of the field quantities. As a result, variations in interfacial strength cause stochastic variations in ignition time relative to the ignition time determined by the material heterogeneity inherent in the microstructures.

Although only the results for three samples (A, B, and C) out of the twenty samples in Distribution-U are shown above, results for all twenty microstructures show the same features and trends. A total of 400 samples are used, involving randomly varying binder-

grain bonding strengths. The trend shown in Figure 53 is analyzed for all twenty sets. To obtain an analytical quantification of the trend, both Distribution-U and Distribution-V are characterized using Weibull distribution functions. The specific forms used here are

$$P_1(t) = 1 - \exp\left[-\left(\frac{t - t_{0,\mathrm{U}}}{\tau_{\mathrm{U}}}\right)^2\right], \tag{4-3-a}$$

$$P_2(t) = 1 - \exp\left[-\left(\frac{t - t_{0,\mathrm{V}}}{\tau_{\mathrm{V}}}\right)^2\right]. \tag{4-3-b}$$

Here, subscript "U" denotes the value obtained from Distribution-U, and subscript "V" denotes the value obtained from Distribution-V.

The dependency of Distribution-V on Distribution-U is analyzed using the median time to criticality $(t_{50,V})$ and the time-scale parameter (τ_{V}) to capture the overall shift of the distribution with respect to time and the slope of the distribution. Subsequently, Equation (4-2) is used to obtain the parameters in Eqs. (4-3-a) and (4-3-b). The median time to criticality $(t_{50,V})$ and time-scale parameter (τ_{V}) for Distribution-V for each sample set are related to, and therefore change with, the ignition time $t_{C,U}$ of the corresponding baseline microstructure in Distribution-U as shown in Figure 54(a-b). The relations are represented by

$$\frac{t_{50,\mathrm{V}}}{t_{50,\mathrm{U}}} = \alpha\left(\frac{t_{\mathrm{C,U}} - t_{50,\mathrm{U}}}{t_{50,\mathrm{U}}}\right) + \beta \text{ , and} \tag{4-4-a}$$

$$\frac{\tau_{\mathrm{V}}}{\tau_{\mathrm{U}}} = \gamma\left(\frac{t_{\mathrm{C,U}} - t_{0,\mathrm{U}}}{\tau_{\mathrm{U}}}\right) + \delta \tag{4-4-b}$$

where the parameters α, β, γ, and δ are fitting constants. The values of those constants are listed in Table 10.

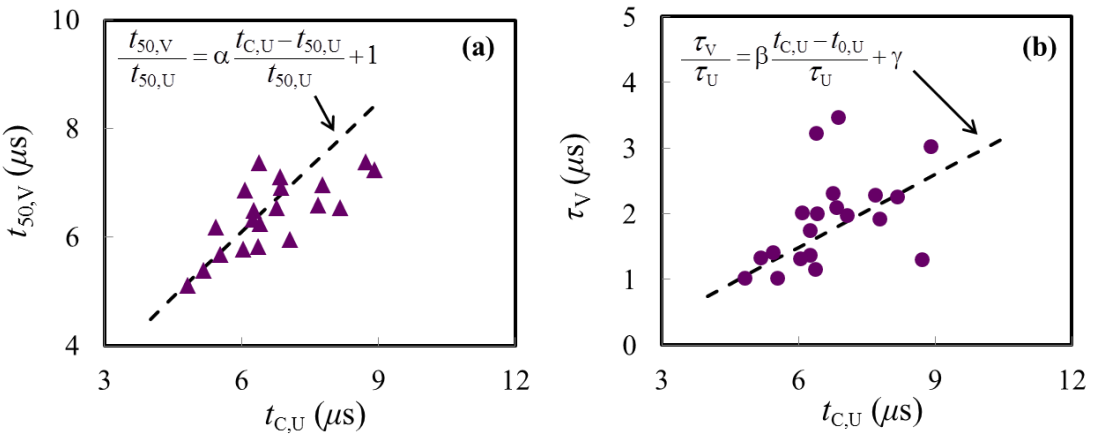

Figure 54: Relation between the Weibull parameters of Distribution-V and the ignition time of M_U ($t_{C,V}$) with the corresponding morphology; (a) Relation between the minimum time to ignition ($t_{0,V}$) for Distribution-V and $t_{C,U}$ in Distribution-U; (b) Relation between the median time to ignition ($t_{50,V}$) for Distribution-V and $t_{C,U}$ in Distribution-U.

Parameter α represents the strength of the effect of morphology variations on the median time to criticality of Distribution-V. A value of α = 1 would indicate a simple direct superposition of the morphology variation effect and the property fluctuation effect for the mean ignition time for Distribution-V. A value of α = 0 would mean no morphology variation effect on the mean ignition time for Distribution-V. Values of α that are between 1 and 0 indicate the second source of stochasticity "diminishes" the effect of the first source of stochasticity. For the conditions studied, the value of α = 0.8 suggests that the influence of the first source is more dominant than that of the second source on the median time to criticality ($t_{50,V}$) of Distribution-V.

Table 10. Parameters used in Eqs. (4-4-a) and (4-4-b)

Parameters	Values (dimensionless)
α	0.8
β	1
δ	0.37
γ	0.43

Parameter β represents the potential scaling of the mean ignition time for Distribution-U that may be required in order to arrive at the ignition times for samples in Distribution-V due to the introduction of the second source of stochasticity (the random fluctuations in interfacial strength). A value of $\beta = 1$ indicates no scaling here. Parameters γ and δ quantify the ratio between the slope of Distribution-V and the slope of Distribution-U. Parameter γ embodies the dependency of the ignition probability distribution associated with Distribution-V on the first source of stochasticity. A value of $\gamma = 0$ would indicate that the slopes of all Distribution-V curves are the same. Higher γ values would suggest stronger dependence of Distribution V probability profiles on Distribution-U. The value obtained for the conditions studied is $\gamma = 0.43$. Parameter δ alone determines the slope of the Distribution-V ignition probability curve for the sample with the microstructure morphology that generates the minimum time to criticality (ideally most ignition sensitive microstructure morphology in Distribution-U) as a function of the slope of the ignition time probability profile associated with Distribution U.

Since all 400 samples have statistically similar microstructure morphologies and the same average interfacial strength with the same level of stochastic variations, their times to criticality can also be treated as one statistical ensemble. Such an analysis is carried out in Figure 55. The result provides an overall quantification of the ignition behavior of the samples with two sources of stochasticity. The result also raises the

question of “how do the contributions of the two sources combine to yield the overall behavior in Figure 55?”.

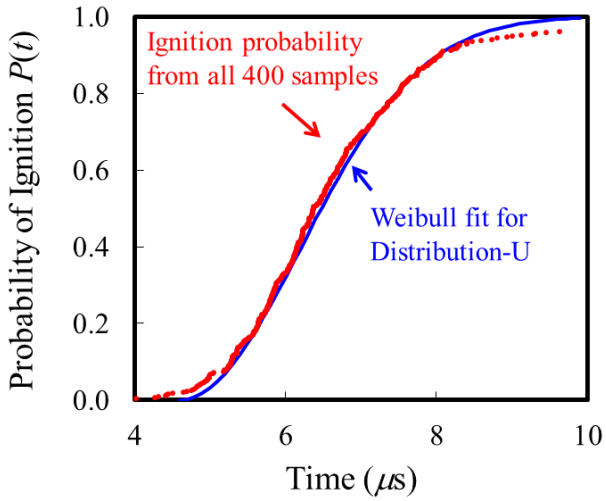

Figure 55: Distribution of ignition probability from all 400 samples (red line) and its Weibull fit (black dotted line) in comparison with the Weibull fit for Distribution-U (blue line).

4.3.4 Combined Models

The first step in developing a model to quantify the combined probability of ignition accounting for both sources of stochasticity is to quantify the probability distributions due to each source, as this quantification provides the basis for superposition. The behaviors of both Distribution-U and Distribution-V are described by the Weibull distribution functions as in Eqs. (4-3-a) and (4-3-b).

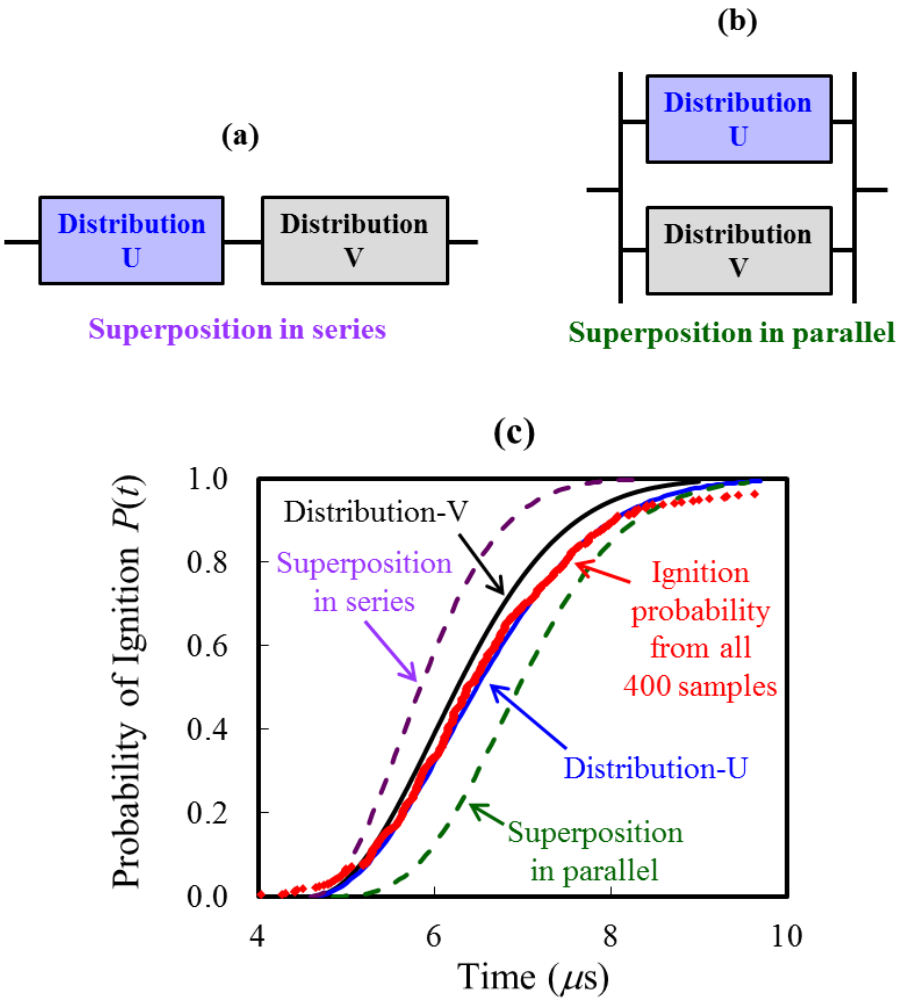

Figure 56: Schematics for (a) series and (b) parallel systems [143], and (c) combined probability in series (violet line) and in parallel (green line) system of Distribution-U (blue line) and Distribution-V (black line) from a microstructure that has the ignition time of t_c = 6.4 μs

To analyze the combined effect of the two types of stochastic variations, two models based on these individual quantifications are first examined. These models are simple parallel and series arrangements shown in Figure 56(a-b). The idea of parallel and serial arrangements, as discussed in Ref. [143], was originally developed to consider the failure of mechanical systems consisting of many components. The failure of one

component of a system is independent of the failure of other components. In the parallel model, the system fails when all components fail. In the serial model, the system fails if any of its components fails.

The superimposed probabilities of ignition for parallel and serial systems are given by [see Ref. [143] for derivations]

$$P_{para}(t)=\left[1-\exp\left\{-\left(\frac{t-t_{0,\mathrm{U}}}{\tau_{\mathrm{U}}}\right)^{2}\right\}\right]\left[1-\exp\left\{-\left(\frac{t-t_{0,\mathrm{V}}}{\tau_{\mathrm{V}}}\right)^{2}\right\}\right], \tag{4-5-a}$$

$$P_{serial}(t)=1-\exp\left\{-\left(\frac{t-t_{0,\mathrm{U}}}{\tau_{\mathrm{U}}}\right)^{2}-\left(\frac{t-t_{0,\mathrm{V}}}{\tau_{\mathrm{V}}}\right)^{2}\right\}. \tag{4-5-b}$$

As discussed in Ref. [143], a parallel system becomes more likely to survive as components are added it, because the probability of failure of the system is obtained by multiplying the failure probabilities of all components. On the other hand, a serial system becomes more likely to fail as more components are added, because the survivability of a system is obtained by multiplying the survivabilities of all components.

Figure 56(c) shows Distribution-U (blue), Distribution-V (black), along with the combined probabilities in series (purple) and in parallel (green). Combining the individual probabilities in a serial fashion shifts the combined probability toward earlier times. On the other hand, combining the individual probabilities in a parallel fashion shifts the combined probability toward later times. Both are far from what is observed in Figure 55 which shows that the combined probability distribution of ignition does not shift in either earlier or later time directions relative to the Distribution-U curve. The actual combined probability curve is simply more spread out toward both early time and long time extremes.

Note that the parallel and serial models assume that the probability of a component's failure is independent of that of other components in the same system [143]. Here, the parameters for Distribution-V may depend on Distribution-U. These factors and the differences in Figure 56 point out the need for a new mathematical model for combining the two probability functions in Eqs. (4-3-a) and (4-3-b).

4.3.5 Nested Probability Distribution Model

To arrive at the joint probability distribution, we propose a nested probability superposition model that combines the effects of the two sources of stochasticity on ignition probability. This nested probability model recognizes the fact that there are "two layers" of probability distributions. The first layer is due to random variations in microstructure morphology. The second layer is associated with the fluctuations in interfacial bonding strength. Note that the random fluctuations in bonding strength can only occur along the boundaries between the binder and the energetic granules, and the discussion of fluctuations in bonding can only be pursued for given microstructures. Because of this constraint, the variations in microstructure morphology must be treated as the first layer of variations which can be made regardless of interfacial strength. On the other hand, the fluctuation in bonding is a second level variation that "rides" with the microstructure, and therefore, is treated as the secondary variation here. This "layering" of variations determines the order or manner in which the superposition of the two levels of probability distributions is carried out. The nested superposition model developed here reflects this fact.

El Otmani et al. [144] considered a nested probability of the Gaussian distribution. For the first layer, there are *n* number of random values that follow the Gaussian

distribution $(\mu, {\sigma_1}^2)$, where μ is the mean and σ_1 is the standard deviation. An arbitrary point among the n values $(x_1, \cdots, x_n)$ is denoted as x_i. For the second layer, there are n sets of values, and the values in each set follow a new Gaussian distribution with the mean value of x_i (from the first layer) and a standard deviation of σ_2. If the values from all sets are combined, then the probability density function [144] that represents the population of all values is

$$f(x) = \frac{1}{\sqrt{2\pi({\sigma_1}^2 + {\sigma_2}^2)}} \exp\left\{-(x-\mu)^2 / \left[2({\sigma_1}^2 + {\sigma_2}^2)\right]\right\}. \quad (4\text{-}6)$$

Figure 57 shows a conceptual illustration of the nested probability function of the Gaussian distribution.

To analyze the how effects of the two sources of variations (in morphology and interfacial strength) combine, we consider a large number of random values that follow the nested probability model. For the first layer, 100,000 random values that follow the Weibull function of Distribution-U [Eq. (4-3-a)] are generated. For the second layer, the same number of sets of random values are generated based on the values in the first layer. The random values of each set in the second layer follow the Weibull function of Distribution-V [Eq. (4-3-b)]. The Weibull parameters $t_{0,V}$ and τ_V in Eq. (4-3-b) are obtained using the linear relation between $t_{C,U}$ and τ_V and the linear relation between $t_{C,U}$ and $t_{50,V}$.

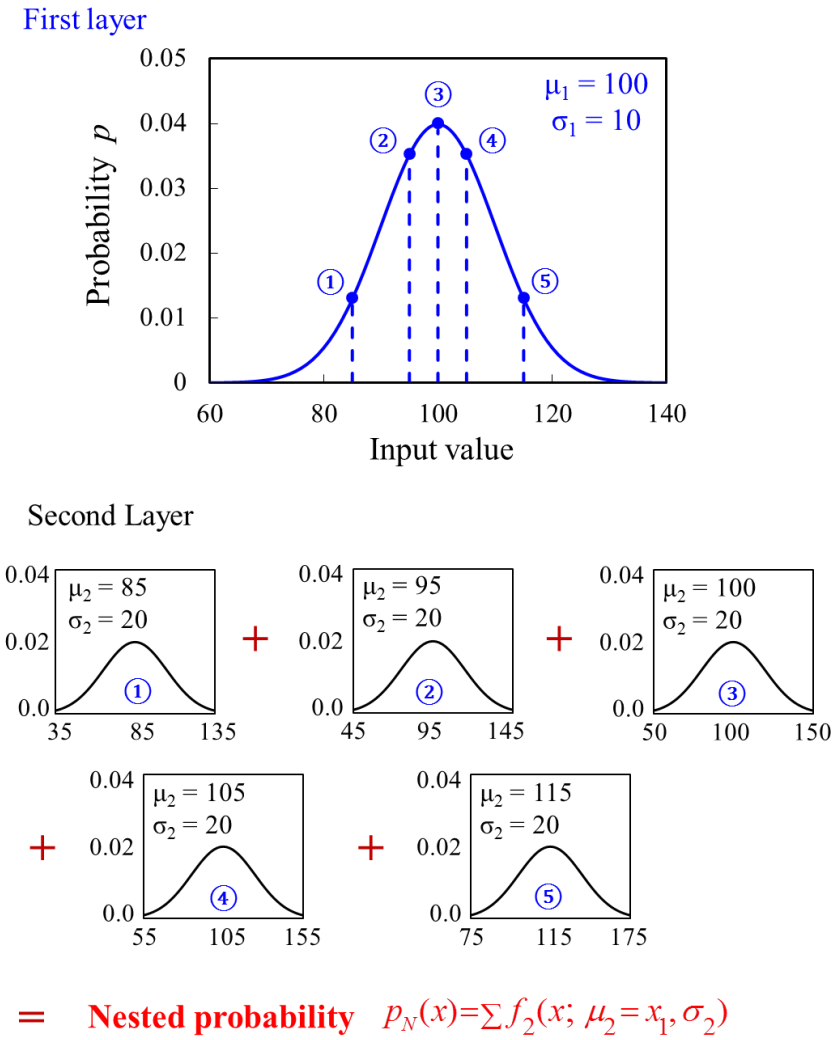

Figure 57: Conceptual diagram for the nested probability function of Gaussian distribution

Ultimately, the properly superimposed, combined ignition probability function must agree with the total ignition probability function obtained with all cases which are considered as a statistical ensemble of one sample set. Figure 58 shows the combined distribution function obtained by using the nested probability (green dots) and the probability distribution of time to criticality represented by all 400 samples (red line). The

closeness between the two curves confirms the validity of the nested superposition model and the insights it yields.

In order to obtain an analytical form of the nested Weibull probability distribution, a finite, discrete mixture model is considered. A general form for this model [145] is

$$P(t) = \sum_{i=1}^{n} w_i p_i(t) \ , \tag{4-7}$$

where $w_i \geq 0$ are weighs for the individual probability density functions $p_i(t)$ for each set of samples in the second layer. The parameters in Eq. (4-7) that represent the combined probability are $w_i = 1/n$, n = 20. The probability $p_i(t)$ is stated in the form of

$$p_i(t) = H\left(t - t_{0,i}\right) \frac{2}{\tau_i} \left(\frac{t - t_{0,i}}{\tau_i} \right) \cdot \exp\left\{ -\left(\frac{t - t_{0,i}}{\tau_i} \right)^2 \right\}, \tag{4-8}$$

where $H(\cdot)$ is the Heaviside unit step function, and $t_{0,i}$ and τ_i are $t_{0,V}$ and τ_V for the i-th microstructural morphology, respectively. The finite, discrete mixture of Weibull distribution functions is equivalent to the nested Weibull distribution, representing the combined probability of ignition. However, the finite mixture of probability distributions is a summation of discrete probability functions. A concise analytical form of the final probability as a continuous function has not yet been obtained through this approach.

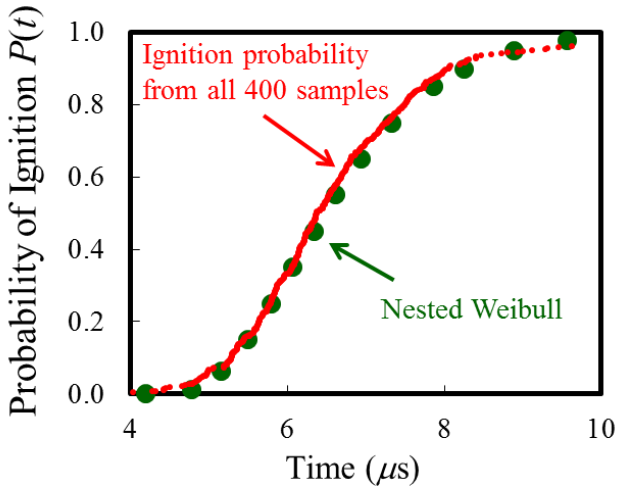

Figure 58: The nested Weibull distribution obtained by generating large number of random values (greed dots) and the probability distribution data from all 400 instantiations (red line)

In Eq. (4-8), the probability function $p_i(t)$ can be represented as a conditional probability, $p_i(t \mid t_c)$, because $p_i(t)$ is valid only if the microstructure with the corresponding morphology ignited at $t = t_{C,U}$. The probability of ignition for an arbitrary sample among a statistical ensemble of all samples is mathematically known as the *joint probability*, $p(t, t_c)$ of two probability functions – a conditional probability function of Distribution-V and a probability function for Distribution-U. That is,

$$\begin{aligned} p(t,t_c) &= p(t \mid t_c) \cdot p(t_c) \\ &= H(t-t_{0,i}) \cdot \frac{2}{\tau_i}\left(\frac{t-t_{0,i}}{\tau_i}\right) \cdot \exp\left\{-\left(\frac{t-t_{0,i}}{\tau_i}\right)^2\right\} \\ &\cdot H(t_{C,U}-t_{0,U}) \cdot \frac{2}{\tau_U}\left(\frac{t_{C,U}-t_{0,U}}{\tau_U}\right) \cdot \exp\left\{-\left(\frac{t_{C,U}-t_{0,U}}{\tau_U}\right)^2\right\}. \end{aligned} \tag{4-9}$$

If all possible microstructures are considered, the final combined probability density function (PDF) is

$$p(t)=\int_{t_{C,U}=t_{0,mor}}^{\infty}\left[H(t-t_{0,i})\cdot\frac{2}{\tau_i}\left(\frac{t-t_{0,i}}{\tau_i}\right)\cdot\exp\left\{-\left(\frac{t-t_{0,i}}{\tau_i}\right)^2\right\}\right.$$
$$\left.\cdot\frac{2}{\tau_U}\left(\frac{t_{C,U}-t_{0,U}}{\tau_U}\right)\cdot\exp\left\{-\left(\frac{t_{C,U}-t_{0,U}}{\tau_U}\right)^2\right\}\right]dt_{C,U}, \quad (4\text{-}10)$$

and the cumulative distribution function (CDF) is

$$P(t)=\int_{\xi=0}^{t}f(\xi)\cdot d\xi$$
$$=\int_{\xi=0}^{t}\int_{t_{C,U}=t_{0,V}}^{\infty}\left[H(\xi-t_{0,i})\cdot\frac{2}{\tau_i}\left(\frac{\xi-t_{0,i}}{\tau_i}\right)\cdot\exp\left\{-\left(\frac{\xi-t_{0,i}}{\tau_i}\right)^2\right\}\right. \quad (4\text{-}11)$$
$$\left.\cdot\frac{2}{\tau_U}\left(\frac{t_{C,U}-t_{0,U}}{\tau_U}\right)\cdot\exp\left\{-\left(\frac{t_{C,U}-t_{0,U}}{\tau_U}\right)^2\right\}\right]dt_{C,U}\cdot d\xi,$$

where τ_i and $t_{0,i}$ are $t_{0,V}$ and τ_V as obtained from Eqs. (4-2), (4-4-a), and (4-4-b).

Figure 59 shows the CDF obtained from a numerical integration of Eq. (4-11) [shown in black line], and the nested Weibull function [shown in green dots]. The distributions from the two approaches provide identical results, confirming that Eq. (4-10) and Eq. (4-11) are the analytical forms of the nested Weibull distribution.

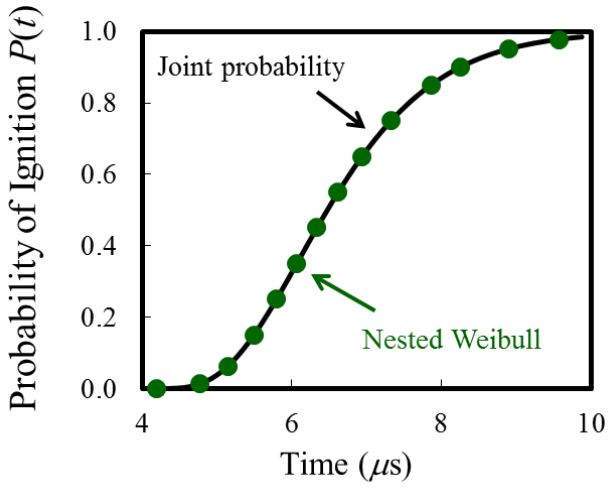

Figure 59: The nested Weibull distribution (green dots) and the CDF from the equation of the Joint probability function (black line).

It should be pointed out that, in the nested probability model, we first obtained the relations between the parameters for distributions associated with the variations in morphology and interfacial strength. Subsequently, we used these relations to obtain the analytical form of the final probability. In experiments, however, the approach is often reversed, and it is not straightforward to separate the effect of one source of variations from the effect of another. For example, Subero-Couroyer et al. [146] performed experiments on the crushing probability of particles with multiple sources of defects. The crushing probabilities arising from each source of defects and multiple sources of defects are quantified using Weibull distribution functions. The Weibull function for samples with multiple sources of coupled defects is equivalent to the nested Weibull function in our model. However, as indicated in Ref. [146], "it is difficult to separate the effect of macroporosity from the combined effect of macroporosity and defects …". By using the nested probability concept, we are able to isolate the effect of defects, as discussed in the next section.

4.3.5 Applications for the Nested Probability Model

To obtain the nested probability model, we first analyzed the relations between the parameters for distributions associated with the variations in morphology and interfacial strength. Subsequently, we used these relations to obtain the analytical form of the final probability. In experiments, however, the approach is often reversed. For example, PBX samples with perfect HMX-binder interfaces have very small or negligible variations in interfacial strength. The probability distribution from this sample set is due to random morphology, which is equivalent to Distribution-U in our model. On the other hand, PBX samples with imperfect HMX-binder interfaces will provide a probability distribution due to the combined effect of variations in bonding strength and variations in morphology. The probability in this case is equivalent to the final nested probability in our model. Therefore, the analysis for actual experiments requires the inverse approach that starts with the final combined data to obtain the relations between the effects of individual sources of heterogeneities.

As an example for the application of the nested probability model, we use experimental data obtained by Subero-Couroyer et al. [146]. They measured the mechanical failure strength of catalyst pellets under compressive loading. Two-parameter Weibull function was used to analyze the effects of process parameters and defects such as drying procedure, macroporosity, or air bubbles. Here, we use two data sets—one set from fresh and used samples and the other set from samples with macropores (denoted as F1M1D1) and without macropores (denoted as F1M0D1).

Subero-Couroyer et al. [146] reported that used catalyst has lower failure strength and wider spread of probability than fresh catalyst does, resulting in changes of Weibull parameters, m and τ. The probability distribution for fresh catalyst group is equivalent to

Distribution-U, and the probability distribution for used catalyst group is equivalent to the final nested probability. To analyze the transition of strength from fresh catalyst to used catalyst using the nested probability model, we make the following assumptions. One is that Weibull modulus m of Distribution-V follows the same value of Distribution-U. Second assumption is that if samples with relatively low strength in the fresh catalyst group become used samples, they will exhibit relatively low strength in the used catalyst group. For samples with relatively high strength in the fresh group, if they degrade, they will exhibit relatively high strength in the used group. Third assumption is that the trend in the second assumption follows a linear relationship between the strength in the fresh group and the strength of the corresponding samples in the used group. Based on the second and third assumptions, the relation between Distribution-U and Distribution-V is plotted in Figure 60, and the analytical form is given as

$$\frac{\sigma_{50,\mathrm{V}}}{\sigma_{50,\mathrm{U}}} = \alpha \frac{\sigma_{\mathrm{C,U}} - \sigma_{50,\mathrm{U}}}{\sigma_{50,\mathrm{U}}} + \beta \tag{4-12}$$

where $\sigma_{50,\mathrm{U}}$ is an average (median) strength in the fresh group. $\sigma_{\mathrm{C,U}}$ is a strength of the individual sample, and $\sigma_{50,\mathrm{V}}$ is an average (median) strength of used catalyst samples for corresponding $\sigma_{\mathrm{C,V}}$. Parameters α and β are fitting constants, where α is a non-negative value. Equation (4-12) is essentially an equivalent form of Eq. (4-4-a). Since the two-parameter Weibull function is utilized for the analysis instead of three-parameter function, only Eq. (4-4-a) is required and Eq. (4-4-b) is disregarded.

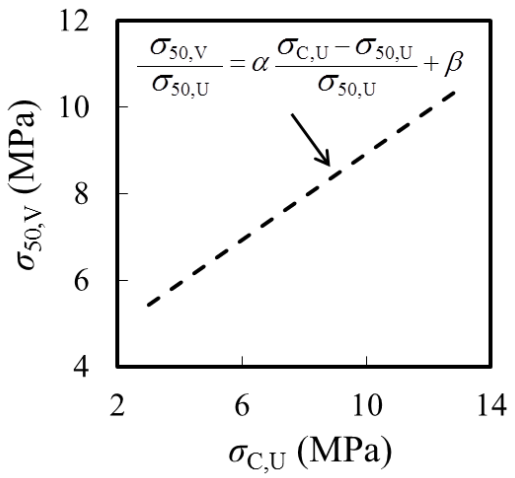

Figure 60: Relation between Distribution-U and Distribution-V

By using Eq. (4-11) and Eq. (4-12) with properly chosen constants α and β, we can obtain the nested probability that matches the probability distribution for the used catalyst group, as plotted in Figure 61. Parameters used in this plot are listed in Table 11.

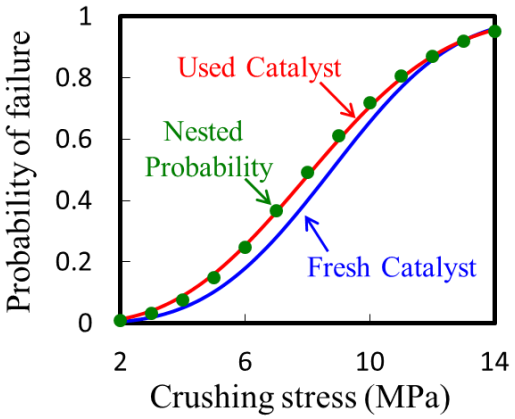

Figure 61: Comparison between probability from used catalyst (red) and nested probability (green)

Equation (4-12) with the fitting constants α and β determines how the degradation affects the strength of individual catalyst particle. Figure 62(a-d) illustrate the effect of

degradation of catalyst. Figure 62(a) shows the probability distribution from fresh catalyst group. If a sample having strength of $\sigma_{C,U}$ = 5 MPa in Figure 62(a) becomes degraded, the probability distribution of the strength of the particle would follow the distribution shown in Figure 62(b). The same process can be applied to samples having $\sigma_{C,U}$ = 8 MPa and $\sigma_{C,U}$ = 13 MPa in the fresh catalyst group, and the probability of the strength of the corresponding used particles would follow the distributions shown in Figure 62(c) and Figure 62(d), respectively.

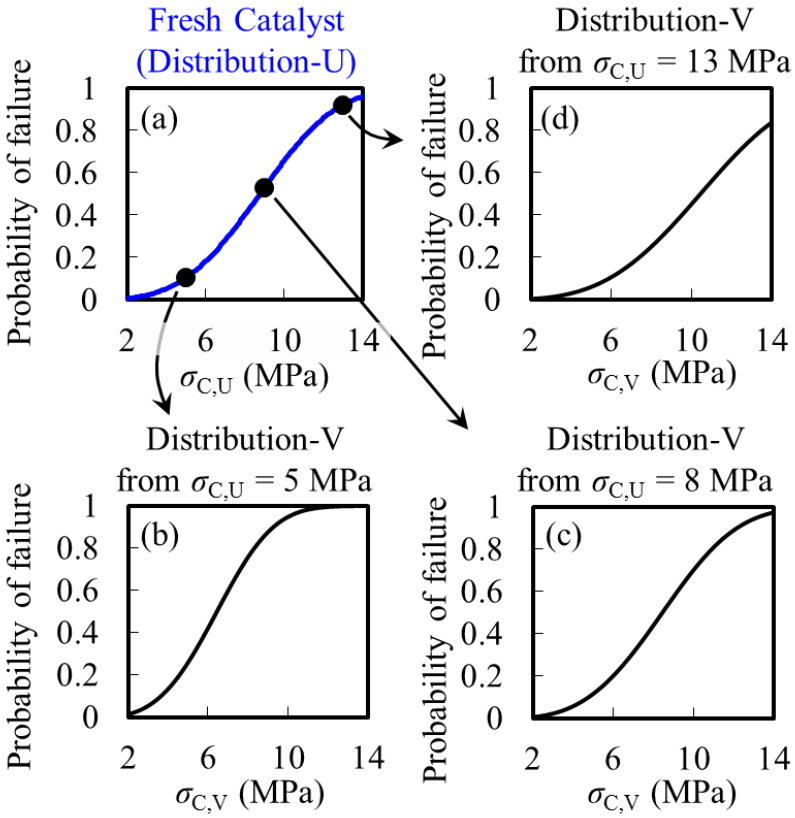

Figure 62: Effect of degradation; (a) Distribution-V from a sample with $\sigma_{C,U}$ = 5 MPa (originally weak strength); (b) Distribution-V from a sample with $\sigma_{C,U}$ = 8 MPa (originally average strength); (c) Distribution-V from a sample with $\sigma_{C,U}$ = 13 MPa (originally strong strength);

Although the application of the nested probability has focused on the two-parameter Weibull function for the analysis above, three-parameter Weibull function can also be used for a closer match with experimental data.

Table 11. Parameters in Eq. (4-12)

Parameters	Values (dimensionless)
α	0.50
β	0.95

It is observed in Ref. [146] that particles with macropores (denoted as F1M1D1) have similar average strengths but narrow spread of probability as compared to particles without macropores (denoted as F1M0D1). This trend is analyzed using the 3-parameter Weibull function, and nested probability model. Figure 63 shows the distribution of nested probability model (in green) and Weibull fitting for the experimental data (in red). Parameters listed in Table 12 provide the closest match between the nested probability and the experimental result in Figure 63.

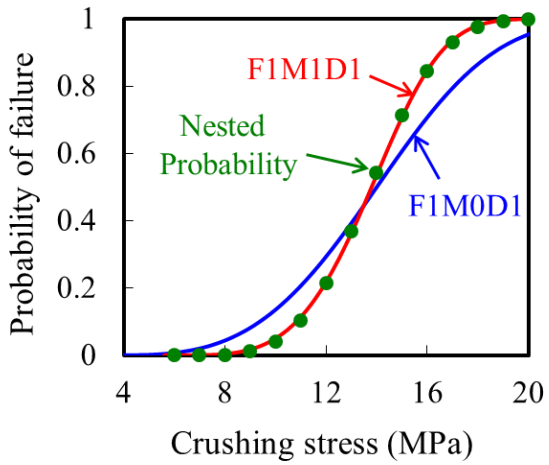

Figure 63: Crushing probability for samples without macropores (blue), with macropores (red), and nested probability (green)

Table 12. Parameters in Eqs. (4-4) and (4-11) for Figure 63

Parameters	Values (dimensionless)
α	0.54
β	0.98
γ	0.0
δ	0.28
m	3.37
τ_U (scaling strength)	12.05
$\sigma_{0,U}$ (cutoff strength)	3.2

Small value of δ (δ =0.28) means the slope of the probability becoming stiffer (small τ of Weibull parameter), indicating that introducing macropores makes sample strength more homogeneous, which agrees with the explanation given in Ref. [146].

4.4 Conclusions

This study focuses on the effects of multiple sources of material stochasticity on the probability of ignition of PBXs under impact loading. The analysis carried out in this paper concerns two types of variations. The first is in microstructural morphology, and the second is in grain-binder interfacial bonding strength. Each source of variations gives rise to a degree of randomness in the locations, sizes and temperatures of hotspots which in turn results in a degree of randomness in the ignition behavior of the materials.

Two sets of calculations are performed. The first set focuses on the effect of the microstructures that have random variations in morphology, but different levels of spatially-uniform bonding strength. The result shows a linear relationship between interfacial strength and median time to criticality of ignition probability. For a given level of uniform bonding strength (e.g., $S_{max} = 35$ MPa), microstructures with more intense hotspots (i.e., higher area fraction and number density of hotspots above a certain threshold) result in earlier ignition than those with less intense hotspots. The second set utilizes the microstructures with random variations in morphology from the first set and adds random fluctuations in interfacial strength to each sample. The result shows that the hotspot attributes – locations, number density, and area fractions – from the microstructures in the second set bear strong resemblance to the hotspot features from the microstructure with the morphology and uniform bonding strength. This resemblance is the underlying reason why the ignition probability distribution due to fluctuations in interfacial strength is dependent on the ignition time of the baseline microstructure morphology.

To understand how the different sources combine to affect the overall ignition behavior, we developed a nested superposition model. The results show that the model captures the interactions between the two sources of variations in material attributes. Although only two sources of stochasticity are considered here, the model can be generalized to analyze the combined effects of multiple sources of stochasticity. It must be pointed out that, in experiments, the final data set comes out as combined probability in most cases, and separation of the effects of the individual sources is often challenging. This separation is only studied here using the two-layered models and simulations.

For an application of the nested probability model, experimental data performed by Subero-Couroyer et al. [146] are used. The analysis for the actual experiment requires the inverse approach. Starting from final combined data, we extracted the relations between the first source and the second source of variations. By using the nested probability model, we have been able to separate and quantify the effect of degradation and macropores.

CHAPTER 5: IGNITION DESENSITIZATION OF PBX VIA ALUMINIZATION

This chapter is based on the work published in Ref. [147].

5.1 Introduction

The study in this chapter focuses on a HMX/Estane/Al PBX. The approach we use is based on a cohesive finite element method (CFEM) we developed in the last few years for PBXs and granular explosives [87, 107-110]. This framework accounts for finite elasticity, viscoelasticity, viscoplasticity, internal fracture, contact, friction, frictional heating, and heat conduction. The overall analyses also entail the use of a hotspot-based ignition criterion and a scheme to quantify the size-temperature states of hotspots in the overall microstructures and in the energetic phase of the microstructures more specifically [107]. The extension here in this paper beyond the previous studies is to add Al to the constituents considered. The calculations quantify the response of the PBX and identify trends which can be used for future, more systematic studies on the behavior of aluminized PBXs. In particular, the calculations presented in this paper are limited to the addition of one population of mono-sized Al particles. The microstructures are designed in a way to keep the total solid (Al and HMX) fraction constant, while the fraction of the HMX is adjusted accordingly as the Al fraction is increased. We adopted this methodology following the practice in the publically available literature on the effect of Al addition [148-152]. The goal here is to identify a possible desensitizing effect of Al in low-velocity impact loading that is beyond the effect of reduced fractions of solid explosive crystals in

an overall PBX. As will become clear, the trend identified by numerical simulations is in qualitative agreement with available experimental data in the literature.

5.2 Framework of Analysis

5.2.1 Materials

The microstructures considered are those of a PBX system consisting of either two (HMX/Estane) or three (HMX/Estane/Al) phases. The HMX grains have multi-faceted edges and a bimodal grain size distribution. The average grain sizes of the large and small grains are 289 μm and 123 μm, respectively. The microstructures generated for the two-phase PBX system is compared to a digitized micrograph of PBX 9501 using the two-point correlation function. Good agreement is found between the function profiles for the computationally generated microstructure and the actual microstructure [See Sec. 4.2.1]. Details of the microstructural attributes of the two-phase (HMX/binder) PBX and the method used to generate the microstructure are described in Sec. 4.2.1. To generate the three-phase system of microstructures, aluminum particles are added to the solid phase of the two-phase (HMX/binder) system. The volume fraction of the Al particles is varied from 0% to 18%. Accordingly, the volume fracture of the HMX grains is varied from 81% to 63%. While the volume fractions of the individual constituents are different in the different samples, the total volume fraction of solid load (HMX and Al) remains constant at 81%. Consequently, the volume fraction of the Estane binder is 19% for all samples. The volume fraction range of Al considered corresponds to an Al mass fraction of 0-25%, which is the range of interest for aluminized PBX in experiments [92, 153, 154]. The aluminum particles in the three-phase PBX microstructures have circular shapes and an average size of 50 μm. Typical Al particles in PBXs used in experiments have sizes that

varies from sub-microns to 150 microns [92, 153], spherical or flake shapes, and monomodal size distributions [155]. Figure 64 shows the five microstructure conditions (with the different volume fractions of HMX grains and Al particles) studied. These images present one sample for each of the five microstructure conditions. Twenty random instantiations or microstructure samples are generated for each of the five cases in Figure 64. The twenty samples for each condition have the same statistical attributes (inducing grain size distribution, average grain size, and the same two-point correlation function profile, etc.) and the same constituent volume fractions. Ten samples among the twenty instantiations with 10% Al contents are shown in Figure 65. Samples between different sets have the same attributes of HMX grains. Figure 66 shows the size distribution of HMX grains for each of the five cases in Figure 64. The size distribution profile of HMX from one set resembles that from another set. More details on the statistical similarity between samples in a microstructure set can be found in Sec. 4.2.1 and in Ref. [139].

In the analyses carried out here, the behavior of HMX granules follow a hyper-elastic constitutive model and admits cohesive fracture above its fracture limit. In the loading regime of interest (non-shock low velocity impact), the HMX crystals are often assumed to undergo very little plastic deformation, since HMX is known to be brittle at the ambient pressure [39]. The Estane binder follows a generalized Maxwell viscoelastic model. Details of the constitutive models for the HMX grains and the binder are described in Ref. [87].

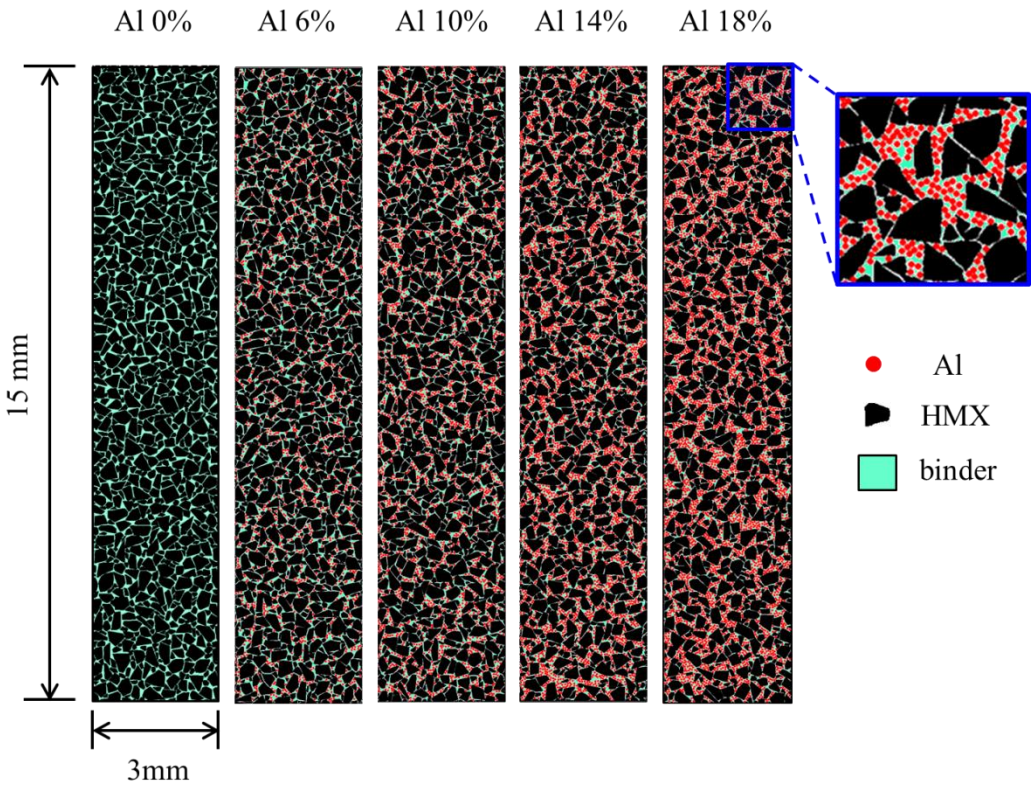

Figure 64. Microstructures with different Al volume fractions (η_{Al} = 0 – 0.18) and HMX volume fractions (η_{HMX} = 0.81 – 0.63). Each image shown represents one sample in a set of twenty statistically similar samples which are random instantiations of the same microstructure condition. Ten of the 20 instantiations for the set with 10% Al are shown in Figure 65.

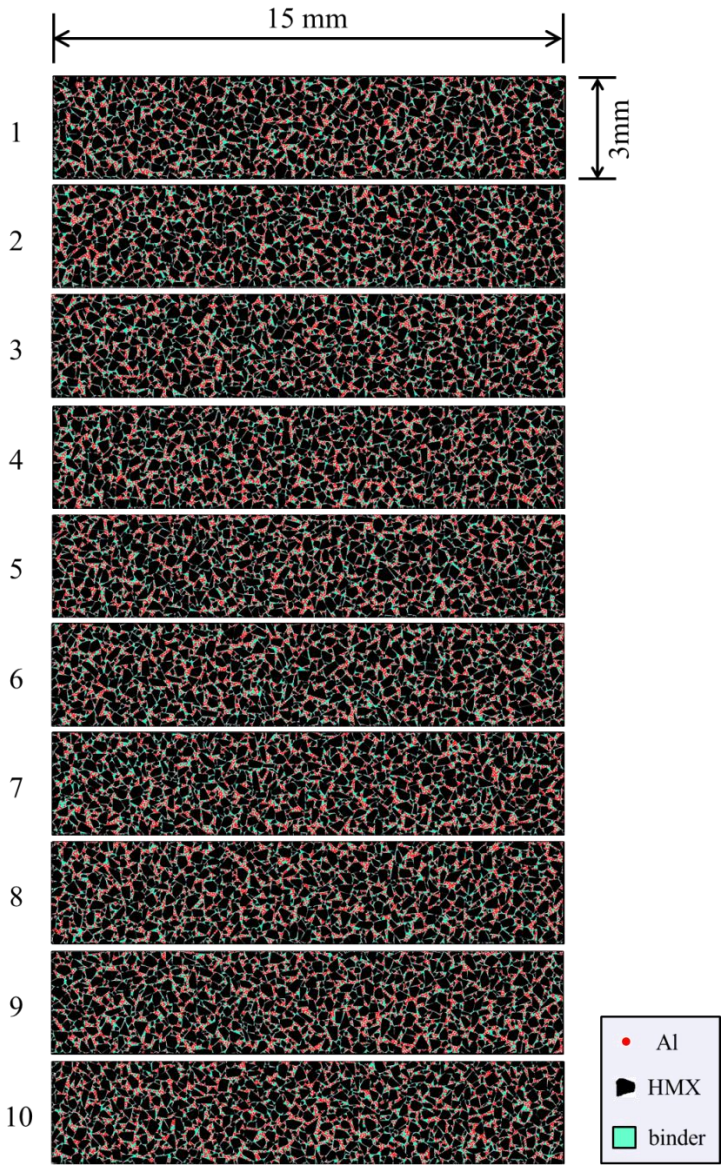

Figure 65. Multiple samples of computationally generated, statistically similar microstructures with a volume fraction of 71% for HMX and 10% for Al

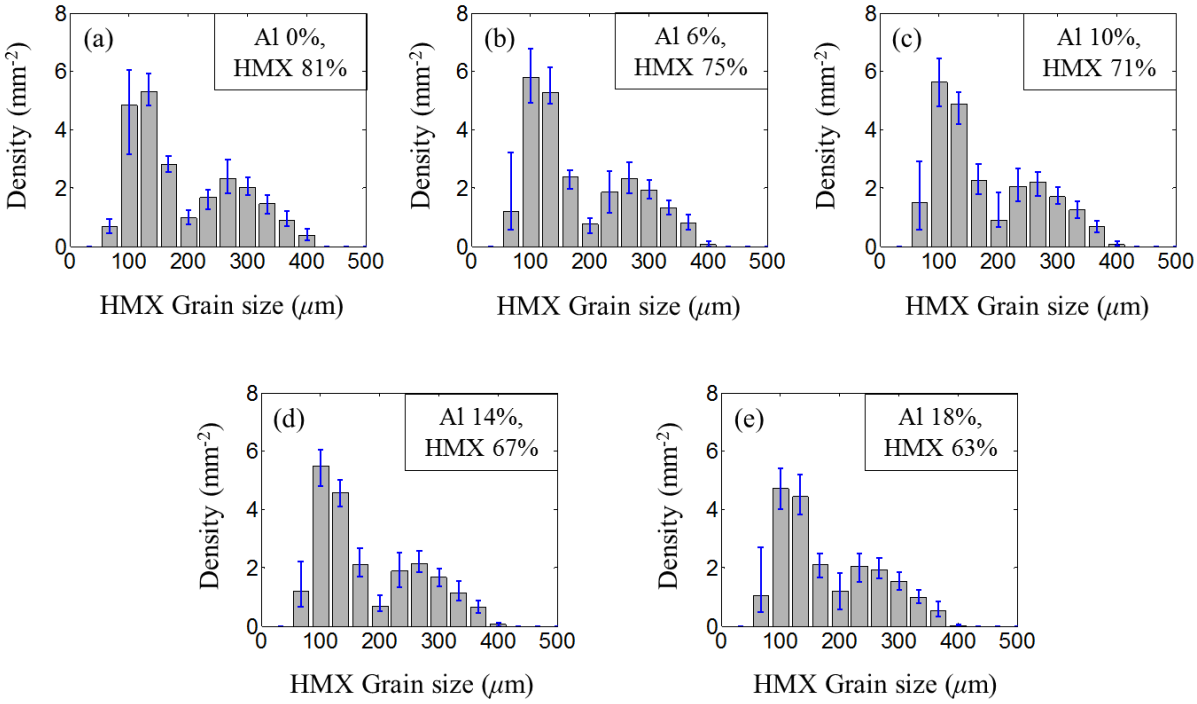

Figure 66. Size distributions of HMX grains for each of the microstructure sets shown in Figure 64. The error bars illustrate the density range among the 20 samples in each set

The behavior of Al follows an elastic-viscoplastic model. The specific form of the constitutive relations used is

$$\hat{\boldsymbol{\tau}} = \mathbf{L} : \left(\mathbf{D} - \mathbf{D}_p \right), \tag{5-1}$$

where **L** is the tensor of elastic moduli. For isotropic elastic response,

$$\mathbf{L} = \frac{E}{1+\nu}\left(\mathbf{I}' + \frac{\nu}{1-2\nu}\mathbf{I} \otimes \mathbf{I} \right). \tag{5-2}$$

Here, **L** is the fourth order identity tensor, E is Young's modulus, ν is Poisson's ratio, α is the thermal expansion coefficient. **D** in Eq. (5-1) is the rate of deformation, which can be decomposed into elastic part and viscoplastic part as

$$\mathbf{D} = \mathbf{D}_e + \mathbf{D}_p, \tag{5-3}$$

where $\mathbf{D}_p$ is the viscoplastic part of $\mathbf{D}$ in the form of

$$\mathbf{D}_p = \frac{3\dot{\bar{\varepsilon}}}{2\bar{\sigma}}\boldsymbol{\tau}', \quad \text{with} \quad \bar{\sigma}^2 = \frac{3}{2}\boldsymbol{\tau}' : \boldsymbol{\tau}'. \tag{5-4}$$

Here, $\bar{\sigma}$ is the Misses equivalent stress, $\boldsymbol{\tau}'$ is the deviatoric part of the Kirchoff stress which is the product of the Jacobian and the Cauchy stress, and $\dot{\bar{\varepsilon}}$ is the equivalent plastic strain rate which has the form of

$$\left.\begin{aligned} \dot{\bar{\varepsilon}} &= \frac{\dot{\bar{\varepsilon}}_1 \dot{\bar{\varepsilon}}_2}{\dot{\bar{\varepsilon}}_1 + \dot{\bar{\varepsilon}}_2}, \\ \dot{\bar{\varepsilon}}_1 &= \dot{\bar{\varepsilon}}_0 \left[\frac{\bar{\sigma}}{g(\bar{\varepsilon}, T)}\right]^n, \\ \dot{\bar{\varepsilon}}_2 &= \dot{\bar{\varepsilon}}_m \exp\left[-a\, g(\bar{\varepsilon}, T)\right], \\ g(\bar{\varepsilon}, T) &= \sigma_0 \left(1 + \frac{\bar{\varepsilon}}{\varepsilon_0}\right)^N \left\{1 - \beta\left[\left(\frac{T}{T_0}\right)^\kappa - 1\right]\right\}. \end{aligned}\right\} \tag{5-5}$$

The above relations consider strain hardening, strain rate dependence of plasticity, and thermal softening. More details of the above constitutive relations and descriptions of the parameters can be found in Ref. [102]. Values of the parameters for Al used here are listed in Table 13. These parameters are chosen to describe the stress-strain behavior 7570 Al alloy [156] over the strain rate range of $1 - 10^6/\mathrm{s}$. Figure 67 shows a comparison of the stress-strain behavior in Ref. [156] and the behavior described by the model utilized in this analysis. Again, just like the microstructure morphologies and other constitutive and interfacial parameters, the parameters for Al used here represent just one specific material data set. More systematic parametric studies can and should be carried out in the future.

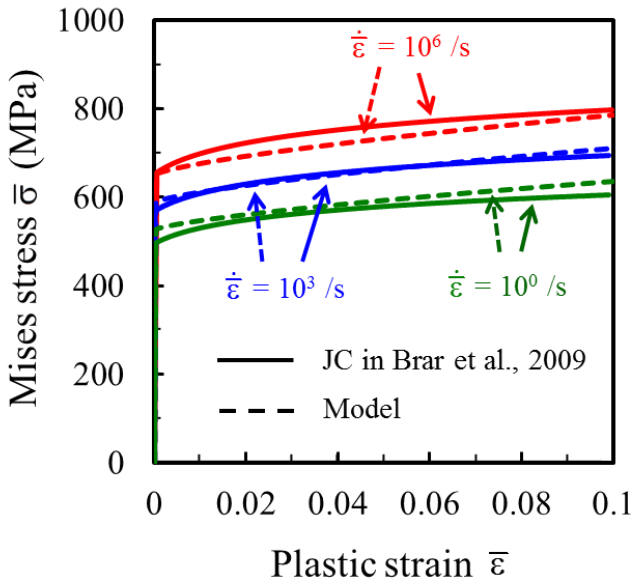

Figure 67. Comparison of viscoplastic stress-strain profiles for Al from the Johnson Cook model in Ref. [156] (indicated in solid line) and the viscoplastic model based on Ref. [102] with parameters in Table 13 (indicated in dotted line).

5.2.2 Loading Configuration

The microstructures are initially stress-free and at rest. The sample size is 15 mm × 3 mm. Impact loading is effected by applying a boundary velocity at the left end of the samples, as shown in Figure 68. A linear velocity ramp is specified over the initial 0.5 μs of loading ($0 \le t \le 0.5$ μs). Specifically, the boundary velocity is linearly increased from zero to the maximum of v = 150 m/s over this period. The top and bottom side boundaries are constrained such that vertical motions do not occur. This configuration approximates the normal impact loading of an infinitely wide material block under the conditions of macroscopically uniaxial strain. For all calculations presented, initial temperature is T = 300 K.

Table 13. Material parameters used for aluminum

Parameters		Values (unit)
Young's modulus E		70 (GPa)
Poisson's ratio v		0.33
density ρ		2.80 (g/cm^3)
Parameters in Eq. (5-5)	n	50.0
	a	5.0
	$\dot{\bar{\varepsilon}}_0$	1.0×10^{-4} (s^{-1})
	$\dot{\bar{\varepsilon}}_m$	8.0×10^{8} (s^{-1})
	σ_0	415 (MPa)
	ε_0	6×10^{-3}
	N	0.07
	β	0.035
	κ	3

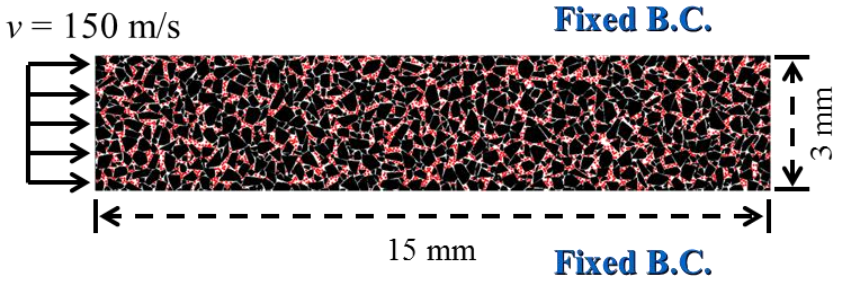

Figure 68. Configuration of loading and boundary conditions considered.

5.2.3 Statistical Model

The analysis is performed in the following steps. First, calculations are carried out using the five sets of microstructure instantiations described in Sec. 2.1, under the loading condition shown in Figure 68. Following the calculations, the ignition criterion described in Sec. 2.4 is used to scan the microstructures for hotspots and detect critical hotspots that have reached the size-temperature threshold. With this approach, once an ensemble (or a set of microstructure instantiations) is analyzed, the distribution of the time to criticality can be uniquely determined for the microstructure set. For each set with a given combination of statistically similar attributes, the time to criticality (t_c) is evaluated as a cumulative probability distribution. The distribution of the time to criticality obtained from each set is fitted to the Weibull distribution with three parameters [127] in the form of

$$P(t) = 1 - e^{-\Phi(t)}, \quad \Phi(t) = \begin{cases} 0, & t \le t_0 \\ \left(\dfrac{t - t_0}{\tau} \right)^m, & t \ge t_0 ; \end{cases} \tag{5-6}$$

where t is the time to criticality, t_0 is the minimum time to criticality, or the cutoff time to criticality below which the probability of ignition is zero, τ is a time-scaling parameter that affects the slope of the distribution curve, and m is a shape parameter.

Barua et al. [108] provided a physical basis for the Weibull distribution interpretation of the probability of time to criticality using Terao's model [128]. They showed that m = 2 for loading conditions involving a propagating stress wave front without reflection from boundaries of a sample (the right-hand boundary for the configuration in Figure 68 and throughout this paper).

5.3 Results and Discussions

A systematic numerical study is carried out, focusing on the effect of the volume fraction of aluminum on ignition. Parameters such as stress, crack length, and frictional dissipation are analyzed. The probability of ignition is obtained via fits to the Weibull distribution for each of the cases studied.

5.3.1 Stress Profiles

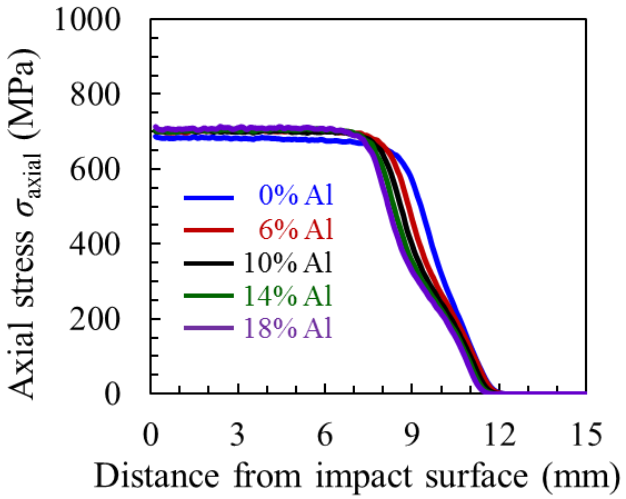

Figure 69. Profiles of axial stress for unaluminized HMX/Estane PBX and aluminized PBX with Al contents between 6 and 18 vol % at t = 4 μs.

Aluminized PBX is known to have higher performance in terms of energy output (up to 25% in terms of power of explosion [153] or up to 30% in terms of work of explosion [157]), depending on measurement. However, the detonation pressure and detonation velocity of aluminized PBX are lower than those of unaluminized PBX [158, 159], since aluminum particles do not react at the detonation front, and instead, generate

a secondary blast at later stages. In contrast to the well-known effects of Al on the performance, there have been few studies on the effect of aluminum on stress in PBXs under non-shock loading. Chakravarthy et al. [140] analyzed the stress profiles in granular explosives and found no significant change in hydrostatic stress or von Mises stress resulting from the addition of aluminum particles in the low velocity regime (v < 200 m/s).

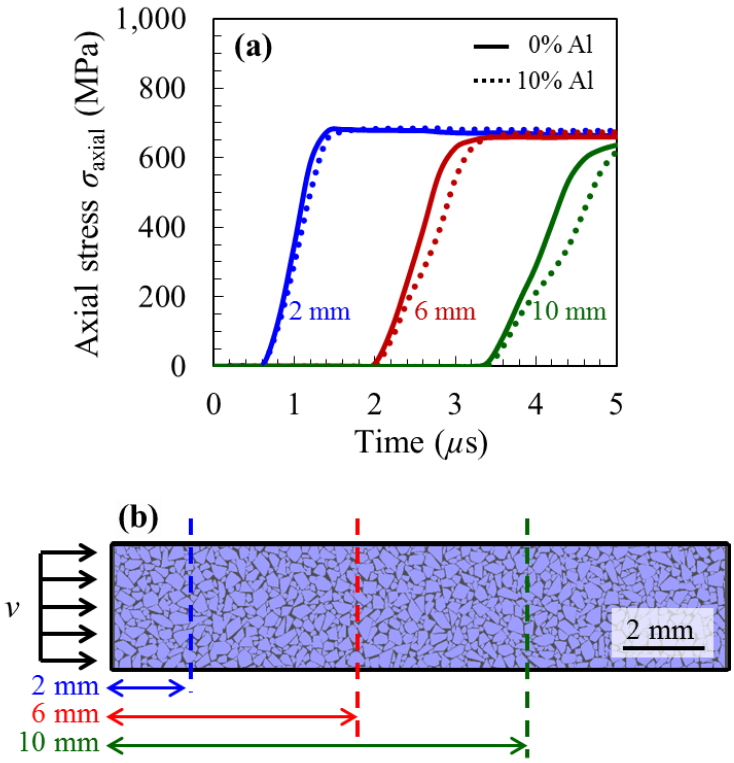

Figure 70. History of axial stress for (a) unaluminized HMX/Estane PBX and (b) aluminized PBX with 10% Al contents for the locations of x = 2, 4, 6 mm

Our results show that there is no significant change in the plateau level of the longitudinal stress as the volume fraction of aluminum is increased from 6% to 18%. Figure 69 shows the spatial profiles of the average longitudinal stress at t = 4 μs. For the aluminized PBX, the stress front shows an elastic precursor, followed by a slower increase

which is indicative of plasticity. This effect of plasticity becomes more pronounced as Al content increases. Specifically, the stress histories for cross-sections at x = 2, 6, 10 mm are plotted in Figure 70 for the cases with 0% and 10% Al. The increasing difference between the stress profiles for the unaluminized PBX and the aluminized PBX indicates that, as the stress wave propagates through the material, longer times are required for the aluminized PBX to reach a steady state of stress. The plasticity of Al and the sliding along Al-binder interfaces caused by the addition of the Al particles lead to an overall weakening of the composite material. This issue will be further analyzed in the future.

5.3.2 Effect of Aluminum on Energy Dissipation

Figure 71 shows a snapshot at t = 4 μs of the energy dissipation per unit volume of material resulting from plastic deformation for microstructures with 6-18% aluminum by volume. As in Figure 69, the profiles show variation along the loading direction, between the wave front and the impact face. Since only aluminum is elastic-viscoplastic and, therefore, has dissipation due to plasticity, higher aluminum content leads to higher levels of plastic dissipation. Note that, for the time shown, plastic dissipation (and therefore plasticity by inference) begins to occur at a distance of approximately 7 mm from the impact face. This location roughly coincides with the peaking of the stress profiles in Figure 69. This synchrony supports the interpretation that the plasticity weakens the composite material and lowers the overall stress.

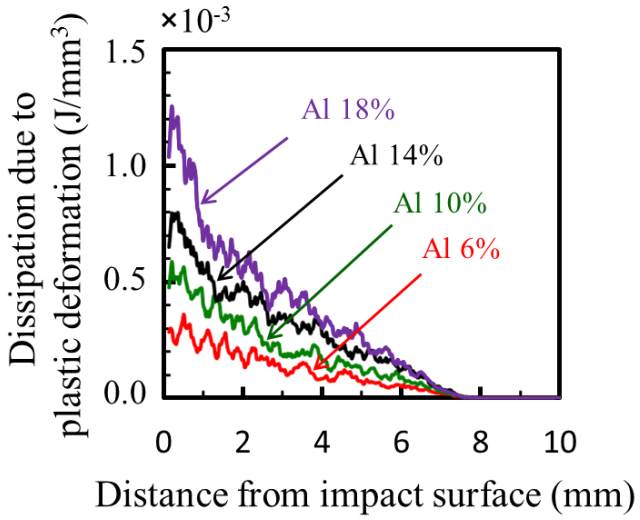

Figure 71. Profiles of density of energy dissipation due to plastic deformation for microstructures with Al contents between 6-18 vol% at t = 4 μs.

Figure 72(a) shows the effect of aluminum on the length density of all cracks (red) and the length density of cracks associated with the HMX grains only (cracks within HMX grains and interfacial cracks between HMX and binder, blue). As more aluminum is added to the materials, less number of HMX particles remain in the microstructure, because aluminum particles replace HMX granules (total solid volume fraction is constant). Therefore, crack density associated with the HMX grains decreases as the volume fraction of aluminum increases. Since the aluminum particles (50 μm in diameter) are smaller than the smaller group of HMX grains (123 μm average diameter), the total sum of surface area of aluminum and HMX granules increases as the aluminum content increases. For this reason, length density of all cracks increases as the volume fraction of aluminum increases.

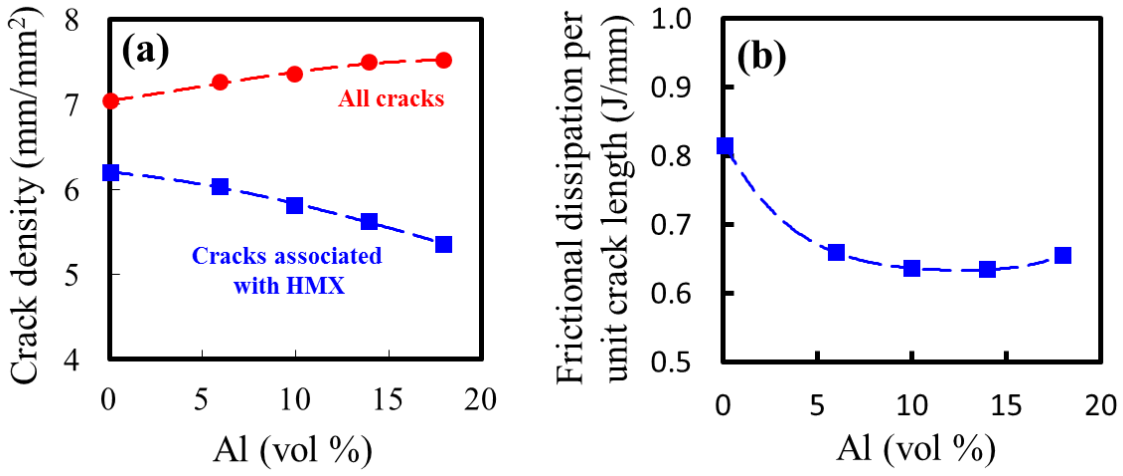

Figure 72. Effect of Al addition on crack densities and frictional dissipation at t = 4 μs; (a) all crack density (red), and density of cracks associated with HMX (blue); (b) frictional dissipation per unit length of cracks associated with the HMX phase

Frictional dissipation in HMX grains is an important mechanism responsible for the development and evolution of hotspots [71, 110], and consequently has a profound impact on hotspot-induced ignition of PBXs. It is important to analyze the frictional dissipation at cracks associated with HMX grains. Figure 72(b) shows the frictional dissipation per unit crack length at cracks associated with the HMX phase. The profile indicates that frictional dissipation at cracks is relatively more intense for the unaluminized HMX/polymer PBX than for the aluminized PBXs. This difference directly affects the hotspot fields in these materials, as discussed below.

5.3.3 Hotspot Quantities and Ignition Probability

In this section, we analyze the hotspot area fraction (fraction of material within hotspots above a certain temperature threshold) and the hotspot number density (number of hotspots per unit volume of material). A threshold of T = 400 K is used as the threshold

temperature for hotspot demarcation. The temperature fields for all microstructures at t = 4 μs after onset of loading are analyzed. At this time, the peak stress reaches a distance of approximately 7 mm from the impact face and fracture initiates in the granules. The fracture leads to frictional dissipation along crack faces. Locations closer to the loading face is subject to longer and more intense loading, as a result, experience more extensive failure, deformation and heating due to deformation and friction. Consequently, more significant heating is observed near the impact surface and ignition is in general a result of hotspots in this region. The hotspot counts reported here concern first 3 mm of the long samples, or more specifically, the top $3 \times 3\ \mathrm{mm}^2$ portion of the samples. Figure 73(a) and Figure 73(b) show hotspot area fraction and the average hotspot number density, respectively. The addition of aluminum particles significantly decreases the hotspot counts, indicating that the aluminized PBXs are less susceptible to creating hotspots that may result in ignition relative to the unaluminized PBX. Note that frictional dissipation per unit crack length [Figure 72(b)] shows a trend that is consistent with that of the hotspot counts [Figure 73]. Also frictional dissipation per unit crack length does not change significantly with the aluminum content over the Al volume fraction range of 10-18%, although a significant difference is seen between that for the unalumnized PBX and that for the aluminized PBXs. A similar trend is seen in the hotspot fields as measured by the hotspot area fraction and hotspot density.

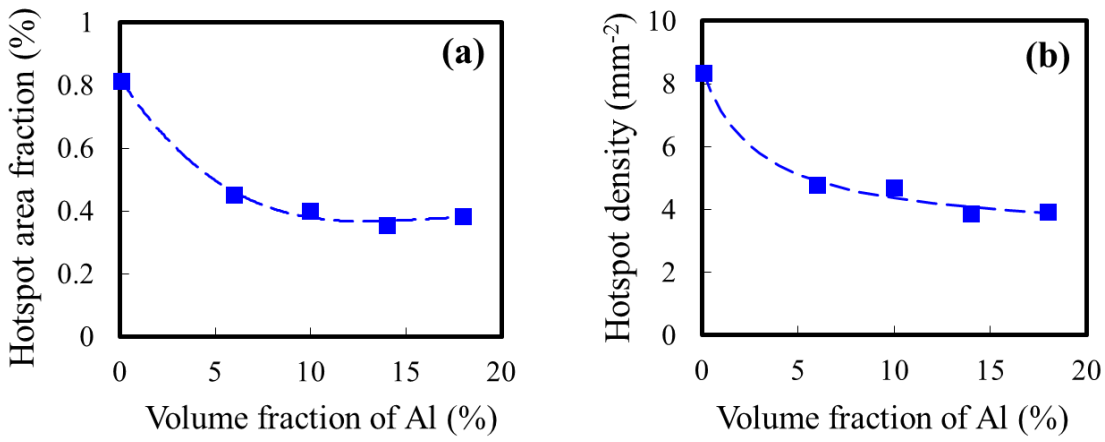

Figure 73. Effect of Al addition on hotspot counts; (a) hotspot area fraction; (b) hotspot number density at *t* = 4 μs.

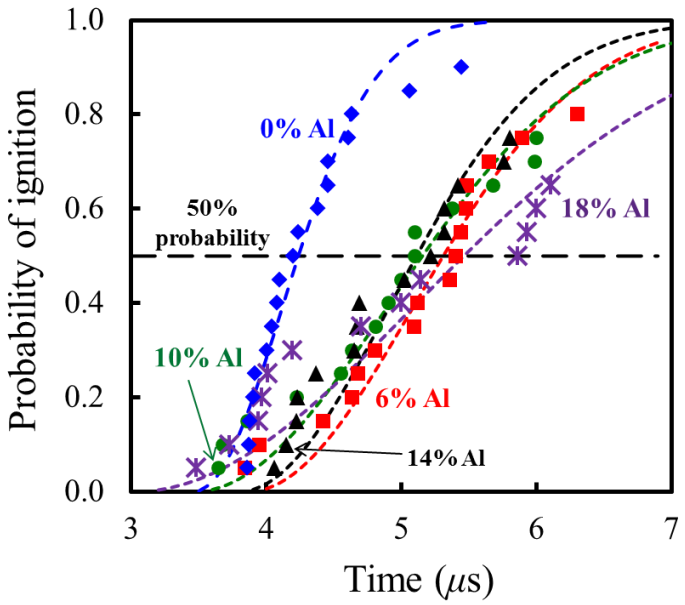

Figure 74. Ignition probabilities for unaluminized PBX and aluminized PBX with 6-18% aluminum by volume.

Table 14. Weibull parameters for data in Figure 74

Al	t_0 (μs)	τ (μs)
0%	3.46	0.93
6%	3.88	1.7
10%	3.40	2.13
14%	3.79	1.58
18%	2.92	3.1

The ignition probability shown in Figure 74 is obtained from the five microstructure sets, each of which having twenty samples. The Weibull parameters of each volume fraction of aluminum are listed in Table 14. The PBX without aluminum has relatively earlier ignition times than the aluminized PBXs. This may be interpreted to mean that adding aluminum in PBX makes the material less sensitive in terms of ignition time. In particular, adding Al causes the probability curves to flatten out to the right (longer times), such that the value of mean time to ignition (t_{50}) or the time by which 50% of the samples have reached criticality is higher for higher Al content. This finding is consistent with the experimental results by Prakash et al. [148] and Radwan [149] as they observed that the insensitivity (required height of impactor for explosion) of HMX based and RDX based PBX increases as Al content increases. However, the ignition probabilities of aluminized PBXs (η_{Al} = 6-18%) in Figure 74 lie close to each other and do not show a clear trend of change with Al volume fraction under the conditions analyzed here. Also, a few samples of the aluminized PBXs reach criticality earlier than the unaluminized PBX, indicating that aluminization may cause the “worst-case” ignition scenarios to become even “worse”. Although the specific reason is unclear at this time, one possible explanation is that the morphological rearrangement of HMX caused by the addition of Al may lead to closer contact of HMX grains in some samples, thereby, accelerating the

development of hotspot in certain cases. More detailed analyses are needed to ascertain the reason and the trend over a wider range of Al content.

5.4 Conclusion

The ignition behavior of PBX microstructures with 6-18% Al by volume is analyzed and compared to that of the corresponding unaluminized PBX. The mean time to ignition (t_{50}) for the aluminized PBXs delays by 1 – 1.7 μs (24 – 60% delay) as compared to that for the corresponding unaluminized PBX. To delineate the mechanisms responsible for the ignition delay, the differences in overall internal stress, dissipations due to fracture and inelasticity, and hotspot field characteristics are quantified. It is found that, for the material configuration studied, aluminization decreases the crack density and frictional energy dissipation in the HMX phase. Aluminization also causes the frictional dissipation per unit crack length to decrease. The lower dissipation may be partly due to the lower overall stress levels in the aluminized materials which results from the relatively weak and somewhat compliant binder-Al interfaces considered here. Overall, the analyses present a preliminary study of the effect of aluminization of PBX for a particular material configuration. Specifically, the analyses consider only one level of interfacial bonding between the binder and the Al particles. Also, only one Al particle size is considered. The fact that the stress front in the aluminized PBX is delayed relative to that in the unaluminzed PBX suggests that plastic deformation and interfacial failure are extensive and significantly influence the behavior of the composites. It remains to be seen how the ignition behavior may change as other material configurations (with significantly different binder-Al interfacial bonding and Al particle sizes) are considered. This will be a topic for further studies.

CHAPTER 6: COMPUTATIONAL PREDICTION OF PROBABILISTIC IGNITION THRESHOLD OF PRESSED GRANULAR HMX UNDER SHOCK LOADING

This chapter is based on the work in collaboration with Christopher Miller and Air Force Research Lab. Specifically, experiments on pressed HMX are performed by Drs. Christopher Molek and Eric Welle in AFRL/RWME at the Eglin AFB, and the risk factor (R) in Chapter 6.3.4 is analyzed by Christopher Miller.

6.1 Introduction

The modeling of shock ignition at the mesoscale level is typically carried out as a part of modeling shock-to-detonation transition (SDT). There are two approaches, depending on whether hotspots are explicitly treated or not. In the literature, the phrase "shock initiation" is often used to emphasize the transition to detonation [160] The first approach involves treating hotspots explicitly based on a chosen mechanism of energy localization [40] (e.g., predominantly plastic pore collapse). The second approach does not involve treating hotspots explicitly, instead ignition is treated via a numerical switch to a burn model (rate law) in large-scale engineering calculations [9]. Both approaches have two basic features. The first is an assumption on the internal energy function (equation of state). The most common is a mass-weighted sum of constituent internal energies which contains the fraction of reacted explosive mass (called progress variable) and heat release from chemical reaction. The second is the rate law that controls the evolution of "burn" via the progress variable. This second approach does not describe the mechanisms of ignition or hotspot evolution. However, it is known that these burn models can be calibrated to match 50% threshold sensitivity of high explosives [161].

The CFEM capability used in this study does not treat the SDT transition and focuses instead on hotspot evolution and the criticality condition for thermal runaway. Studies emphasizing the SDT transition and studies focusing on the processes leading up to and the attainment of thermal runaway (which ultimately lead to the SDT transition) are parallel and mutually reinforcing. Thermal runaway studies allow ignition thresholds to be established (focus of this paper) and can provide input for SDT analyses. In our study, the CFEM framework tracks arbitrary fracture and post-fracture contact and friction explicitly and captures hotspots generated by various dissipation mechanisms including friction, viscoelasticity, viscoplasticity, and heat conduction. The criticality condition for thermal explosion is identified as the ignition thresholds (boundaries between go and no-go). The justification for this assumption is based on the careful analysis of in-material gauge records of HMX and TATB based explosives by James and Lambourn [162]. They showed that the reaction (behind the shock wave front) is a function of shock strength and time along the particle path, and is independent of local flow variables behind the shock such as pressure and temperature. In other words, "the growth in the pressure or temperature fields does not feed back to the reaction rate". This observation is fundamental to the present study because it implies that the criticality of hotspots in the sense of thermal explosion [163] directly correlates to the initiation of detonation. It also implies that the collective behavior of hotspots may influence the time to detonation, but may not affect the minimum shock threshold condition for initiating detonation, at least to first order. However, the role of distributed hotspots on the go-no-go criticality is not yet well understood [164]. Based on the observations above, we assume that there is a one-to-one correlation between the existence of critical hotspots which lead to local thermal runaway and the occurrence of eventual detonation. In this paper, we do not consider the issue of subsequent burn after initiation and the time needed to reach

detonation. Although these are important issues by themselves, they are topics for separate studies.

The remaining sections consists of three parts. The first part describes the computational framework used to study shock ignition and includes discussion on microstructure representation, loading configuration, and constitutive relations. The second part discusses simulation results with focus on shock ignition thresholds in terms of the modified James function and a probabilistic quantification of the thresholds. The third part focuses on the major findings, which include predicted James type ignition thresholds for pressed HMX powders, the effect of particle size on the James ignition thresholds, comparison with experimental measurements, and the probability distribution of the thresholds as a function of the James number (J) as introduced by Gresshoff and Hrousis [161].

6.2 Framework and Analysis

6.2.1 Material

The materials are pressed granular HMX (Octahydro-1,3,5,7-tetranitro-1,3,5,7-tetrazocine) with microstructures consisting of HMX grains without binder. In the experiments, materials with different grain sizes are referred to as different "classes". Of particular interest are Class 3, which has an average grain size of d_{avg} = 358 μm, and Class 5, which has an average grain size of d_{avg} = 6.7 μm initially. These HMX grains are then pressed, causing the grain sizes to become somewhat smaller than their original sizes (see Fig. 4 in Ref. [165]) due to fracture. Both classes have a density that is 94% the theoretical maximum density (TMD). Figure 75 shows scanning electron microscope (SEM) images of the microstructures of these two classes of HMX. A small number of abnormally large

grains (referred to as “boulders”) are present in the Class 5 material. Samples prepared for shocked experiments are cylindrical pellets with a diameter of 0.5 inches and a height of 0.5 inches.

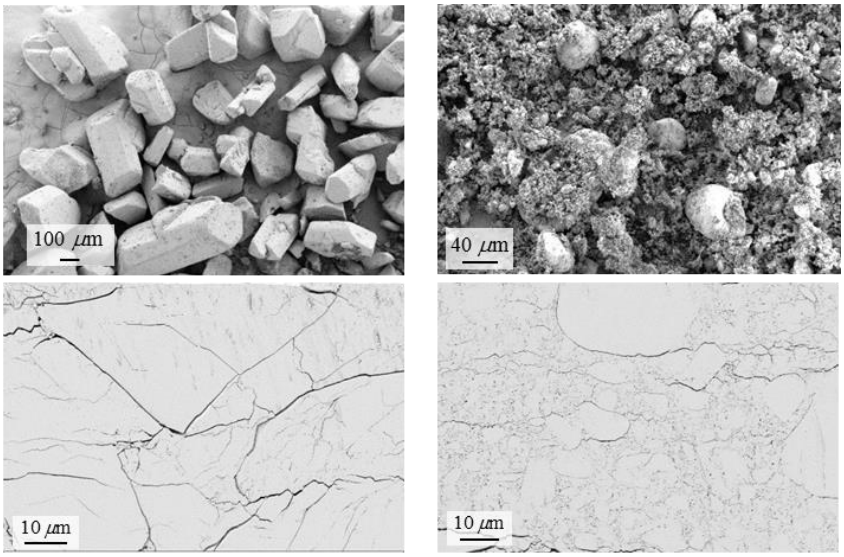

Figure 75. SEM images of materials used in experiments, (a) Class 3 HMX and (b) Class 5 HMX. Images in the upper row show HMX crystals and images in the lower row show the microstructures made out of the corresponding HMX Classes after pressing. The images are provided courtesy of R. R. Wixom at Sandia National Laboratories.

The materials and the experimental procedure of Welle et al. [27] serve as a basis and starting point for the computational analysis. In the experiments, multiple samples for each material class and load condition are tested to quantify the ignition threshold distribution. Similarly, for systematic computational quantification of the probabilistic ignition behavior, statistically similar sample sets with multiple (5) samples are computationally generated and tested under identical loading conditions. The computationally generated microstructures mimic the attributes of the experimental

microstructures. The generation uses 2D Voronoi tessellation [108]. The computationally generated samples are designed to achieve two objectives: (1) maintain statistical consistency among samples for each material setting (e.g., consistency in grain size distributions, grain volume fraction, and grain shapes for a given average grain size) and (2) focus on trends in key microstructure attribute (grain size) among the different classes of materials. To this end, each sample set follows a mono-modal grain size distribution with a specific average grain size that lies between the average grain sizes of Class 3 and Class 5. This approach allows primary trends in material behavior-microstructure relations to be identified and quantified while a significant degree of similitude is maintained between the experiments and simulations for relative comparison. The differences between the experimental samples and computationally generated samples are as follows. The experimental samples have a relatively density that is 94% of the TMD and, more importantly, the voids are too small to be resolved explicitly via finite element meshing at the overall size scale of samples analyzed. Therefore, a phenomenological approach for accounting for the effects of voids is taken in the simulations. Specifically, the effects of the voids are considered through variations in the bulk properties of the grains based on the fact that small-scale voids weaken the stiffness and strength of materials. Details of the weakening effect due to voids and the method of implementation are provided later in this section. The second simplification is that the large "boulders" in the Class 5 experimental samples are not considered in the computationally generated microstructures, as their percentage is small (<10%) and accounting for such large grains would require much larger representative volumes which are computationally prohibitive for the large number of statistical calculations pursued here. Although the computationally generated microstructures are not "exact" representations or reproductions of the experimental samples, major attributes are captured, allowing trends in the effects of grain size on ignition behavior to be delineated. It is worth pointing out that what is pursued here is not

meant to be and cannot be the "final" word on the effects of microstructure on ignition of the materials. Rather, it is meant to be a first step in the computational prediction of ignition thresholds to be followed by future analyses on how voids and bimodal distributions of grain sizes affect the ignition behavior of heterogeneous energetic materials. Those calculations will involve explicit resolution of small-scale defects and clustering of grain sizes.

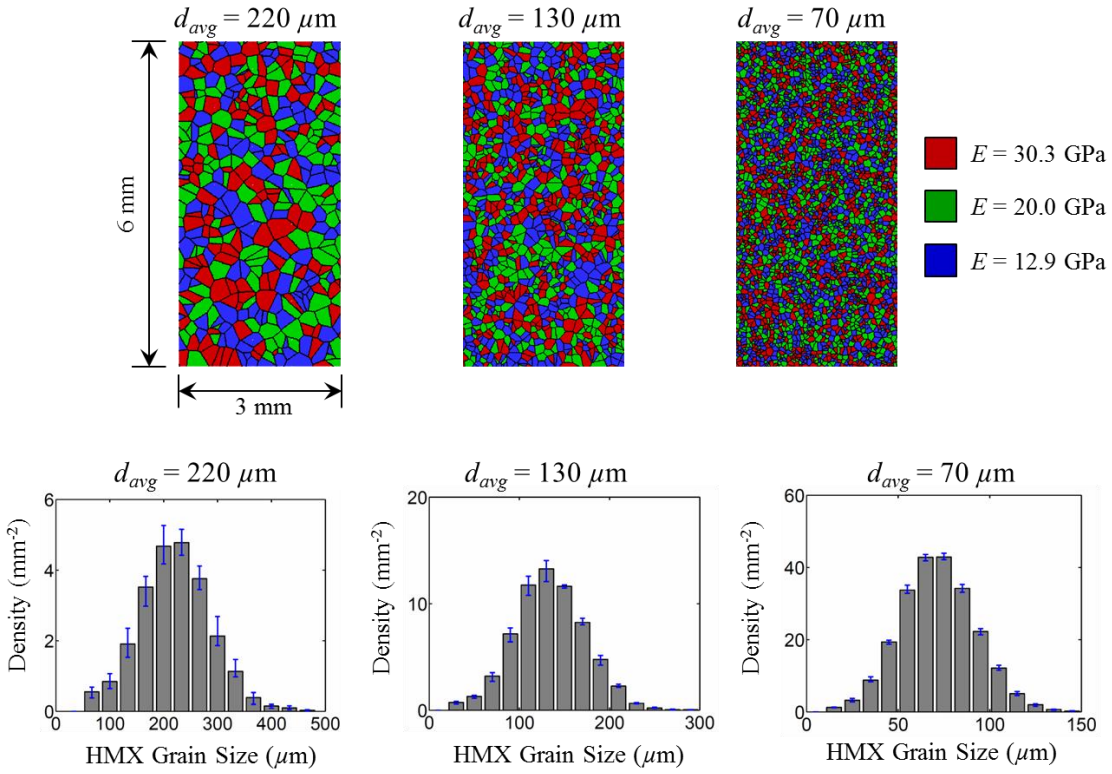

Figure 76. Computationally generated microstructures and the size distributions of HMX grains in the microstructures for d_{avg} = 70, 130, and 220 µm. Each microstructure image shown represents one sample in a set of five statistically similar samples which are random instantiations of the same microstructure conditions.

The grains generated by the Voronoi tessellation have random, multifaceted surfaces interlocking with each other. Wu et al. [44] showed that simulations of Brazilian compression of PBX using microstructures generated with this approach match experiments reasonably well. In our analysis, since frictional dissipation along crack faces under compression is an important mechanism for hotspot generation, the Voronoi tessellation method for generating microstructures is preferred to ensure well-defined intergranular interfaces. This method also allows for the generation of large numbers of microstructures with random variations in morphology and a high-degree of statistical similitude in microstructure attributes, such as grain shape and grain size distributions.

The average grain size of the experimental samples for Class 3 (d_{avg} = 358 μm) is around 50 times larger than the average grain size of Class 5 (d_{avg} = 6.7 μm). Since larger grains require a proportionally larger sample size or representative volume element (RVE), to resolve the large Class 3 grain size with the same fine mesh resolution as required for the small Class 5 grain size, computational models with an extremely large number of degrees of freedom (DoF) would be needed. To keep the overall DoF at a reasonable level for the large number of statistical runs, we take a parametric approach, focusing on the trend in the size effect rather than the absolute sizes. Specifically, we consider the average grain sizes range of d_{avg} = 70 – 220 μm, which lie between the sizes of the Class 3 and Class 5 HMX. The resulting microstructural domain of each sample is $3 \times 6\ \text{mm}^2$. Although the computationally generated samples have much smaller domain size than the size of experimental samples, the size of 3 mm of the computational samples is at least one order of magnitude larger than the length scale of the largest average grain size (d_{avg} = 220 μm) considered, giving sufficient volumetric representation of the microstructures. Liu [166] reported the minimum size of the RVE to be 1.5 mm for a sample with an average grain size of 125 μm. His finding supports our choice of sample size here for the

range of grain sizes considered. In addition, as it will be clarified in Sec. 3.1., the height of 6 mm is long enough so that the stress attenuates significantly when it reaches to the bottom of the domain, such that the ignition is determine by material events near the impact face and materials and boundaries far away from the impact face have no influence on the ignition outcome under the conditions considered here.

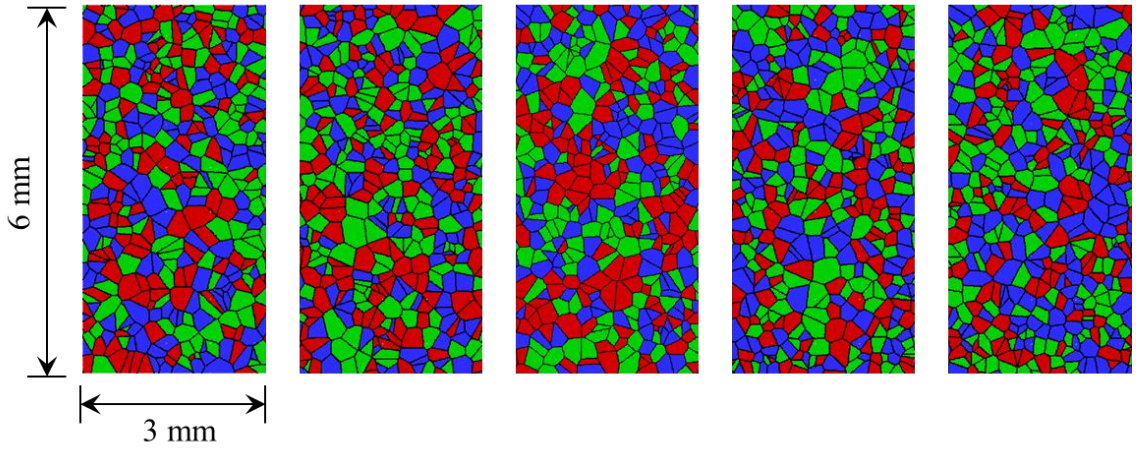

Figure 77. Multiple samples of computationally generated, statistically similar microstructures with the average grain size of d_{avg} = 220 μm

Three sets of microstructures are generated with average grain sizes of d_{avg} = 70, 130, and 220 μm, respectively. Each set consists of five samples which have statistically the same attributes in terms of grain size distribution and specific grain boundary surface area. In total, 15 samples (3 sizes x 5 samples for each size) are generated and used. The microstructure sets and corresponding grain size distributions are shown in Figure 76. To illustrate the random variations in microstructure morphology within a particular microstructure set, Figure 77 shows the five samples having the same average grain size of d_{avg} = 220 μm.

The microstructures of samples in the experiments have inherently heterogeneous characteristics, including micro and nano scale voids [167], microcracks, variations in material properties of the HMX grains, and directionality of constituent behavior due to crystalline anisotropy. These heterogeneities are phenomenologically accounted for in a unified manner via random variations in the elastic modulus of the grains. Researchers have analyzed the variations of the elastic moduli due to various factors including defects through experiments and computation. Yang et al. [168] performed an MD simulation of a copper plate with a void and found that the elastic modulus decreases as the volume fraction of the void increases. Hudson et al. [169, 170] quantified the voids in RDX crystals and assigned a defect score to each grain. By using nano-indentation, they measured the elastic modulus and found grains with more defects (high defect scores) have a lower elastic modulus. These findings provide justification and serve as a guide for the use of varying elastic modulus values of HMX to phenomenologically account for heterogeneities in the microstructures we analyze.

Three levels of elastic modulus (E = 30.3, 20.0, and 12.9 GPa) are randomly assigned to the HMX grains. These levels are determined based on a study of the anisotropy of the elastic behavior of HMX and data in the literature on how voids affect elastic moduli. Specifically, the maximum and minimum values of the Young's modulus of HMX are determined from the stiffness tensor provided by Sewell at al. [171] The intermediate value is taken to be the Voigt-Ruess-Hill (VRH) average of the stiffness tensor. A similar case has been studied by Dimas et al. [172]. The microstructure they studied has a Young's modulus that varies randomly spatially. The random variations in their study follow a lognormal distribution, with the mean value representing the effective modulus of the simplified homogeneous material. Similarly, in our study, the effective modulus corresponds to the VRH average (E = 20.0 GPa) of the stiffness tensor. To

determine the maximum and the minimum values of the bulk modulus of HMX, the same ratio as used in the change of Young's modulus is used to increase or decrease from the average bulk modulus. The grains with the high level of Young's modulus (E = 30.3 GPa) are assumed to lie in orientations that have the highest stiffness. The high level of bulk modulus of these grains represents ideal crystals without voids or defects. The grains with the low level of Young's modulus (E = 12.9 GPa) are assumed to lie in an orientation that have a lower stiffness. The low level of bulk modulus of these grains represents the crystals with significant amounts of voids or defects. A parametric study is carried out with further variations from these values. It is found that the changes do not have a significant influence on the ignition behavior of the materials. Part of the reason lies in the fact that heating is primarily an outcome of fracture and inelasticity. We suspect that the effect of modulus inhomogeneity is indirect, through perturbing the fields and inducing fracture and inelastic deformation.

The HMX grains of the samples in the experiments are simply pressed mechanically, leading to very weak or no bonding along the grain boundaries. In the simulations, the bonding strength along the grain boundaries is assumed to be zero.

6.2.2 Loading Configuration

The shock experiments carried out use an Electric Gun to launch thin flyers, generating a planar shockwave in the HMX samples [27]. Each sample is placed in a steel cup that only allows one face to be exposed to receive the flyer impact. The samples are subjected to shock loading with various combinations of pulse intensities and durations (as determined by the velocity and thickness of the flyer, respective). Four different flyer thicknesses ranging from 23 μm to 183 μm are used. For each flyer thickness

(corresponding to a specific pulse duration), different shots with different flyer velocities are conducted on the same material. The ignition response of a sample is recorded as "go" if the sample ignites and as "no go" if the sample does not ignite. The results of the experiments are plotted in Figure 78(a-b).

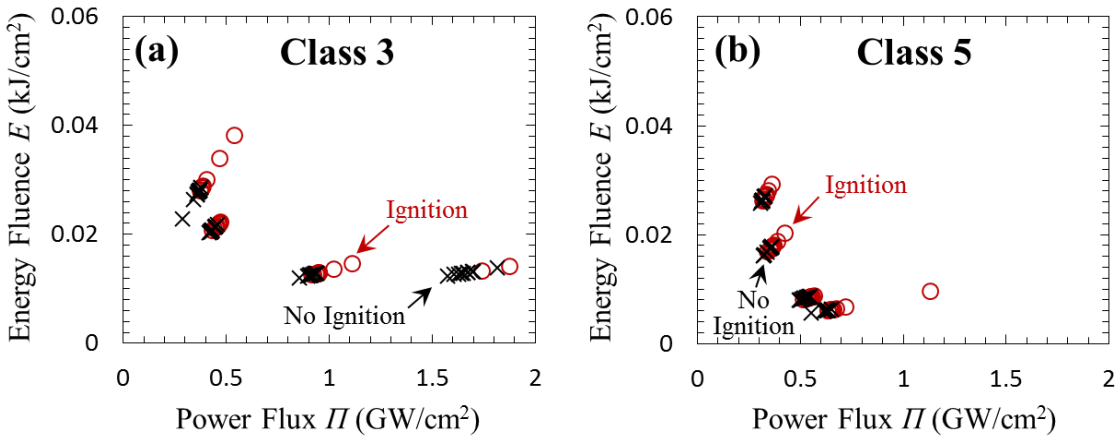

Figure 78. Ignition threshold determination from experiments using multiple samples of a material with different flyer velocities at each flyer thickness (or pulse duration), (a) Class 3 and (b) Class 5

Table 15. Material properties of flyer and specimen and conditions of experiments

	Parameters	Flyer 1	Flyer 2	Specimen
Material properties		Parylene-C [173]	Kapton [173]	HMX
	Longitudinal wave Speed c (m/s)	2,228	2,741	3,750
	Density ρ (kg/m^3)	1,286	1.414	1,910
Experimental condition	Flyer velocity v_{fly}	2 – 4.2 km/s	1.5 – 2 km/s	Stationary
	Thickness H	23 – 37 μm	111 – 183 μm	12.7 mm

The simulations emulate the experiments directly. The computationally generated specimens are initially stress-free and at rest. Impact loading is effected by applying a prescribed boundary velocity at the impact face (top boundary of the sample), as shown

in Figure 79(a). The left and right boundaries are constrained such that lateral expansion does not occur. This confinement mimics the effect of the steel cup holding the experimental sample. This is a 2D model and the conditions of plane-strain prevail. This configuration approximates the shock pulse loading of a sample driven by a thin flyer under conditions of approximate macroscopic uniaxial strain. The pulse intensity and duration are chosen to correspond to the loading characteristics in the experiments. The experiment conditions and relevant parameters are given in Table 15. The imposed velocity at the top boundary (U_p) of the sample is determined by the ratio between the longitudinal wave impedances (ρc) of the flyer and the HMX sample as

$$U_p = \frac{\rho_{fly} c_{fly}}{\rho_{fly} c_{fly} + \rho_{HMX} c_{HMX}} V_{fly}, \tag{6-1}$$

where ρ_{fly} is density of the flyer, c_{fly} is wave speed in the flyer, ρ_{HMX} is density of HMX, c_{HMX} is wave speed of HMX, and V_{fly} is the launching velocity of the flyer. The range of loading analyzed in the experiment corresponds to the imposed particle velocity range of $U_p = 500 - 1200$ m/s (approximate flyer velocity range of 1.5 - 4 km/s) and the range of pulse duration of τ = 20 – 130 ns. The specific particle velocity levels considered in the computational analysis are U_p = 500, 700, 900, and 1200 m/s and the range of pulse duration analyzed is τ = 10 – 280 ns. The pulse duration increment between successive durations depends on load intensity and varies between $\Delta\tau$ = 1 – 12 ns, as listed in Table 16. The pulse duration is the time it takes the longitudinal wave to traverse a round trip in the flyer. For each velocity and sample, 10 different pulse durations are considered, yielding 600 microstructure-loading combinations (4 velocities × 10 pulse durations × 3 grain sizes × 5 microstructures). The profile of the imposed shock pulse at the boundary is shown in Figure 79(b). The velocity rapidly increases from zero to the particle velocity of U_p during the ramp time of t_{ramp} = 10 ns. This velocity is kept constant until the pulse

time τ is reached. After the pulse time ($t \geq \tau$), the top boundary is released and no external loading is applied, while the boundaries on the left, right, and the bottom remain constrained in their normal directions. The computational prediction of the "go" and "no go" threshold in this paper follows the same procedure as used in experiments of Figure 78(a-b). As an example of the results, the "go" and "no go" thresholds from each microstructure of grain sizes of 70 – 220 μm are plotted in Figure 80(a-c). The symbols represent either "go" or "no-go" for each combination of flyer velocity and pulse duration. The data points are along vertical lines in Figure 80 because the simulations are performed for different pulse durations at each flyer velocity which determines the energy flux. On the other hand, experiments are performed at different flyer velocities for each flyer thickness which determines pulse duration, resulting in the data points to line up along diagonal lines in the energy fluence-power flux space. This slight difference in how the computational and experimental data points populate the domain of analysis does not affect comparison of the two data sets in any way. A total of five microstructures for each grain size are used for the computational analysis, and Figure 80(a-c) show the results from only one microstructure of each grain size. Details of the computational approach and models are given in the next two sections.

Table 16. Load conditions and load increments analyzed

U_p (m/s)	500	700	900	1200
PU_p (GW/cm^2)	0.173	0.366	0.65	1.273
Range of E (kJ/cm^2)	0.0169 - 0.0507	0.0132 - 0.0416	0.0094 - 0.042	0.0045 - 0.0429
Range of pulse duration τ (ns)	100 - 280	40 - 112	20 - 65	10 - 34
minimum τ interval (ns)	12	6	3	1

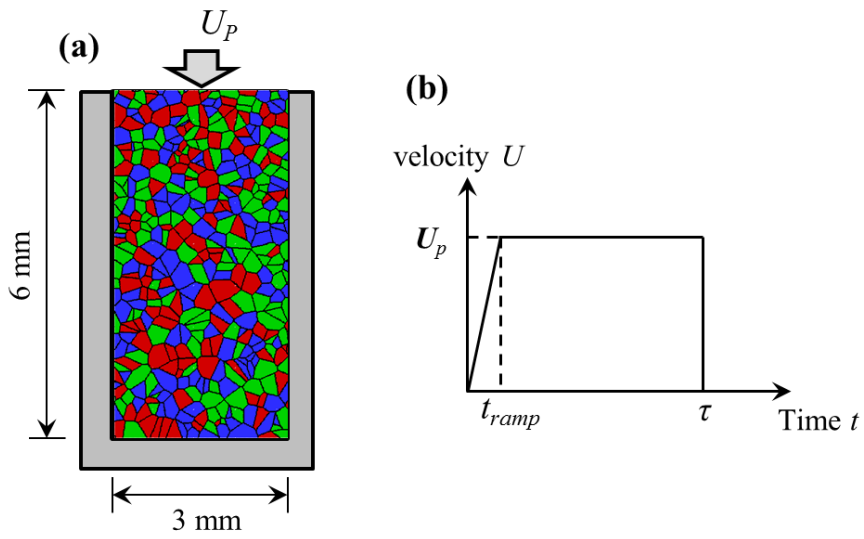

Figure 79. (a) Configuration of computational model of shock experiments, loading, and boundary conditions considered, and (b) load history imposed on the top boundary of the domain.

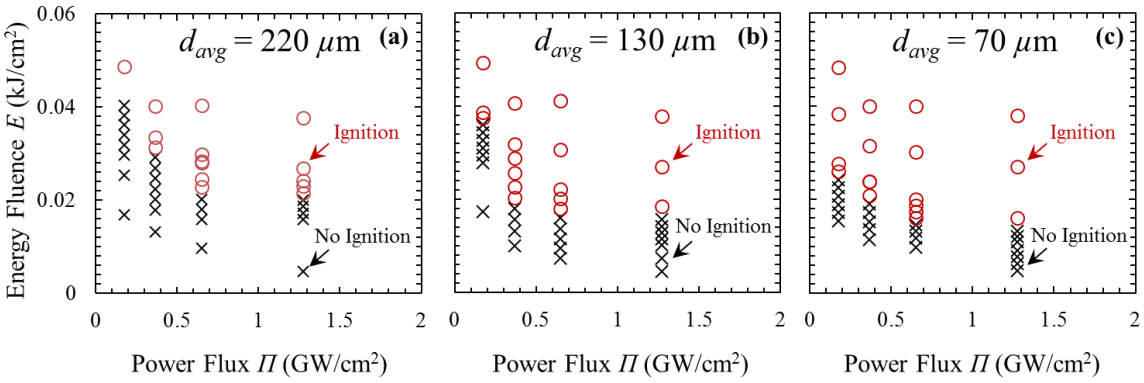

Figure 80. Ignition threshold determination from computation using one microstructure of each grain size, (a) d_{avg} = 220 μm, (b) d_{avg} = 130 μm, and (c) d_{avg} = 70 μm. Multiple pulse durations are used for each load intensity.

6.2.3 Constitutive Relations

The simulations are performed using a recently developed Lagrangian cohesive finite element framework [87, 107, 108, 110]. This framework allows quantification of the effects of microstructure and thermal-mechanical processes, including bulk deformation, interfacial debonding, fracture of grains, and subsequent frictional heating. The constitutive relations for the grains are those of a hydrostatic stress-dependent elasto-viscoplastic material. Specifically, the deviatoric part of the stress tensor carried by the material follows an elasto-viscoplastic constitutive law and the hydrostatic part of the stress tensor carried by the material follows the Birch-Murnaghan equation of state (B-M EOS). The term "pressure" and the variable "*P*" refer to the hydrostatic part of the stress in the following discussion. Additionally, an artificial viscosity model for numerical stability is used in association with the EOS. A bi-linear traction-separation model is used for cohesive elements to account for fracture in grains and along grain boundaries. A contact detection algorithm and a subsequent contact force model are used for surfaces after fracture. The Coulomb friction damping model is used for surface elements that are in contact. Fourier's heat conduction model is coupled with the mechanical deformation and failure models to account for thermal conduction in the material. Details of the algorithm and models are provided in Chapter 2 of this thesis. A brief outline of the constitutive and interfacial relations and the verification are given below.

The deviatoric part of the rate of deformation $\mathbf{D}'$ can be decomposed into an elastic part and a viscoplastic part as

$$\mathbf{D}' = \mathbf{D}'_e + \mathbf{D}'_p , \tag{6-2}$$

where $\mathbf{D}'_p$ is the viscoplastic part of $\mathbf{D}'$ in the form of

$$\mathbf{D}'_p = \frac{3\dot{\bar{\varepsilon}}}{2\bar{\sigma}}\boldsymbol{\tau}', \text{ with } \bar{\sigma}^2 = \frac{3}{2}\boldsymbol{\tau}' : \boldsymbol{\tau}'. \tag{6-3}$$

Here, $\bar{\sigma}$ is the Misses equivalent stress, $\boldsymbol{\tau}'$ is the deviatoric part of the Kirchoff stress, and $\dot{\bar{\varepsilon}}$ is the equivalent plastic strain rate which has the form of

$$\left.\begin{aligned} \dot{\bar{\varepsilon}} &= \frac{\dot{\bar{\varepsilon}}_1 \dot{\bar{\varepsilon}}_2}{\dot{\bar{\varepsilon}}_1 + \dot{\bar{\varepsilon}}_2}, \\ \dot{\bar{\varepsilon}}_1 &= \dot{\bar{\varepsilon}}_0 \left[\frac{\bar{\sigma}}{\mathrm{g}(\bar{\varepsilon}, T)}\right]^m, \\ \dot{\bar{\varepsilon}}_2 &= \dot{\bar{\varepsilon}}_{\mathrm{m}} \exp\left[-a\,\mathrm{g}(\bar{\varepsilon}, T)\right], \\ \mathrm{g}(\bar{\varepsilon}, T) &= \sigma_0 \left(1 + \frac{\bar{\varepsilon}}{\varepsilon_0}\right)^N \left\{1 - \beta\left[\left(\frac{T}{T_0}\right)^\kappa - 1\right]\right\}, \end{aligned}\right\} \tag{6-4}$$

where $\bar{\varepsilon} = \int_0^t \dot{\bar{\varepsilon}}\, dt$ is the equivalent plastic strain, $\dot{\bar{\varepsilon}}_0$ and $\dot{\bar{\varepsilon}}_m$ are reference strain rates, m and a are rate sensitivity parameters for a low strain rate and a high strain rate, respectively, σ_0 is the quasi-static yield stress, ε_0 is a reference strain, N is the strain hardening exponent, T_0 is a reference temperature, and β and κ are thermal softening parameters. The function $\mathrm{g}(\bar{\varepsilon}, T)$ represents the quasi-static stress-strain response at ambient temperature. The above relations consider strain hardening and strain-rate dependence of plasticity. The details of the above constitutive relations and descriptions of the parameters can be found in Ref. [102]. The values of the parameters for HMX used in this study are listed in Table 2. The parameters are calibrated to match the experimental wave profile obtained by Dick et al. [103]. The verification of the calibrated parameters is described in Ref. [174].

The volumetric part of the response is described by the Birch-Murnaghan equation of state (B-M EOS). The specific form of the equation is provided in Chapter 2. Previous

studies [100, 175, 176] show discrepancies in the parameters of B-M EOS for HMX. Landerville et al. [100] reported that the parameters vary to a large degree among experiments due to inherent noise of experiments and inconsistencies in fitting ranges and schemes. The parameter values used in this study are $K_0 = 16.71\ GPa$ and $K_0' = 7.79$ as reported in Ref. [100] which lie in between the values of Gump et al. [175] and Yoo et al. }[176]. Figure 81 shows the pressure – volume relations from models with and without the B-M EOS.

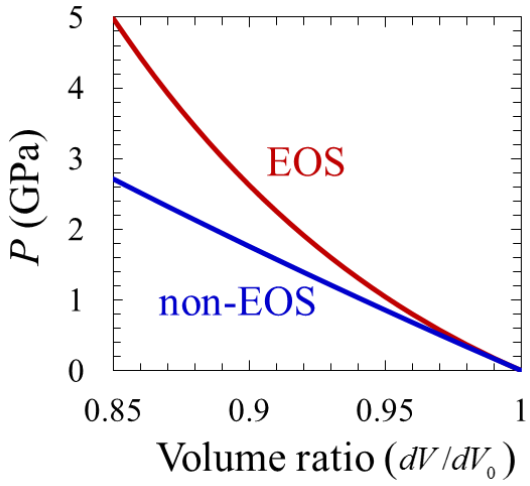

Figure 81. Pressure - volume relations with the Birch-Murnaghan EOS and without the EOS

An artificial viscosity scheme is implemented to obtain stable shock response under high-intensity loading. The artificial viscosity is a commonly used practical approach to solve issues associated with overshoot of stress at shock wave fronts and spurious oscillations behind the front. von Neuman and Richtmyer [61] first introduced the artificial viscosity method with a quadratic term of velocity gradient for 1-D wave propagations. Later, Landshoff [177] proposed a linear term for the velocity gradient.

Campbell et al. [178] explained the effect of each term. The specific form used in this study is

$$q = \begin{cases} \rho c_L l a \{\mathrm{tr}(\boldsymbol{D})\} - \rho c_Q l^2 \{\mathrm{tr}(\boldsymbol{D})\}^2, & \text{if } \mathrm{tr}(\boldsymbol{D}) < 0; \\ 0, & \text{if } \mathrm{tr}(\boldsymbol{D}) \geq 0. \end{cases} \tag{6-5}$$

In the above relations, q is a pressure correction associated the artificial viscosity, ρ is mass density of the material, l is a characteristic grid length taken as the square root of the element area ($\sqrt{A}$), and $\mathrm{tr}(\boldsymbol{D}) = D_{11} + D_{22} + D_{33}$ is the trace of the rate of deformation tensor. c_L and c_Q are viscous parameters for the linear term and the quadratic term, respectively. The values are $c_L = 0.06$ and $c_Q = 1.5$, as reported in Ref. [38]. A elasto-viscoplastic material under shock loading shows less significant overshoot and oscillations of stress compared with a material with elastic behavior due to energy dissipation associated with plastic deformation. We carried out stability analyses not only for conditions of viscoplasticity, but also for the conditions of the more challenging elasticity. Figure 82 shows a comparison between the pressure profiles of a shock wave with artificial viscosity and without artificial viscosity for an elastic model of HMX under loading with $U_p = 400\ m/s$. The algorithm with the artificial viscosity allows stable shock profiles without stress overshoot and spurious oscillations to be obtained. To verify the implementation, the calculated relation between shock velocity and particle velocity ($U_S - U_P$) is compared to that from experiments [179], as shown in Figure 83. The numerical result agrees with the experimental data.

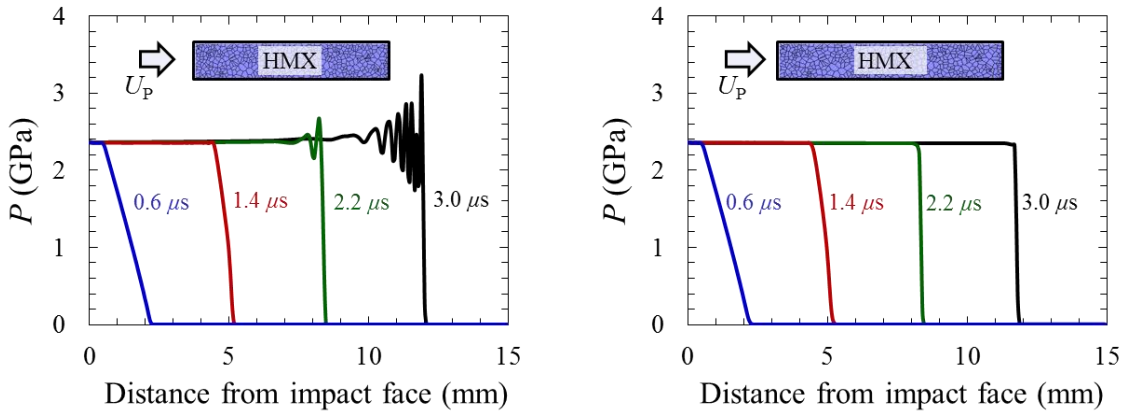

Figure 82. Comparison between the pressure profiles of a shock wave, (a) without artificial viscosity and (b) with artificial viscosity for an elastic model of HMX under a shock intensity of v = 400 m/s

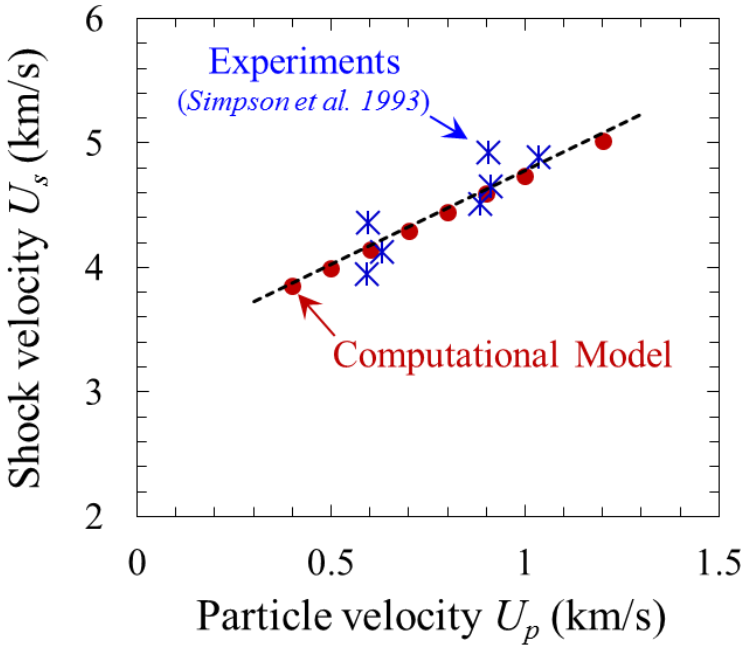

Figure 83. Comparison of calculated U_s – U_p relation and experimental data of HMX

Interfacial debonding and arbitrary fracture patterns are explicitly captured by the use of cohesive elements embedded throughout the finite element model. The cohesive elements follow a bilinear traction separation law described by Zhai et al. [99]. The cohesive relation embodies an initial reversible separation processes with a certain separation limit, followed by irreversible damage and separation beyond the limit. A cohesive surface pair is considered as failed and, therefore, has no further tensile strength if the separation reaches a critical distance. A verification of the cohesive element framework is provided in Ref. [87].

The formation of a crack (inside a gain or along a grain boundary) results in the creation of two surfaces. At each computational time step, the entire domain is scanned and such surfaces are identified. The corresponding nodal coordinates of all possible pairs of surfaces are compared to detect surface contact and overlap. Penalty forces are applied to strongly discourage interpenetration and maintain proper contact of the surfaces. Detailed descriptions of the multi-step contact algorithm and the penalty forces are given in Chapter 2. Frictional heating due to sliding along surfaces in contact is assessed using the Coulomb friction law. The stick-slip state is determined by the normal force between contact surface pairs.

Temperature in the material under dynamic loading rises locally due to inelastic bulk dissipation and frictional dissipation along interfaces. Heat conduction is considered. The specific form of the heat equation is

$$\rho c_v \frac{\partial T}{\partial t} = k\nabla^2 T + \eta \dot{W}^p + \dot{W}^{fric}, \tag{6-6}$$

where c_v is specific heat, T is temperature, t is time, k is thermal conductivity, η is the fraction of plastic work that is converted into heat, $\dot{w}^p$ is the rate of plastic work, and $\dot{w}^{fric}$ is the rate of frictional dissipation.

6.3 Results and Discussions

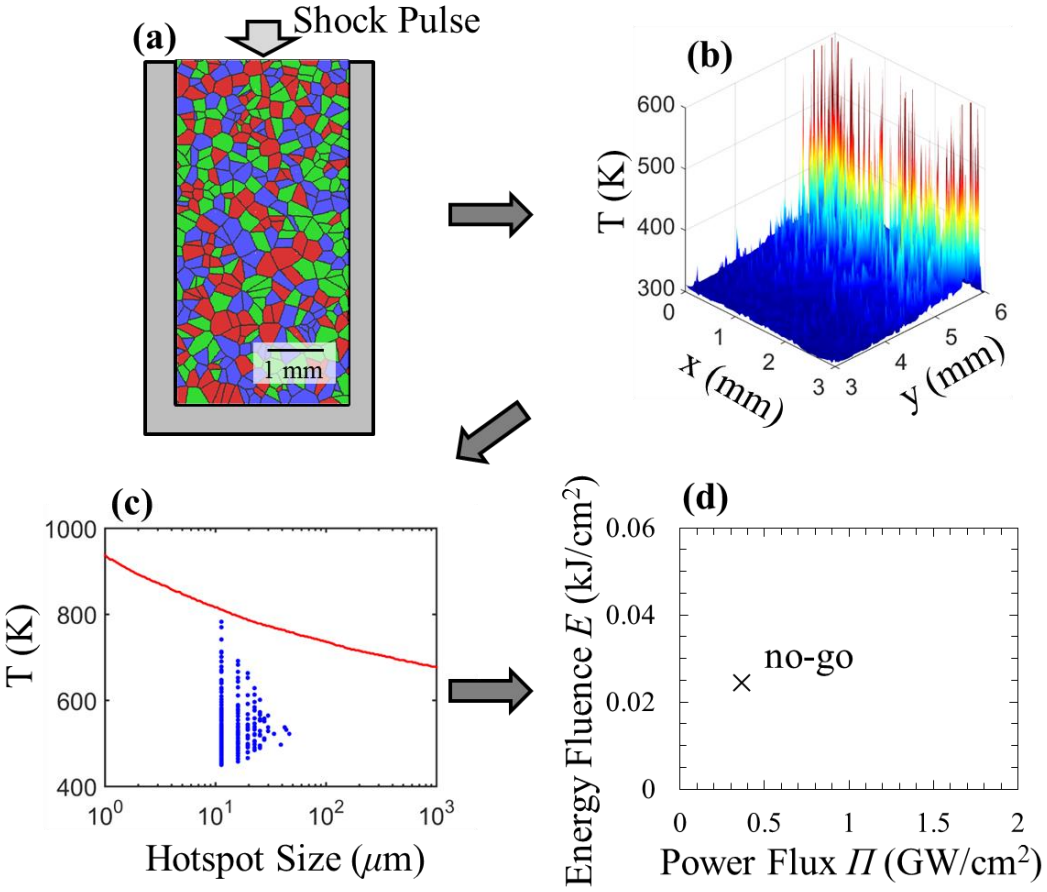

Figure 84. Illustration of the analysis on hotspot based ignition prediction. (a) Microstructure generation and CFEM calculation, (b) Temperature field, (c) Hotspot characterization and determination of the criticality, and (d) Record of "go" and "no-go" for each sample in Π – E space.

A systematic quantification of the ignition of the HMX samples is carried out, focusing on the shock intensity, shock pulse duration, and the average grain size of the microstructure. The analysis is performed in the following steps. First, calculations are carried out using multiple samples under the loading conditions as discussed in Chapter 6.2.2. Stress and temperature profiles are obtained and the attenuation of the stress is also analyzed to ascertain validity of the results relative to experiments. Second, the ignition criterion described in Chapter 3.2 is used to identify critical hotspots that have reached the size-temperature threshold. The ignition of the sample is determined by the existence of sufficient critical hotspots. Third, for samples that do not ignite, the likelihood of ignition is analyzed based on the proximity of the most dominant hotspots to the ignition threshold. Figure 84 illustrates an analysis on the likelihood of ignition of a hotspot that does not reach criticality.

6.3.1 Analysis of Stress and Temperature

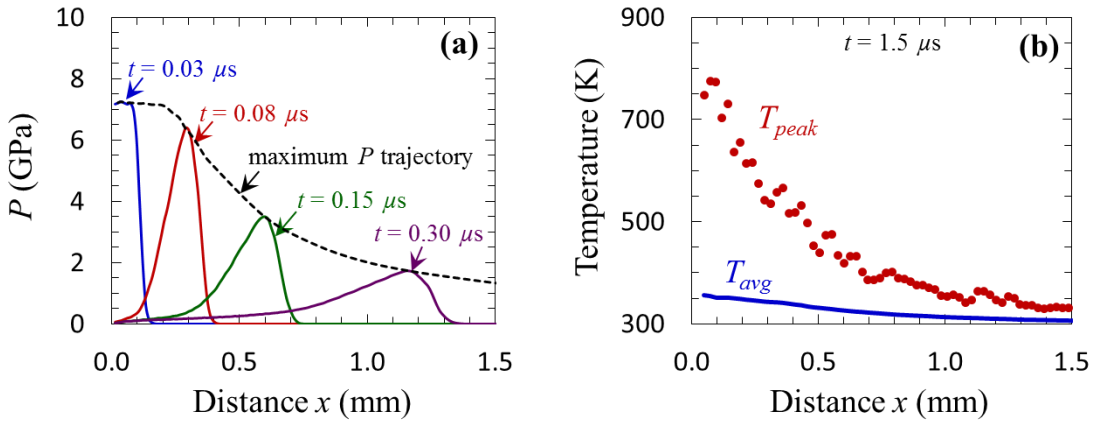

Figure 85. (a) The calculated trajectory of peak pressure and (b) corresponding temperature profile under shock pulse loading with U_p = 900 m/s, τ = 38 ns for a sample of d_{avg} = 220 μm.

As the shock wave propagates through the material, the temperature of the material increases due to energy dissipation from material inelasticity and friction along crack faces. The peak pressure trajectory from the calculations and the corresponding temperature profile under shock loading with $U_p = 900\ m/s$ and $\tau = 38$ ns are shown in Figure 85. Note that the peak pressure as well as the average and peak temperatures decrease as the shock wave propagates through the material.

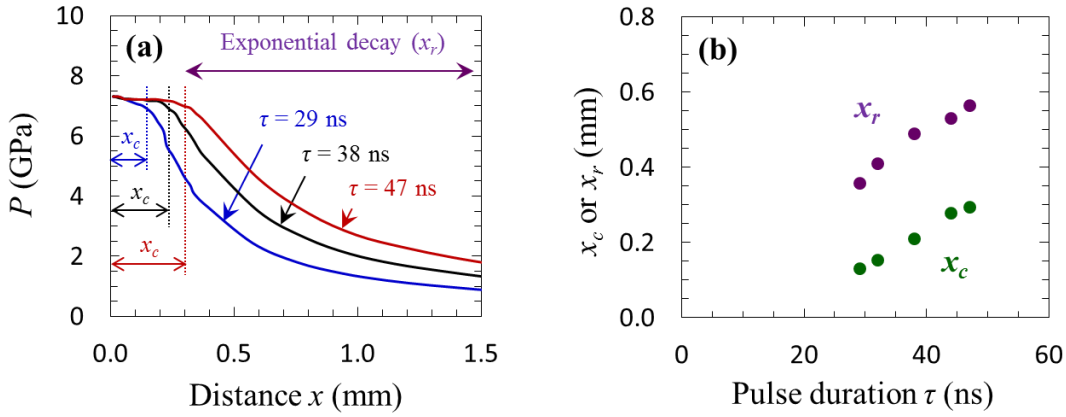

Figure 86. Effect of pulse duration on stress attenuation under shock pulse loading with U_p = 900 m/s for a sample of d_{avg} = 220 μm, (a) profiles of pressure for the durations of τ = 29, 38, and 47 ns and (b) corresponding rarefaction point (x_c) and decay distance scaling parameter (x_r).

Impact by a thin flyer creates a short duration pulse, which attenuates as the shock wave propagates through the material, as described in Ref. [180]. Initially, the peak pressure remains constant from the impact face to the rarefaction point (x_c), after which release waves from the impact face overtake the shock wave, causing attenuation of the peak pressure. The distance (x_c) and the degree of attenuation vary depending on the material and initial pulse duration (which depends on flyer thickness), as described in Ref. [181]. The attenuation of pressure is often quantified with an exponential form in terms of

distance from the impact face, as discussed in Ref. [182]. The exponential form has been shown to model the dependence of particle velocity (U_p) on the shock velocity (U_s) [183]. The trajectories of peak pressure for different pulse durations between $\tau = 29 - 47$ ns are shown in Figure 86(a). The trend can be described by

$$P_{peak} = P_1 \exp\left(-\frac{x - x_c}{x_r}\right) + P_2, \text{ for } x > x_c, \tag{6-7}$$

where the rarefaction point is at $x = x_c$ at which the peak pressure begins to attenuate. x_r is a scaling parameter that defines the slope of the attenuation. P_2 is the asymptotic pressure at far distances and $(P_1 + P_2)$ is the peak plateau pressure on the interval $0 \leq x \leq x_c$. The trajectories of the peak pressure as shown in Figure 86(a) are fitted to Eq. (6-7) for the range of $x \leq 3$ mm. Figure 86(b) shows the dependence of x_r and x_c on pulse duration τ. As the pulse duration (τ) increases, the rarefaction distance (x_c) increases, indicating that the peak pressure plateaus for a longer distance before it starts to attenuate. Likewise, as the pulse duration (τ) increases, the distance scaling parameter (x_r) decreases, indicating that the pressure attenuates more slowly as it propagates through the material. Figure 87 shows the relationship between the pulse duration and the distance parameters (x_r and x_c) over the range of $U_p = 700 - 1200\ m/s$. The relationships between the pulse duration and distance parameters, x_r and x_c, are linear. The distance parameters for all shock intensities considered fall along the same lines, indicating that they are highly dependent on pulse duration but are not strong functions of the load intensity. The effect of shock intensity on attenuation is captured by P_1 and P_2. The values of the parameters for the linear relationships between pulse duration τ and the distance parameters, x_r and x_c, are listed in Table 17. The threshold time (t_0^c) for x_c in Figure 87 and Table 17 is 10 *n*s which is equal to the ramp time of the applied boundary loading (Figure 79(b)). This coincidence

indicates that if the pulse duration is as short as the ramp time, the shock wave begins to attenuate instantly without staying at plateau.

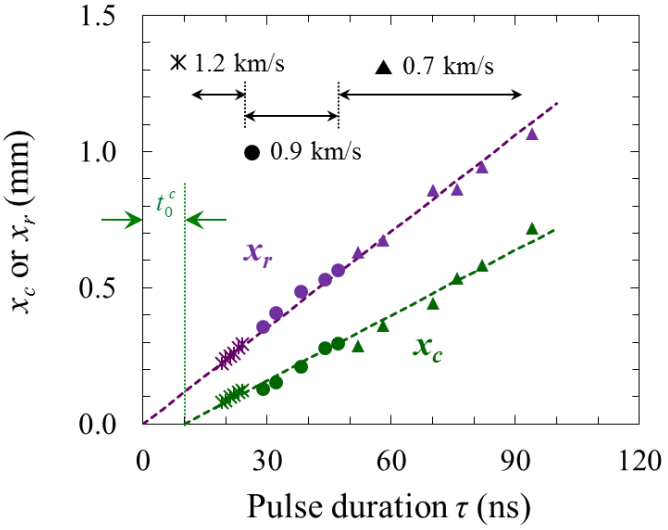

Figure 87. Relationship between pulse duration and distance parameters (x_r and x_c) over the loading range of U_p = 700 – 1200 m/s

Table 17. Coefficients of the linear relations between x_r and τ and between x_c and τ

$x_r = a_r \cdot (\tau - t_0^r)$	$a_r = 0.0118\ mm/ns$	$t_0^r = 0\ ns$
$x_c = a_c \cdot (\tau - t_0^c)$	$a_c = 0.0080\ mm/ns$	$t_0^c = 10\ ns$

6.3.2 Ignition Threshold

The samples in the experiments are 12.7 mm in length, which is a sufficient distance to see the stress attenuate to very low levels as the loading pulse reaches the bottom of the samples. The attenuation is so pronounced, that only a small portion of the samples close to the impact face experience severe enough loading over the duration of

the experiments to yield hotspots having the potential to cause ignition. Indeed, the computational results show that most hotspots are generated within a distance of 0 < x < 1 – 2 times of x_c from impact face and no hotspots are seen for any distance x > 4 – 5 times of x_c. Therefore, the shock pressure significantly diminishes as the wave reaches x = 6 mm. Specifically at this distance, the pressure of a sample subjected to loading with $U_p = 700\ m/s$ and $U_p = 900\ m/s$ decreases to 10% and 5% of the initial shock pressure, respectively. Welle et al. [184] investigated the effect of sample height and found no significant variations in the ignition threshold for a height range of 6 -19 mm. Because of this, we stop our calculations when the stress wave reaches the bottom of the samples and analyze the temperature field for hotspots, knowing that further propagation and reflection of the wave from the bottom have negligible effects on hotspot formation. This approach is essentially equivalent to using an infinitely long sample in which the stress wave does not reflect.

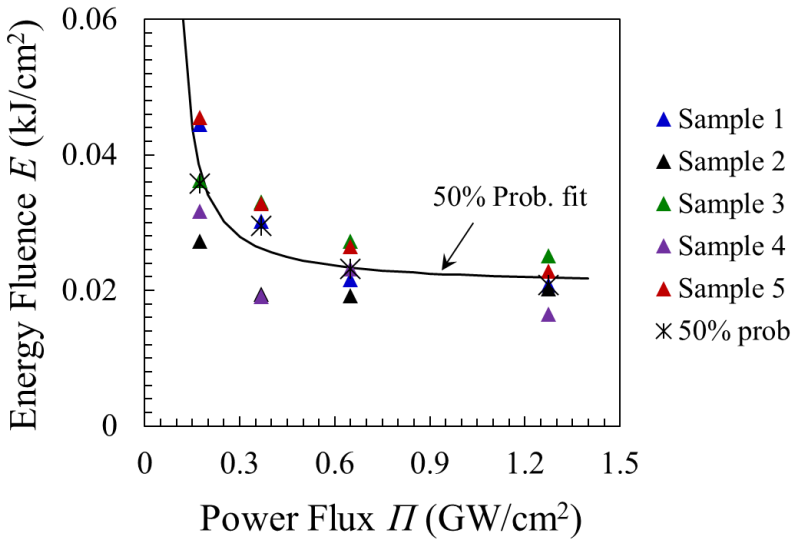

Figure 88. Minimum energy required for ignition from five samples and 50% probability. The samples used here have statistically similar microstructures with the average grain size of d_{avg} = 220 μm

The critical energy threshold for ignition is analyzed using the hotspot ignition criterion discussed in Chapter 3.2. Figure 88 shows the minimum energy input E required for ignition (or energy fluence). Here, the shock intensity is expressed in a power flux form (i.e., $\Pi = PU_p$). Power flux (Π) is the energy rate imparted to the sample per unit area of the impact face. Energy fluence (E) is the total energy imparted to the sample per unit area, which is identical to the time integration of the power flux ($E = \int_0^\tau \Pi \, dt$). Five statistically equivalent samples are computationally analyzed at each shock intensity. The different samples, just like different samples of the same material in experiments, require slightly different levels of energy fluence (as reflected in slightly different pulse durations they require for reaching ignition) under the same load intensity. Although the individual samples have the same overall statistical microstructural attributes therefore mimicking multiple samples of the same material batch in experiments, the random grain shapes and grain distributions cause the samples to have local fields that fluctuate, thereby giving rise to slightly different behaviors and slightly different energy fluence values even under the same overall loading condition. The asterisk '$\ast$' in the figure demarcates the threshold for 50% probability of ignition as determined by all samples over the entire load regime analyzed. To determine this 50% threshold, the following James-type relation is used to provide an overall fit.

$$1 = \frac{E_c}{E} + \frac{\Pi_c}{\Pi}, \tag{6-8}$$

where the cutoff energy fluence E_c and the cutoff power flux Π_c are fitting parameters which represent asymptotic thresholds for the critical energy fluence and the critical power flux, respectively. This relation is based on the James relation [37] and is obtained by replacing the specific kinetic energy ($\Sigma = 0.5{U_p}^2$) in the James relation by the power flux

($\Pi = PU_p$), see Welle et al. [27]. The data points above the 50% threshold curve correspond to ignition probabilities higher than 50%, and the points below the 50% threshold curve represent correspond to ignition probabilities lower than 50%.

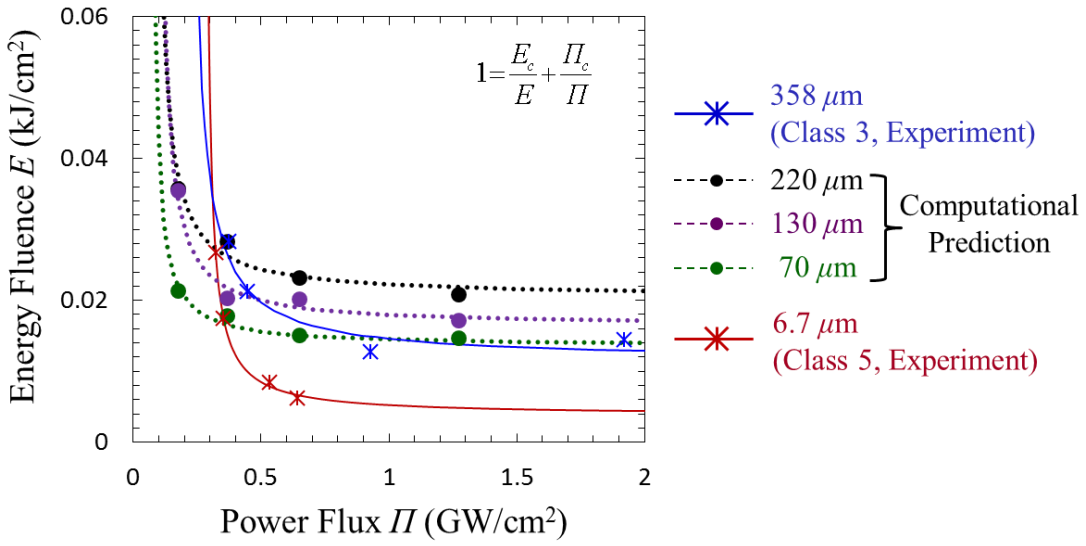

Figure 89. Computationally predicted 50% ignition thresholds from all grain sizes analyzed (d_{avg} = 70, 130, and 220 μm) and experimentally measured thresholds for Class 3 and Class 5 HMX.

Table 18. Parameters in the modified James relation for materials with different grains sizes from experiments and computations

	d_{avg} (μm)	E_c (kJ/cm^2)	Π_c (GW/cm^2)
Experiments	358 (Class 3)	0.01157	0.2072
	6.7 (Class 5)	0.00377	0.2776
Computations	220	0.0205	0.0798
	130	0.0163	0.0919
	70	0.0135	0.0683

The 50% ignition thresholds for the three materials with the average grain sizes of d_{avg} = 70, 130, 220 μm are shown in Figure 89. The corresponding parameters for the modified James relation (Eq. (6-8)) for these three cases are listed in Table 18. In general, a higher loading rate (power flux) results in a lower energy required for ignition (lower energy fluence) as indicated by Eq. (6-8). For a given loading rate (power flux), smaller grain sizes lead to lower ignition thresholds. This effect is more pronounced under strong shock loading (power flux greater than 0.5 GW/cm^2). Khasainov et al. [124] mentioned that heterogeneous explosives with high surface area (corresponding to smaller grains) are more sensitive than those with less surface area (corresponding to larger grains). They observed this trend only at high intensity regime ($P/P_c >> 1$). As shown in Figure 89, the discrepancy in the sensitivity levels of different grain sizes increases as the power flux increases, whereas the sensitivity level discrepancy converge as the power flux decreases until its critical value is reached. The trends observed in the computational predictions are in good agreement with those observed in experimental data, as overlaid in Figure 89. Moreover, the computationally predicted thresholds for grain sizes of d_{avg} = 70, 130, 220 μm lie in the same range as the thresholds obtained by experiments for Class 3 (d_{avg} = 360 μm) and Class 5 (d_{avg} = 6.7 μm) samples with a marginal degree of deviation. Overall, the experimentally measured thresholds are lower than the computational predictions. The difference between the experimental observations and computational predictions may be attributed to the following factors. First, the average grain sizes for Class 3 and Class 5 HMX in the experiments become smaller during the pressing process. So, the actual grain sizes are somewhat smaller than the nominal values stated here. Molek et al. [165] reported that the grain sizes of Class 3 and fluid-energy-milled HMX (d_{avg} = 4 μm) decrease by roughly one or two orders of magnitude after sample preparation. Similar results can also be found in Ref. [185]. Therefore, the ignition thresholds of Class 3 and Class 5 HMX shown in Figure 89 are actually for grains sizes smaller than nominal values

stated in the figure. Second, the computational model is based on a relative density of 100% (fully packed HMX) and provides only a phenomenological account of voids and other defects in the material, whereas the experimental samples have a relative density of less than 100% (94% TMD). Christensen et al.[186] observed that LX-17 PBX samples with higher relative densities are less sensitive (having higher ignition thresholds) than samples with lower relative densities. Third, large "boulders" in the experimental samples are not considered in the simulations, as pointed out earlier. What is important to note is that the overall trends are consistent, with smaller grain yielding lower ignition thresholds. The explicit account of voids and void collapse and consideration of vastly different grain size groups in a microstructure will be the topic of a future study.

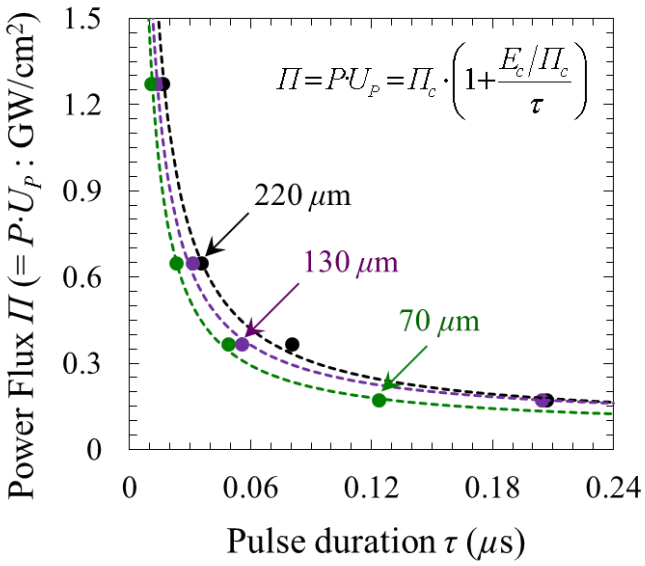

Figure 90. Fifty percent (50%) ignition probability thresholds in the Π - τ space and the equivalent James relation.

In the modified James relation (Eq. (6-8)), the power flux ($\Pi = PU_p$) is related to the shock intensity, similar to the specific kinetic energy ($\Sigma = 0.5{U_p}^2$). It also represents the rate of energy imparted to the material ($\Pi = dE/dt$) per unit area of material surface.

The ignition threshold between input energy E and power flux Π in the E - Π space can also be represented in the Π - τ space. Specifically, the modified James relation as expressed in the Π - τ space is

$$\Pi = P \cdot U_P = \Pi_c \cdot \left(1 + \frac{E_c / \Pi_c}{\tau}\right), \tag{6-9}$$

where E_c and Π_c are the same parameters as in Eq. (6-8). This equation in the Π - τ space is an equivalent form of the modified James relation (Eq. (6-8)). Figure 90 shows the 50% ignition thresholds (data points denoted by the symbols) for the three grain sizes in the Π - τ space and the corresponding equivalent James relations obtained via curve fitting. To study the application of the equivalent James relation to experimental data, we examine the shock initiation threshold of TATB obtained by Honodel et al. [187]. Figure 91 shows a comparison of the fits with the equivalent James relation (Eq. (6-9)) and the Walker-Wasley relation ($P^n\tau = C$) [36]. Both the Walker-Wasley relation and the equivalent James relation have two fitting parameters. The equivalent James relation follows more closely the data points over the entire range, while the Walker-Wasley relation deviates from the experiments in the longer pulse (lower load intensity) regime. The closeness of the fit in the Π - τ space using the equivalent James relation (Eq. (6-9)) is the same as the closeness of the fit in the E - Π space using the modified James relation (Eq. (6-8)), because Eq. (6-8) and Eq. (6-9) are algebraically equivalent. The difference is that the Π - τ space directly relates to the physical conditions of the experiments (thickness of the flyer required for ignition at given flyer velocity implied by the energy flux), whereas the E - Π space emphasizes the amount of energy required for ignition at given energy input rate into the material.

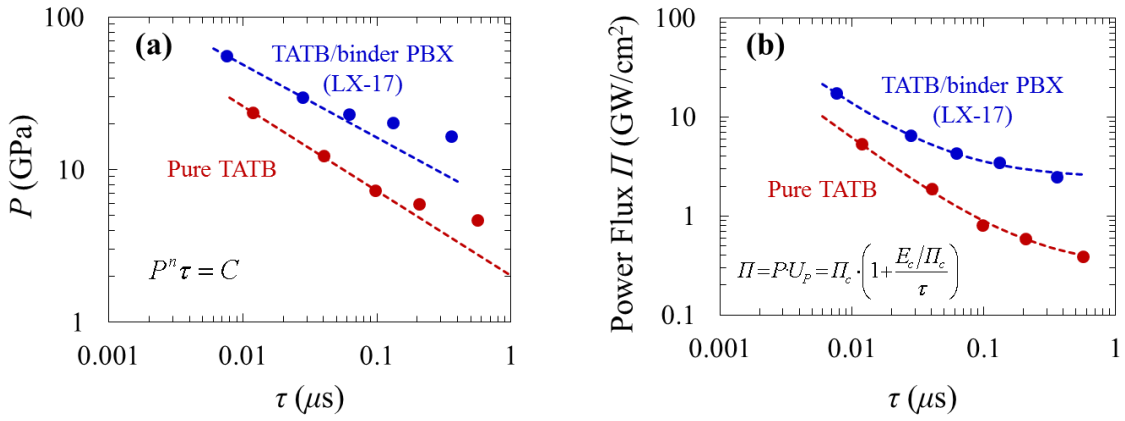

Figure 91. Comparison of the ignition threshold characterizations using (a) the Walker-Wasley relation ($P^n\tau = C$) and (b) the equivalent James relation. The ignition data of LX-17 and TATB is from Ref. [187].

6.3.3 Probabilistic Quantification: Ignition Threshold for any Given Probability of Ignition

The ignition threshold represented by Eq. (6-8) indicates the shock loading conditions for 50% probability of ignition. To incorporate the energy and power flux conditions required for greater than or less than 50% ignition probability, Gresshoff and Hrousis [161] expanded on the modified James relation by introducing a James number, *J*. The specific form of the equation is

$$\frac{1}{J} = \frac{E_c}{E} + \frac{\Pi_c}{\Pi}, \tag{6-10}$$

where $J = 1$ is the modified James relation, $J > 1$ corresponds to shock loading conditions resulting in greater than 50% ignition probability, and $J < 1$ corresponds to shock loading conditions resulting in less than 50% ignition probability. As an example of the application of Eq. (6-10), Figure 92 shows the modified James relation with for $J = 0.75$, 1.0, and 1.25

using the data for microstructures with $d_{avg} = 220$ μm. Each J number accounts for all combinations of loading conditions (i.e., energy fluence and power flux) which results in a certain probability of ignition. The three lines in Figure 92 for J = 0.75, 1.0, and 1.25 correspond to the three probability fits of 10%, 50%, and 90%, respectively.

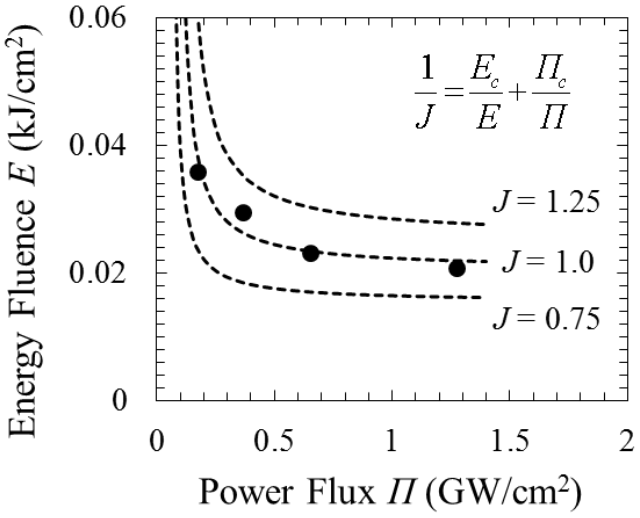

Figure 92. Modified James relation with J = 0.75, 1.0, and 1.25 for the material with d_{avg} = 220 μm

Figure 93 shows the relationship between J (James number) and the ignition probability from the experiment and the computational prediction for all samples. The truncated normal probability distribution function ($\mathscr{P}(J)$) is used to fit the ignition probability around a mean value of J = 1 The specific form of the function is

$$\mathscr{P}(J) = \frac{\Phi(J) - \Phi(0)}{\Phi(\infty) - \Phi(0)}, \tag{6-11}$$

where $\Phi(J)$ is cumulative normal probability distribution in the form of

$$\Phi(J) = \frac{1}{\sigma\sqrt{2\pi}} \int_{-\infty}^{J} \exp\left[\frac{-(x-\mu)^2}{2\sigma^2}\right] dx = \frac{1}{2}\left[1 + \mathrm{erf}\left(\frac{J-\mu}{\sqrt{2}\sigma}\right)\right], \tag{6-12}$$

where μ is the mean value, σ is the standard deviation. Note that $\Phi(\infty) = 1$. The parameters used to represent the ignition probability of the samples are listed in Table 19. By combining Eqs. (6-10), (6-11), and (6-12), we can obtain a direct relation between the ignition probability $\mathscr{P}$ and the shock loading condition parameters E and Π in the form of

$$\mathscr{P}(E,\Pi) = \frac{1}{1-\mathrm{erf}\left(-\mu/\sqrt{2}\sigma\right)}\left[\mathrm{erf}\left(\frac{E\Pi}{\sqrt{2}\sigma\left(\Pi E_c + E\Pi_c\right)} - \frac{\mu}{\sqrt{2}\sigma}\right) - \mathrm{erf}\left(\frac{-\mu}{\sqrt{2}\sigma}\right)\right], \tag{6-13}$$

where $\mathrm{erf}(\cdot)$ is the Gauss error function. Under the conditions of the current paper $\Phi(0) \approx 2 \times 10^{-5}$, therefore, for the range of $0 \le J \le \infty$, the difference between $\Phi(J)$ and $\mathscr{P}(J)$ is on the order of 2×10^{-5}, which is negligible. As a result, with $J = \mu = 1$ representing an ignition probability of 50%, Eq. (6-13) simplifies to

$$\mathscr{P}(E,\Pi) = \frac{1}{2} + \frac{1}{2}\mathrm{erf}\left[\frac{1}{\sqrt{2}\sigma}\left(\frac{E\Pi}{\Pi E_c + E\Pi_c} - 1\right)\right]. \tag{6-14}$$

In the above relations, the standard deviation σ, mean μ, cutoff energy fluence E_c and cutoff power flux Π_c are material constants whose values are determined by experiments or computations reported here (see Table 18 and 19). Once these parameters are determined for a material, the probability of ignition $\mathscr{P}$ under any loading condition as measured by E and Π can be calculated directly from Eqs. (6-13) or (6-14). The probability $\mathscr{P}$ as a function of E and Π can also be represented as a function of the pulse duration τ and either power flux Π or input energy E. In the previous section, we have shown that the ignition threshold between input energy E and power flux Π in the E - Π space can be

represented in the Π - τ space (see Figure 89 and 90). Similarly, the ignition probability $\mathscr{P}$ in Eq. (6-14) can be recast in the Π - τ space and in the E - τ space as, respectively,

$$\mathscr{P}(\Pi,\tau)=\frac{1}{2}+\frac{1}{2}\text{erf}\left[\frac{1}{\sqrt{2}\sigma}\left(\frac{\Pi/\Pi_c}{1+\tau_c/\tau}-1\right)\right], \quad \text{and} \tag{6-15}$$

$$\mathscr{P}(E,\tau)=\frac{1}{2}+\frac{1}{2}\text{erf}\left[\frac{1}{\sqrt{2}\sigma}\left(\frac{E/E_c}{1+\tau/\tau_c}-1\right)\right], \tag{6-16}$$

where the $\tau_c = E_c/\Pi_c$ is a material-dependent time-scale constant. The values of τ_c from experiments and computations are listed in Table 20. Note that although τ_c can be used as a reference time, is not a measure related to the pulse duration required for ignition in any sense. For high-intensity loading, the pulse duration required for ignition τ can be smaller than τ_c. Likewise, for low-intensity loading, τ can be larger than τ_c.

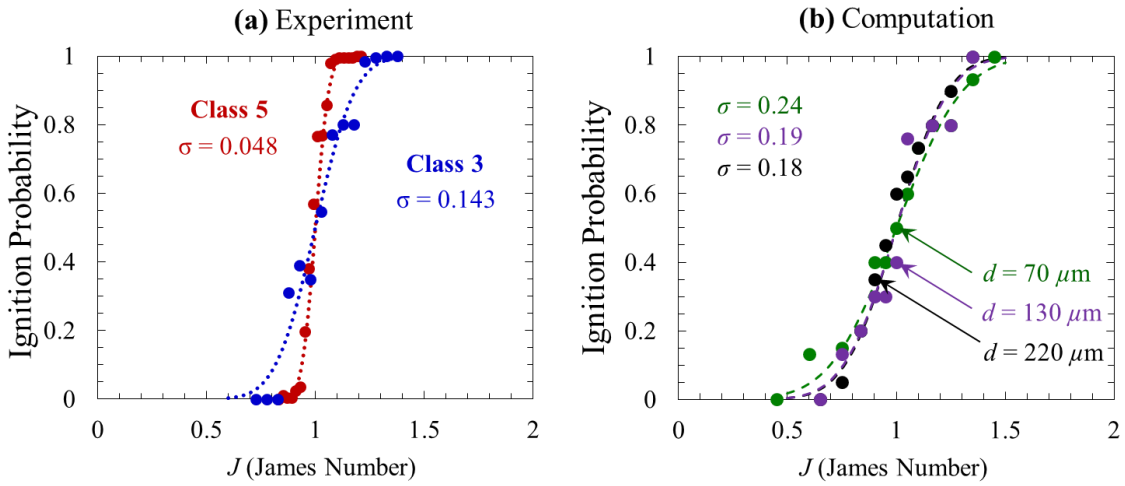

Figure 93. Relationship between J and the ignition probability from (a) experimental results of Class 3 and Class 5 HMX and (b) computational results of grains sizes of d_{avg} = 70, 130, and 220 μm

Table 19. Mean value and standard deviation for the ignition probability distributions for materials with different grain sizes from experiments and computations

	d_{avg} (μm)	μ	σ
Experiments	358 (Class 3)	1.0	0.143
	6.7 (Class 5)	1.0	0.048
Computations	220	1.0	0.18
	130	1.0	0.19
	70	1.0	0.24

Table 20. Time scale parameter τ_c obtained from experiments and computations

	d_{avg} (μm)	τ_c (ns)
Experiments	358 (Class 3)	55.8
	6.7 (Class 5)	13.6
Computations	220	257
	130	177
	70	198

The *J*-probability distribution for Class 3 samples from the experiments has a wider spread than that for the Class 5 samples, as shown in Figure 93(a). This trend is consistent what is reported by with Schwarz [188, 189] who found that samples with lower specific interface areas (SIA) demonstrate a wider spread of ignition probability. The computational predictions for the three average grain sizes ($d_{avg} = 70, 130, \text{and } 220$ μm) in Figure 93(b) have similar *J*-probability distributions. The difference between the experimental and computational results may be attributed to the following factors. First, the grain size distribution of the experimental Class 5 samples is much wider than that of

the Class 3 samples (see Table 1 in Ref. [184]). On the other hand, the grain size distributions of the computational microstructures have the same spread (see Figure 76). Second, the experimental samples have a much larger average grain size difference while the differences between the average grain sizes of the computational microstructure sets are much smaller. The difference between Class 3 and Class 5 is 53 times, whereas the differences among the computational sets are at most 3 times. The similarity in the distributions of ignition probability among the three computational sets does not mean that average grain size does not significantly affect ignition. On the contrary, the average grain size significantly affects the ignition thresholds for all ignition probability levels (as seen in section 3.2). For example, the thresholds for $J=1$ (or 50% ignition probability) for the different grain sizes are significantly different, as shown in Figure 89 and by the parameters E_c and Π_c in Table 18.

The distributions of ignition probability from the experiments have standard deviations of $\sigma = 0.048 - 0.14$ and the calculated distributions have standard deviations of $\sigma = 0.18 - 0.24$. As mentioned earlier, samples with larger specific interface areas (SIA) result in narrower distributions of ignition probability. The experimental samples have much larger SIAs than the computational samples. Specifically, the SIAs of the computationally-generated microstructures are $0.03 - 0.09\ \mathrm{m^2/g} \pm 0.0014\ \mathrm{m^2/g}$, one order of magnitude smaller than the SIAs of the samples used in the experiments ($0.866 - 1.62\ \mathrm{m^2/g}$) [27]. One reason for this difference is that the computational samples do not explicitly resolve very small voids and defects inside the grains as well as the surface roughness of the grains. For example, the same order of magnitude of SIA with minimal roughness on surfaces of Al particles is attainable for average particle sizes of a few hundred nanometers (see Table 1 and the SEM images in Yarrington et al. [190]). It is possible to explicitly consider these features in the model in the future, but such an

analysis is beyond the scope of the current work, which focuses on a new method for predicting ignition thresholds. The differences in experimentally measures and theoretically calculated SIA are discussed by Sánchez et al. [191] who compared measured SIA values and theoretically obtained SIA values based on particle size distributions. They reported that measured SIA values are an order of magnitude higher than theoretical SIA values due to particle morphology (roughness) and internal micro porosity.

Overall, the distribution curves in Figure 93 shows is that (1) J serves as an effective normalizing parameter for the examination of the probability of ignition distribution around a given reference probability level (which is taken as $J = 1$ or 50% of ignition probability here) for samples with different microstructural attributes, and (2) the ignition probability spread or the distribution around a given reference probability level depends on the microstructure heterogeneity fluctuations in the samples of a given sample set – or, simply put, how "similar to" or "different from" each other the multiple samples in a set are statistically. Specifically, the material-dependent 50% ignition threshold can be analyzed in the $E - \Pi$ space as seen in Figure 89, and the ignition probability around this 50% threshold can be analyzed through the relation between J and the probability $\mathscr{P}$ given in Figure 93. By combining these two relations, we can obtain the material-dependent ignition probability map as shown in Figure 94. This process is equivalent to obtaining Eq. (6-14) by combining Eq. (6-10) and Eq. (6-12). As Figure 94 shows, the ignition probability level in the $E - \Pi$ space is highly dependent on microstructure.

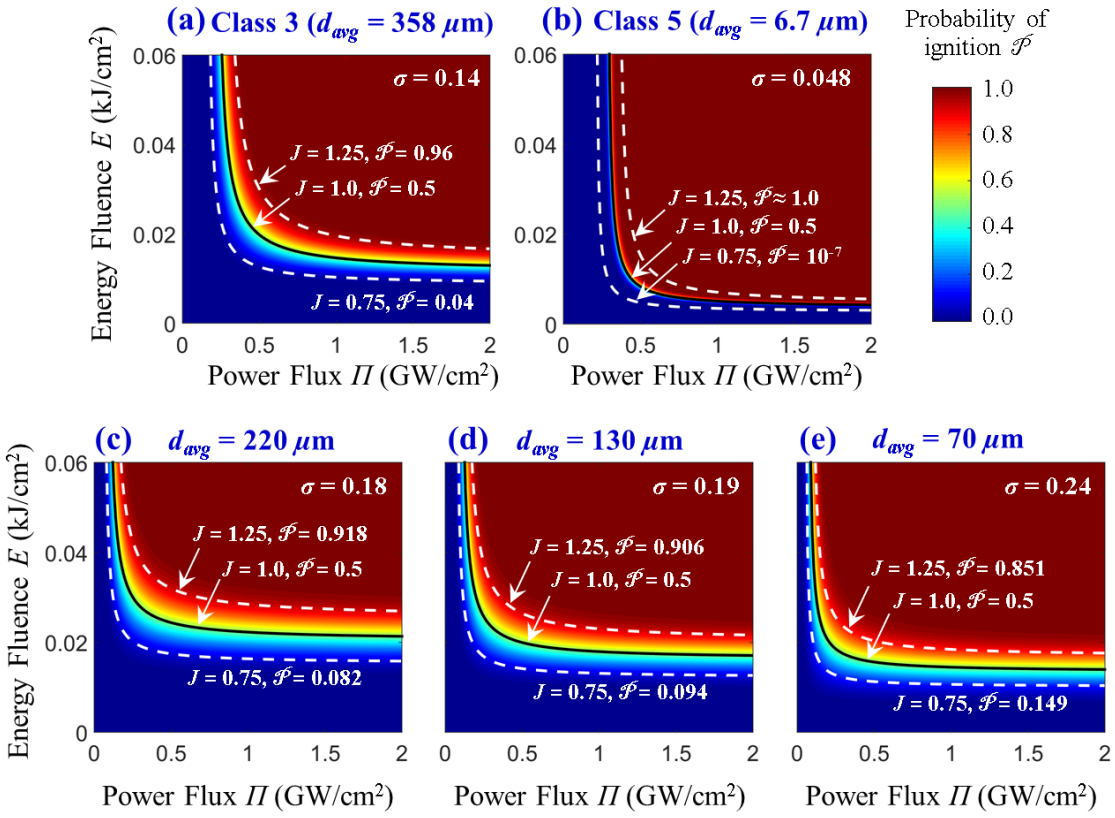

Figure 94. Ignition probability distribution maps, (a-b) obtained from experiments for (a) Class 3 and (b) Class 5 pressed HMX, and (c-e) predicted from simulations for samples with (c) d_{avg} = 220 μm, (d) d_{avg} = 130 μm, and (e) d_{avg} = 70 μm. The vertical axes of all figures have the same scale and unit as shown in the left most plot in the top and bottom rows.

6.3.4 Microscopic Ignition Risk Factor (R)

While J allows overall, macroscopic, material level ignition risk to be quantified, it is also possible and desirable to assess the ignition risk at the microscopic, individual sample level by studying its unique hotspot evolution. In the end, a relationship between the ignition of individual samples and the ignition risk of a material can emerge from such an analysis. To this end, we focus on the state of individual hotspots in a sample and

introduce a quantitative measure to assess the risk for ignition of each individual hotspot, with the understanding that the most dominant hotspots with the highest risk factors determine the ignition risk of a sample. The specific risk factor we define here is the *R*-value, or "risk" value for an individual hotspot. It can also be referred to as the hotspot ignition risk determinant (HIRD) and depends on the proximity of a hotspot's size-temperature state to the criticality condition. *R* is a measure for the proximity of a hotspot to the ignition threshold defined as

$$R = \frac{(T - T_i)}{(T_c - T_i)}, \tag{6-17}$$

where T is the temperature of a hotspot of diameter d, T_c is the critical threshold temperature for ignition for a hotspot of diameter d, and T_i is an initial reference temperature (chosen here as 300 K). Since the temperature and size combination of a hotspot depends on the area we choose to analyze (smaller cores of a hotspot have higher temperatures), the hotspot core size and *R*-value are calculated for different temperature levels (see Figure 95 – "Step 1"). The maximum value of *R* for each hotspot is taken as the *R*-value for that particular hotspot (Figure 95 – "Step 2"). This definition of *R* is a direct measure of how close a hotspot is to the ignition threshold. If $R = 0$, the hotspot is at the initial temperature ($T = T_i$) of the material at the beginning of loading. If $R = 1$, the hotspot is deemed critical ($T = T_c$) or has reached criticality. Subcritical hotspots have $0 < R < 1$. The *R* value of a hotspot is the maximum value of *R* calculated using different cutoff temperatures in the analysis of the size-temperature state of that hotspot. The *R*-value allows hotspots to be grouped and analyzed via an *R*-curve, based on a histogram of all the *R* values for a sample. Figure 95 illustrates the number and states of critical and subcritical hotspots in a sample (see "Step 3"). It is important to note that $R > 1$ indicates hotspot states that are above the ignition threshold. Since the focus of the analysis here is

only on the attachment of the threshold, such values are rounded down to 1 in the analysis carried out here. This treatment simply means that $R \geq 1$ indicates ignition, and since the ignition threshold is the sole concern here, no post ignition analysis is carried out.

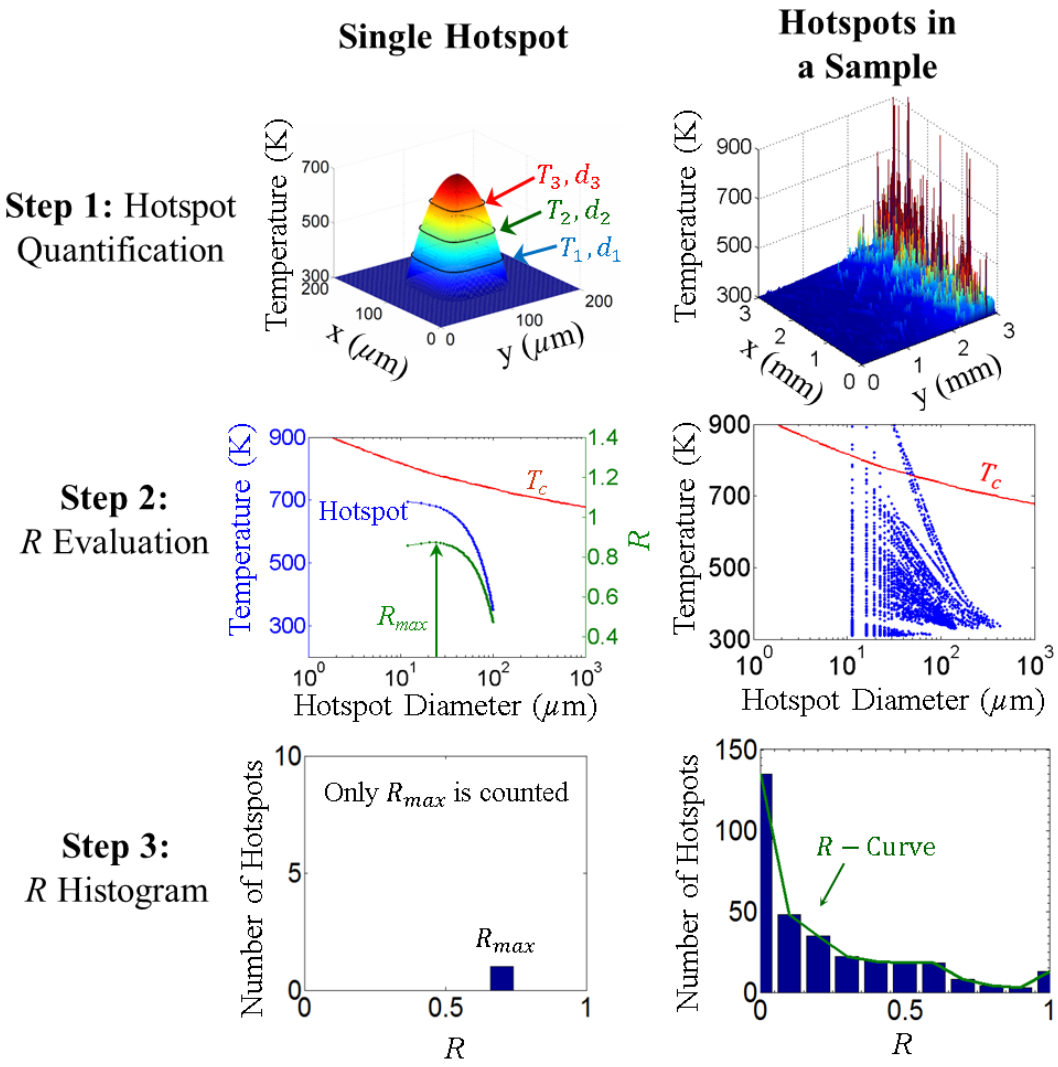

Figure 95. The evaluation of *R*-value from a single hotspot and the *R*-Curve from a temperature field.

Characterizing each sample with an *R*-curve makes it possible to compare the relative states of multiple samples in a holistic manner, accounting for the influence of all

dominant hotspots. Figure 96 shows the average *R*-curves for the samples with the average grain sizes of d_{avg} = 70, 130, and 220 μm under identical loading conditions (U_p = 900 m/s and τ = 35 ns). Each *R*-curve shows the average hotspot count of the five statistically similar samples in the set. The error bars show the extent of variations among the five samples. When compared to the experimental results for varying grain sizes, these *R*-curves demonstrate the correlation of hotspot quantity to overall sample sensitivity, which has been demonstrated to be related to the average grain size. Samples with increased sensitivity to ignition are found to have a higher number of subcritical hotspots. In other words, for any given *R* value, the samples with lower average grain sizes have, on average, greater than or equal to the number of hotspots as samples with larger average grain sizes.

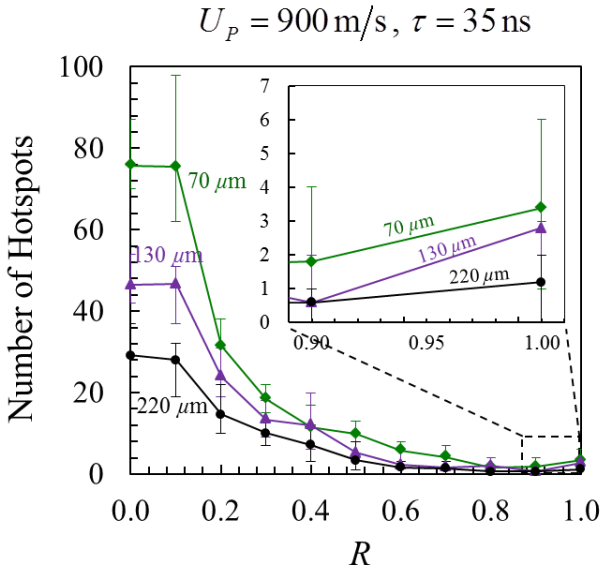

Figure 96. Comparison of *R*-curves between sample sets with average grain sizes of d_{avg} = 70, 130, and 220 μm. The error bars indicate degree of variations among multiple samples in each material set.

As a practical matter in the analysis reported here, in order to obtain a single *R*-value for each loading condition and sample, the average of the top two *R*-values in the sample is used. Two hotspots in the RVE correspond to a hotspot density of $0.22\,mm^{-2}$.

Ten *R*-values are used for each loading condition: five samples and the highest two *R*-values per sample. Since T_i = 300 K, $R = 0$ corresponds to $J = 0$. This makes intuitive sense because the only way for *J* to remain zero is if the sample has not been subjected to loading and no temperature increase is observed.

The *R*-value and *R*-curve focus on the local conditions of individual hotspots in a particular sample. Both the *R*-value and the *J*-value measure the likelihood of ignition. Note that for a given *J* value, some samples in a material set have ignited (with $R \geq J$) while other samples have not ignited (with $R < J$). For example, for $J = 1$, 50% of all samples in a material set have reached criticality by definition (with $R \geq 1$) and 50% of the samples have not reached criticality (with $R < 1$). Therefore, *R* is inherently related to *J* with some statistical deviation due to microstructure stochasticity, reflecting the fact that *J* measures the aggregate statistical behavior of a material sample set and *R* measures the behavior of individual samples in the set. A practical difference between *R* and *J* is that *R* can be calculated from the outcome of a single simulation after analyzing the hotspot map of the sample, while *J* requires analyzing the results from multiple samples (experimentally or computationally). *R* can be used to predict and relate to the ignition probability of a material under given loading conditions. While *J* quantifies the result of this analysis and does not have the predictive power or usage – its ability to measure the ignition probability of a material only exists after the outcomes of a set of experiments or simulations have been analyzed and tabulated. Figure 97 shows the correlation between *R* and *J* for the three grain sizes. By studying the relationship between *J* and *R*, the inherent connection between sample loading conditions and hotspot development may be further understood. If there appears to be a strong correlation between *R* and *J*, it may be possible to calculate the probability of ignition from a smaller number of samples without having

to run a large number of tests or calculations to determine where the ignition threshold for $J = 1$ lies.

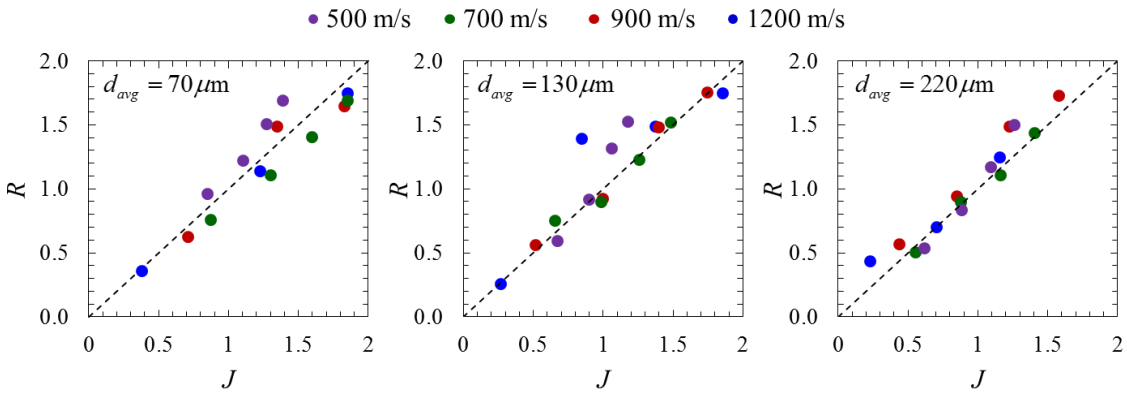

Figure 97. Correlation between *J* and *R* for average grain sizes of d_{avg} = 70, 130, and 220 μm

6.4 Conclusion

The ignition thresholds of energetic materials have so far been exclusively determined through experiments. While many forms of ignition thresholds have been proposed, one of the most widely used is the James or James-type ignition relation. In this chapter, we present a computational approach for predicating the James-type ignition thresholds via multiphysics simulations. The prediction is based on material microstructural attributes and fundamental constituent as well as interfacial properties. The prediction does not involve calibration or curve fitting with respect to the predicted behavior (ignition threshold), nor does it require prior information about the predicted behavior. The simulations consider the configuration and conditions of actual experiments. The approach emulates analysis procedures in experiments. Although the approach is applicable to many energetic materials such as polymer-bonded explosives (PBX), granular explosives (GX), and single-crystalline energetic crystals, the materials

of focus in the current paper are pressed granular HMX explosives with average grains sizes between 70 μm and 220 μm. The choice reflects the interest in comparing the computational predictions with experimental results. James-type relations between the power flux and energy fluence for different probabilities of ignition are predicted. To this end, statistically similar microstructure sample sets are computationally generated based on features of micrographs of materials used in actual experiments. The predicted thresholds are in general agreement with measurements from shock experiments in terms of trends. In particular, it is found that grain size significantly affects the ignition sensitivity of the materials at higher energy fluxes, with smaller sizes leading to lower energy thresholds required for ignition. For example, the 50% ignition threshold of the material with an average grain size of 220 μm is approximately 1.4-1.6 times that of the material with an average grain size of 70 μm in terms of energy fluence. The simulations account for the controlled loading of thin-flyer shock experiments with flyer velocities between 1.5 and 4.0 km/s, constituent elasto-viscoplasticity, fracture, post-fracture contact and friction along interfaces, bulking inelastic heating and interfacial frictional heating, and heat conduction. The constitutive behavior of the materials is described using a finite deformation elasto-viscoplastic formulation and the Birch-Murnaghan equation of state. The ignition thresholds are determined via an explicit analysis of the size and temperature states of hotspots in the materials and a hotspot based ignition criterion. The approach, relations, and capabilities developed here are useful for the analysis and design of heterogeneous energetic materials.

CHAPTER 7: SHOCK IGNITION THRESHOLDS OF POLYMER BONDED EXPLOSIVES AND THE EFFECT OF INITIAL DEFECTS

This chapter is based on the work in collaboration with Yaochi Wei.

7.1 Introduction

The chapter focuses on the prediction of the ignition event of polymer bonded explosives (PBXs) under thin pulse shock-wave loading including microstructure effects. Of particular interest are random morphology, HMX particle size distribution, binder properties, and initial defects. The specific type of the initial defect considered is the initial debonding at the interfaces between energetic crystals and a binder in PBXs. The configuration of thin pulse shock loading on PBX allows us to use simple and well-defined boundary conditions. A foundation of the proposed framework is based on James and Lambourn's observation [162] and the assumption that critical thresholds of hot spots for self-sustained thermal explosion correlate (or are equivalent) to the ignition thresholds for initiating detonation under plane shock loading. James and Lambourn found that the reaction behind the shock wave front is a function of shock strength and time along the particle path, and is independent of local flow variables behind the shock such as pressure and temperature. Therefore, the growth in the pressure or temperature fields does not feed back to the reaction rate. Based on the observations above, we assume that there is a one-to-one correlation between the existence of critical hotspots which lead to local thermal runaway and the occurrence of eventual detonation. In this section, we do not consider the issue of subsequent burn after reaching the critical state and the time needed to reach detonation.

7.2 Framework of Analysis

7.2.1 Materials

The HMX-based PBXs studied in this section are PBX 9404 and PBX 9501. PBX 9404 consists of HMX (94 wt.%), Nitrocellulose (3 wt.%), and a plasticizer (3 wt.%). PBX 9501 consists of HMX (95 wt.%), Estane (2.5 wt.%), and a plasticizer (2.5 wt.%). Since both types of PBXs have similar HMX fractions, the difference of initiation responses come from the binder material. Although the binder of PBX 9404 is stiffer than that of PBX 9501 [192], the detonation responses are known to be similar [10].

In this study, the microstructures that are computationally generated have an HMX grain volume fraction of 81% and a binder volume fraction of 19%. Although PBX 9501 and PBX 9404 include HMX particles close to 92% by volume fraction, some particles are too small to be resolved by micrographs, resulting in less volume fraction than the actual microstructures of PBX 9501 and PBX 9404 are composed of. For example, Benson and Conley [39] observed the binder volume fraction of 26% from a micrograph of PBX 9501, and Mas et al. [142] observed the binder volume fraction of 23%, and obtained a stress-strain behavior using an explicit finite element framework. Barua et al. [87] used a PBX microstructure with the HMX volume fraction of 82% and obtained stress-strain curves that match experimental data using the cohesive FEM (CFEM) which is the baseline framework of this study.

The HMX particles in PBX microstructures typically have random polygonal shapes as shown in Ref. [39, 101, 141]. To obtain PBX microstructures similar to that of experimental samples, we use a grain library consisting of grains extracted from microstructures generated by the Voronoi tessellation method. Details of the

microstructural attributes of the two-phase (HMX/binder) PBX and the method used to generate the microstructure are described in Ref. [139]. This approach allows us to achieve large numbers of samples with prescribed statistical attributes. Multiple microstructures with the same attributes but random morphologies are generated. This method is equivalent to carrying out multiple experiments on statistically similar microstructure samples. To illustrate the random variations in microstructure morphology, Figure 98 shows five samples with the same packing density of η = 0.81 and their respective grain size distributions. The HMX grains in the microstructures have an average size of 210 μm and a monomodal size distribution with a standard deviation of 66 μm. The same set of microstructure morphologies is used for both PBX 9501 and PBX 9404.

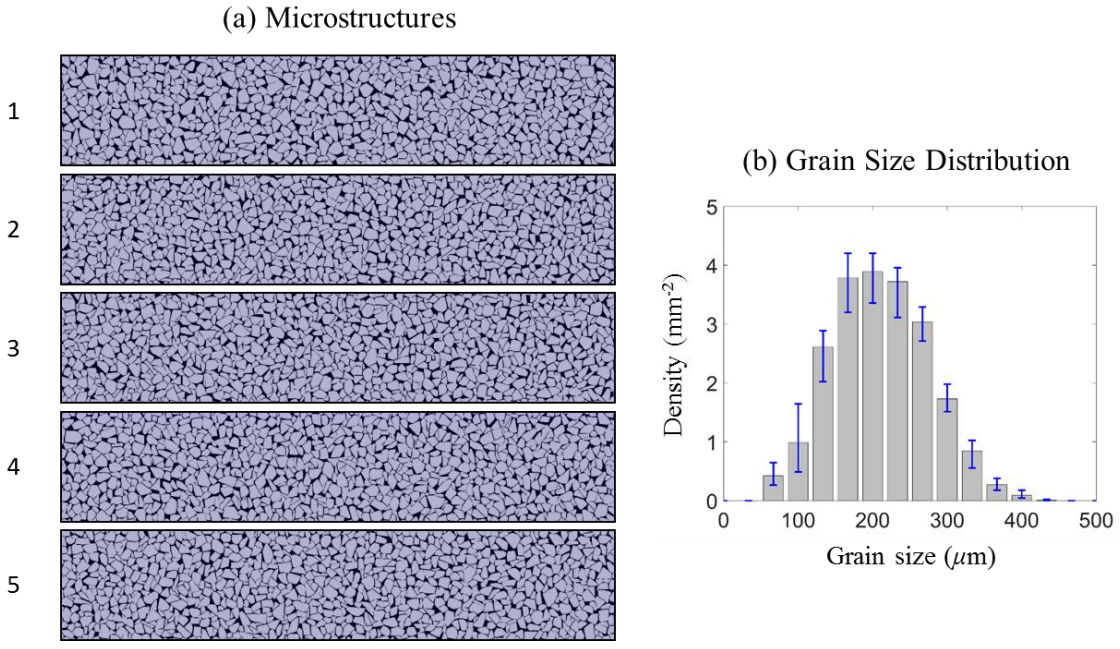

Figure 98. Computationally generated microstructures with a grain volume fraction of η = 0.81 (a) Images of multiple instantiations and (b) HMX grain size distribution.

7.2.2 Loading Configuration

The computational approach in this study emulates thin flyer experiments launched by an electric gun (E-gun) on PBX as done in the experiments by Weingart et al. [193]. The impact of a thin flyer onto a sample creates a pulse wave at the boundary as seen in Figure 99 of Ref. [194], and the stress wave propagates through the sample. The boundary conditions and the loading conditions are designed to imitate such experiments. Specifically, an impact loading is effected by applying a prescribed particle velocity at the impact face (left boundary of the sample) for a specified time duration as shown in Figure 99. The top and bottom boundaries are constrained such that lateral expansion does not occur. The framework is two dimensional, and the conditions of plane-strain prevail. This configuration approximates the planar shock pulse loading of a sample under conditions of approximate macroscopic uniaxial strain. The imposed particle velocity and duration are chosen to correspond to the loading characteristics in the shock experiments [193], in which flyer velocities range from 1 km/s to 5 km/s, and the flyer thickness varies from 1.27 mm to 25 μm. The imposed particle velocity is obtained from the ratio between the longitudinal wave impedances (ρU_s) of the flyer and the PBX sample via

$$U_p = \frac{\rho_{fly} U_{s,fly}}{\rho_{fly} U_{s,fly} + \rho_{PBX} U_{s,PBX}} V_{fly} \tag{7-1}$$

where ρ_{fly} is density of the flyer, $U_{s,fly}$ is wave speed in the flyer, ρ_{PBX} is density of PBX, $U_{s,PBX}$ is wave speed of PBX, and v_{fly} is the launching velocity of the flyer. The wave speed U_s is a linear function of the particle velocity U_p.

Table 21. Material properties of flyer and specimen and experimental conditions in Ref. [193]

	Parameters	Flyer (Polyester)	Specimen (PBX9404)
Material properties	Density ρ (kg/m^3)	1414	1840
	Parameter a in $U_s - U_p$ relation	1.48	2.48 (Ref. [195])
	Parameter b in $U_s - U_p$ relation (km/s)	1.66	2.45 (Ref. [195])
Experiment condition	Flyer velocity v_{fly}	1 – 5 km/s	Stationary
	Thickness H	25 μm – 1.27 mm	6 – 19.1 mm

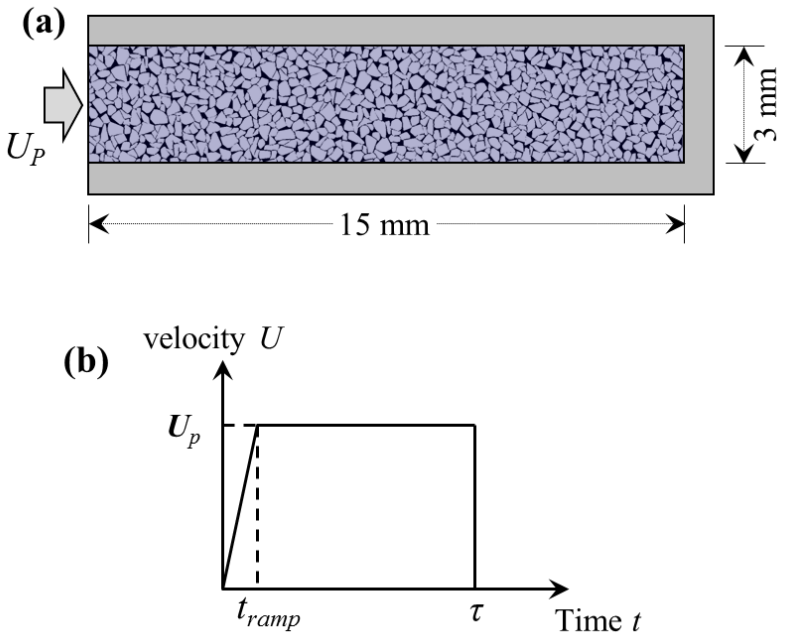

Figure 99. (a) Configuration of computational model of shock experiments, loading, and boundary conditions considered, and (b) load history imposed on the top boundary of the domain.

The dimensions and the material properties of the flyer and the specimen are listed in Table 21. The range of loading conditions analyzed in the experiment corresponds to

the imposed particle velocity range of U_p = 371 – 1960 m/s. (flyer velocity range of 1 - 5 km/s). In this analysis, we impose a particle velocity range of U_p = 200 – 1200 m/s. The pulse duration is the time it takes the longitudinal wave to traverse a round trip in the flyer. The range of flyer thickness in the experiment corresponds to a pulse duration of τ = 8 – 980 ns. The pulse duration we impose ranges from 30 ns to 4.5 μs. The increment of the pulse duration between successive durations depends on load intensity and varies between 2 ns and 50 ns. The loading conditions used in this analysis are listed in Table 22, including the imposed velocity, the range of pulse durations, and the minimum increment between successive durations. The profile of the imposed shock pulse at the boundary is shown in Figure 99(b). The velocity rapidly increases from zero to the particle velocity of U_P during the ramp time of t_{ramp} = 10 ns. This velocity is kept constant until the pulse time τ is reached. After the pulse time ($t \geq \tau$), the left boundary is released and no external loading is applied, while the boundaries on the top, bottom, and right remain constrained in their normal directions. For each velocity and sample, ten different pulse durations are considered, yielding 300 microstructure-loading combinations (6 velocities × 10 pulse durations × 5 microstructures).

Table 22. Load conditions and load increments analyzed

U_p (m/s)	200	400	600	800	1000	1200
$P \cdot U_p$ (GW/cm^2)	0.0208	0.0972	0.243	0.465	0.773	1.18
Range of pulse duration τ (ns)	1500 - 4550	200 - 1200	50 - 300	30 - 180	30 - 80	20 - 60
Range of E (kJ/cm^2)	0.0350 - 0.106	0.0196 - 0.123	0.0100 - 0.0731	0.00917 - 0.0819	0.0400 - 0.0482	0.0327 – 0.0453
minimum τ interval (ns)	50	30	10	5	2	2

7.2.3 Constitutive Relations

The simulations are performed using a recently developed Lagrangian cohesive finite element framework explained in Chapter 2. The numerical approach used in this study explicitly captures the hotspot evolutions due to thermo-mechanical energy dissipations of two-phase PBX microstructures subject to a shock pulse loading. Details of the algorithm and models are provided in Chapter 2 of this thesis. A brief outline of the constitutive relations and relevant parameters are given below.

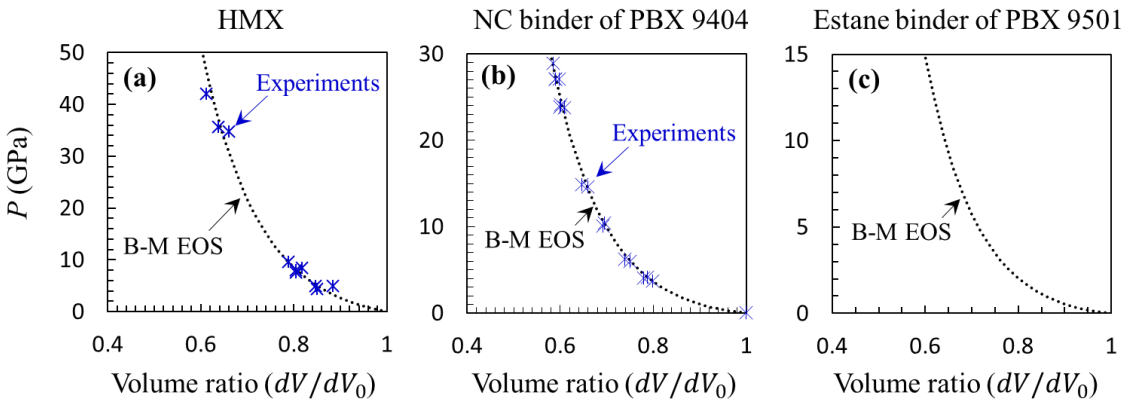

Figure 100. Pressure – volume (*P* – *V*) relation of (a) HMX, (b) NC binder estimated from cellulose acetate, (c) Estane binder. The vertical axes of all figures have the same unit as shown in the left most plot.

The volumetric part of the stress tensor is described by the Birch-Murnaghan equation of state (B-M EOS). The specific form of the equation is provided in Chapter 2. The parameter values used for HMX in this study are $K_0 = 16.71\ GPa$ and $K_0' = 7.79$ as reported in Ref. [100]. Figure 100(a) shows the pressure - volume curve for the HMX particles. The pressure - volume relation for the binder of PBX 9404 is estimated from the $P - V$ data of cellulose acetate in Ref. [196] with the replacement of the density by 1.65 g/cm^3. The same estimation based on cellulose acetate properties was made by Swift et al.

[197] and Moore at al. [198]. The parameters of B-M EOS for the binder of PBX 9404 is obtained by a curve fitting of the pressure - volume data as shown in Figure 100(b). The parameters of B-M EOS for HMX, the NC binder of PBX 9404, and the Estane binder of PBX 9501 are listed in Table 23. Dattelbaum and Stevens [101] obtained the parameters of B-M EOS for the Estane binder of PBX 9501 with various temperatures based on their experiments. The initial bulk modulus, K_0, decreases as the temperature increases. However, the first derivative K_0' shows consistent values with the average of K_0' = 12.95. We chose the entire set of K_0 values in Ref. [101] with K_0' = 12.95. The pressure - volume curve for the Estane binder is shown in Figure 100(c).

Table 23. Parameters of B-M equation of state for HMX and the NC binder

Parameters	HMX	NC	Estane
K_0 [GPa]	16.71	5.797	*T* dependent
K_0'	7.79	10.61	12.95

The deviatoric part of the constitutive behavior of the HMX grains is described by an elasto-viscoplastic model. The details of the elasto-viscoplasticity model and the descriptions of the parameters can be found in Ref. [102]. The parameters of the plasticity model for HMX used in this study are listed in Table 2. The parameters are calibrated to match the experimental wave profile obtained by Dick et al. [103]. The verification of the calibrated parameters is described in Ref. [174].

Table 24. Parameters of the Prony series for the binder of PBX 9404

Frequency (Hz)	G_i (MPa)	Frequency (Hz)	G_i (MPa)
10^{-8}	45.52	10^{1}	169.9
10^{-7}	50.12	10^{2}	204.5
10^{-6}	55.19	10^{3}	249.3
10^{-5}	59.53	10^{4}	299.4
10^{-4}	75.63	10^{5}	361.6
10^{-3}	84.48	10^{6}	381.8
10^{-2}	96.22	10^{7}	387.0
10^{-1}	113.0	10^{8}	320.6
1	126.4		$G_e = 0$

The deviatoric part of the constitutive behavior of the polymer binders is described by a Prony series. The specific form of the Prony series is in Eq. (2-37). The detailed descriptions of the form are explained in Chapter 2. The modulus of the binder is highly dependent on the temperature and the loading rate. Tucker [199] measured the storage modulus of nitrocellulose/plasticizer mixture over a wide range of stress wave frequency (10^{-8} – 10^{8} Hz) and temperature (223 – 323 K). By using the Williams–Landell–Ferry (WLF) shift function, a master curve was obtained which the storage modulus $G'(\omega)$ curves from all temperatures analyzed are overlaid as shown in Fig. 10-10 in Ref. [199]. We choose 17 points along the modulus line from 10^{-8} Hz to 10^{8} Hz in Fig. 10-10 of Ref. [199] as shown in Figure 101(a), and convert the 17 modulus values to the Prony series parameters as tabulated in Table 24 for the binder of PBX 9404. Mas et al. [104] showed the storage modulus $G'(\omega)$ for the binder of PBX 9501 as shown in Figure 101(b) and the Prony series parameters as tabulated in Table 25.

Table 25. Parameters of the Prony series for the binder of PBX 9501 [104]

Frequency (Hz)	G_i (MPa)	Frequency (Hz)	G_i (MPa)
10^{-6}	0.00417	10^{5}	2.6182
10^{-5}	0.00741	10^{6}	12.882
10^{-4}	0.01585	10^{7}	52.481
10^{-3}	0.03802	10^{8}	223.87
10^{-2}	0.06761	10^{9}	436.52
10^{-1}	0.08913	10^{10}	457.09
1	0.1156	10^{11}	346.74
10^{1}	0.1422	10^{12}	251.19
10^{2}	0.1622	10^{13}	177.83
10^{3}	0.2218	10^{14}	117.49
10^{4}	0.4753	10^{15}	75.858
			$G_e = 0$

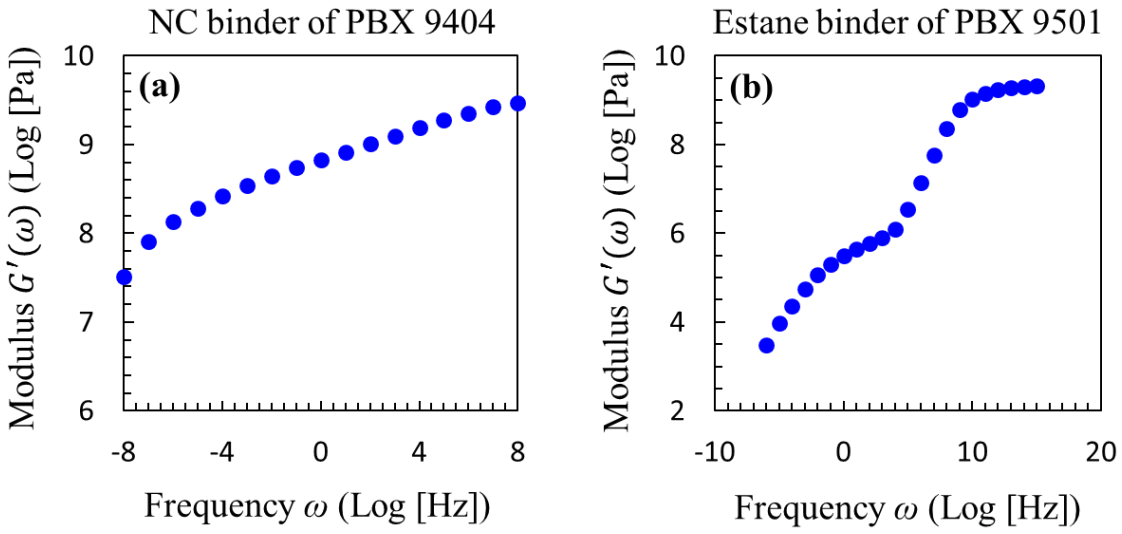

Figure 101. Moduli of the binders of (a) PBX 9404 chosen from Ref. [199] and (b) PBX 9501 presented in Ref. [104].

7.3 Results and Discussion

7.3.1 Shock Initiation Thresholds

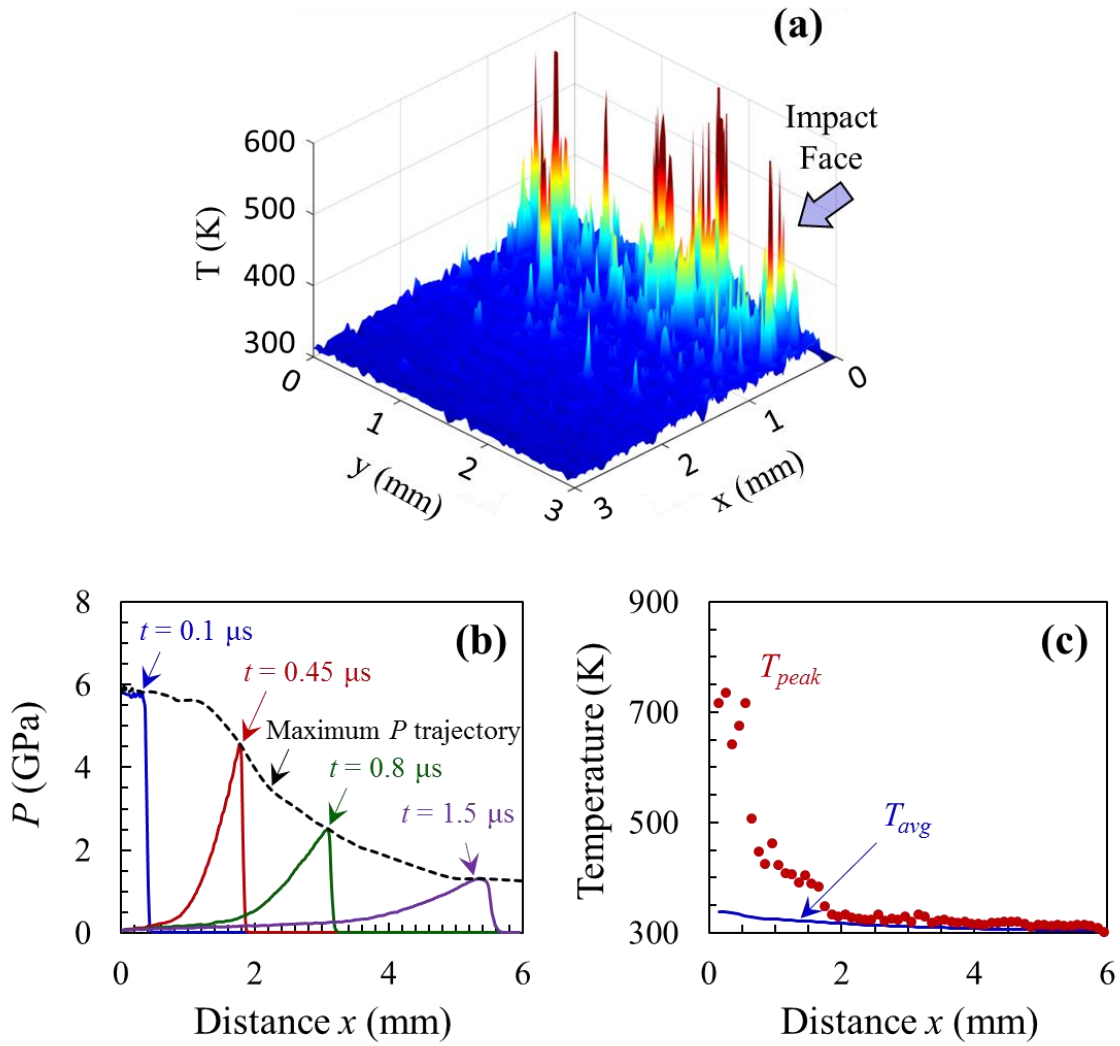

Figure 102. (a) The temperature field of 3 × 3 mm^2 section near the impact surface in the 3 × 15 mm^2 domain, (b) trajectory of peak pressure, and (c) corresponding temperature profile under shock pulse loading with U_p = 800 m/s and τ = 125 ns for a PBX 9404 sample

Predictive calculations are performed in the following steps: First, a group of similar samples having computationally generated microstructures as described in Sec. 7.2.1 are subject to one of the loading conditions discussed in Sec. 2.2. Second, at a preset time interval, the initiation criterion described in Sec. 2.3 is used to identify critical hotspots that have reached the size-temperature criterion. Then a sample is said to be initiated if it has a sufficient number of critical hotspots. Third, for each loading condition, the initiation probability is calculated from the ratio between the ignited samples and the total samples used. Fourth, 50% ignition probability and the required load conditions are extracted from the initiation distribution.

As a shock wave propagates into the material, the temperature of the material increases due to energy dissipation from material inelasticity and friction along crack interfaces. Figure 102(a) shows a typical example of temperature field in the initial 3 × 3 mm^2 area near the impact face of a PBX 9404 sample that was subjected to a shock pulse of U_p = 800 m/s and τ = 125 ns. Hotspots are clustered near the impact surface and rapidly disappear as the distance from the impact face increases because of the stress wave attenuation. Figure 102(b-c) shows the peak pressure trajectory and the corresponding peak and average temperature profiles. Clearly, the peak temperature follows the pattern of the peak pressure as a function of distance from the interface. Although not shown here, similar results are obtained for PBX 9501.

Five statistically equivalent samples are computationally analyzed at each shock pulse intensity (or particle velocity). Different computational samples, just like real samples of the same material in experiments, require slightly different pulse durations under the same shock intensity to locate the threshold boundary. Although individual

samples have the same statistical microstructural attributes, random grain shapes and grain distributions cause the samples to have local fields that fluctuate, thereby giving rise to slightly different behaviors and slightly different energy values even under the same loading conditions. As an example, Figure 103 shows the minimum pulse duration required for initiation for each sample of PBX 9404. The 'X' mark in the figure demarcates the threshold for 50% probability of initiation as determined by all samples over the entire load regime analyzed.

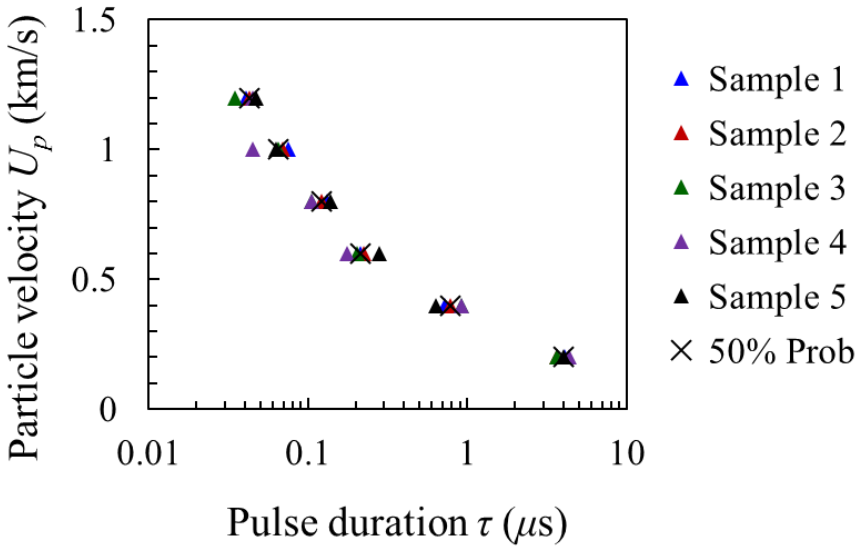

Figure 103. Minimum pulse durations required for initiation predicted from five PBX 9404 samples and the durations for 50% ignition probability. The samples used here have statistically similar microstructures.

As seen in Figure 102(a), shock pulse attenuates as it propagates into the material, generating hotspots clustered near the impact surface. As shock intensity increases, less duration of shock pulse is required for ignition. But shorter pulses result in a faster stress attenuation and a narrower band of hotspot clusters near the impact surface. This trend is analyzed in Figure 104(a-b) which shows the two temperature fields of PBX 9404: one

subject to a low shock intensity and long duration (U_p = 0.4 km/s and τ = 800 ns) and the other a high shock intensity and short duration (U_p = 1.0 km/s and τ = 68 ns). The sample under a low-intensity shock has hotspots dispersed over a half (8 mm) of the computational domain (15mm). On the other hand, the sample under a high-intensity shock has hotspots very close to the impact surface, and no hotspots are seen in the rest of the domain. To quantify this localization behavior, hotspot density is analyzed in terms of area fraction over the shock intensities of U_p = 0.2 – 1.2 km/s for the pulse durations corresponding to the 50% ignition probability obtained from Figure 103. Hotspots with T > 400 K are considered for the analysis. As shown in Figure 104(c), a high-intensity shock generates a higher hotspot density than a low-intensity shock, because a severe energy dissipation occurs near the impact surface under a high-intensity shock. On the contrary, a low-intensity shock generates hotspots further from the impact surface than a high-intensity shock as shown in Figure 104(d).

Predicted initiation thresholds with 50% probability are further analyzed using two types of well-known initiation threshold functions proposed by Walker and Wasley [36] and James [37]. Walker-Wasley threshold is represented by load pressure (P) and load duration (τ). The specific form is

$$P^2\tau = C, \tag{7-2}$$

where C is a material-dependent fitting parameter. James threshold is represented by a hyperbole in terms of input energy ($E = PU_p\tau$) and load intensity in the form of specific kinetic energy ($\Sigma = 0.5{U_p}^2$). Recently, Welle et al. [27] modified James threshold by replacing the specific kinetic energy with a power flux ($\Pi = PU_p$), The resulting form is

$$\frac{\Pi_c}{\Pi}+\frac{E_c}{E}=1, \tag{7-3}$$

where E_c and Π_c are fitting parameters which represent asymptotic thresholds for the critical energy and the critical power flux, respectively.

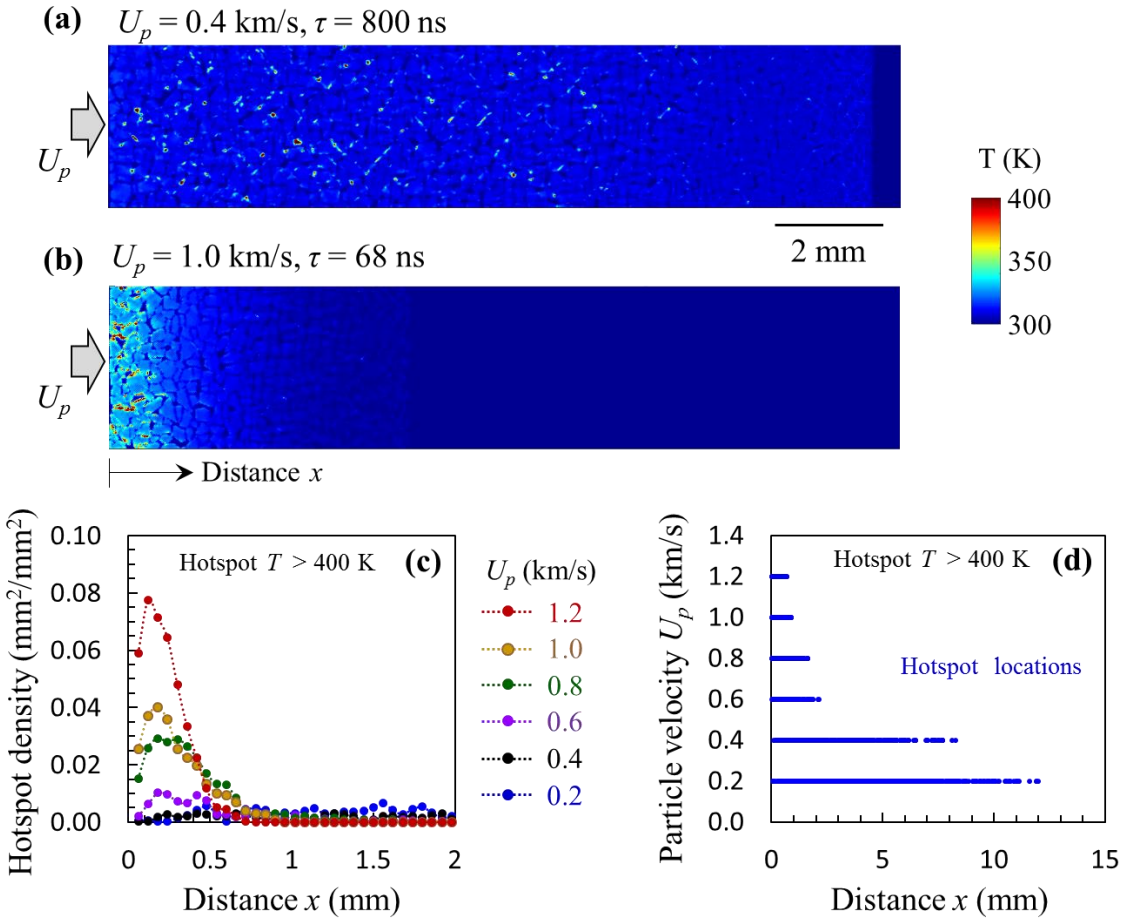

Figure 104. (a-b) The temperature field of PBX 9404 under shock pulses of (a) U_p = 0.4 km/s and τ = 800 ns and (b) U_p = 1 km/s and τ = 68 ns. The pulse durations chosen correspond to the 50% ignition probability. (c-d) For PBX 9404 samples under shock intensities of U_p = 0.2 – 1.2 km/s with the corresponding pulse durations of 50% ignition probability, (c) hotspot density profiles and (d) hotspot distances from the impact surface. Hotspots with T > 400 K are considered.

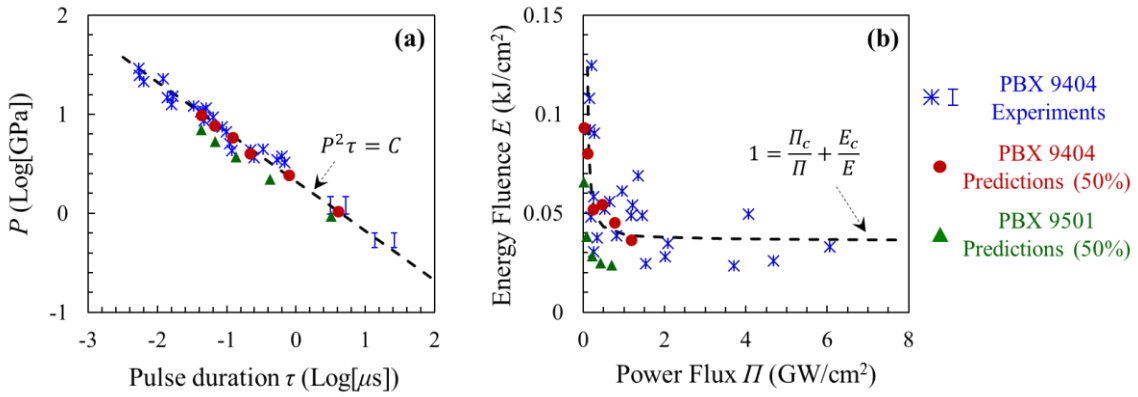

Figure 105. Initiation thresholds obtained from the computational predictions with 50% probability and the experiments ('✳' from Ref. [193] and '⌶' from Ref. [200]) plotted (a) in the P - τ space in log scale and (b) E – Π space.

Figure 105(a) shows a comparison in the P - τ space between the experimental thresholds of PBX 9404 [193, 200] and the computational predictions (50% initiation probability). We also added PBX 9501 for comparison, because they are often said to behave comparably, but PBX 9501 is known to be slightly more sensitive than PBX 9404. The dotted line in Figure 105(a) represents the Walker-Wasley relation. The PBX 9501 prediction is in agreement with the experimental observation. PBX 9501 is slightly more sensitive than PBX 9404. Figure 105(b) shows a representation of the same data shown in Figure 105(a) in the E - Π space with a dotted line for the modified James relation. For this figure, U_s - U_p relation of PBX9404 obtained by Roth [195] is used to convert the pressure of the experimental data to the particle velocity (U_p). Overall, the computationally obtained initiation threshold of PBX 9404 is in good agreement with that observed in experiments. The predicted initiation threshold of HMX/Estane PBX has not been compared to experiments, since no corresponding experimental data is found. The parameters of E_c and Π_c for the experiments and our predictions are listed in Table 26.

Table 26. Parameters in the Walker-Wasley and the James initiation thresholds

	C (10^{12} Pa^2·s)	Π_c (GW/cm^2)	E_c (kJ/cm^2)
Experiments [193, 200] (PBX 9404)	4.58	0.0997	0.0345
Predictions (PBX 9404)	4.09	0.0115	0.0474
Predictions (PBX 9501)	2.10	0.0119	0.0260

7.3.2 Probability of Ignition

As shown in Figure 105(b), there exists a significant data points scatter in both experimental measurements and numerical simulation. These scatter may be attributed to, as pointed out by Gresshoff and Hrousis [161], both experimental uncertainties and material-driven uncertainties. Both types of uncertainty exist in the experiment, but the current simulation considers only selected aspects of the latter uncertainty. Therefore, the threshold lines represented by Eq. (7-2) and (7-3) in Figure 105(a-b) indicate the shock loading conditions for 50% probability of ignition. Additionally, Gresshoff and Hrousis [161] combined the James criterion with an assumption about the initiation probabilistic distribution (scatters due to the two types of uncertainty) by introducing James number, J. with the specific form of

$$\frac{\Pi_c}{\Pi}+\frac{E_c}{E}=\frac{1}{J}. \tag{7-4}$$

This number, defined in Eq, (7-4) serves further as a metric to define safety and performance margins in a probabilistic fashion.

Using the same approach, we may introduce Walker-Wasley number, W, to represent the probability of ignition in the P – τ space with the form of

$$\frac{P^2\tau}{C} = W, \tag{7-5}$$

where W = 1 is the James relation as in Eq. (7-2), W > 1 corresponds to shock loading conditions resulting in greater than 50% ignition probability, and W < 1 corresponds to shock loading conditions resulting in less than 50% ignition probability. As an example of the application of Eq. (7-4) and Eq. (7-5), we presented in Figure 106(a-b), the probability lines based on the Walker-Wasley relation with W = 0.5, 1.0, and 2.0 and the modified James relation with J = 0.5, 1.0, and 1.5. Each W and J number accounts for all combinations of the loading conditions (i.e., pressure and pulse duration for W and energy fluence and power flux for J) that result in the specified probability of ignition.

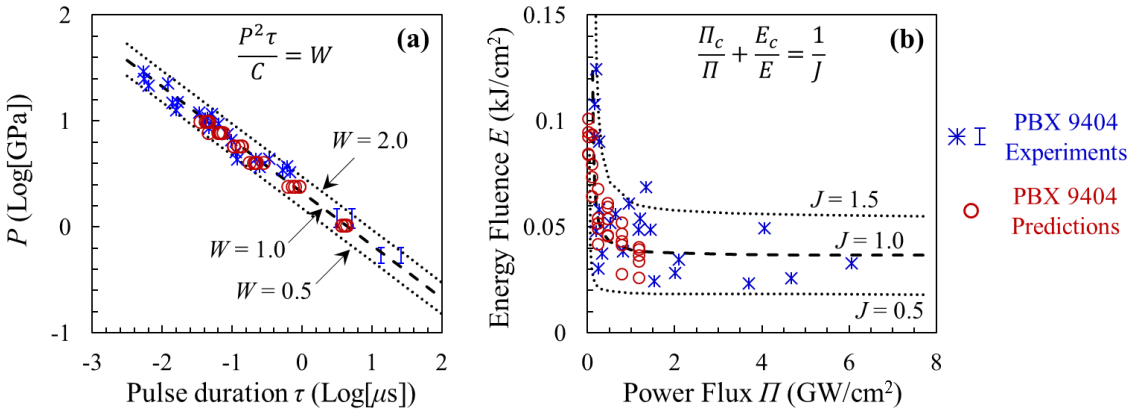

Figure 106. (a) Modified Walker-Wasley relation with W = 0.5, 1.0, and 2.0 and (b) modified James relation with J = 0.5, 1.0, and 1.5 for PBX 9404

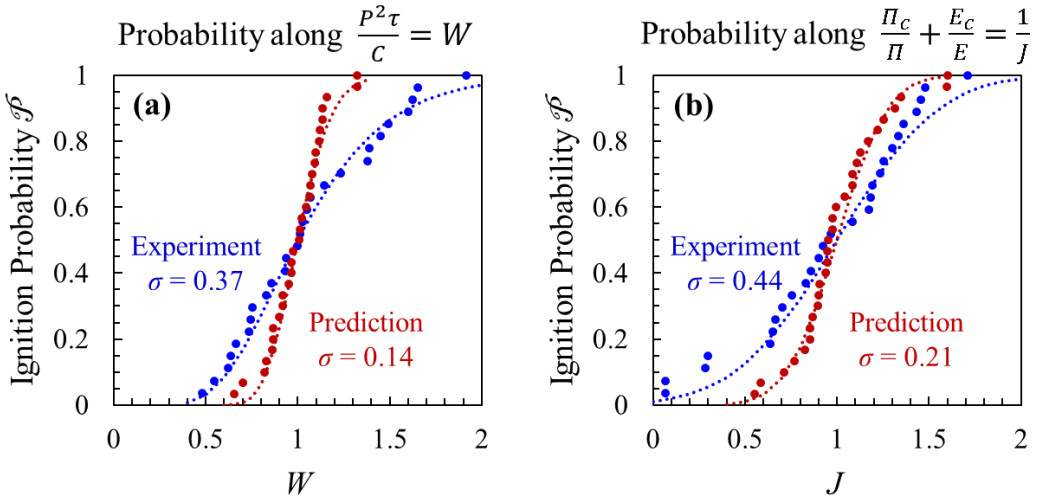

Figure 107. (a) Relationship between *W* and the ignition probability with log-normal distribution fit and (b) relationship between *J* and the ignition probability with normal distribution fit from experimental results and computational predictions of PBX 9404

Figure 107(a-b) shows a comparison of experimental measurements and computational prediction of ignition probability as a function of *W* or *J* for PBX 9404. Assuming that the scatter of the data about the threshold line of $W = 1$ is symmetric in Figure 106(a) on a log-log scale, a log-normal distribution function P (*W*) is used to analyze the initiation probability around a median value of $W = 1$. The specific form of the function is

$$\mathscr{P}(W) = \frac{1}{\sigma\sqrt{2\pi}} \int_{-\infty}^{W} \frac{1}{x} \exp\left[-\frac{(\ln x)^2}{2\sigma^2}\right] dx = \frac{1}{2}\left[1 + \operatorname{erf}\left(\frac{\ln W}{\sqrt{2}\sigma}\right)\right], \tag{7-6}$$

where σ is the standard deviation. By combining Eqs. (7-5) and (7-6), we can obtain a direct relation between the ignition probability $\mathscr{P}$ and the shock loading condition parameters *P* and *τ* in the form of

$$\mathscr{P}(P,\tau)=\frac{1}{2}+\frac{1}{2}\,\mathrm{erf}\left[\frac{1}{\sqrt{2}\sigma}\left(\ln(P^2\tau)-\ln C\right)\right]. \tag{7-7}$$

Similarly, the initiation probability in the E – Π space as shown in Figure 106(b) is analyzed using a normal distribution function P (J), assuming again that the scatter of the data about the threshold line of J = 1 is symmetric in a linear scale. Using the approach to obtain Eqs. (7-6) and (7-7), one finds the initiation probability in terms of J or E and Π as

$$\mathscr{P}(J)=\frac{1}{\sigma\sqrt{2\pi}}\int_{-\infty}^{J}\exp\left[-\frac{(x-1)^2}{2\sigma^2}\right]dx=\frac{1}{2}\left[1+\mathrm{erf}\left(\frac{J-1}{\sqrt{2}\sigma}\right)\right],\ \text{and} \tag{7-8}$$

$$\mathscr{P}(E,\Pi)=\frac{1}{2}+\frac{1}{2}\,\mathrm{erf}\left[\frac{1}{\sqrt{2}\sigma}\left(\frac{E\Pi}{\Pi E_c+E\Pi_c}-1\right)\right]. \tag{7-9}$$

In the above relations, Eqs. (7-6), (7-7), (7-8), and (7-9), the standard deviation σ, Walker-Wasley parameter C, cutoff energy fluence E_c and cutoff power flux Π_c are material constants whose values are determined by experiments or computations reported here (see Table 26). Once these parameters are determined for the material, the probability of ignition $\mathscr{P}$ under any (this is limited to plane thin pulse loadings, not any loadings) loading condition as measured by P and τ or E and Π can be calculated directly from Eq. (7-7) or Eq. (7-9). The W–probability distribution has the standard deviation of 0.37 for experiments and 0.14 for computational predictions. Likewise, the J–probability distribution has the standard deviation of 0.44 for experiments and 0.21 for computational predictions. The standard deviation values obtained from the ignition probability of the samples in Figure 107(a-b) are listed in Table 27. Overall, the computationally predicted standard deviations are smaller than experimental observations. The difference may be attributed to the following factors. First, the loading conditions such as pulse durations and pressure in simulations are more precisely controlled than those in experiments (experimental uncertainties are not considered in computation). Second, the experimental

data shown in this paper are the collection of work by multiple groups of researchers (Weingart et al. [193], Gittings [201], Trott and Jung [202], all of which presented in Weingart et al. [193] and Christiansen and Taylor [203] presented in Hayes [200]). Thirdly, the distribution of computational morphology is very limited. Therefore, uncertainties in microstructures and experimental setups may have influenced the differences.

Table 27. Standard deviations presented in Figure 107(a-b)

	Log-normal distribution along $P^2\tau/C=W$	Normal distribution along $\Pi_c/\Pi+E_c/E=1/J$
Experiments [193, 200] (PBX 9404)	0.37	0.44
Predictions (PBX 9404)	0.14	0.21

7.3.2 Effect of Initial Debonding

Microstructures with initial defects are generated to study the effects of defects on the ignition behavior of PBX 9501. The specific type of initial defect considered debonding sites at the interfaces between energetic granules and the Estane binder. Three debonding levels (0%, 50%, and 100%) are considered. These levels indicate different ratios between the debonded grain boundaries (with zero bonding strength) and the total grain boundaries. A debonding level of 0% means the grains are perfectly bonded to the binder, 50% means half of the surface of each and every grain is debonded, and 100% means the entire boundary of each and every grain is initially debonded. The interface with initial debonding has zero cohesive strength and immediately creates fracture upon impact. The microstructures with the three levels of initial debonding are shown in Figure

108. Five samples are generated for each debonding level. The samples in each debonding level have similar attributes such as volume fraction and grain size distribution.

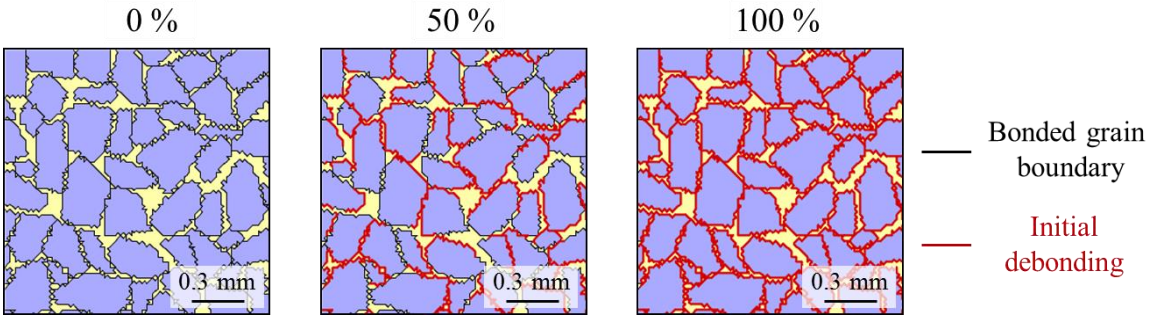

Figure 108. Microstructures with initial debonding at the interfaces between grains and the binder. Three debonding levels (0%, 50%, and 100%) are shown.

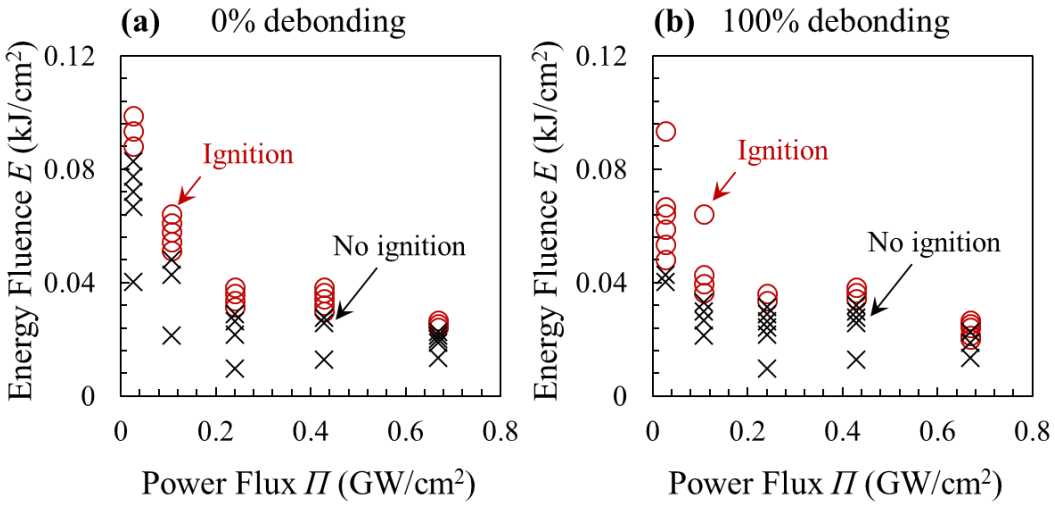

Figure 109. Ignition threshold determination from (a) a sample with 0% debonding and (b) a sample with 100% debonding

The critical energy threshold for ignition is analyzed using the hotspot ignition criterion discussed in Chapter 3.2. The ignition response of a sample is recorded as “go” if the sample explodes and as “no go” if the sample does not explode. As an example, Figure 109 shows the results from a sample with 0% debonding level and a sample with

100% debonding level. In general, a higher loading rate (power flux) results in low energy required for ignition (lower energy fluence) for both 0% and 100% debonding levels.

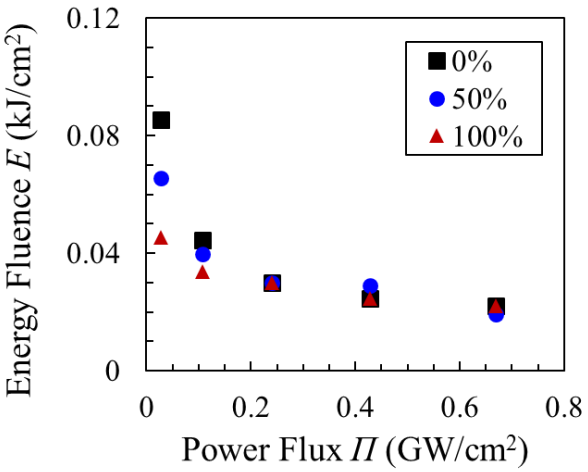

Figure 110. Computationally predicted 50% ignition thresholds of PBX 9501 from all levels of initial debonding analyzed.

Five statistically equivalent samples are computationally analyzed at each energy input rate (or power flux). The different samples require slightly different levels of energy fluence under the same load intensity or power flux (energy input rate). The threshold for 50% probability of ignition is determined from all samples over the entire load regime analyzed. Figure 110 shows the 50% ignition thresholds of PBX 9501 (HMX/Estane) for the three levels of initial debonding (0%, 50%, and 100%). At a low-intensity loading regime ($U_p \leq 400\,\mathrm{m/s}, \Pi \leq 0.11\,\mathrm{GW/cm^2}$), a sample with a low debonding level requires higher energy for ignition as compared to that with a high debonding level. For example, at $\Pi = 0.03\,\mathrm{GW/cm^2}$ ($U_p = 200\,\mathrm{m/s}$), the energy required for the sample with 0% debonding to ignite is nearly twice of the energy required for the sample with 100% debonding, and the energy required for the sample with 50% debonding falls in between the energy for the sample with 0% debonding and the energy for the sample with 100%

debonding. This trend is more pronounced under a low-intensity loading. Under a high-intensity loading, the level of initial debonding does not affect the ignition sensitivity of the material.

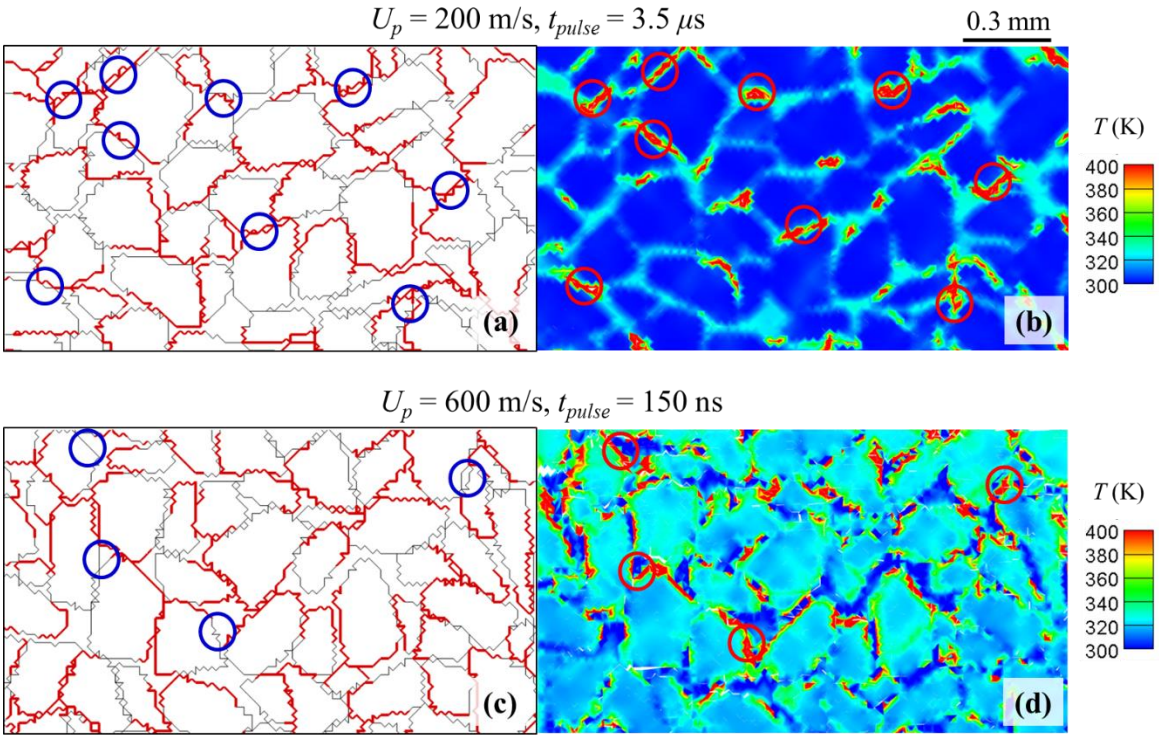

Figure 111. Strong correlations between (a) initial debonding sites and (b) hotspot locations for a low intensity loading (U_p = 200 m/s), and weak correlations between (c) initial debonding sites and (d) hotspot locations for a high intensity loading (U_p = 600 m/s). As an example, several hotspot locations are demarcated by '◯' and the corresponding interfaces are demarcated by '◯'.

To understand the mechanism of the distinct difference in sensitivity under a low-intensity loading and a negligible difference under a high-intensity loading, the correlation between hotspot locations and the initial debonding sites are analyzed. Figure 111(a) shows the microstructure with 50% initial debonding level and Figure 111(b) shows the

hotspot locations under a low-intensity loading ($U_p = 200\,\mathrm{m/s}$). Most hotspots in Figure 111(b) are located at the initially debonded interfaces in Figure 111(a). On the contrary, for a high-intensity loading, this correlation is weak. Figure 111(c) shows the microstructure with 50% initial debonding level and Figure 111(d) shows the hotspot locations under a high-intensity loading ($U_p = 600\,\mathrm{m/s}$). Several hotspots in Figure 111(d) are located at the interfaces where the bonding is initially intact in Figure 111(c).

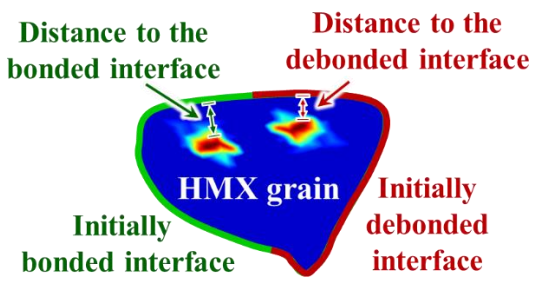

Figure 112. Illustration of proximity measurement from hotspots to the debonded interface (in red) and to the bonded interface (in green).

The correlations observed in Figure 111 are quantified using the proximity from a hotspot to the interface. To illustrate the method of quantification, Figure 112 shows the distance between the hotspot and the nearest debonded interface (indicated in red) and the distance between the hotspot and the nearest intact interface (indicated in green). The distances are obtained from all hotspots of which the temperature is higher than 400 K ($T > 400$ K). Figure 113 shows the histogram of the distance from hotspots to the nearest interfaces. Since there are more hotspots near the interfaces than inside the grains, the number of hotspot decreases as the distance measured increases. The sum of hotspot area for a given range of distance in each bin is normalized by the total sum of hotspot area in the domain. For a low-intensity loading ($U_p = 200\,\mathrm{m/s}$), the clear difference between Figure 113(a) and Figure 113(b) indicates that more hotspots are generated near the

interfaces that are initially debonded than those generated near the interfaces that are intact. For the intensity of $U_p = 600\,\mathrm{m/s}$, the disparity between Figure 113(c) and Figure 113(d) is less than that for the intensity of $U_p = 200\,\mathrm{m/s}$. For the intensity of $U_p = 1000\,\mathrm{m/s}$, there is no preference of hotspot locations between the intact interfaces and the initially debonded interfaces as shown in Figure 113(e-f). The results suggest that, under a high intensity, interfaces between grains and the binder fail regardless of the bonding condition, and the influence of initial defects on the material sensitivity depends on the loading intensity due to the shift of the preferable locations of hotspot formation. Therefore, the effect of initial debonding on the ignition sensitivity is more pronounced under a weak intensity loading than under a strong intensity loading.

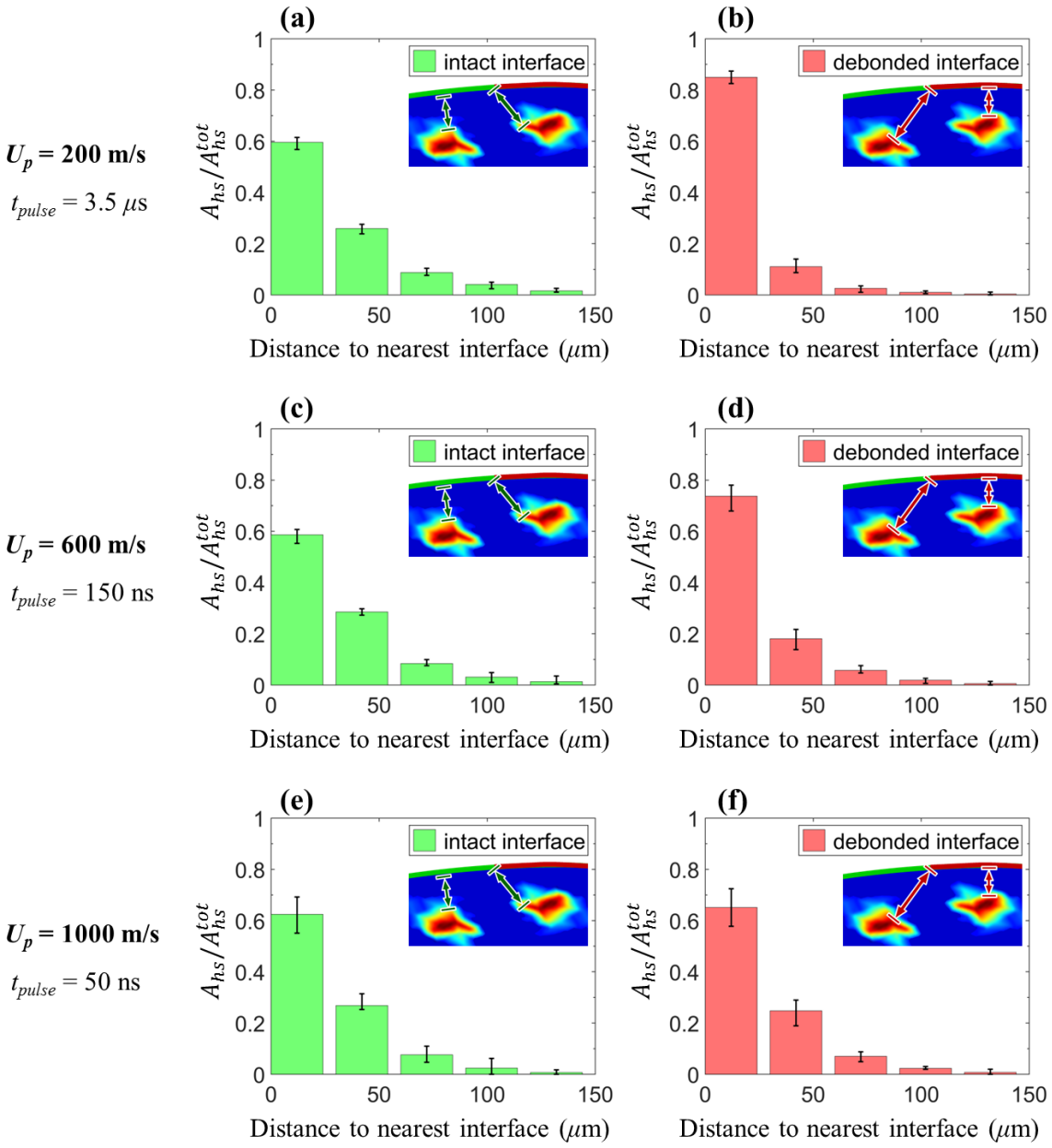

Figure 113. Histogram of hotspot area fraction with respect to the distance from the intact interface (in green) and the distance from the initially debonded interface (in red) subject to the load intensity of (a-b) U_p = 200 m/s, (c-d) U_p = 600 m/s, and (e-f) U_p = 1000 m/s.

7.4 Conclusion

The initiation thresholds of PBX 9404 and PBX 9501 are predicted in terms of shock intensities and pulse durations via multiphysics simulations. The prediction is based on material microstructural attributes and fundamental constituents. The simulations consider the configuration and conditions of actual experiments performed by Weingart et al. [32]. The simulations account for the controlled loading of thin-flyer shock experiments. The predicted initiation threshold of PBX 9404 is in good agreement with shock experiments. The predicted initiation threshold of PBX 9501 has not been compared to experiments, since no corresponding experimental data is found. Experiments of Run-to-Detonation [8, 59] suggest that both PBX9501 and PBX9404 have a similar level of sensitivity.

The initiation thresholds obtained are represented in the form of Walker-Wasley relation ($P^2\tau = C$) and the James relation ($\Pi_c/\Pi + E_c/E = 1$). The stochastic nature of initiation behavior is analyzed and represented in terms of probability distribution functions. Once the standard deviation parameter is determined for a given material, the probability of ignition $\mathscr{P}$ under any loading condition can be obtained.

The effect of initial debonding on the ignition sensitivity is analyzed with different amounts of debonding for a wide range of load intensity. The samples with the initial debonding of 50% level are more sensitive than those with no debonding but less sensitive than those with the initial debonding of 100% level. This feature is more pronounced in the low-intensity loading regime and becomes negligible in the high-intensity regime. The results suggest that, under low-intensity loading, fracture and subsequent hotspot formation are more influenced by initial debonding than those under high-intensity loading.

CHAPTER 8: SUMMARY AND FUTURE DIRECTION

8.1 Summary

Safety in the handling of explosives and the vulnerability to accidental stimuli relate to the sensitivity of the materials. The material heterogeneity of explosives is an important factor that affects the material sensitivity, since the energy imparted by external insults is converted into heating in localized regions of the heterogeneous material, known as hotspots, and the ignition and subsequent detonation are caused by exothermic chemical reaction at the hotspots. The aim of this study is to understand the mechanisms of hotspot evolution from the dynamic response of solid explosives subject to a wide range of impact intensity, and computationally predict the initiation sensitivity accounting for microstructural heterogeneities.

In order to achieve the aim of the study, this thesis presents the relevant work in the following chapters. Chapter 2 presents the numerical modeling framework used in this study. The framework is based on 2-D Lagrangian cohesive finite element (CFEM) accounting for large deformation, energy dissipations due to plastic and viscoelastic deformation, transgranular crack propagation in arbitrary directions, debonding at the interfaces, frictional heating. The framework is initially developed by Barua [87], and further improved for this study by adding the capability of handling initial voids and initial defects in the microstructure and shock response under extreme pressure with numerical stability and reliability. The framework is designed to model the fully coupled thermo-mechanical behavior of explosive composites and predict the ignition sensitivity.

Hotspot fields resulting from impact loading on granular explosives (GXs) and polymer-bonded explosives (PBXs) are characterized with respect to their size

distributions and temperatures in Chapter 3. In this chapter, a new criterion is established for the ignition conditions of explosive material. Hotspots are explicitly obtained and quantified from the CFEM framework, and the ignition criterion is used to determine the material sensitivity. For different loading configurations and materials, the study has yielded the critical impact velocity for ignition and critical time required for ignition as a function of material and impact velocity. The critical time to ignition is also highly affected by microstructure morphology. The stochasticity of the material sensitivity is analyzed using multiple samples with statistically similar microstructural attributes. The analyses have focused on the influence of random microstructure morphology variations on the critical time to ignition and obtained the probability distribution of the time to criticality. This probability distribution is quantified as a function of microstructural attributes including grain volume fraction, grain size and specific binder-grain interface area. The predicted threshold velocity v_c for ignition is consistent with available experimental data of PBX 9501.

The random morphology is not the only factor that affects the stochastic ignition behavior. In fact, the stochastic hotspot generation is caused by a combined effect of various sources in the sample. Chapter 4 discusses the development of an approach that computationally predicts the probability of ignition of polymer-bonded explosives (PBXs) accounting for the combined effect of two sources of stochasticity in microstructural attributes – random morphologies of constituent phases and the bonding strength of the grain-binder interfaces. A nested superposition model is proposed in order to understand how the different sources combine to affect the overall ignition behavior. The model captures the interactions between the two sources of variations in material attributes. In experiments, the final data set comes out as combined probability in most cases, and separation of the effects of the individual sources is often challenging. As an application

of the nested probability model, experimental data performed by Subero-Couroyer et al. [146] are used. The analysis for the actual experiment requires the inverse approach. Starting from final combined data, we extracted the relations between the first source and the second source of variations. By using the nested probability model, we have been able to separate and quantify the effect of degradation and macropores. Although only two sources of stochasticity are considered for the combined probability in Chapter 4, the approach developed in this chapter can be applied to an analysis on the effect of three or more sources of stochasticity combined.

The inclusions in PBXs affect the ignition sensitivity. Chapter 5 discusses the ignition desensitization of PBX via aluminization. Specifically, it analyzes the effect of Al addition on crack densities, hotspot fractions, and ignition probability. The ignition behavior of PBX microstructures with 6-18% Al by volume is analyzed and compared to that of the corresponding unaluminized PBX. The mean time to ignition (t_{50}) for the aluminized PBXs delays by 1 – 1.7 μs (24 – 60% delay) as compared to that for the corresponding unaluminized PBX. To delineate the mechanisms responsible for the ignition delay, the differences in overall internal stress, dissipations due to fracture and inelasticity, and hotspot field characteristics are quantified. It is found that, for the material configuration studied, aluminization decreases the crack density and frictional energy dissipation in the HMX phase. Aluminization also causes the frictional dissipation per unit crack length to decrease.

Chapter 6 discusses the prediction on ignition threshold of pressed HMX with different grain sizes subject to shock loading. The prediction is based on the James-type ignition thresholds via multiphysics simulations. First, “go” and “nogo” of the ignition event is recorded for each combination of power flux and energy fluence for each sample.

Then, statistically similar microstructure sample sets yield the probabilities of ignition for each loading condition. The 50% ignition thresholds from the computational predictions are in general agreement with measurements from shock experiments provided by AFRL. The stochasticity of ignition threshold is analyzed from multiple samples subject to the same load condition and represented in the form of ignition probability as a function of a normalization parameter J which incorporates the load intensity (power flux) and the energy input (energy fluence). The material-dependent ignition probability map is obtained for a wide range of loading conditions.

The analysis is expanded in Chapter 7 by including the shock ignition predictions of PBXs with different types of binder and initial defects. The specific types of binder considered is Estane which is the binder of PBX 9501 and Nitrocellulose (NC) which is the binder of PBX 9404. The type of initial defect considered is the debonding at the interfaces between energetic crystals and a binder in PBXs. The predicted initiation threshold of PBX 9404 is in good agreement with shock experiments. The initiation thresholds obtained are represented in the form of Walker-Wasley relation ($P^2\tau = C$) and the James relation ($\Pi_c/\Pi + E_c/E = 1$). The stochastic nature of initiation behavior is analyzed and represented in terms of probability distribution functions, and the material-dependent ignition probability map is obtained. The analysis of this chapter is further expanded to the effect of initial debonding. Three levels of debonding (0%, 50%, 100%) at the interfaces between HMX grains and the Estane binder are considered. The results show that the material becomes more sensitive with the increase in the debonding level, and fracture and subsequent hotspot formation are more influenced by initial debonding under low-intensity loading than those under high-intensity loading.

8.2 Suggestions for Future Directions

So far, this study has focused on the relationship between microstructural aspects and the performance of explosives in terms of ignition sensitivity. The microstructural aspects analyzed in this study include random morphology, average grain size, different binder types, metallic inclusions, and initial debonding between energetic grains and the binder. Although many aspects of microstructural attributes are analyzed in this study as mentioned above, there are many other factors that affect the hotspot formation.

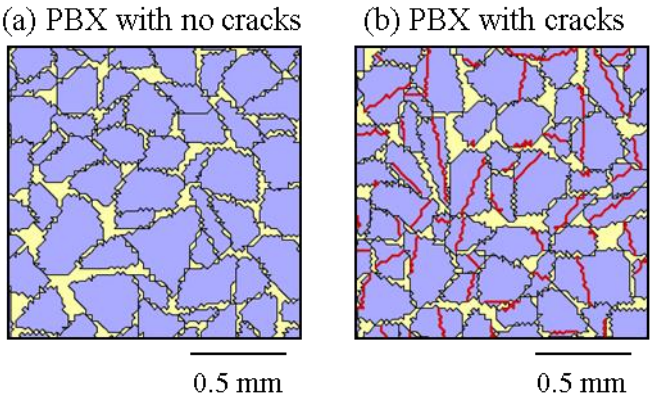

Figure 114. PBX microstructure (a) without transgranular cracks and (b) with transgranular cracks

Stress concentration at the initial defects are known for one of the main hotspot formation mechanisms. This study has considered the effect of initial debonding between energetic grains and the binder. Other type of initial defects which should be considered are transgranular cracks and micropores in the energetic grains. The transgranular cracks occur during manufacturing PBXs. The energetic particles break to small pieces in the pressing process. Molek et al. [165] reported that the particle size decreases by roughly one or two orders of magnitude after sample preparation, which suggests a significant amount of initial cracks in PBXs. The computational framework used in this thesis allows

to generate microstructures with initial transgranular cracks in PBXs as shown in Figure 114. The initial transgranular cracks as indicated by red lines in Figure 114(b) are defined as a path consisting of cohesive elements with zero traction strength.

Micropores affect the material sensitivity, since the pore collapse is one of the main hotspot formation mechanism under shock loading as mentioned in Chapter 1. The computational framework developed in this thesis permits the analysis on the microstructure with voids. For example, the microstructure shown in Figure 1 has voids between particles, and the particles can directly interact with each other without intermediate medium. Chapter 3 shows the analysis on granular HMX with voids and compares the sensitivity of the granular HMX including voids to the sensitivity of PBX without a void. Modeling of micropore in Lagrangian framework, however, requires higher numerical reliability than modeling of granular HMX with voids because of a severe stress localization and jetting at the pore under shock loading. To alleviate the issue of element distortion at the pore, a fine mesh should be assigned to the vicinity of the pore.

Chemical reaction is another important subject for predicting the ignition sensitivity of energetic materials. The research in this thesis so far has utilized a criticality threshold based on hotspot size and temperature for the ignition criterion, instead of explicit modeling of chemical reaction. Chemical reaction of β-HMX has been studied by many researchers [176, 204, 205], but it is a complicated process involving multiple radicals which vary significantly depending on the temperature. Tarver and Tran [34] proposed a simplified 4-step chemical kinetics model for the HMX decomposition. A new framework based on a two-dimensional finite difference method (FDM) is developed to analyze the reaction behavior of HMX. This framework utilizes the Tarver's 4-step kinetics model and conduction and predicts the thermal runaway of hotspots based on the

temperature data obtained from the CFEM calculation. The results from this framework are compared to experiments and analytical data from literature. The detailed information of the framework is provided in APPENDIX. This framework can be used to analyze the effect of the hotspot coalescence. The current model of hotspot criticality threshold based on hotspot size and temperature is applicable to individual hotspots. The hotspots in close proximity would interact each other and might evolve to a combined critical hotspot. The FDM framework introduced here can be used to analyze the criticality of a cluster of several hotspots if each hotspot in the cluster is below the current criticality criterion.

Another direction of future research is to predict the detonation behavior. As mentioned in Chapter 1, reactive burn models do not explicitly capture hotspot formations during shock loading. Instead, the models estimate hotspot quantities based on loading pressure or input energy. As remarked by Horie [68], direct use of local hotspots at the grain level for macro scale calculation is challenging due to its complexity. The Lagrangian CFEM framework used in this thesis cannot model reactive flow during the detonation process, but it can provide hotspot quantities for various microstructure types and loading conditions. The gap between these two approaches can be linked via the measure of hotspot. For example, the number density and the area fraction of hotspot are obtained in Chapter 4 as shown in Figure 52 and Nichols III and Tarver [72] obtained the relation between hotspot densities and burn rates using a reactive flow model. Combining the two models can provide a complete understanding from local hotspot formation based on microstructures to the final detonation.

APPENDIX: A FRAMEWORK ACCOUNTING FOR CHEMICAL DECOMPOSITION OF HMX

A new framework based on the two-dimensional finite difference method (FDM) including chemical reaction is developed. The FDM framework developed here accounts for heat conduction and the thermal decomposition of β-HMX based on the 4-step chemical kinetics model proposed by Tarver and Tran [34]. This framework does not allow mass transfer or mechanical deformation. The process of the 4-step model is

$$\begin{aligned} &\beta\text{-HMX (A)} \rightarrow \delta\text{-HMX (B)} \rightarrow \text{solid intermediates (C)} \\ &\rightarrow \text{intermediate gases (D)} \twoheadrightarrow \text{final gas (E)}, \end{aligned} \tag{A-1}$$

where '→' indicates 1st order reaction, and '➔' indicates 2nd order reaction. The equations of mass change between compositions are

$$\left.\begin{aligned} &\frac{d[A]}{dt} = -k_1[A]; \quad \frac{d[B]}{dt} = k_1[A] - k_2[B]; \quad \frac{d[C]}{dt} = k_2[B] - k_3[C] \\ &\frac{d[D]}{dt} = k_3[C] - k_4[D]^2; \quad \frac{d[E]}{dt} = k_4[D]^2 \end{aligned}\right\}, \tag{A-2}$$

where k is the Arrhenius reaction rate constant ($k = Z \cdot \exp(E_A/RT)$). The heat equations for the 1st order reaction (A → B) and the 2nd order reaction (D ➔ E) are

$$\left.\begin{aligned} &\frac{dQ_1}{dt} = q_1^c k_1[A] \\ &\frac{dQ_4}{dt} = q_4^c k_4[D]^2 \end{aligned}\right\}, \tag{A-3}$$

where q_i^c is the heat of reaction for the i-th step.

As an example of application, the time taken to the reaction of HMX is obtained for three different initial temperatures, 600 K, 620 K, and 650 K. The results are shown in Figure 115. This particular calculation does not consider the heat conduction between the hotspots and the environment (Adiabatic condition). The temperature decreases at the early stage of the process because the first two steps in the chemical kinetics model are endothermic. The temperature increases rapidly at the last stage because of the exothermic process of the last two steps in the chemical kinetics model. As the temperature increases from 600 K to 650 K, the time to decomposition decreases from 790 s to 21 s.

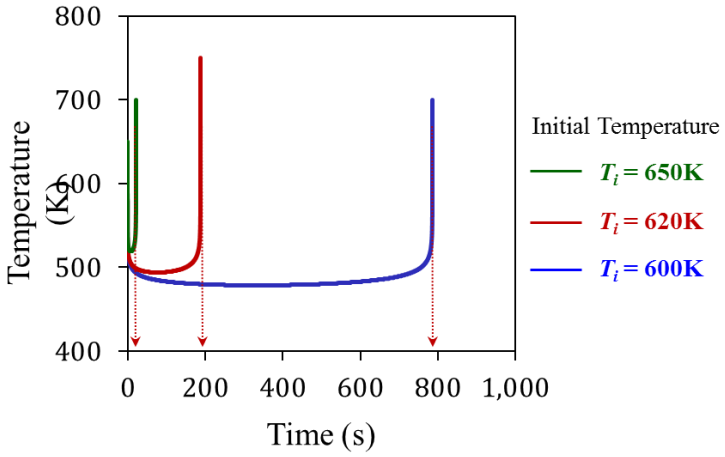

Figure 115. Evolution of temperature due to the reaction of β-HMX with various initial temperatures

To verify the implementation of the 4-step kinetics model, the decomposition time obtained from the FDM calculation is compared to the experiments [35], as shown in Figure 116. Adiabatic condition indicates no heat transfer between the hotspot and the environment. Isothermal condition assumes an infinite rate of heat transfer between β-HMX and the environment. Therefore, the temperature of β-HMX is kept constant as the given temperature (i.e., initial temperature) regardless of its endothermic or exothermic process. Adiabatic condition represents infinitely large HMX with uniform temperature,

and isothermal condition represents extremely small HMX of which heat is transferred instantly to its surroundings. For low temperature, the decomposition takes long time, which facilitates the influence of heat conduction, and the experimental results follow the calculations with the isothermal condition. For high temperature, the decomposition time is short, and the experimental results follow the calculation with the adiabatic condition. The crossover of the results between the adiabatic condition and the isothermal condition is in the millisecond order (t = 10^{-3} s), which coincides with the thermal diffusion time scale of millisecond. The characteristic diffusion time can be estimated as d^2/α where d is a typical hotspot size which is in the order of micrometer and α is the thermal diffusivity (α = 2.17 × 10^{-7} m^2/s).

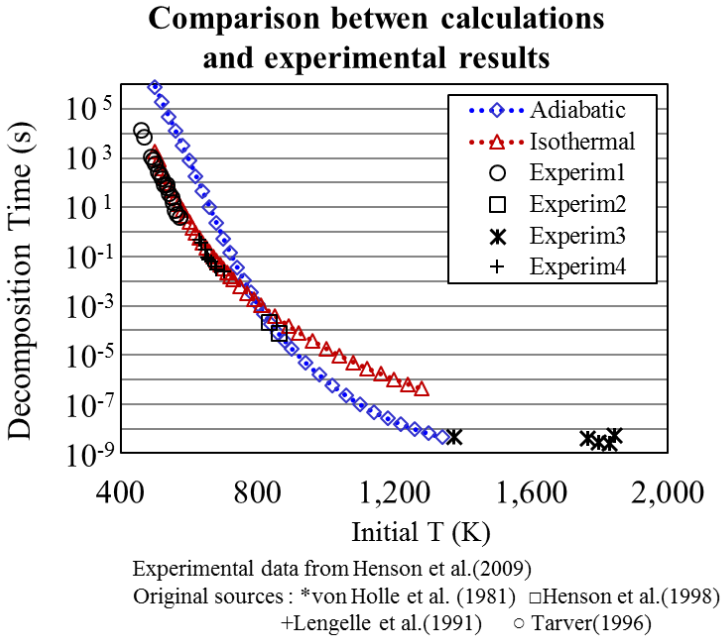

Figure 116. Comparison of the decomposition time of β-HMX between computational results and experimental results

The ignition criterion based on hotspot size and temperature is analyzed based on the FDM framework. The framework adopts the 4-step kinetics model (Tarver et al., 2004

in Ref. [34]) and heat conduction. The minimum initial temperature that leads to thermal runaway for each hotspot diameter is obtained. The results from the framework are compared to Tarver's previous work (Tarver et al., 1996 in Ref. [33]), as shown in Figure 117.

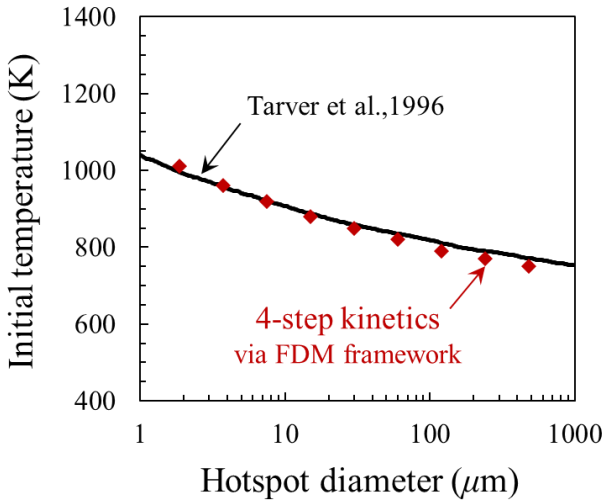

Figure 117. Criticality thresholds from Ref. [33] and from FDM calculation based on Ref. [34]

The time scale of chemical reaction differs by several orders of magnitude from the time scale of hotspot evolution driven by mechanical loading. Specifically, for the hotspot size in the range of 10 – 100 μm, the reaction time of the hotspot at the critical temperature threshold is in the order of 0.1 – 1 millisecond, whereas the hotspot evolution through mechanical loading is in the order of microsecond. Therefore, two-step approach is utilized to model the hotspot ignition behavior over the wide range of the time scale. At the first step, hotspot temperature field is obtained from the CFEM framework. At the second step, the hotspot field and the corresponding microstructure data are imported to the FDM-based chemical reaction framework. The FDM framework considers the chemical decomposition of HMX and the conduction of HMX and Estane binder. The

chemical decomposition of Estane is not considered. This two-step approach assumes that there is no further temperature rise at the hotspot due to mechanical loading if the shock wave has passed. As an application of this approach, two hotspot fields are obtained from the CFEM framework: one with the maximum hotspot temperature of T_{max} = 760 K which is below the ignition criterion and the other with the maximum temperature of T_{max} = 850 K which is above the ignition criterion. Figure 118 shows the evolution of the hotspot fields due to chemical reaction and heat conduction. The hotspots in Figure 118(a) are eventually dissipated, whereas the hotspot with T = 850 K in Figure 118(b) evolves and reaches thermal runaway.

In this section, a two-dimensional FDM framework including the Tarver's four-step chemical kinetics model is developed. The framework allows to study the effect of the chemical decomposition of HMX on the evolution of hotspots for the time scale range from microseconds to seconds. The computational predictions on time to ignition are compared to experimental observations. The results show that the experiments agree well with the computational model. A new criticality criterion based on hotspot size and temperature obtained from the FDM framework shows negligible difference from the previously reported criticality criterion in Ref. [33]. The framework uses the hotspot fields from the CFEM calculations and provides the evolution of the temperature field due to chemical reaction and conduction. The results show that the hotspots with their maximum temperature below the criticality criterion eventually dissipate in the domain. If a hotspot is over the criticality criterion, the hotspot reaches to thermal runaway.

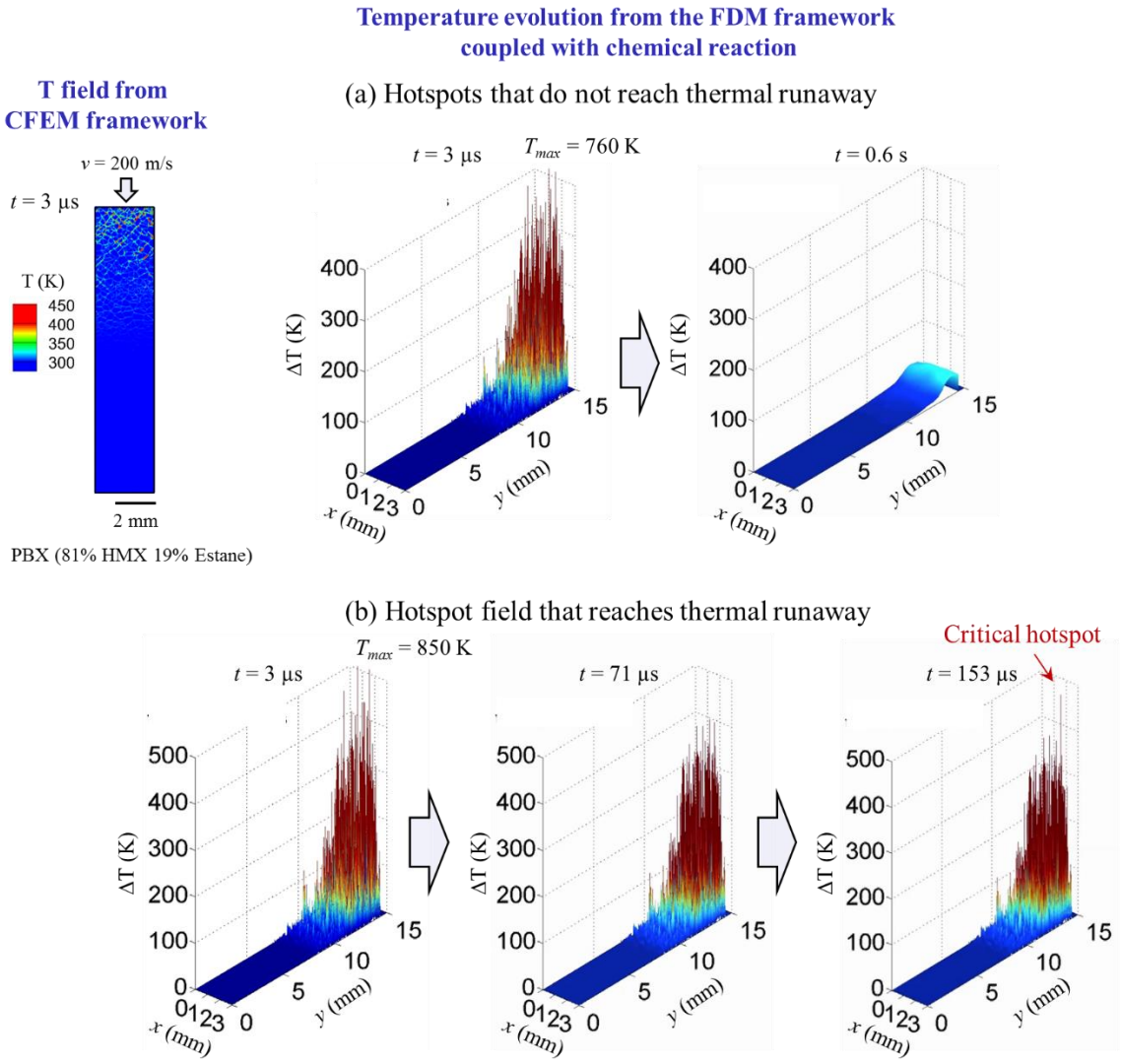

Figure 118. Evolution of temperature due to the decomposition of HMX and conduction in PBX from two temperature fields: (a) T field with T_{max} = 760 K (below the criticality) and (b) T field with T_{max} = 850 K (above the criticality)

REFERENCES

[1] M. H. Keshavarz and H. R. Pouretedal, "Simple empirical method for prediction of impact sensitivity of selected class of explosives," *Journal of Hazardous Materials,* vol. 124, pp. 27-33, 2005.

[2] B. W. Asay, *Non-Shock Initiation of Explosives*: Springer, 2010.

[3] W. H. Andersen and N. A. Louie, "Projectile Impact Ignition Characteristics of Propellants .1. Deflagrating Composite Explosive," *Combustion Science and Technology,* vol. 20, pp. 153-160, 1979.

[4] W. H. Andersen and G. P. Stillman, "Projectile Impact Ignition Characteristics of Propellants .3. Effect of Particle-Size and Porosity," *Combustion Science and Technology,* vol. 32, pp. 237-244, 1983.

[5] B. A. Mason, L. J. Groven, and S. F. Son, "The role of microstructure refinement on the impact ignition and combustion behavior of mechanically activated Ni/Al reactive composites," *Journal of Applied Physics,* vol. 114, Sep 21 2013.

[6] F. P. Bowden and A. D. Yoffe, *Initiation and growth of explosion in liquids and solids*: Cambridge University Press, 1952.

[7] F. P. Bowden and A. D. Yoffe, *Fast reactions in solids*: Butterworths Scientific Publications, 1958.

[8] C. L. Mader, *Numerical modeling of explosives and propellants,* 2nd ed.: CRC press, 1998.

[9] E. L. Lee and C. M. Tarver, "Phenomenological model of shock initiation in heterogeneous explosives," *Physics of Fluids,* vol. 23, pp. 2362-2372, 1980.

[10] J. N. Johnson, P. K. Tang, and C. A. Forest, "Shock-wave initiation of heterogeneous reactive solids," *Journal of Applied Physics,* vol. 57, pp. 4323-4334, 1985.

[11] A. W. Campbell, W. C. Davis, and J. R. Travis, "Shock Initiation of Detonation in Liquid Explosives," *Physics of Fluids,* vol. 4, pp. 498-510, 1961.

[12] A. W. Campbell, W. C. Davis, J. B. Ramsay, and J. R. Travis, "Shock Initiation of Solid Explosives," *Physics of Fluids,* vol. 4, pp. 511-521, 1961.

[13] J. T. Mang, R. P. Hjelm, and E. G. Francois, "Measurement of Porosity in a Composite High Explosive as a Function of Pressing Conditions by Ultra-Small-Angle Neutron Scattering with Contrast Variation," *Propellants, Explosives, Pyrotechnics,* vol. 35, pp. 7-14, 2010.

[14] N. K. Bourne and A. M. Milne, "The temperature of a shock-collapsed cavity," *Proceedings of the Royal Society a-Mathematical Physical and Engineering Sciences,* vol. 459, pp. 1851-1861, Aug 8 2003.

[15] N. K. Bourne and J. E. Field, "Explosive ignition by the collapse of cavities," *Proceedings of the Royal Society a-Mathematical Physical and Engineering Sciences,* vol. 455, pp. 2411-2426, Jul 8 1999.

[16] R. A. Austin, N. R. Barton, W. M. Howard, and L. E. Fried, "Modeling pore collapse and chemical reactions in shock-loaded HMX crystals," *Journal of Physics: Conference Series,* vol. 500, p. 052002, 2014.

[17] R. A. Austin, N. R. Barton, J. E. Reaugh, and L. E. Fried, "Direct numerical simulation of shear localization and decomposition reactions in shock-loaded HMX crystal," *Journal of Applied Physics,* vol. 117, p. 185902, 2015.

[18] S. Chidester, L. Green, and C. Lee, "A frictional work predictive method for the initiation of solid high explosives from low-pressure impacts," Lawrence Livermore National Lab., CA (United States)1993.

[19] M. M. Chaudhri, "Photographic Evidence for Ignition by Friction in a Deflagrating Explosive Single-Crystal," *Journal of Physics D-Applied Physics*, vol. 25, pp. 552-557, Mar 14 1992.

[20] R. V. Browning and R. J. Scammon, "Microstructural model of ignition for time varying loading conditions," *Shock Compression of Condensed Matter-2001, Pts 1 and 2, Proceedings*, vol. 620, pp. 987-990, 2002.

[21] C. Gruau, D. Picart, R. Belmas, E. Bouton, F. Delmaire-Sizes, J. Sabatier, *et al.*, "Ignition of a confined high explosive under low velocity impact," *International Journal of Impact Engineering*, vol. 36, pp. 537-550, Apr 2009.

[22] J. P. Curtis, A. G. Jones, C. T. Hughes, and J. E. Reaugh, "Modeling Violent Reaction Following Low Speed Impact on Confined Explosives," *Shock Compression of Condensed Matter - 2011, Pts 1 and 2*, vol. 1426, 2012.

[23] H. Czerski and W. G. Proud, "Relationship between the morphology of granular cyclotrimethylene-trinitramine and its shock sensitivity," *Journal of Applied Physics*, vol. 102, Dec 1 2007.

[24] S. G. Bardenhagen, H. Luo, R. W. Armstrong, and H. Lu, "Detailed Characterization of Pbx Morphology for Mesoscale Simulations," *Shock Compression of Condensed Matter - 2011, Pts 1 and 2*, vol. 1426, 2012.

[25] C. B. Skidmore, D. S. Phillips, S. F. Son, and B. W. Asay, "Characterization of HMX particles in PBX 9501," *Shock Compression of Condensed Matter - 1997,* vol. 429, pp. 579-582, 1998.

[26] G. M. Swallowe and J. E. Field, "Effect of polymers on the drop-weight sensitiveness of explosives," in *7th International Symposium on Detonation*, Annapolis, Maryland, 1981, pp. 24-35.

[27] E. J. Welle, C. D. Molek, R. R. Wixom, and P. Samuels, "Microstructural effects on the ignition behavior of HMX," *Journal of Physics: Conference Series,* vol. 500, p. 052049, 2014.

[28] J. E. Field, N. K. Bourne, S. J. P. Palmer, S. M. Walley, J. Sharma, and B. C. Beard, "Hot-Spot Ignition Mechanisms for Explosives and Propellants [and Discussion]," *Philosophical Transactions: Physical Sciences and Engineering,* vol. 339, pp. 269-283, 1992.

[29] N. Semenoff, "Kinetics of Chain Reactions," *Chemical Reviews,* vol. 6, pp. 347-379, 1929/10/01 1929.

[30] D. A. Frank-Kamenetskii, *Zhurnal Fizicheskoi Khimii,* vol. 13, 1939.

[31] P. H. Thomas, "On the Thermal Conduction Equation for Self-Heating Materials with Surface Cooling," *Transactions of the Faraday Society,* vol. 54, pp. 60-65, 1958.

[32] T. Boddington, P. Gray, W. Kordylewski, and S. K. Scott, "Thermal Explosions with Extensive Reactant Consumption - a New Criterion for Criticality," *Proceedings of the Royal Society of London Series a-Mathematical Physical and Engineering Sciences,* vol. 390, pp. 13-30, 1983.

[33] C. M. Tarver, S. K. Chidester, and A. L. Nichols, "Critical conditions for impact- and shock-induced hot spots in solid explosives," *Journal of Physical Chemistry,* vol. 100, pp. 5794-5799, Apr 4 1996.

[34] C. M. Tarver and T. D. Tran, "Thermal decomposition models for HMX-based plastic bonded explosives," *Combustion and Flame,* vol. 137, pp. 50-62, Apr 2004.

[35] B. F. Henson, B. W. Asay, L. B. Smilowitz, and P. M. Dickson, "Ignition chemistry in HMX from thermal explosion to detonation," *Shock Compression of Condensed Matter-2001, Pts 1 and 2, Proceedings,* vol. 620, pp. 1069-1072, 2002.

[36] F. E. Walker and R. J. Wasley, "Critical Energy for Shock Initiation of Heterogeneous Explosives," *Explosivstoffe,* vol. 17, pp. 9-13, 1969.

[37] H. R. James, "An extension to the critical energy criterion used to predict shock initiation thresholds," *Propellants Explosives Pyrotechnics,* vol. 21, pp. 8-13, Feb 1996.

[38] D. J. Benson, "Computational methods in Lagrangian and Eulerian hydrocodes," *Computer Methods in Applied Mechanics and Engineering,* vol. 99, pp. 235-394, 1992.

[39] D. J. Benson and P. Conley, "Eulerian finite-element simulations of experimentally acquired HMX microstructures," *Modelling and Simulation in Materials Science and Engineering,* vol. 7, pp. 333-354, May 1999.

[40] M. R. Baer, "Modeling heterogeneous energetic materials at the mesoscale," *Thermochimica Acta,* vol. 384, pp. 351-367, Feb 25 2002.

[41] R. Menikoff, "Granular explosives and initiation sensitivity," Los Alamos National Laboratory2000.

[42] J. Zhang, T. L. Jackson, J. D. Buckmaster, and J. B. Freund, "Numerical modeling of shock-to-detonation transition in energetic materials," *Combustion and Flame,* vol. 159, pp. 1769-1778, Apr 2012.

[43] N. K. Rai and H. S. Udaykumar, "Mesoscale simulation of reactive pressed energetic materials under shock loading," *Journal of Applied Physics,* vol. 118, p. 245905, 2015.

[44] Y.-Q. Wu and F.-L. Huang, "A micromechanical model for predicting combined damage of particles and interface debonding in PBX explosives," *Mechanics of Materials,* vol. 41, pp. 27-47, Jan 2009.

[45] C. Gruau and D. Picart, "Numerical prediction of high explosive ignition under low velocity impact," *Foundations Civil and Environmental Eng,* vol. 12, pp. 33-48, 2008.

[46] R. Panchadhara and K. A. Gonthier, "Mesoscale analysis of volumetric and surface dissipation in granular explosive induced by uniaxial deformation waves," *Shock Waves,* vol. 21, pp. 43-61, Feb 2011.

[47] J. Gilbert, S. Chakravarthy, and K. A. Gonthier, "Computational analysis of hot-spot formation by quasi-steady deformation waves in porous explosive," *Journal of Applied Physics,* vol. 113, May 21 2013.

[48] C. W. Hirt, A. A. Amsden, and J. L. Cook, "An arbitrary Lagrangian-Eulerian computing method for all flow speeds," *Journal of Computational Physics,* vol. 14, pp. 227-253, 1974/03/01 1974.

[49] A. Robinson, T. Brunner, S. Carroll, R. Drake, C. Garasi, T. Gardiner, *et al.*, "ALEGRA: An Arbitrary Lagrangian-Eulerian Multimaterial, Multiphysics Code," presented at the 46th AIAA Aerospace Sciences Meeting and Exhibit, 2008.

[50] J. M. Owen and M. Shashkov, "Arbitrary Lagrangian Eulerian remap treatments consistent with staggered compatible total energy conserving Lagrangian methods," *Journal of Computational Physics,* vol. 273, pp. 520-547, 9/15/ 2014.

[51] Z.-Y. Zhu, B. Ma, C.-M. Tang, and X.-L. Cheng, "Molecular dynamic simulation of thermite reaction of Al nanosphere/Fe2O3 nanotube," *Physics Letters A,* vol. 380, pp. 194-199, 1/8/ 2016.

[52] R. M. Eason and T. D. Sewell, "Molecular Dynamics Simulations of the Collapse of a Cylindrical Pore in the Energetic Material α-RDX," *Journal of Dynamic Behavior of Materials,* vol. 1, pp. 423-438, 2015.

[53] K. Lee, K. Joshi, S. Chaudhuri, and D. S. Stewart, "Mirrored continuum and molecular scale simulations of the ignition of high-pressure phases of RDX," *The Journal of Chemical Physics,* vol. 144, p. 184111, 2016.

[54] K. Kline, Y. Horie, J. J. Dick, and W. Wang, "Impact Response of PBX 9501 Below 2 GPA," *AIP Conference Proceedings,* vol. 620, pp. 411-414, 2002.

[55] L. I. Jun-Ling, F. U. Hua, T. A. N. Duo-Wang, L. U. Fang-Yun, and C. H. E. N. Rong, "Fracture Behaviour Investigation into a Polymer-Bonded Explosive," *Strain,* vol. 48, pp. 463-473, 2012.

[56] Z. P. Tang and W. W. Wang, "Discrete element modeling for shock processes of heterogeneous materials," *Shock Compression of Condensed Matter-2001, Pts 1 and 2, Proceedings,* vol. 620, pp. 679-684, 2002.

[57] G. J. Ball, "A Free-Lagrange method for unsteady compressible flow: Simulation of a confined cylindrical blast wave," *Shock Waves,* vol. 5, pp. 311-325, Feb 1996.

[58] G. J. Ball, B. P. Howell, T. G. Leighton, and M. J. Schofield, "Shock-induced collapse of a cylindrical air cavity in water: a Free-Lagrange simulation," *Shock Waves,* vol. 10, pp. 265-276, Sep 2000.

[59] N. Bourne and J. Field, "Shock-induced collapse of single cavities in liquids," *Journal of Fluid Mechanics,* vol. 244, pp. 225-240, 1992.

[60] D. D. Dlott, "New Developments in the Physical Chemistry of Shock Compression," *Annual Review of Physical Chemistry, Vol 62,* vol. 62, pp. 575-597, 2011.

[61] J. von Neumann and R. D. Richtmyer, "A Method for the Numerical Calculation of Hydrodynamic Shocks," *Journal of Applied Physics,* vol. 21, pp. 232-237, 1950.

[62] S. B. Segletes, "Thermodynamic stability of the Mie–Grüneisen equation of state, and its relevance to hydrocode computations," *Journal of Applied Physics,* vol. 70, pp. 2489-2499, 1991.

[63] T. J. Ahrens, D. L. Anderson, and A. E. Ringwood, "Equations of state and crystal structures of high-pressure phases of shocked silicates and oxides," *Reviews of Geophysics,* vol. 7, pp. 667-707, 1969.

[64] L. Davison, *Fundamentals of Shock Wave Propagation in Solids (Chap. 3)*: Springer Berlin Heidelberg, 2008.

[65] L. Davison, *Fundamentals of Shock Wave Propagation in Solids (Chap. 13)*: Springer Berlin Heidelberg, 2008.

[66] R. Menikoff and M. S. Shaw, "Review of the Forest fire model for high explosives," *Combustion Theory and Modelling*, vol. 12, pp. 569-604, 2008.

[67] R. Menikoff and M. S. Shaw, "Reactive burn models and ignition & growth concept," *New Models and Hydrocodes for Shock Wave Processes in Condensed Matter*, vol. 10, 2010.

[68] Y. Horie and Y. Hamate, "A new approach to the reactive burn modeling of heterogeneous explosives," *Materials Science Forum*, vol. 465-466, pp. 1-12, 2004.

[69] J. Dienes and J. Kershner, "Multiple-shock initiation via statistical crack mechanics," Los Alamos National Lab., NM (United States)1998.

[70] J. K. Dienes, J. Middleditch, J. D. Kershner, Q. Zuo, and A. Starobin, "Progress in statistical crack mechanics: An approach to initiation," in *Proceedings of the 12th Symposium (International) on Detonation*, 2002.

[71] J. K. Dienes, Q. H. Zuo, and J. D. Kershner, "Impact initiation of explosives and propellants via statistical crack mechanics," *Journal of the Mechanics and Physics of Solids*, vol. 54, pp. 1237-1275, Jun 2006.

[72] A. L. Nichols III and C. M. Tarver, "A statistical hot spot reactive flow model for shock initiation and detonation of solid high explosives," in *Twelfth International Symposium on Detonation, Office of Naval Research, San Diego, CA*, 2002.

[73] Y. Hamate and Y. Horie, "A Statistical Approach on Mechanistic Modeling of High-Explosive Ignition," *AIP Conference Proceedings,* vol. 706, pp. 335-338, 2004.

[74] Y. Hamate and Y. Horie, "Ignition and detonation of solid explosives: a micromechanical burn model," *Shock Waves,* vol. 16, pp. 125-147, Dec 2006.

[75] G. N. Hassold and D. J. Srolovitz, "Brittle-Fracture in Materials with Random Defects," *Physical Review B,* vol. 39, pp. 9273-9281, May 1 1989.

[76] P. M. Duxbury, S. G. Kim, and P. L. Leath, "Size effect and statistics of fracture in random materials," *Materials Science and Engineering: A,* vol. 176, pp. 25-31, 1994.

[77] J. Andersons, E. Poriķe, and E. Spārniņš, "The effect of mechanical defects on the strength distribution of elementary flax fibres," *Composites Science and Technology,* vol. 69, pp. 2152-2157, 2009.

[78] V. V. Silberschmidt and J. L. Chaboche, "The Effect of Material Stochasticity on Crack Damage Interaction and Crack-Propagation," *Engineering Fracture Mechanics,* vol. 48, pp. 379-387, Jun 1994.

[79] J. N. Plohr, B. E. Clements, and F. L. Addessio, "Dynamically driven phase transformations in damaged composite materials," *Shock Compression of Condensed Matter - 2005, Pts 1 and 2,* vol. 845, pp. 266-269, 2006.

[80] H. Tan, Y. Huang, C. Liu, G. Ravichandran, and G. H. Paulino, "Constitutive behaviors of composites with interface debonding: the extended Mori-Tanaka method for uniaxial tension," *International Journal of Fracture,* vol. 146, pp. 139-148, Aug 2007.

[81] H. Tan, C. Liu, Y. Huang, and P. H. Geubelle, "The cohesive law for the particle/matrix interfaces in high explosives," *Journal of the Mechanics and Physics of Solids,* vol. 53, pp. 1892-1917, Aug 2005.

[82] K. Yanase and J. W. Ju, "Effective Elastic Moduli of Spherical Particle Reinforced Composites Containing Imperfect Interfaces," *International Journal of Damage Mechanics,* vol. 21, pp. 97-127, Jan 2012.

[83] M. Ostoja-Starzewski, P. Y. Sheng, and I. Jasiuk, "Influence of Random Geometry on Effective Properties and Damage Formation In Composite Materials," *Journal of Engineering Materials and Technology,* vol. 116, pp. 384-391, 1994.

[84] A. J. Goupee and S. S. Vel, "Multiscale thermoelastic analysis of random heterogeneous materials Part II: Direct micromechanical failure analysis and multiscale simulations," *Computational Materials Science,* vol. 48, pp. 39-53, Mar 2010.

[85] S. S. Vel and A. J. Goupee, "Multiscale thermoelastic analysis of random heterogeneous materials Part I: Microstructure characterization and homogenization of material properties," *Computational Materials Science,* vol. 48, pp. 22-38, Mar 2010.

[86] A. M. Freudenthal, "Statistical Approach to Brittle Fracture," in *Fracture : An Advanced Treaties*. vol. 2, H. Liebowitz, Ed., ed New York and London: Academic Press, 1971.

[87] A. Barua and M. Zhou, "A Lagrangian framework for analyzing microstructural level response of polymer-bonded explosives," *Modelling and Simulation in Materials Science and Engineering,* vol. 19, p. 055001, Jul 2011.

[88] D. A. Frank-Kamenetskii, *Diffusion and Heat Exchange in Chemical Kinetics*. New York: Plenum Press, 1969.

[89] M. R. Baer, R. J. Gross, J. W. Nunziato, and E. A. Igel, "An Experimental and Theoretical-Study of Deflagration-to-Detonation Transition (Ddt) in the Antigranulocytes Explosive, Cp," *Combustion and Flame,* vol. 65, pp. 15-30, Jul 1986.

[90] P. E. Luebcke, P. M. Dickson, and J. E. Field, "An Experimental Study of the Deflagration-To-Detonation Transition in Granular Secondary Explosives," *Proceedings: Mathematical and Physical Sciences,* vol. 448, pp. 439-448, 1995.

[91] R. Menikoff, "Compaction wave profiles in granular HMX," in *Shock Compression of Condensed Matter*, Melville, 2002, pp. 979-982.

[92] A. M. Grishkin, L. V. Dubnov, V. Y. Davidov, Y. A. Levshina, and T. N. Mikhailova, "Effect of Powdered Aluminum Additives on the Detonation Parameters of High Explosives," *Combustion Explosion and Shock Waves,* vol. 29, pp. 239-245, Mar-Apr 1993.

[93] T. Belytschko, W. K. Liu, B. Moran, and K. Elkhodary, "Chapter 4. Lagrangian Meshes," in *Nonlinear finite elements for continua and structures*, ed: John Wiley & Sons, 2013.

[94] T. Belytschko, R. L. Chiapetta, and H. D. Bartel, "Efficient large scale non-linear transient analysis by finite elements," *International Journal for Numerical Methods in Engineering*, vol. 10, pp. 579-596, 1976.

[95] X. P. Xu and A. Needleman, "Numerical Simulations of Fast Crack-Growth in Brittle Solids," *Journal of the Mechanics and Physics of Solids,* vol. 42, pp. 1397-&, Sep 1994.

[96] X. P. Xu and A. Needleman, "Numerical simulations of dynamic crack growth along an interface," *International Journal of Fracture,* vol. 74, pp. 289-324, 1996.

[97] G. T. Camacho and M. Ortiz, "Computational modelling of impact damage in brittle materials," *International Journal of Solids and Structures,* vol. 33, pp. 2899-2938, Aug 1996.

[98] P. Rahul-Kumar, A. Jagota, S. J. Bennison, S. Saigal, and S. Muralidhar, "Polymer interfacial fracture simulations using cohesive elements," *Acta Materialia,* vol. 47, pp. 4161-4169, Nov 12 1999.

[99] J. Zhai, V. Tomar, and M. Zhou, "Micromechanical simulation of dynamic fracture using the cohesive finite element method," *Journal of Engineering Materials and Technology-Transactions of the Asme,* vol. 126, pp. 179-191, Apr 2004.

[100] A. C. Landerville, M. W. Conroy, M. M. Budzevich, Y. Lin, C. T. White, and I. I. Oleynik, "Equations of state for energetic materials from density functional theory with van der Waals, thermal, and zero-point energy corrections," *Applied Physics Letters,* vol. 97, p. 251908, Dec 20 2010.

[101] D. M. Dattelbaum and L. L. Stevens, "Chap 4. Equations of State of Binders and Related Polymers," in *Static Compression of Energetic Materials*, S. M. Peiris and G. J. Piermarini, Eds., ed Virginia, USA: Springer, 2008, pp. 127-202.

[102] M. Zhou, A. Needleman, and R. J. Clifton, "Finite-Element Simulations of Shear Localization in Plate Impact," *Journal of the Mechanics and Physics of Solids,* vol. 42, pp. 423-458, Mar 1994.

[103] J. J. Dick, D. E. Hooks, R. Menikoff, and A. R. Martinez, "Elastic-plastic wave profiles in cyclotetramethylene tetranitramine crystals," *Journal of Applied Physics,* vol. 96, pp. 374-379, Jul 2004.

[104] E. M. Mas, B. E. Clements, B. Blumenthal, C. M. Cady, G. T. Gray, and C. Liu, "A Viscoelastic Model for PBX Binders," *AIP Conference Proceedings,* vol. 620, pp. 661-664, 2002.

[105] L. Green, A. Weston, and J. Van Velkinburg, "Mechanical and Frictional Behavior of Skid Test Hemispherical Billets," California Univ., Livermore. Lawrence Livermore Lab.1971.

[106] P. M. Dickson, G. R. Parker, L. B. Smilowitz, J. M. Zucker, and B. W. Asay, "Frictional Heating and Ignition of Energetic Materials," *AIP Conference Proceedings,* vol. 845, pp. 1057-1060, 2006.

[107] A. Barua, S. Kim, Y. Horie, and M. Zhou, "Ignition criterion for heterogeneous energetic materials based on hotspot size-temperature threshold," *Journal of Applied Physics,* vol. 113, p. 064906, Feb 14 2013.

[108] A. Barua, S. Kim, Y. Horie, and M. Zhou, "Prediction of probabilistic ignition behavior of polymer-bonded explosives from microstructural stochasticity," *Journal of Applied Physics,* vol. 113, p. 184907, 2013.

[109] A. Barua, Y. Horie, and M. Zhou, "Energy localization in HMX-Estane polymer-bonded explosives during impact loading," *Journal of Applied Physics,* vol. 111, p. 054902, Mar 2012.

[110] A. Barua, Y. Horie, and M. Zhou, "Microstructural level response of HMX-Estane polymer-bonded explosive under effects of transient stress waves," *Proceedings of the Royal Society a-Mathematical Physical and Engineering Sciences,* vol. 468, pp. 3725-3744, Nov 2012.

[111] A. Barua and M. Zhou, "Computational analysis of temperature rises in microstructures of HMX-Estane PBXs," *Computational Mechanics,* vol. 52, pp. 151-159, Jul 2013.

[112] M. R. Baer, D. K. Gartling, and P. E. DesJardin, "Probabilistic models for reactive behaviour in heterogeneous condensed phase media," *Combustion Theory and Modelling,* vol. 16, pp. 75-106, 2012.

[113] C. R. Siviour, P. R. Laity, W. G. Proud, J. E. Field, D. Porter, P. D. Church, *et al.*, "High strain rate properties of a polymer-bonded sugar: their dependence on applied and internal constraints," *Proceedings of the Royal Society a-Mathematical Physical and Engineering Sciences,* vol. 464, pp. 1229-1255, May 8 2008.

[114] W. Weibull, "A Statistical Distribution Function of Wide Applicability," *Journal of Applied Mechanics,* vol. 18, pp. 293-297, 1951.

[115] R. W. Armstrong, C. S. Coffey, V. F. Devost, and W. L. Elban, "Crystal Size Dependence for Impact Initiation of Cyclotrimethylenetrinitramine Explosive," *Journal of Applied Physics,* vol. 68, pp. 979-984, Aug 1 1990.

[116] P. Howe, R. Frey, B. Taylor, and V. Boyle, "Shock initiation and the critical energy concept," in *Sixth Symposium (International) on Detonation*, Coronado, California, 1976.

[117] S. Lecume, C. Spyckerelle, and F. Sommer, "Structure of Pristine Crystal Defects Revealed by AFM and Microtomography," *AIP Conference Proceedings,* vol. 706, pp. 997-1000, 2004.

[118] A. Chakravarty, M. J. Gifford, M. W. Greenaway, W. G. Proud, and J. E. Field, "Factors Affecting Shock Sensitivity of Energetic Materials," *AIP Conference Proceedings,* vol. 620, pp. 1007-1010, 2002.

[119] H. R. James, "Shock Initiation Thresholds for Insensitive High Explosives," *AIP Conference Proceedings,* vol. 955, pp. 937-940, 2007.

[120] H. R. James, P. J. Haskins, and M. D. Cook, "Prompt Shock Initiation of Cased Explosives by Projectile Impact," *Propellants, Explosives, Pyrotechnics,* vol. 21, pp. 251-257, 1996.

[121] R. Wild and E. von Collani, "Modelling of Explosives Sensitivity Part 2: The Weibull-Model," *Economic Quality Control,* vol. 17, pp. 195-220, 2002.

[122] R. K. Eckhoff, M. Ngo, and W. Olsen, "On the minimum ignition energy (MIE) for propane/air," *Journal of Hazardous Materials,* vol. 175, pp. 293-297, Mar 15 2010.

[123] G. W. Snedecor and W. G. Cochran, *Statistical Methods*, 8th ed.: Iowa State University Press, 1989.

[124] B. A. Khasainov, B. S. Ermolaev, H. N. Presles, and P. Vidal, "On the effect of grain size on shock sensitivity of heterogeneous high explosives," *Shock Waves,* vol. 7, pp. 89-105, Apr 1997.

[125] R. J. Spear and V. Nanut, "Reversal of particle size/shock sensitivity relationship at small particle size for pressed heterogeneous explosives under sustained shock loading," *Journal of Energetic Materials,* vol. 7, pp. 77-114, 1989/03/01 1989.

[126] R. Wild and E. von Collani, "Modelling of explosives sensitivity part 1: The Bruceton method," *Economic Quality Control,* vol. 17, pp. 113-122, 2002.

[127] Y. Li and M. Zhou, "Prediction of fracture toughness of ceramic composites as function of microstructure: I. Numerical simulations," *Journal of the Mechanics and Physics of Solids,* vol. 61, pp. 472-488, Feb 2013.

[128] K. Terao, *Irreversible Phenomena: Ignitions, Combustion and Detonation Waves (Chap. 3)*: Springer, 2007.

[129] J. Gilbert and K. Gonthier, "Meso-Scale Computation of Uniaxial Waves in Granular Explosives-Analysis of Deformation Induced Ignition," in *50th AIAA Aerospace Sciences Meeting including the New Horizons Forum and Aerospace Exposition*, 2012.

[130] M. Tsue, T. Kadota, D. Segawa, and H. Yamasaki, "Statistical analysis of onset of microexplosion for an emulsion droplet," *Symposium (International) on Combustion,* vol. 26, pp. 1629-1635, // 1996.

[131] S. K. Chidester, C. M. Tarver, and R. Garza, "Low amplitude impact testing and analysis of pristine and aged solid high explosives," in *Eleventh (International) Symposium on Detonation*, 1998.

[132] J. J. Dick, "Measurement of the Shock Initiation Sensitivity of Low-Density Hmx," *Combustion and Flame,* vol. 54, pp. 121-129, 1983.

[133] D. Preston, G. Brown, C. B. Skidmore, B. L. Reardon, and D. A. Parkinson, "Small-scale explosives sensitivity saftey testing: A departure from Bruceton," *AIP Conference Proceedings,* vol. 1426, pp. 713-716, 2012.

[134] Y. Ko, R. W. Anderson, and V. S. Arpaci, "Spark ignition of propane-air mixtures near the minimum ignition energy: Part I. An experimental study," *Combustion and Flame,* vol. 83, pp. 75-87, 1991/01/01 1991.

[135] H. Rinne, "Chap. 11: Parameter estimation Maximum likelihood approaches," in *The Weibull Distribution: A Handbook,* ed: CRC Press, 2008.

[136] D. Hayes and D. Mitchell, "Constitutive equation for the shock response of porous hexanitrostilbene (HNS) explosive," Sandia Labs., Albuquerque, NM (USA) SAND-78-0035C, 1978.

[137] L.-J. Wen, Z.-P. Duan, L.-S. Zhang, Z.-Y. Zhang, Z.-C. Ou, and F.-L. Huang, "Effects of HMX Particle Size on the Shock Initiation of PBXC03 Explosive," *Int. J. Nonlinear Sci. Numer. Simul.,* vol. 13, p. 189, 2012.

[138] Y. Hamate, "A computational study of microstructure effects on shock ignition sensitivity of pressed RDX," *AIP Conference Proceedings,* vol. 955, pp. 923-926, 2007.

[139] S. Kim, A. Barua, Y. Horie, and M. Zhou, "Ignition probability of polymer-bonded explosives accounting for multiple sources of material stochasticity," *Journal of Applied Physics,* vol. 115, p. 174902, 2014.

[140] S. Chakravarthy, K. A. Gonthier, and R. Panchadhara, "Analysis of mesoscale heating by piston supported waves in granular metalized explosive," *Modelling and Simulation in Materials Science and Engineering,* vol. 21, p. 055016, 2013.

[141] C. Liu, "Specific surface: a missing parameter in high-explosive modeling," Los Alamos National Laboratory (LANL), Los Alamos, NM (United States) LA-UR-14-20512, 2003.

[142] E. M. Mas, B. E. Clements, A. Ionita, and P. Peterson, "Finite Element Method Calculations on Statistically Consistent Microstructures of PBX 9501," *AIP Conference Proceedings,* vol. 845, pp. 487-490, 2006.

[143] J. I. McCool, *Using the Weibull Distribution*: John Wiley & Sons, Inc., 2012.

[144] S. El Otmani and A. Maul, "Probability distributions arising from nested Gaussians," *Comptes Rendus Mathematique,* vol. 347, pp. 201-204, Feb 2009.

[145] G. K. Miller, *Probability: Modeling and Applications to Random Processes*, 1 ed.: Wiley, 2006.

[146] C. Subero-Couroyer, M. Ghadiri, N. Brunard, and F. Kolenda, "Weibull analysis of quasi-static crushing strength of catalyst particles," *Chemical Engineering Research & Design,* vol. 81, pp. 953-962, Sep 2003.

[147] S. Kim, Y. Horie, and M. Zhou, "Ignition Desensitization of PBX via Aluminization," *Metallurgical and Materials Transactions A,* vol. 46, pp. 4578-4586, 2015/10/01 2015.

[148] V. Prakash, V. K. Phadke, R. K. Sinha, and H. Singh, "Influence of aluminium on performance of HTPB-based aluminised PBXs," *Defence Science Journal,* vol. 54, pp. 475-482, Oct 2004.

[149] M. Radwan, "Explosive characteristics of aluminized plastic bonded explosives based on octogen and polyurethane binder," in *32nd Int'l Annual Conference of ICT*, Karlsruhe, Germany, 2001, p. 44.

[150] W. A. Trzcinski, S. Cudzilo, and L. Szymanczyk, "Studies of detonation characteristics of aluminum enriched RDX compositions," *Propellants Explosives Pyrotechnics,* vol. 32, pp. 392-400, Oct 2007.

[151] M. F. Gogulya, A. Y. Dolgoborodov, and M. A. Brazhnikov, "Fine structure of detonation waves in HMX-Al mixtures," *Chemical Physics Reports,* vol. 17, pp. 51-54, 1998.

[152] A. S. Kumar, V. B. Rao, R. K. Sinha, and A. S. Rao, "Evaluation of Plastic Bonded Explosive (PBX) Formulations Based on RDX, Aluminum, and HTPB for Underwater Applications," *Propellants, Explosives, Pyrotechnics,* vol. 35, pp. 359-364, 2010.

[153] P. P. Vadhe, R. B. Pawar, R. K. Sinha, S. N. Asthana, and A. S. Rao, "Cast aluminized explosives," *Combustion Explosion and ShockWaves,* vol. 44, pp. 461-477, Jul-Aug 2008.

[154] Y. L. Zhu, H. Huang, H. Ren, and Q. J. Jiao, "Influence of Aluminum Particle Size on Thermal Decomposition of RDX," *Journal of Energetic Materials,* vol. 31, pp. 178-191, 2013.

[155] C. G. Rumchik and J. L. Jordan, "Effect of Aluminum Particle Size on the High Strain Rate Properties of Pressed Aluminized Explosives," *AIP Conference Proceedings,* vol. 955, pp. 795-798, 2007.

[156] N. S. Brar, V. S. Joshi, and B. W. Harris, "Constitutive Model Constants for Al7075-T651 and Al7075-T6," *Shock Compression of Condensed Matter - 2009, Pts 1 and 2*, vol. 1195, pp. 945-948, 2009.

[157] J. F. Moxnes, T. L. Jensen, and E. Unneberg, "Energetic Measures of Effectiveness of Aluminized Explosives," *Advanced Studies in Theoretical Physics*, vol. 7, pp. 1051–1069, 2013.

[158] M. F. Gogulya, M. N. Makhov, A. Y. Dolgoborodov, M. A. Brazhnikov, V. I. Arkhipov, and V. G. Shchetinin, "Mechanical sensitivity and detonation parameters of aluminized explosives," *Combustion Explosion and Shock Waves*, vol. 40, pp. 445-457, Jul-Aug 2004.

[159] L. Orth-Farrell and H. Krier, "Simulation of Detonation in High Explosives with Aluminum Particles," *Combustion Science and Technology*, vol. 161, pp. 69-88, 2000/12/01 2000.

[160] Y. Horie, "Hot Spots, High Explosives Ignition, and Material Microstructure," *Materials Science Forum*, vol. 767, pp. 3-12, 2014.

[161] M. Gresshoff and C. A. Hrousis, "Probabilistic Shock Threshold Criterion," in *14th International Detonation Symposium*, Coeur d'Alene, ID, 2010.

[162] H. R. James and B. D. Lambourn, "On the systematics of particle velocity histories in the shock-to-detonation transition regime," *Journal of Applied Physics*, vol. 100, p. 084906, 2006.

[163] A. G. Merzhanov and V. G. Abramov, "Thermal Explosion of Explosives and Propellants. A review," *Propellants, Explosives, Pyrotechnics*, vol. 6, pp. 130-148, 1981.

[164] B. D. Lambourn, H. J. Lacy, C. A. Handley, and H. R. James, "A simple model for the pressure field from a distribution of hotspots," *Journal of Physics: Conference Series,* vol. 500, p. 052023, 2014.

[165] C. D. Molek, E. J. Welle, R. R. Wixom, M. B. Ritchey, P. Samuels, and Y. Horie, "Microstructural Characterization of Pressed HMX Material Sets at Differing Densities," in *APS SCCM-2015*, Tampa, FL, In press.

[166] C. Liu, "On the minimum size of representative volume element: An experimental investigation," *Experimental Mechanics,* vol. 45, pp. 238-243, 2005/06/01 2005.

[167] R. R. Wixom, A. S. Tappan, A. L. Brundage, R. Knepper, M. B. Ritchey, J. R. Michael, *et al.*, "Characterization of pore morphology in molecular crystal explosives by focused ion-beam nanotomography," *Journal of Materials Research,* vol. 25, pp. 1362-1370, Jul 2010.

[168] X. Yang, T. Zhou, and C. Chen, "Effective elastic modulus and atomic stress concentration of single crystal nano-plate with void," *Computational Materials Science,* vol. 40, pp. 51-56, 2007.

[169] R. J. Hudson, "Investigating the factors influencing RDX shock sensitivity," PhD thesis, Applied Science and Engineering, Cranfield University, 2012.

[170] R. J. Hudson, P. Zioupos, and P. P. Gill, "Investigating the Mechanical Properties of RDX Crystals Using Nano-Indentation," *Propellants, Explosives, Pyrotechnics,* vol. 37, pp. 191-197, 2012.

[171] T. D. Sewell, R. Menikoff, D. Bedrov, and G. D. Smith, "A molecular dynamics simulation study of elastic properties of HMX," *The Journal of Chemical Physics,* vol. 119, pp. 7417-7426, 2003.

[172] L. S. Dimas, D. Veneziano, T. Giesa, and M. J. Buehler, "Random Bulk Properties of Heterogeneous Rectangular Blocks With Lognormal Young's Modulus: Effective Moduli," *Journal of Applied Mechanics,* vol. 82, pp. 011003-011003, 2015.

[173] C. M. May and C. M. Tarver, "Modeling Short Shock Pulse Duration Initiation of LX-16 and LX-10 Charges," *AIP Conference Proceedings,* vol. 1195, pp. 275-278, 2009.

[174] D. B. Hardin, "The Role of Viscoplasticity in the Deformation and Ignition Response of Polymer Bonded Explosives," Doctor of Philosophy, Mechanical Engineering, Georgia Institute of Technology, 2015.

[175] J. C. Gump and S. M. Peiris, "Isothermal equations of state of beta octahydro-1,3,5,7-tetranitro-1,3,5,7-tetrazocine at high temperatures," *Journal of Applied Physics,* vol. 97, p. 053513, 2005.

[176] C.-S. Yoo and H. Cynn, "Equation of state, phase transition, decomposition of beta-HMX (octahydro-1,3,5,7-tetranitro-1,3,5,7-tetrazocine) at high pressures," *The Journal of Chemical Physics,* vol. 111, pp. 10229-10235, 1999.

[177] R. Landshoff, "A numerical method for treating fluid flow in the presence of shocks," DTIC Document1955.

[178] J. Campbell and R. Vignjevic, "Chap. 19 Artificial Viscosity Methods for Modelling Shock Wave Propagation," in *Predictive Modeling of Dynamic Processes*, ed: Springer, 2009, pp. 349-365.

[179] R. L. Simpson, F. H. Helm, and J. W. Kury, "Non-Reactive HMX Shock Hugoniot Data," *Propellants, Explosives, Pyrotechnics,* vol. 18, pp. 150-154, 1993.

[180] A. Migault, "Concepts of Shock Waves," in *Impacts on Earth*. vol. 505, D. Benest and C. Froeschlé, Eds., ed: Springer Berlin Heidelberg, 1998, pp. 79-112.

[181] A. R. McMillan, W. M. Isbell, and A. H. Jones, "High Pressure Shock Wave Attenuation," General Motors, Virginia DASA 2425, 1971.

[182] C. Wall and M. Franson, "Validation of a Pressed Pentolite Donor for the Large Scale Gap Test (LGST) at DSTO," Defence Science and Technology Organisation, Department of Defense, Austrailia2013.

[183] R. Khurana, P. C. Gautam, R. Rai, A. Kumar, A. C. Sharma, and M. Singh, "Studies on Shock Attenuation in Plastic Materials and Applications in Detonation Wave Shaping," *Journal of Physics: Conference Series,* vol. 377, p. 012051, 2012.

[184] E. J. Welle, C. D. Molek, R. R. Wixom, P. Samuels, and J. Langhals, "Microstructure effects on the initiation threshold behavior of HMX and PBXN-5," in *15th International Detonation Symposium*, 2014.

[185] N. J. Burnside, S. F. Son, B. W. Asay, and C. B. Skidmore, "Particle characterization of pressed granular HMX," in *Shock Compression of Condensed Matter*, 1997, p. 571.

[186] J. S. Christensen, M. Gresshoff, and K. J. McMullen, "Probabilistic shock threshold development for LX-17," in *15th International Detonation Symposium*, 2014.

[187] C. A. Honodel, J. R. Humphrey, R. C. Weingart, R. S. Lee, and P. Kramer, "Shock initiation of TATB formulations," in *Proceedings Seventh Symposium (International) on Detonation*, Annapolis, MD, 1981, pp. 425-434.

[188] A. C. Schwarz, "Study of factors which influence the shock-initiation sensitivity of hexanitrostilbene (HNS)," Sandia National Laboratories, Albuquerque, NM USA SANDBD-2372, 1981.

[189] A. C. Schwarz, "Shock initiation sensitivity of hexanitrostilbene (HNS)," in *Seventh Symposium (International) on Detonation*, Annapolis, Maryland (USA), 1981, pp. 1024-1028.

[190] C. D. Yarrington, S. F. Son, T. J. Foley, S. J. Obrey, and A. N. Pacheco, "Nano Aluminum Energetics: The Effect of Synthesis Method on Morphology and Combustion Performance," *Propellants Explosives Pyrotechnics,* vol. 36, pp. 551-557, Dec 2011.

[191] F. Sánchez, A. M. Bolarín, P. Molera, J. E. Mendoza, and M. Ocampo, "Relationship between particle size and manufacturing processing and sintered characteristics of iron powders," *Revista Latinoamericana de Metalurgia y Materiales,* vol. 23, pp. 35-40, 2003.

[192] R. N. Mulford and D. C. Swift, "Mesoscale modelling of shock initiation in HMX-based explosives," *Shock Compression of Condensed Matter-2001, Pts 1 and 2, Proceedings,* vol. 620, pp. 415-418, 2002.

[193] R. C. Weingart, R. K. Jackson, C. A. Honodel, and R. S. Lee, "Shock Initiation of Pbx-9404 by Electrically Driven Flyer Plates," *Propellants and Explosives,* vol. 5, pp. 158-162, 1980.

[194] H. K. Springer, C. M. Tarver, J. E. Reaugh, and C. M. May, "Investigating short-pulse shock initiation in HMX-based explosives with reactive meso-scale simulations," *Journal of Physics: Conference Series,* vol. 500, p. 052041, 2014.

[195] J. Roth, "Shock sensitivity and shock Hugoniots of high-density granular explosives," in *Fourth Symposium (International) on Detonation, White Oak*, 1970.

[196] S. P. Marsh, "LASL Shock Hugoniot data. Los Alamos series on dynamic material properties," *University of California, Berkeley, CA*, 1980.

[197] D. Swift, R. Mulford, R. Winter, P. Taylor, D. Salisbury, E. Harris, *et al.*, "Mesoscale modelling of reaction in HMX-based explosives," in *Twelfth International Detonation Symposium*, San Diego, CA, 2002, p. 967.

[198] D. S. Moore, S. D. McGrane, and D. J. Funk, "Ultrashort Laser Shock Dynamics," in *ShockWave Science and Technology Reference Library*, Y. Horie, Ed., ed Berlin, Heidelberg: Springer, 2007, pp. 47-104.

[199] J. Tucker, "A whole life assessment of extruded double base propellants," PhD, Department of Engineering and Applied Science, Cranfield University, 2013.

[200] D. B. Hayes, "A Pnt detonation criterion from thermal explosion theory," in *6th International Detonation Symposium*, Coronado, CA, 1976, pp. 95-100.

[201] E. F. Gittings, "Initiation of a solid explosive by a short-duration shock," in *Proc. Fourth Symp.(Int.) on Detonation*, Arlington, 1965, pp. 373-380.

[202] B. Trott and R. Jung, "Effect of pulse duration on the impact sensitivity of solid explosives," in *Proceedings Fifth Symposium (International) on Detonation*, Pasadena, CA, 1970, pp. 191-205.

[203] D. E. Christiansen and J. W. Taylor, "HE Sensitivity Study," Los Alamos Scientific Lab, Los Alamos, NM LA-5440-MS, 1973.

[204] M. R. Manaa, L. E. Fried, C. F. Melius, M. Elstner, and T. Frauenheim, "Decomposition of HMX at Extreme Conditions: A Molecular Dynamics Simulation," *The Journal of Physical Chemistry A,* vol. 106, pp. 9024-9029, 2002/10/01 2002.

[205] O. Sharia and M. M. Kuklja, "Modeling Thermal Decomposition Mechanisms in Gaseous and Crystalline Molecular Materials: Application to β-HMX," *The Journal of Physical Chemistry B,* vol. 115, pp. 12677-12686, 2011/11/10 2011.